A FIRST PRINCIPLES STUDY OF DEFECTS IN SEMICONDUCTORS

Submitted by Jonathan Paul Goss to the University of Exeter as a thesis for the degree of Doctor of Philosophy in Physics in the Faculty of Science, January 1997.

This thesis is available for the Library use on the understanding that it is copyright material and that no quotation from the thesis may be published without proper acknowledgement.

Declaration: I certify that all material in this thesis which is not my own work has been identified and that no material is included for which a degree has previously been conferred upon me,

Abstract

This thesis reports the results of *ab initio* calculations performed using AIMPRO, a local-spin-density-functional, real-space cluster code. The clusters are typically 70-200 atoms in size and are all hydrogen terminated to passivate the surface dangling bonds. Using this approach a large number of defects have been examined in diamond, silicon, and gallium arsenide.

Defects in diamond are of great interest from an optical point of view, and the properties of a range of vacancy-impurity complexes are examined in detail. Synthetic diamonds grown using transition metal catalysts exhibit pronounced optical features which have been correlated with nickel. Reported here are the structures of Ni point defects and Ni-impurity complexes.

Transition metals are also important impurities in Si due to the device implications. Substitutional Ni undergoes a subtle Jahn-Teller distortion in the negative charge state, which is reproduced in these calculations. Ni-H_2 complexes are also reported.

Finally, the use of C as an acceptor in GaAs has many advantages such as its low diffusivity and samples can be doped with high concentrations. However, C readily complexes with H to form electrically inactive centres. Reported here are the results of a study of the anharmonicity of the C-H stretch mode and the structures of di-carbon-hydrogen complexes that exhibit strongly polarised local vibrational modes.

Acknowledgements

I would like to thank the Physics Department and EPSRC for providing the necessary environment and funds for the duration of my PhD in Exeter.

I would very much like to acknowledge the following people for their contributions to my PhD.

First of all Bob Jones for his stalwart supervision, tuition and sense of humour. Also the AIMPRO-family: Malc, Pat, Chris (for whom I gratefully acknowledge top tips on EPR and groovy diagram - Fig. 3.2, LHS), and Sven for their diverse forms of rôle model. Spudman^{TM} [1], The-P***-Artist-Formally-Known-As-Lard and Stevie-B have made the contents of this thesis slightly less mystifying to me, as well as the consumption of C_2H_5OH increase exponentially. And there are all the others that have been involved somewhere down the line: Paul Sitch, Bernd, Vitor, Deepak, Joci, Antonio, Ben Hur, Gerd, Steve Maynard...

More generally, I have found my time at Exeter both more enlightening and more hazy in part due to my non-AIMPRO, Exeter-family: Big-Nose, Paul Rawlins, Will, Susie, GP, JMR, Mauro, 'Topher Townsley, Sai, Mike, Jonathan Warren, Tim, Elaine, Paul Wright, Huseyin, Mehmet, and too many others to mention.

I would like to thank my (real-life?) family: Prim, Sid, Dave and Jackie, for their support when I gave up a life of leisure in the NHS for three years hard labour in the salt mines.

Finally my (most heart-felt) thanks must go to long suffering Sarah for her constant support and encouragement since time began.

[1] *Serum sum, ergo sum*

Contents

Contents **4**

List of Publications **8**

List of Tables **10**

List of Figures **13**

1 Introduction **19**

2 Theory **23**

2.1 Introduction 23
2.2 The problem posed 24
2.3 The Born-Oppenheimer approximation 25
2.4 Hartree-Fock Theory 25
2.5 Parameterised Hartree-Fock methods 28
2.5.1 Complete neglect of differential overlap 29
2.5.2 CNDO/1 31
2.5.3 CNDO/2 31
2.5.4 Intermediate neglect of differential overlap 32
2.5.5 Neglect of diatomic differential overlap 32
2.5.6 Summary 32
2.6 Hartree-Fock theory of the homogeneous electron gas 33
2.7 Correlation 33
2.8 Density functional theory 34
2.9 The local density approximation 36
2.10 Determination of the Kohn-Sham orbitals 37
2.11 Pseudopotentials 37
2.12 AIMPRO methodology 40
2.12.1 Evaluation of the Hartree energy 41
2.12.2 Exchange-correlation energy 42

2.12.3 Arrival at the eigenvalue equation . . . 44
2.13 The self-consistent cycle . . . 45
2.13.1 The 'Fermi temperature' . . . 47
2.14 Structural optimisation . . . 47
2.14.1 Atomic forces . . . 48
2.14.2 Conjugate gradients optimisation . . . 48
2.15 Vibrational modes . . . 49
2.15.1 Musgrave-Pople valence force potentials . . . 50
2.15.2 Anharmonicity . . . 51
2.15.2.1 Quantifying anharmonicity . . . 51
2.15.2.2 Theoretical approach . . . 53
2.15.2.3 Electrical anharmonicity . . . 57
2.15.2.4 Theoretical evaluation of χ. . . . 58
2.15.3 Effective charges . . . 59
2.16 Multiplets . . . 60
2.17 Electronic transitions . . . 60
2.17.1 Transition states . . . 61
2.17.2 Radiative lifetimes . . . 61
2.18 Clusters . . . 61
2.19 Summary . . . 64

3 Experimental techniques 65
3.1 Introduction . . . 65
3.2 Localised vibrational mode spectroscopy . . . 66
3.2.1 Infra-red absorption . . . 66
3.2.2 Raman scattering . . . 70
3.2.3 Summary . . . 72
3.3 Electron paramagnetic resonance . . . 73
3.3.1 Dipolar magnetic moment . . . 73
3.3.2 Absorption and derivative outputs . . . 74
3.3.3 Nuclear Zeeman effect . . . 74
3.3.4 The hyperfine interaction . . . 75
3.3.5 Spin orbit coupling . . . 76
3.3.6 High spin centres . . . 76
3.3.7 Low symmetry defects . . . 76
3.3.8 Optical detection of magnetic resonance . . . 77
3.3.9 Summary . . . 77
3.4 Photoluminescence . . . 78

3.5 Deep level transient spectroscopy 82

4 Vacancy-X complexes in diamond 87
4.1 Introduction 87
4.2 The vacancy 89
4.3 Vacancy-nitrogen complexes 90
4.3.1 Cluster and basis. 91
4.3.2 The vacancy bordered by a N atom 92
4.3.3 The vacancy bordered by three N atoms 94
4.3.4 Conclusions 96
4.4 The vacancy-silicon complex 96
4.4.1 Cluster and basis. 97
4.4.2 Results 97
4.5 The vacancy-phosphorus complex. 99
4.5.1 Introduction 99
4.5.2 Cluster and basis. 100
4.5.3 Results 100
4.5.4 Summary 103
4.6 Vacancy-hydrogen complexes 103
4.6.1 Introduction 103
4.6.2 Cluster and basis 104
4.6.3 VH 105
4.6.4 VH_2 107
4.6.5 VH_3 and VH_4 109
4.6.6 Stabilities of VH_n 110
4.6.7 V_2H 111
4.6.8 Conclusion 111
4.7 Summary 112

5 Nickel and Ni-X centres in diamond and Si 114
5.1 Nickel in diamond 114
5.1.1 Introduction 114
5.1.2 Experimental background 115
5.1.2.1 Magnetic centres 115
5.1.2.2 Optical centres 116
5.1.3 Electronic structure of Ni in group IV semiconductors 117
5.1.4 Previous calculations 119
5.1.5 AIMPRO calculations 120
5.1.5.1 Cluster and basis 120

5.1.5.2 Nickel carbonyl . . . 121
5.1.5.3 Interstitial Ni^+ . . . 121
5.1.5.4 The Ni_i^+-B_s^- complex . . . 123
5.1.5.5 Substitutional Ni^- . . . 124
5.1.5.6 The Ni_s^--N_s^+ complex . . . 126
5.1.5.7 Substitutional Ni^+ . . . 127
5.1.5.8 The Ni_s^+-B_s^- complex . . . 128
5.1.5.9 Radiative lifetimes . . . 128
5.1.6 Conclusions . . . 130
5.2 Nickel and nickel-hydrogen complexes in Si . . . 133
5.2.1 Introduction . . . 133
5.2.2 Cluster and basis . . . 134
5.2.3 Results . . . 135
5.2.4 Conclusions . . . 139

6 Carbon-Hydrogen complexes in GaAs. 140
6.1 Introduction . . . 140
6.2 Anharmonic theory of the C_{As}-H complex. . . . 140
6.2.1 Introduction. . . . 140
6.2.2 Experimental background & previous theoretical studies. . . . 141
6.2.3 Clusters and basis. . . . 143
6.2.4 Prussic acid molecule: HCN . . . 143
6.2.5 The C_{As}-H stretch mode . . . 146
6.2.6 The intensity of the overtone . . . 150
6.2.7 Conclusions . . . 151
6.3 Theory of hydrogenated C_{As}-dimers. . . . 152
6.3.1 Clusters and basis. . . . 155
6.3.2 Results. . . . 155
6.3.2.1 The $(C_{As})_2$-H complex. . . . 156
6.3.2.2 The $(C_{As})_2$-H_2 complex. . . . 158
6.3.3 Conclusions. . . . 160

7 Conclusions 161

A Character tables 165

B Jahn-Teller distortions 166

References 168

List of Published Papers

Listed in reverse chronological order:

1. 'First principles theory of impurity-vacancy complexes in diamond', J. P. Goss, R. Jones, S. J. Breuer, P. R. Briddon, and S. Öberg, proceedings of the 23rd International Conference on the Physics of Semiconductors, 1996, pp. 2577-80, (World Scientific, Singapore, New Jersey, London, Hong Kong), ed. M. Scheffler and R. Zimmermann.
2. 'Is hydrogen anti bonded in hydrogenated GaAs:Mg?' R. Bouanani-Rabi, B. Pajot, C. P. Ewels, S. Öberg, J. Goss, R. Jones, Y. Nissim, B. Theys, and C. Blaauw. To be published in the proceedings of SLCS96, 'Shallow Level Centers in Semiconductors', Amsterdam, 1996.
3. 'The twelve line 1.682 eV luminescence center in diamond and the vacancy-silicon complex', J. Goss, R. Jones, S. J. Breuer, P. R. Briddon, and S. Öberg, Phys. Rev. Lett. **77**, 3041 (1996).
4. 'Limitations to n-type doping in diamond: the phosphorus-vacancy complex', R. Jones, J. E. Lowther, and J. Goss, Appl. Phys. Lett. **69**, 2489 (1996).
5. 'The nitrogen-pair oxygen defect in silicon', F. Berg Rasmussen, S. Öberg, R. Jones, C. Ewels, J. Goss, J. Miro, and P. Deák, NATO ARW 'Early Stages of Oxygen Precipitation in Silicon', ed. R. Jones, Kluwer Academic Press, p. 319.
6. 'Local modes of the H_2^* dimer in germanium', M. Budde, B. Bech Neilsen, R. Jones, J. Goss, and S. Öberg, Phys. Rev. B **54**, 5485 (1996).
7. 'The nitrogen-pair oxygen defect in Silicon', F. Berg Rasmussen, S. Öberg, R. Jones, C. Ewels, J. Goss, J. Miro, and P. Deák, Mat. Sci. Eng. B, **36**, 91-95 (1996).
8. 'Theory of nickel and nickel-hydrogen complexes in silicon', R. Jones , S. Öberg, J. Goss, P. R. Briddon, and A. Resende, Phys. Rev. Lett **75**, 2734 (1995).
9. 'Ni complexes in diamond', J. Goss, A. Resende, R. Jones, S. Öberg, and P. R. Briddon, Mat. Sci. Forum Vol. **196-201**, pp 67-72 (1995), Trans Tech Publications, Switzerland.

10. 'The NNO defect in Silicon', F. Berg Rasmussen, S. Öberg, R. Jones, C. Ewels, J. Goss, J. Miro, and P. Deák, Mat. Sci. Forum Vol. **196-201**, pp 791-796 (1995), Trans Tech Publications, Switzerland.
11. 'The H_2^* defect in crystalline germanium', M. Budde, B. Bech Neilsen, R. Jones, S. Öberg, and J. Goss, Mat. Sci. Forum Vol. **196-201**, pp 879-884 (1995), Trans Tech Publications, Switzerland.
12. 'Theory of the NiH2 complex in Si and the CuH2 complex in GaAs', R. Jones, J. Goss, S. Öberg, P. R. Briddon, and A. Resende, Mat. Sci. Forum Vol. **196-201**, pp 921-926 (1995), Trans Tech Publications, Switzerland.
13. 'H interacting with intrinsic defects in Si', B. Bech Neilsen, L. Hoffmann, M. Budde, R. Jones, J. Goss, and S. Öberg, Mat. Sci. Forum Vol. **196-201**, pp 933-938 (1995), Trans Tech Publications, Switzerland.
14. 'The nitrogen-pair oxygen defect in silicon', F. Berg Rasmussen, S. Öberg, R. Jones, C. Ewels, J. Goss, J. Miro, and P. Deák, E-MRS, Strasbourg, (1995).
15. 'H passivated defects in InP', C. P. Ewels, S. Öberg, P. R. Briddon, J. Goss, R. Jones, S. Breuer, R. Darwich, and B. Pajot, Solid State Communications 93 5, pp.459-460 (1995). Paper for SLCS94, 'Shallow Level Centers in Semiconductors', Berkeley, 1994.
16. 'The Hydrogen complexes in GaAs and InP doped with Magnesium', R. Rahbi, B. Pajot, C. Ewels, S. Öberg, J. Goss, R. Jones, Y. Nissim, B. Theys, and C. Blaauw. Solid State Communications 93 5, pp.462 (1995). Paper for SLCS94, 'Shallow Level Centers in Semiconductors', Berkeley, 1994.
17. 'Theoretical and Isotopic Infrared Absorption Investigations of Nitrogen-Oxygen Defects in Silicon', R. Jones, C. Ewels, J. Goss, J. Miro, P. Deák, S. Öberg, and F. Berg Rasmussen, Semiconductor Science and Technology **9**, 2145-48, (1994).
18. 'Ab Initio Calculations of Anharmonicity of the C-H stretch mode in HCN and GaAs', R. Jones, J. Goss, C. Ewels, and S. Öberg, Phys. Rev. B **50**, 8378-88, (1994).

List of Tables

2.1 Parameterisation of the exchange-correlation energy in Ref. [27]. . . 34
2.2 Parameterisation of the exchange-correlation used in AIMPRO. . . 35

4.1 A summary of the classification of diamonds. 88
4.2 The atomic basis used for the calculations in Sec. 4.3. 91
4.3 The atomic basis used for the calculations in Sec. 4.4. 97
4.4 The atomic basis used for the calculations in Sec. 4.5. 100
4.5 The atomic basis used for the calculations in Sec. 4.3. 105
4.6 The H/D stretch modes (cm^{-1}) associated with four charge/spin states of VH. 107
4.7 The H/D stretch modes (cm^{-1}) associated with three charge states of VH_2. 108
4.8 The H/D stretch modes (cm^{-1}) associated with the neutral VH_3, VH_4, and V_2H complexes. 110
4.9 The total energies of the clusters containing VH_n and VH_{n-1}-H_{b-c} systems for n=1,2,3,4. Note that in all cases, H prefers to be located within the vacancy. 110
4.10 A table of the main optical transitions expected for VH_n, $n = 1, 2, 3$ in diamond. 112

5.1 The atomic basis used for the calculations in Sec. 5.1. 121
5.2 The dipole-allowed transitions for Ni and Ni-X centres. The transitions are written in terms of the absorption. All transition energies [eV], ΔE, are found from the difference between the calculated Kohn-Sham eigenvalues, and the dipole matrix elements squared are also listed (P_{ij}^2). The radiative lifetimes, τ are listed in ns unless stated otherwise. 129
5.3 The atomic basis used for the calculations in Sec. 5.2. 134
5.4 Vibrational Modes (cm^{-1}) for the TM-H_2^- AB defect 138

6.1 The atomic basis used for the calculations in Sec. 6.2. 143

6.2 The calculated and experimental [191] structure (Å) and vibrational modes (cm^{-1}) of the HCN molecule. 143
6.3 Calculated energy double derivatives for HCN (a.u.). 144
6.4 Calculated polynomial coefficients (a.u.) for the fit to the vibronic potential of HCN. 145
6.5 Calculated and observed anharmonic C-H frequencies (cm^{-1}) of the HCN molecule. 145
6.6 Calculated double derivatives for C_{As}-H (a.u.). 147
6.7 Calculated and observed [70, 215] LVMs (cm^{-1}) due to C_{As}-H in GaAs. 147
6.8 Calculated polynomial coefficients (a.u.) for the fit to the vibronic potential of C_{As}-H in GaAs. 147
6.9 Calculated and experimental [51, 207, 208] anharmonic C_{As}-H frequencies (cm^{-1}) for the *ab initio* bond length, 1.126 Å. 148
6.10 Calculated and experimental [51, 207, 208] anharmonic C_{As}-H frequencies (cm^{-1}) for the lengthened C-H bond (1.161 Å). 148
6.11 The atomic basis used for the calculations in Sec. 6.3. 155
6.12 The bond lengths of the relaxed $(C_{As})_2$, $(C_{As}) - H$, $(C_{As})_2 - H$ and $(C_{As})_2 - H_2$. The C_1-Ga and C_2-Ga lengths are to the common Ga neighbour. The 'back' bonds refer to the three remaining C-Ga separations shown in Figs. 6.9 and 6.10. All lengths are in Å. 156
6.13 The C-H stretch modes of the lowest energy C_1-H-Ga-C_2 system (cm^{-1}) for the various combinations of carbon and hydrogen isotopes in the 132 and 164 atom clusters. Note, the C_1-H stretch mode is unaffected by a change in mass of C_2. 156
6.14 The projection onto the [110], [$1\bar{1}0$], and [001] directions of the C-H stretch mode of the C_{1h} symmetry $(C_{As})_2H$ complex, calculated in the 132 atom cluster (cm^{-1}). The C atoms are labelled 1 and 2 according to Fig. 6.9. The mode is symmetric about the C_{1h} mirror plane. 157
6.15 The C-H stretch modes for the 133 atom clusters (cm^{-1}) and total energies for the 133 and 165 atom clusters, E_{tot} (eV), relative to the (1,3) pairing for the seven configurations of the $(C_{As})_2H_2$ complex. The models are labelled according to pairing of hydrogen atoms as described in Fig. 6.10. 158

6.16 The C-H stretch modes of the lowest energy $(C_{As})_2H_2$ model (1,3) (Fig. 6.10) in the 133 and 165 atom clusters (cm^{-1}). Since the two C-H units are practically decoupled, only a subset of the permutations of isotopes is required. The modes are not shifted significantly by the Ga mass. 158

6.17 The projection onto the [110], [$1\bar{1}0$], and [001] directions of the normal stretch modes of the C_1 symmetry $(C_{As})_2H_2$ complex (cm^{-1}). The C atoms are labelled 1 and 2 according to Fig. 6.10. 159

List of Figures

1.1 Diagram showing the 71-atom tetrahedral cluster ($X_{35}H_{36}$). 20

2.1 Plots showing the solutions to the secular equations 2.41 where (a) $N_o = 30$, and (b) $N_o = 90$. The displacement, x, is in a.u., and the wavefunctions have been shifted vertically so that each is zeroed about its energy level. 56

2.2 A plot of the polynomial potential as plotted in Fig. 2.1 also showing the Morse potential fit. 57

2.3 A plot of the *non-linear* dipole moment of the $C_{As} - H$ complex in GaAs, $p(x)$, x in a.u. 58

2.4 A graph showing the dependence on cluster size of the band-gap for diamond, Si, Ge, and GaAs. The group-IV materials clusters are made up as follows: $X_{35}H_{36}$, $X_{71}H_{60}$, and $X_{181}H_{116}$. There are two possible arrangements of each GaAs cluster - Ga centred and As centred. The three clusters are $X_{19}Y_{16}H_{36}$, $X_{31}Y_{40}H_{60}$, and $X_{89}Y_{92}H_{116}$. In the graph, $\times$'s indicate Ga centred clusters and $\bigcirc$'s As centred clusters. (*cf.* experimental values of the band-gap: 5.5, 1.17, 0.75, and 1.42 eV for diamond, Si, Ge, and GaAs respectively.) 64

3.1 The one-dimension phonon-dispersion for a material with zinc blende like structure. 67

3.2 On the left is shown how the experiment is set up such that the modulation is used as a reference to enhance the modulated output using a phase sensitive detector (PSD). On the right is shown a schematic of the absorption and absorption derivative EPR spectra. The 'wave' indicated by '(MA)' shows the modulated absorption produced by the modulated magnetic field, $\Delta\mathbf{B}$. 75

3.3 Schematic representations of PL in the cases where (a) the transition observed is from the first excited state to the ground state, and (b) where, since such a transition is forbidden, a transition from the second excited state to the ground state, as suggested for the N2/N3 optical systems in diamond [74]. 79
3.4 Schematic representations of (a) absorption and (b) PLE where transitions involving all excited states are seen. 80
3.5 Schematics of the conduction (E_C) and valence (E_V) bands bending at the p-n or Schottky junction. Plots are shown for two reverse biases, V_1 and V_2. The junction is located at x=0, and the distances x_i and λ_i are described in the text. 83
3.6 A plot of the reverse bias pulse and capacitance response. 84
3.7 A graph showing how the capacitance transient changes with increasing temperature, T. $T_0 < T_1 < T_2 < T_3 < T_4$. Also marked is the *time-window* for which the DLTS spectrum is taken. Note, for temperatures T_0 and T_4 there is no change in capacitance over the range of the time-window. 85
3.8 A plot showing a typical DLTS spectrum. There are three peaks which correspond approximately to the energies of three deep traps. 86

4.1 The spin-polarised Kohn-Sham eigenvalues for the V-N complex in diamond. Only the states in the region of the gap are plotted. Arrows indicate occupation and spin, and the empty boxes show empty states. The 'valence band tops' have been aligned to facilitate comparison. 92
4.2 A contour plot for one of the e-level wavefunctions (au) of $[V\text{-}N]^-$. The plane passes through the vacancy site which is at the centre of the plot, and also through the N and one C atom. Note that the level is nodal at the N atom. The second e-level is qualitatively similar. . 93
4.3 The spin-polarised Kohn-Sham eigenvalues for the $[V\text{-}N_3]^0$ complex in diamond. Shown are the $^2A_1$ ground state, and the ^2E excited state associated with the N3 optical transition. Also shown is an $^2A_1$ excited state which is found to be the lowest in energy. This is associated with the N2 vibronic centre. Only the states in the region of the gap are plotted. Arrows indicate occupation and spin, and the empty boxes show empty states. 94

4.4 A schematic representation of the relaxed split-vacancy geometry of the V-Si complex. The solid circles represent C atoms, the empty circle the relaxed Si site, and the dashed circles the diamond lattice sites. 98
4.5 The spin-polarised Kohn-Sham eigenvalues for the V-Si complex in diamond in the region of the band gap. The notation is as in Fig. 4.1, and the 'valence band tops' aligned. 99
4.6 Kohn-Sham eigenvalues of the [P-V] complex in diamond in vicinity of the band gap. The arrows and filled boxes denote spin polarised and non-polarised occupied levels respectively and the empty boxes empty levels. (a) An 86 atom cluster representing pure diamond. (b,c) Spin-polarised levels for the neutral P-V defect. Note the $e''^{\uparrow}$-level is full and the $e'^{\downarrow}$ level is half-filled giving a $^2E'$ ground state. (d) shows the levels of $[\text{P-V}]^-$ where all gap levels are filled. 101
4.7 The pseudo-wavefunction for an $e''^{\uparrow}$ state (au×10). Note that the amplitude near P is negligible. 102
4.8 The Kohn-Sham eigenvalues for the VH^n (n=+1,0,-1) complex in diamond as follows: (a) 1+, (b)&(c) neutral, (d)&(e) 1- (S=0), and (f)&(g) 1- (S=1). The eigenvalues of different charge states have been shifted to bring the valence band tops into agreement to facilitate comparison, and only the levels in the region of the gap are plotted. Arrows indicate occupation and spin-direction, the filled boxes indicate filled *spin-averaged* levels and the empty boxes show unoccupied levels. 106
4.9 The Kohn-Sham eigenvalues for the VH_2^n (n=1+,0,1-) complex in diamond as follows: (a)&(b) 1+, (c) neutral, and (d)&(e) 1-. The notation is as in Fig. 4.8, and the charge states have been shifted to bring the valence band edges into alignment. 108
4.10 The Kohn-Sham eigenvalues for the neutral VH_3 and VH_4 complexes in diamond. The notation is as in Fig. 4.8. 109

5.1 The variation of potential energy with $\langle 111 \rangle$ displacement of the interstitial nickel atom from the relaxed structure. The curve shown with X's denotes case (i) when the four surrounding carbon atoms are not relaxed at each Ni position, and the curve shown with triangles denotes case (ii) when the four nearest neighbours are free to relax. 122

5.2 A schematic representation of the electronic structure (Kohn-Sham eigenvalues) of the two interstitial Ni defects examined in this work. (a) and (b) correspond to the Ni_i^+ spin up and spin down electronic levels respectively, with the arrows signifying filled states and the boxes empty states. Similarly, (c) and (d) corresponds to the up and down KS-levels of the Ni_i^+-B_s^- complex. The levels have been shifted linearly to facilitate comparison. 123

5.3 A contour plot of the pseudo-wavefunction associated with one of the three Ni_s^- $t_2^{\uparrow}$ states taken through the $\{1\bar{1}0\}$ plane; the x-axis is along $\langle 001\rangle$, and the y-axis along $\langle 110\rangle$. The wavefunction amplitude is in au$\times$10. The Ni atom is at the centre of the plot and marked with the white square. The two C atoms are marked with black circles. The plot shows the *anti-bonding* character of the wavefunction, i.e. there is a node in the wavefunction between the Ni atom and its four C neighbours. 125

5.4 A schematic representation of the electronic structure (Kohn-Sham eigenvalues) of the four substitutional Ni defects examined in this work. (a) and (b) correspond to the Ni_s^- spin up and spin down electronic levels respectively, with the arrows signifying filled states and the boxes empty states. Similarly, (c) and (d) correspond to $Ni_s^-N_s^+$, (e) and (f) to Ni_s^+, and (g) and (h) to $Ni_s^+B_s^-$. Once more, all the levels have been linearly shifted to facilitate comparison. . . 126

5.5 Ni-H_2 Complex with H at anti-bonding (AB) sites. 137

6.1 The C_{As}-H defect in GaAs. 142

6.2 (a) Potential energy (au) versus displacement from equilibrium, x, (au) for C-H stretch in HCN. The oscillator wavefunctions for the ground (b), first (c) and second (d) excited states are also shown. The horizontal lines show the energies of these states. 144

6.3 The variation of the fundamental (a) and overtone (b) frequencies in cm^{-1} with the change in the equilibrium C-H length (Å) in HCN. Curve (c) shows the the fundamental frequency $\times 2$ and its difference from (b) demonstrates that the anharmonicity varies slowly with the C-H length. The horizontal lines show the experimental frequencies (3312 and 6521.7 cm^{-1}) [191]). 146

6.4 (a) Potential energy (au) versus displacement from equilibrium, x, (au) for C-H stretch in GaAs. The oscillator wavefunctions for the ground (b), first (c) and second (d) excited states are also shown. The horizontal lines show the energies of these states. 148

6.5 The variation of the fundamental (a) and overtone (b) frequencies in cm^{-1} with the change in the equilibrium C-H length (Å) for C-H in GaAs. Curve (c) shows the the fundamental frequency $\times 2$ and its difference from (b) demonstrates that the anharmonicity varies slowly with the C-H length. The horizontal line shows the experimental frequency (2635.2 cm^{-1} [51]) 149

6.6 Curve (a) shows the dipole moment of the cluster (au) versus the change in the equilibrium C-H length (Å) for GaAs. Curve (b) shows the product of oscillator wavefunctions $\Psi_0(x)\Psi_2(x)$ shifted vertically upwards. 150

6.7 The intensity of the overtone versus the degree of electrical anharmonicity λ. The C-H length is 1.126 Å in curve (a) and 1.161 Å in curve (b). 151

6.8 Schematic diagram of the C_2H defect thought to be responsible for the 2688 cm^{-1} band as suggested in Ref.[216]. 153

6.9 Schematic diagram of the three configurations of the C_2H defect. 1, 2, and 3 label bond centred sites in which the H atoms have been sited in this study. 154

6.10 Schematic diagram of seven configurations of the C_2H_2 defects examined in this paper. The H sites are labelled using the numbers 1-7, and they can be paired into seven unique defect configurations as follows: (1,2), (1,3), (1,4), (3,5), (3,6), (4,5), and (6,7). 154

B.1 A diagram showing the splittings of a t_2-level with C_{3v} and C_{2v} distortions to illustrate the Jahn-Teller effect. 166

'*Of bell or knocker there was no sign; through these frowning walls and dark window openings it was not likely that my voice could penetrate. The time I waited seemed endless, and I felt doubts and fears crowding upon me. What sort of place had I come to, and among what kind of people? What sort of grim adventure was it on which I had embarked?*'

Extract from '*Dracula*', Bram Stoker.

Chapter 1

Introduction

Beatrice: 'You kill me to deny it, but a man of science hath no better grasp of English than a lawyer doth ethics.'

'Much Ado About Nothing', William Shakespeare.

Presented within this thesis are the results of first principles calculations of the geometry, electronic structure, and optical properties of a variety of defects in diamond, silicon and GaAs.

'First principles' refers to the fact that no experimental data is required as input for the calculations, except for the atomic numbers of the constituent atoms. This is in contrast to a number of alternative methods, such as the 'complete neglect of differential overlap' (CNDO) and similar approximations (INDO, MNDO, MINDO, etc.) which use (for example) ionisation energies and electron affinities to parameterise some of the integrals. Simple potential methods such as those due to Keating [1] and Tersoff [2] are derived from bulk properties. These have the advantage that they can be used to treat large systems very quickly, but suffer from the fact that the potentials are not sufficiently transferable: that is they do not describe atomic environments that differ very much from that of bulk. It is therefore highly desirable to pursue the first principles approach. Until relatively recently, this has proved difficult for a number of reasons.

The original approach due to Hartree and Fock [3] uses an anti-symmetric wavefunction made up from one-electron states to model a system of N-electrons. However, this approach suffers from a crippling scaling problem so that in practice only very small systems are tractable problems. This obstacle was overcome to some extent by Hohenberg and Kohn [4], and Kohn and Sham [5] who formulated density functional theory (DFT). Under this approach a system of atoms can be represented simply from the electron density $n(\mathbf{r})$ instead of the complex anti-symmetric wavefunctions adopted in Hartree-Fock and related methods.

A difficulty remains in the computation of the exchange and correlation energies. This is usually circumvented by invoking the local density approximation (LDA), where the exchange-correlation energy density at a point $\mathbf{r}$ with density n is taken to be that of the homogeneous electron gas with the same electron density. This can be readily extended to spin-polarised systems and is then termed the local spin density approximation (LSDA).

In the past decade the availability of faster, more powerful computing resources has made possible the study of larger and more challenging problems. These include the determination of the most energetically favourable surface reconstructions [6, 7], the geometry of dislocations [8], as well as a plethora of point defect structures.

The LSDA can be applied to DFT in a number of ways, and the code used throughout this thesis has been named AIMPRO - *Ab initio* modelling program. AIMPRO uses a real space approach, which makes the code ideal for the calculation of the structures of molecules, such as C_{60} [9] and ferrocene [10]. In the case of defects however, a cluster must be constructed that is sufficiently large that the local environment of the defect closely resembles that of the bulk material. Typically, the clusters used in this thesis contain 70-200 atoms. A schematic representation of a 71-atom tetrahedral cluster (atom centred) is shown in Fig. 1.1. In AIMPRO the

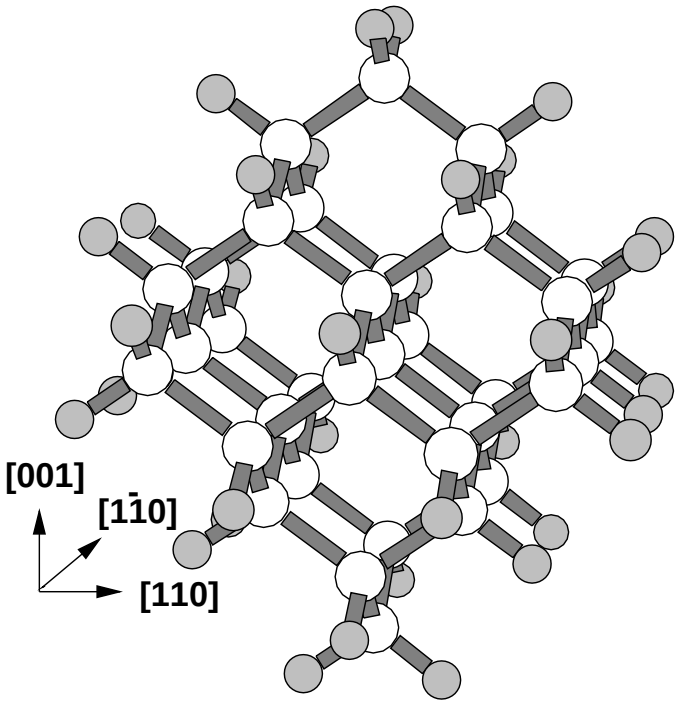

Figure 1.1: Diagram showing the 71-atom tetrahedral cluster ($X_{35}H_{36}$).

Kohn-Sham orbitals are expanded in a basis of Gaussian functions, as is the fit to the charge density. The electron-ion interaction is treated using the norm-conserving

pseudopotentials of Bachelet, Hamann, and Schlüter [11], except for the case of hydrogen, for which the bare Coulomb potential is used. The structure is optimised from the analytically derived forces using a conjugate gradients algorithm.

Using this approach, a number of experimentally measurable quantities can be obtained. These include localised vibrational modes, the symmetries[1] of the ground and excited states in optical transitions, and semi-qualitatively the transition energies and radiative lifetimes. Thus, AIMPRO can be used not only to examine the detailed structures of defects to correlate with experiment, but also provide information to experimentalist colleagues as a guide to where to look for, for example, a one-phonon side band in photoluminescence. In fact, collaboration with experimental groups has proved highly productive in a number of cases such as the T-line [12] and the hydrogenated vacancy and interstitial [13] in Si.

The contents of this thesis can be summarised as follows. Chapter 2 describes in some detail the background to the theory, touching on Hartree-Fock methods, and parameterised Hartree-Fock methods (especially CNDO). However, the main aim is to discuss the AIMPRO formalism. The methods and approximations adopted for the calculations of experimental observables are detailed in this Chapter and their limitations explained.

Following this, Chapter 3 outlines a number of the more commonly used experimental techniques. These are: localised vibrational mode spectroscopy, electron paramagnetic resonance (EPR), luminescence spectroscopy techniques, and deep level transient spectroscopy.

The background Chapters are followed by three Chapters containing the results of the *ab initio* calculations. The first (Chapter 4) concerns the class of vacancy-related optical defects in diamond formed particularly after irradiation and annealing. They are characterised by strong and sharp optical peaks, and are made up of vacancies complexed with one or more impurity atoms. Good agreement with experiment is found in the case of a single N atom in the neutral or negative charge states. The quantitative agreement in the case of three N atoms is slightly less satisfactory, although the calculations have provided a clear qualitative picture.

Si and P both readily complex with a vacancy and form a split-vacancy structure. The former gives rise to a complex set of zero-phonon lines, which can be understood from a negative charge state of the centre. The latter may be responsible for a broad red donor-acceptor recombination band, but much more importantly is likely to lie at the root of the difficulty in producing n-type semiconducting diamond using phosphorus.

[1]The character tables of the key point groups studied in this thesis are given in Appendix A.

The location and presence of H in diamond has long been a matter of heated discussion. Following recent observation of H-related centres in polycrystalline diamond using EPR, the structure and electronic properties of vacancy-hydrogen complexes are also presented in Chapter 4, but no firm conclusions can be made regarding this class of centres.

Chapter 5 continues the theme of luminescent centres in diamond. Diamonds which are produced using the high temperature, high pressure method exhibit pronounced optical peaks. Many of these have been correlated with Ni introduced from the solvent-catalyst. Ni is known to give rise to a number of EPR signals, and a number of assignments have been made in the past to both substitutional and interstitial Ni centres. The results presented here show that there is no requirement for an interstitial species, and many assignments may have been made on the strength of unreliable calculations. The geometries and electronic structures of Ni, Ni-N and Ni-B centres are reported.

The final section in Chapter 5 examines substitutional Ni and Ni-hydrogen complexes in silicon. In contrast with diamond, Ni_s^- in Si is known to undergo a Jahn-Teller distortion to form a low symmetry centre. This is reproduced in these calculations. Furthermore, evidence is provided for hydrogen adopting the anti-bonding site in the Ni-H_2 complex.

The final results Chapter concerns a range of centres that have been observed in GaAs using infrared absorption spectroscopy. C is a common impurity, and is often intentionally introduced as an acceptor due to its low diffusivity and high doping concentrations. However, hydrogen readily complexes with C to form electrically inactive centres. This C_{As}-H centre exhibits a characteristic local vibrational mode at 2635 cm^{-1}. However, the isotope shifts suggest that this mode is very anharmonic. It is anharmonicity that breaks the symmetry selection rules that prevent an overtone, but to date, the overtone to this centre has not been observed. Chapter 6 shows that one solution may be that *electrical* anharmonicity reduces the intensity of the overtone.

A further set of bands related to C-H stretch modes have been seen in heavily doped samples. Interestingly, some of them exhibit strong (nearly 100%) polarisation in one of the two $\langle 110 \rangle$ directions normal to the growth direction. It is thought that C-pairs are formed during growth, and H bonded to one of these C atoms gives rise to the polarised absorption. The structures and local vibrational modes of a number of such centres with one or two hydrogen atoms are reported.

General conclusions are presented in Chapter 7.

Chapter 2

Theory

> 'As far as the laws of mathematics refer to reality, they are not certain; and as far as they are certain, they do not refer to reality.'
>
> - Albert Einstein

2.1 Introduction

A variety of theoretical methods and approximations are used by the academic community to model many-body problems. In this Chapter, I shall start from stating the initial problem, and step through the construction of a number of methods adopted to solve it. Starting with the Born-Oppenheimer approximation, I shall outline Hartree-Fock theory (Sec. 2.4), and a number of parameterised Hartree-Fock methods (Sec. 2.5) which are based on the Roothaan equations. Finally I shall outline density functional theory (Sec. 2.8) and the local density approximation for the exchange-correlation energy (Sec. 2.9).

However, the main goal of this Chapter is to detail the approximations and techniques employed in the '*Ab Initio* Modelling PROgram' or AIMPRO. AIMPRO is a self-consistent density functional code applied to a real-space atomic-clusters developed in Exeter and Newcastle over the last ten years. The use of atomic clusters makes the program ideally suited to calculations of molecular structures and has been successfully applied to the class of carbon structures termed 'fullerenes' [9]. However, the main thrust of this thesis is to explore the properties of defects in solids. AIMPRO models bulk-material with large clusters (typically 70-150 atoms) where the surface 'dangling bonds' are saturated with hydrogen atoms. The charge density and wavefunctions are expanded in terms of a Gaussian basis, and models the electron-ion interaction via norm-conserving pseudopotentials (Sec.2.11).

AIMPRO can currently calculate a number of experimental observables, including localised vibrational modes, and electronic transition energies and rates. The

methods used are outlined in Sec. 2.15 and Sec. 2.17 respectively. Other observable quantities that may be estimated using AIMPRO are binding energies, and reorientation and migration barriers. The AIMPRO methodology is reviewed in Ref. [14].

2.2 The problem posed

Fundamentally, we wish to solve the many-body Schrödinger equation for a specific set of atoms in a specific configuration, i.e.

$$\hat{H}\Psi_i = E_i\Psi_i,$$

where $\hat{H}$ is the many-body Hamiltonian, and Ψ_i is the many-body wavefunction corresponding to the i^{th} state which has energy E_i. In general, Ψ_i is a function of the electron spin and co-ordinates as well as the nuclear positions. For all but the most simple of problems, this is an intractable problem.

Adopting atomic units[1] the Schrödinger equation for a set of electrons in a field due to ions of charge Z_a at sites $\mathbf{R}_a$ is given by:

$$\left\{-\sum_a \frac{1}{2M_a}\nabla_a^2 - \frac{1}{2}\sum_\mu \nabla_\mu^2 + \frac{1}{2}\sum_{\nu\neq\mu}\frac{1}{|\mathbf{r}_\mu - \mathbf{r}_\nu|} - \sum_{\mu,a}\frac{Z_a}{|\mathbf{r}_\mu - \mathbf{R}_a|} + \frac{1}{2}\sum_{a\neq b}\frac{Z_a Z_b}{|\mathbf{R}_a - \mathbf{R}_b|} - E\right\}\Psi(r) = 0. \tag{2.1}$$

This can alternatively (using obvious notation) be written as

$$\{T_{\text{ion}} + T_{\text{e}} + V_{\text{e-e}} + V_{\text{e-i}} + V_{\text{i-i}} - E\}\Psi(r) = 0. \tag{2.2}$$

Here r is used to denote the positions and the spins of the electrons, i.e. ($\mathbf{r}_1, s_1, \mathbf{r}_2, s_2, \mathbf{r}_3, s_3, ...$).

Any practical method of solving Eq. 2.1 must first *decouple* the motion of the electrons and ions. One may then calculate the effective potential felt by each electron due to the other electrons and ions. From there one may calculate the forces on the ions, optimise the ion positions with respect to the total energy, and hence derive the equilibrium geometry.

Returning to the first step, one needs to separate the electron and ion components of the many-body wavefunctions, and this is achieved under the adiabatic or *Born-Oppenheimer* approximation.

[1] In the atomic units system, $\hbar$, e, m_{e}, and $4\pi\varepsilon_0$ are taken to be unity. Then, 1 a.u. of energy is equivalent to 27.212 eV, and 1 a.u. of length is 0.529 Å.

2.3 The Born-Oppenheimer approximation

One assumes that, due to the large mass of the ions compared to that of the electron, the motion of the ions simply modulates the electronic wavefunction, i.e.

$$\Psi_{\text{Total}}(r, R) = \chi(R)\Psi(r, R). \tag{2.3}$$

Here $\chi(R)$ is an amplitude dependent on the positions of the ions, and $\Psi(r, R)$ is a solution of

$$\{T_{\text{e}} + V_{\text{e-e}} + V_{\text{e-i}} + V_{\text{i-i}} - E\}\Psi(r) = 0.$$

R denotes the nuclear co-ordinates $(\mathbf{R}_1, \mathbf{R}_2, ...)$. Substituting Eq. 2.3 into Eq. 2.2, multiplying through by $\Psi^*(r, R)$ and integrating over r, one arrives at the equation:

$$\begin{aligned}\{T_{\text{ion}}(R) + E(R) + W(R) - E_T\}\,\chi(R) = \\ \sum_a \int \Psi^*(r, R)\frac{1}{M_a}\nabla_a\Psi(r, R)\nabla_a\chi(R)dr.\end{aligned} \tag{2.4}$$

The sum is over the nuclei. The left hand is simply the Schrödinger equation for the ions moving in a potential $E + W$, where

$$W(R) = -\sum_a \frac{1}{2M_a}\int \Psi^*(r, R)\nabla_a^2\Psi(r, R)dr$$

is due to the electrons moving along with the nuclei. $W(R)$ is negligibly small. The right hand side of Eq. 2.4 is zero if $\Psi(r, R)$ is real and corresponds to a non-degenerate ground state. Otherwise this term is a small perturbation, which can be important in the case of a degenerate ground state. Here it can lead to symmetry breaking as in the case of a Jahn-Teller distortion [15]. If the right hand side is neglected, then the electron and ion motions are decoupled.

The term $E(R)$ represents the potential energy of the ions averaged over the state $\Psi(r, R)$, and the minimum of E therefore represents the ground state of the system. This is usually what one seeks in these calculations.

2.4 Hartree-Fock Theory

One way to construct the many-body wavefunction, $\Psi(r, R)$, is from a single Slater determinant of N one-electron spin-orbitals[2]:

$$\Psi(r) = \frac{1}{\sqrt{N!}}\det|\psi_\mu(r)|, \quad \psi_\mu(r) = \psi(\mathbf{r})\chi_\alpha(s).$$

[2]The determinant form of the wavefunction ensures that the anti-symmetry under particle exchange, required by the Pauli exclusion principle, is included.

$\chi_\alpha(s)$ is a spin function which satisfies:

$$\sum_s \chi^*_\alpha(s)\chi_\beta(s) = \delta_{\alpha\beta},$$

with the sum over up and down spins, and the orbitals satisfy:

$$\int \psi^*_i(\mathbf{r})\psi_j(\mathbf{r})d\mathbf{r} = \delta_{ij}.$$

In each case δ is the standard Kronecker delta function.

The averaged energy of a such determinental wavefunction is, adopting Dirac notation, $\langle\Psi|\hat{H}|\Psi\rangle$. This has been shown [16] to be given by:

$$E = \sum_\lambda \langle\lambda|T + V_{\mathrm{e-i}} + V_{\mathrm{i-i}}|\lambda\rangle + \frac{1}{2}\sum_{\lambda,\mu}\{\langle\lambda\mu|V_{\mathrm{e-e}}|\lambda\mu\rangle - \langle\lambda\mu|V_{\mathrm{e-e}}|\mu\lambda\rangle\}, \tag{2.5}$$

where the sums are over the occupied spin-orbitals. Note, the second summation involve *four-centre* integrals. Alternatively, Eq. 2.5 may be written as:

$$E = -\frac{1}{2}\sum_{\lambda,s}\int \psi^*_\lambda(\mathbf{r},s)\nabla^2\psi_\lambda(\mathbf{r},s)d\mathbf{r} + \int n(\mathbf{r})V_{\mathrm{e-i}}d\mathbf{r} + E_{\mathrm{H}} + E_{\mathrm{x}} + E_{\mathrm{i-i}}, \tag{2.6}$$

where we have introduced the Hartree, exchange, and ion-ion energies (E_{H}, E_{x}, and $E_{\mathrm{i-i}}$), and the electron density, n:

$$E_{\mathrm{H}} = \frac{1}{2}\int \frac{n(\mathbf{r}_1)n(\mathbf{r}_2)}{|\mathbf{r}_1 - \mathbf{r}_2|}d\mathbf{r}_1 d\mathbf{r}_2, \tag{2.7}$$

$$E_{\mathrm{x}} = -\frac{1}{2}\sum_{\lambda\mu}\sum_{s_1 s_2}\int \psi^*_\lambda(r_1)\psi^*_\mu(r_2)\frac{1}{|\mathbf{r}_1 - \mathbf{r}_2|}\psi_\mu(r_1)\psi_\lambda(r_2)d\mathbf{r}_1 d\mathbf{r}_2, \tag{2.8}$$

$$E_{\mathrm{i-i}} = \frac{1}{2}\sum_{a\neq b}\frac{Z_a Z_b}{|\mathbf{R}_a - \mathbf{R}_b|}, \text{ and} \tag{2.9}$$

$$n(\mathbf{r}) = \sum_{\lambda,s}|\psi_\lambda(\mathbf{r},s)|^2. \tag{2.10}$$

The total energy (for a given set of nuclei), E, is then minimised subject to orthonormal ψ_λ by introducing Lagrange multipliers $E_{\lambda\mu}$, giving the Hartree-Fock (HF) equations for each orbital λ:

$$\left\{-\frac{1}{2}\nabla^2 + V_{\mathrm{e-i}}(\mathbf{r}) + V^{\mathrm{H}}(\mathbf{r}) + V^{\mathrm{x}}_\lambda(\mathbf{r}) - E_\lambda\right\}\psi_\lambda(r) = \sum_{\mu\neq\lambda}E_{\lambda\mu}\psi_\mu(r). \tag{2.11}$$

Here

$$V^{\mathrm{H}}(\mathbf{r})\psi_\lambda(r) = \frac{\delta E_{\mathrm{H}}}{\delta\psi^*_\lambda} = \int\frac{n(\mathbf{r}_1)\psi_\lambda(r)}{|\mathbf{r} - \mathbf{r}_1|}d\mathbf{r}_1,$$

$$V^{\mathrm{x}}_\lambda(\mathbf{r})\psi_\lambda(r) = \frac{\delta E_{\mathrm{x}}}{\delta\psi^*_\lambda} = -\sum_{\mu s_1}\int\psi^*_\mu(r_1)\psi_\lambda(r_1)\frac{1}{|\mathbf{r} - \mathbf{r}_1|}\psi_\mu(r)d\mathbf{r}_1$$

are the Hartree and exchange potentials respectively, and the expression for the exchange involves a sum over occupied orbitals μ whose spin are the same as that of λ.

Next, one performs a unitary transformation on the Slater determinant to diagonalise $E_{\lambda\mu}$ reducing the right hand side of Eq. 2.11 to zero. The total energy can then be found by multiplying the HF equations (2.11) by $\psi^*_\lambda(r)$, integrating over $\mathbf{r}$ and summing over λ and s, to give:

$$-\sum_{\lambda,s}\int \psi^*_\lambda(r)\frac{1}{2}\nabla^2\psi_\lambda(r)d\mathbf{r} \quad + \quad \sum_{\lambda,s}\int \psi^*_\lambda(r)V_{\mathrm{e-i}}(\mathbf{r})\psi_\lambda(r)d\mathbf{r}$$
$$+\sum_{\lambda,s}\int \psi^*_\lambda(r)V^{\mathrm{H}}(\mathbf{r})\psi_\lambda(r)d\mathbf{r} \quad + \quad \sum_{\lambda,s}\int \psi^*_\lambda(r)V^{\mathrm{x}}_\lambda(\mathbf{r})\psi_\lambda(r)d\mathbf{r} - \sum_{\lambda,s}E_\lambda = 0$$

Then, the first and second terms are the kinetic energy associated with the electrons and the electron-ion interaction energy respectively. The terms involving the Hartree and exchange potentials are simply twice the Hartree and exchange energies respectively. Therefore, we now have:

$$T_{\mathrm{e}} + E_{\mathrm{e-i}} + 2E_{\mathrm{H}} + 2E_{\mathrm{x}} - \sum_\lambda E_\lambda = 0.$$

Then the total energy is found by removing the double counting and adding the ion-ion energy term:

$$E_{\mathrm{total}} = \sum_\lambda E_\lambda - E_{\mathrm{H}} - E_{\mathrm{x}} + E_{\mathrm{i-i}}.$$

In practice the HF equations are solved *self-consistently* by making a sensible initial guess at the set of $\psi_\lambda(r)$ and calculating the Hartree and exchange potentials. These output potentials are then fed back into the HF equations to calculate a new set of $\psi_\lambda(r)$. This cycle is repeated until the input and output potentials are sufficiently close. Usually, the initial guesses for the spin-orbitals are related to atomic orbitals.

Using HF methods, one can arrive at a very good agreement for structures and vibrational modes of small molecules. However, a number of four-centre integrals are required for the exchange energy. This leads to a prohibitively heavy computational effort for systems of more than a few atoms, and therefore the simulation of defects in bulk materials is impractical. To apply HF theory to larger problems, a number of semi-empirical *parameterisations* have been developed where these time consuming integrals are no longer calculated, or are performed approximately.

2.5 Parameterised Hartree-Fock methods

There are a number of paradigms for parameterising the basic HF equations, each having a different level of approximation. For the purposes of this thesis, only the basic approximations are outlined. One particular method, the original formulation of the complete neglect of differential overlap approximation [17], is described in detail.

The first stage is to expand the one-electron wavefunctions in a linear combination of atomic orbitals (LCAO), ϕ_μ:

$$\psi_i = \sum_\mu c_{\mu i}\phi_\mu.$$

Then one can write the (differential) HF equations in an algebraic expression, termed the Roothaan equations. The Roothaan equations are given by:

$$\sum_\nu \left(F_{\mu\nu} - \varepsilon_i S_{\mu\nu}\right) c_{\nu i} = 0 \tag{2.12}$$

where $F_{\mu\nu}$ is the Fock matrix and $S_{\mu\nu}$ is the overlap matrix:

$$\begin{aligned} F_{\mu\nu} &= H_{\mu\nu} + \sum_{\lambda\sigma} P_{\lambda\sigma}\left[\langle\mu\nu|\lambda\sigma\rangle - \frac{1}{2}\langle\mu\lambda|\nu\sigma\rangle\right] \\ S_{\mu\nu} &= \int \phi_\mu(r)\phi_\nu(r)dr \end{aligned} \tag{2.13}$$

and ε_i are the one-electron energies. $H_{\mu\nu}$ and $P_{\lambda\sigma}$ are the core Hamiltonian matrix elements and the density matrix elements respectively, and $\langle\mu\nu|\lambda\sigma\rangle$ are the differential overlap matrix elements:

$$\begin{aligned} H_{\mu\nu} &= \int \phi_\mu(r) H^{\text{core}} \phi_\nu(r) dr \\ P_{\lambda\sigma} &= 2\sum_i^{\text{occ}} c^*_{\lambda i} c_{\sigma i} \\ \langle\mu\nu|\lambda\sigma\rangle &= \int\int \phi_\mu(r_1)\phi_\nu(r_1)\frac{1}{|r_1 - r_2|}\phi_\lambda(r_2)\phi_\sigma(r_2)dr_1 dr_2 \end{aligned}$$

At this stage there are no approximations. However, one can utilise the fact that many of the integrals are very small or zero and begin to neglect *systematically* some of the matrix elements.

The *zero-differential overlap approximation* [18] (ZDOA) is the starting point for many semi-empirical methods. The ZDOA sets all but a few terms in the differential overlap matrix identically to zero:

$$\langle\mu\nu|\lambda\sigma\rangle = \langle\mu\mu|\lambda\lambda\rangle\delta_{\mu\nu}\delta_{\lambda\sigma},$$

and the overlap integrals, $S_{\mu\nu}$ are neglected in the normalisation of the molecular orbitals. To retain some of the overlap character that is required to treat chemical bonding correctly, the Hamiltonian matrix elements, $H_{\mu\nu}$, are treated semi-empirically.

The ZDOA simplifies the Roothaan equations to become:

$$\begin{aligned} \sum_{\nu} F_{\mu\nu} c_{\nu i} &= \varepsilon_i c_{\mu i} \\ F_{\mu\nu} &= \begin{cases} H_{\mu\mu} - \frac{1}{2} P_{\mu\mu} \langle \mu\mu | \mu\mu \rangle + \sum_{\lambda} P_{\lambda\lambda} \langle \mu\mu | \lambda\lambda \rangle & \nu = \mu \\ H_{\mu\nu} - \frac{1}{2} P_{\mu\nu} \langle \mu\mu | \nu\nu \rangle & \mu \neq \nu. \end{cases} \end{aligned} \tag{2.14}$$

This vastly reduces the number of 2-electron integrals and removes all 3- and 4-centre integrals. Note, these equations only apply to *closed shell* molecules, that is to say spin zero systems. One can extend these equations to a spin polarised system simply by writing down Eq. 2.14 for each spin.

2.5.1 Complete neglect of differential overlap

The degree to which the ZDOA is applied varies from one method to another, but the simplest form is the *complete neglect of differential overlap* approximation, CNDO [19]. Here Eq. 2.14 applies, but in order that rotational invariance is maintained, one is required to further approximate the remaining 2-electron integrals by:

$$\langle \mu\mu | \lambda\lambda \rangle = \gamma_{AB},$$

where γ_{AB} is the *average* electrostatic repulsion between any electron on atom A and any electron on atom B. Thus, these integrals depend only on the nature of the atoms A & B, and not on the type of orbitals. Under CNDO, only the valence electrons are explicitly considered.

Thus the Fock matrix elements for the CNDO approximation are given as:

$$F_{\mu\nu} = \begin{cases} H_{\mu\mu} - \frac{1}{2} P_{\mu\mu} \gamma_{AA} + \sum_{\lambda} P_{BB} \gamma_{AB} & \nu = \mu,\ \phi_\mu \text{ on atom A} \\ H_{\mu\nu} - \frac{1}{2} P_{\mu\nu} \gamma_{AB} & \nu \neq \mu, \phi_\mu \text{ on atom A}, \phi_\nu \text{ on atom B} \end{cases}$$

where $P_{BB} = \sum_{\lambda}^{B} P_{\lambda\lambda}$ is the total electron density associated with atom B. Applying the same approximations to the core Hamiltonian ($\hat{\mathbf{H}} = -\frac{1}{2}\nabla^2 - \sum_B \mathbf{V}_B$) one arrives at:

$$H_{\mu\nu} = \begin{cases} U_{\mu\mu} - \sum_{B \neq A} \langle \mu | \mathbf{V}_B | \mu \rangle, & \nu = \mu, \phi_\mu \text{ on atom A} \\ U_{\mu\nu} - \sum_{B \neq A} \langle \mu | \mathbf{V}_B | \nu \rangle, & \phi_\mu,\ \phi_\nu \text{ on A} \\ \left\langle \mu \left| -\frac{1}{2}\nabla^2 - \mathbf{V}_A - \mathbf{V}_B \right| \nu \right\rangle & \\ \qquad - \sum_{C \neq A,B} \langle \mu | \mathbf{V}_C | \nu \rangle, & \phi_\mu \text{ on A},\ \phi_\nu \text{ on B} \end{cases} \tag{2.15}$$

where

$$U_{\mu\nu} = \left\langle \mu \left| -\frac{1}{2}\nabla^2 - \mathbf{V}_A \right| \nu \right\rangle,$$

and $-\mathbf{V}_i$ is the potential due to the nucleus and core electrons on atom i.

If the atomic orbital basis is made up from s, p, d, ... atomic functions, then $U_{\mu\nu}$, $\mu \neq \nu$ are zero by symmetry. Again, to maintain rotational invariance $\langle\mu|\mathbf{V}_B|\mu\rangle$ must be a constant, V_{AB}, which describes the interaction of any electron on atom A with the core of atom B. Furthermore, neglect of monatomic differential overlap means that $\langle\mu|\mathbf{V}_B|\nu\rangle = 0,\ \mu \neq \nu$. The term involving a summation over C in Eq. 2.15 is a three-centre integral, and thus is neglected, leaving the first term, called the 'resonance integral', which is a measure of the possible lowering of the electron energy by existing simultaneously in the fields of two atoms. Rotational invariance requires that this term is a constant $\beta_{\mu\nu}$, which is assumed to be proportional to the overlap, i.e. $\beta_{\mu\nu} = \beta^o_{AB} S_{\mu\nu}$.

Applying these further conditions to Eqs. 2.15, we arrive at

$$H_{\mu\nu} = \begin{cases} U_{\mu\mu} - \sum_{B\neq A} V_{AB}, & \nu = \mu,\ \phi_\mu \text{ on A} \\ 0, & \mu \neq \nu,\ \phi_\mu,\ \phi_\nu \text{ both on A} \\ \beta^o_{AB} S_{\mu\nu}, & \mu \neq \nu,\ \phi_\mu \text{ on A},\ \phi_\nu \text{ on B} \end{cases} \tag{2.16}$$

This expression can now be substituted into the Fock matrix, giving

$$F_{\mu\nu} = \begin{cases} U_{\mu\mu} + \left(P_{AA} - \frac{1}{2}P_{\mu\mu}\right)\gamma_{AA} + \sum_{B\neq A}(P_{BB}\gamma_{AB} - V_{AB}) & \nu = \mu \\ \beta^o_{AB} S_{\mu\nu} - \frac{1}{2}P_{\mu\nu}\gamma_{AB} & \mu \neq \nu \end{cases} \tag{2.17}$$

One can write the summation in Eq. 2.17 as

$$\sum_{B\neq A} -Q_B\gamma_{AB} + (Z_B\gamma_{AB} - V_{AB}),$$

where Q_B is the net charge on atom B. Here $(Z_B\gamma_{AB} - V_{AB})$ is the difference between the potentials due to the valence electrons and core of atom B, termed the *penetration integral* [20]. This demonstrates one of the advantages of this approach: physical quantities are readily separable allowing simple interpretation of the results of any calculation.

Finally, combining all the approximations, an expression for the total energy can be written down:

$$E_{\text{tot}} = \frac{1}{2}\sum_{\mu\nu} P_{\mu\nu}(H_{\mu\nu} + F_{\mu\nu}) + \sum_{A<B} Z_A Z_B R^{-1}_{AB}.$$

Now one must decide how to evaluate an number of terms: $S_{\mu\nu}$, $U_{\mu\nu}$, V_{AB}, γ_{AB}, and β^o_{AB}. Under the CNDO approximations there are historically two systems adopted, termed CNDO/1 and CNDO/2.

2.5.2 CNDO/1

- The overlap integrals are directly evaluated. The repulsion integrals are approximated by integrals of s-orbitals on atoms A and B:

$$\gamma_{AB} = \int\int s_A^2(r_1)\frac{1}{|r_1 - r_2|}s_B^2(r_2)dr_1dr_2.$$

- The electron-ion interaction V_{AB} is also calculated using an s-orbital on atom A:

$$V_{AB} = Z_B \int \frac{s_A^2(r)}{|r - R_B|}dr.$$

- The one-electron Hamiltonian matrix elements, $U_{\mu\mu}$, are obtained by fitting to atomic ionisation energies.

- Finally, the bonding parameters, β_{AB}^o are approximated by the expression

$$\beta_{AB}^o = \frac{1}{2}(\beta_A^o + \beta_B^o),$$

  and each β_A^o is empirically fitted to *ab initio* calculations for each atomic species.

CNDO/1 was the first parameterisation under the CNDO approximation, but this was quickly superseded by CNDO/2.

2.5.3 CNDO/2

There are two improvements made to the CNDO/1 parameterisation.

1. The penetration integral is neglected which means that the electron-ion integrals V_{AB} are no longer evaluated separately, but instead are related to the repulsion term, $V_{AB} = Z_B\gamma_{AB}$. There is no *physical* justification for this approximation, but it often predicts bond-length reasonably well.

2. Instead of fitting the $U_{\mu\mu}$ using only the ionisation potential, an average of the ionisation potential and electron affinities is used. This should make CNDO/2 better suited to modelling the tendencies for atomic orbitals to both gain and lose electrons than CNDO/1.

In all other ways CNDO/2 is the same as CNDO/1.

In summary, CNDO-type calculations are based on the HF quantum mechanical description. The approximations neglect the vast majority of integrals, making the calculation of large systems of atoms possible. However, in the process a great deal

of the interaction information is lost. The fact that the method has been successful in describing a range of problems is primarily due to the fact that fitting some of the terms to experimental and/or *ab initio* data in some way replaces the neglected terms by building the information into the integrals that remain.

It should be noted, however, the neglect of exchange integrals means that spin-sensitive systems will not be correctly described. This is in some part corrected by the following method.

2.5.4 Intermediate neglect of differential overlap

CNDO explicitly excludes the two-electron exchange integrals. These are crucial to provide a description of any system where an electron spin distribution is important such as finding the relative energies of different spin states. If one includes exchange for electrons on the same atom, i.e. one retains one-centre monatomic differential overlap integrals, this problem is mitigated to some extent and is termed the *intermediate neglect of differential overlap*, (INDO) [21, 22]. In the formalism of Slater [23], these integrals are established by using a fit to experimental atomic energy levels. There are no other major differences between CNDO and INDO.

2.5.5 Neglect of diatomic differential overlap

The next logical extension is to neglect only diatomic differential overlap, and thus such a method would include dipole-dipole interactions of the form $\langle s_A p_A | s_B p_B \rangle$. This level of approximation is naturally termed the *neglect of diatomic differential overlap*, (NDDO).

2.5.6 Summary

In summary, these approximate, empirical methods have been developed to circumvent the prohibitive computational demands of the *ab initio* HF method. Although the approximations allow one to treat large systems of atoms very rapidly, terms in the calculations are being sacrificed for this speed, and consequently the description of a system of atoms using these methods will always be inferior to first principles methods.

One example of where this can be important is where CNDO methods get the ordering of electronic levels wrong. This is the case for the negatively charged substitutional Ni impurity in diamond [24] where CNDO calculations produce a *rogue* a_1 level below instead of above a t_2 level. This leads to the defect possessing an effective spin of S=1/2, whereas experimental evidence shows that the true spin state is S=3/2 [25].

2.6 Hartree-Fock theory of the homogeneous electron gas

As stated above, HF theory can only be applied to simple systems. One such situation is the homogeneous electron gas, where the ions form a uniform background. A solution to Eq. 2.11 then takes the form of a set of plane waves of the form,

$$\psi_\lambda(\mathbf{r}, s) = \frac{1}{\sqrt{\Omega}} e^{i\mathbf{k}.\mathbf{r}} \chi_\alpha(s),$$

where λ labels the wave-vector $\mathbf{k}$ and spin α, and Ω is the volume of the primitive unit cell. Since the electron density, n, is uniform, E_{H} and $E_{\mathrm{i-i}}$ exactly cancel $E_{\mathrm{e-i}}$ to give the energy levels:

$$E_\lambda = E_{\mathbf{k},\alpha} = \frac{1}{2}k^2 + V^{\mathrm{x}}_{\mathbf{k}}.$$

It can be shown that by writing $\eta = k/k_f$ (where the electron density is given by $n = \frac{1}{3\pi^2}k_f^3$), the exchange potential is:

$$\begin{aligned} V^x_{\mathbf{k}} &= -4\left(\frac{3n}{8\pi}\right)^{\frac{1}{3}} F(\eta), \\ F(\eta) &= \frac{1}{2} + \frac{1-\eta^2}{4\eta}\ln\left(\frac{1+\eta}{1-\eta}\right). \end{aligned}$$

Since the density of states is given by

$$N(E) = \frac{4\pi k^2}{8\pi^3}\frac{1}{|\nabla E_{\mathbf{k}}|},$$

the singularity in the derivative of $V^x_{\mathbf{k}}$ as $\eta \to 1$ leads to a zero density of states as $k \to k_f$, which is incorrect, and is due to the absence of correlation in the calculations. This error can be surmounted by constructing wavefunctions made up of combinations of determinants, a method which is termed 'configuration interaction' (CI), but this is extremely computationally demanding and only a few atoms can be treated in this manner.

2.7 Correlation

In 1980, Ceperley and Alder [26] performed quantum Monte-Carlo calculations on the non-spin-polarised and spin-polarised electron gases to find a better estimate of the ground state energies. This method includes the correlation energy, E_{c} which is missing from HF. Defining the correlation energy per electron, ϵ_{c}, polarisation ξ and the Wigner-Seitz radius of each electron r_s by:

$$E_{\mathrm{c}} = \Omega n \epsilon_{\mathrm{c}}(n, \xi), \quad \xi = \frac{(n_\uparrow - n_\downarrow)}{n}, \quad r_s = (4\pi n/3)^{1/3}, \tag{2.18}$$

	γ	β_1	β_1	
Non-polarised	-0.1423	1.0529	0.3334	
Polarised	-0.0843	1.3981	0.2611	
	A	B	C	D
Non-polarised	0.0311	-0.0480	0.0020	-0.0116
Polarised	0.0155	-0.0269	0.0007	-0.0048

Table 2.1: Parameterisation of the exchange-correlation energy in Ref. [27].

then $\epsilon_{\rm c}$ for $\xi = 0$ and $\xi = 1$ are given as [27]:

$$\epsilon_{\rm c} = \begin{cases} \gamma\{1 + \beta_1\sqrt{r_s} + \beta_2 r_s\}^{-1}, & \text{for } r_s \geq 1 \\ B + (A + Cr_s)\ln(r_s) + Dr_s, & \text{for } r_s < 1 \end{cases}$$

The values of the coefficients are given in Table 2.1.

In the case of a partially polarised gas, i.e. where $0 < \xi < 1$, the correlation energy is taken to be the average over the polarised and non-polarised cases [28]:

$$\begin{aligned} \epsilon_c(n,\xi) &= \epsilon_c^{\rm np}(n) + f(\xi)(\epsilon_c^{\rm p}(n) - \epsilon_c^{np}(n)) \\ f(\xi) &= \frac{(1+\xi)^{4/3} + (1-\xi)^{4/3} - 2}{2^{4/3} - 2}. \end{aligned}$$

To a good approximation, the exchange-correlation energies vary as αn^{s_1} and βn^{s_2} for the non- and fully-polarised cases respectively, and AIMPRO uses the simplified expression for the non-polarised case $E_{\rm xc}$:

$$E_{\rm xc} = \Omega A n^{1.30917}, \tag{2.19}$$

For polarised gases, AIMPRO uses:

$$E_{\rm xc} = \Omega \sum_{i,s} A_i n_s^{p_i+1} n_{1-s}^{q_i}, \tag{2.20}$$

where A_i, p_i and q_i are given in Table 2.2. The subscript $1-s$ in Eq. 2.20 refers to the opposite spin to that over which is being summed. The error in this approximation is very small for low electron density ($n < 1$), but for larger density values, an alternative set of parameters is used A_i', p_i' and q_i' (also given in Table 2.2). However, this approximation is poorer at low densities.

2.8 Density functional theory

If one wishes to perform first principles calculations for large systems of atoms, one needs to circumvent the computationally intensive aspects of HF theory in some way. One solution which has been highly successful over the past decade is density

i	A_i	p_i	q_i
1	-0.9305	0.3333	0.0000
2	-0.0361	0.0000	0.0000
3	0.2327	0.4830	1.0000
4	-0.2324	0.0000	1.0000
i	A'_i	p'_i	q'_i
1	-0.9305	0.3333	0.0000
2	-0.0375	0.1286	0.0000
3	-0.0796	0.0000	0.1286

Table 2.2: Parameterisation of the exchange-correlation used in AIMPRO.

functional theory (DFT). At the centre of this method the *electron density* is treated as the fundamental variable [4, 5] instead of the one-electron wavefunctions as in HF. This is possible since there is a one-to-one correspondence between the a non-degenerate, non-polarised ground state wavefunction, $\Psi(r)$ and the electron density $n(\mathbf{r}_1)$ defined by the expression:

$$n(\mathbf{r}_1) = \sum_{\mu} \int \delta(\mathbf{r}_1 - \mathbf{r}_\mu)|\Psi(r)|^2 dr.$$

This in turn arises from the result that for the electron Hamiltonian, $H = T_{\mathrm{e}} + V_{\mathrm{e-e}} + V_{\mathrm{e-i}}$, there is a one-to-one correspondence between the external potential $V_{\mathrm{e-i}}$ and the ground state electron density. This can be easily proved as follows. Suppose that this is not true, i.e. there exist two potentials with the same n. Then, from the variational principle, if Ψ_1 and Ψ_2 are the ground state (normalised) wavefunctions for the two potentials V_1 and V_2 with density n, and if $H_i\Psi_i = E_i\Psi_i$, then

$$\begin{aligned} E_1 = \langle\Psi_1|H_1|\Psi_1\rangle < \langle\Psi_2|H_1|\Psi_2\rangle &= E_2 + \langle\Psi_2|V_1 - V_2|\Psi_2\rangle \\ &= E_2 + \int (V_1 - V_2)n(\mathbf{r})d\mathbf{r}. \end{aligned}$$

But similarly

$$E_2 < E_1 + \int (V_2 - V_1)n(\mathbf{r})d\mathbf{r}.$$

Adding these equations gives us

$$E_2 + E_1 < E_1 + E_2,$$

which is a contradiction. Thus, $V_{\mathrm{e-i}}$ is uniquely defined by n, and hence Ψ is a unique functional of n. Remarkably, this means that the many-body wavefunction which is dependent on (3 spatial +1 spin)×(number of electrons) variables is uniquely defined by the charge density which is a function of only three spatial variables and spin.

It has also been shown [4] that the total energy, E, is also a functional of the electron density:

$$E[n] = T[n] + E_{\mathrm{e-i}}[n] + E_{\mathrm{H}}[n] + E_{\mathrm{xc}}[n] + E_{\mathrm{i-i}}, \tag{2.21}$$

where

$$\begin{aligned} E_{\mathrm{e-i}}[n(\mathbf{r})] &= -\int n(\mathbf{r}) \sum_a \frac{Z_a}{|\mathbf{r} - \mathbf{R}_a|} d\mathbf{r}, \\ E_{\mathrm{H}}[n(\mathbf{r})] &= \frac{1}{2} \int \frac{n(\mathbf{r}_1) n(\mathbf{r}_2)}{|\mathbf{r}_1 - \mathbf{r}_2|} d\mathbf{r}_1 d\mathbf{r}_2, \\ E_{\mathrm{i-i}} &= \frac{1}{2} \sum_{a \neq b} \frac{Z_a Z_b}{|\mathbf{R}_a - \mathbf{R}_b|}. \end{aligned}$$

The expressions for the kinetic energy, T, and the exchange-correlation energy, E_{xc}, are not obviously functionals of n in the way $E_{\mathrm{e-i}}$ and E_{H} are. Kohn and Sham [5] provided a paradigm for treating the kinetic term by introducing a set of orthonormal orbitals[3] as a basis for the (spin polarised) charge density:

$$n_s(\mathbf{r}) = \sum_\lambda \delta_{s_\lambda, s} |\psi_\lambda(r)|^2.$$

Then the kinetic energy can be written as

$$T = -\frac{1}{2} \sum_{\lambda, s} \int \psi_\lambda^* \nabla^2 \psi_\lambda d\mathbf{r}.$$

The only remaining term in Eq. 2.21 is E_{xc}. An *exact* expression for this is not known, so in practice some form of approximation must be adopted, the most common of which is termed the local density approximation (LDA).

2.9 The local density approximation

One assumes that for any small region in the system, the exchange-correlation is the same as that for the uniform electron gas with the same electron density. This approximation applies to a *spin zero* system, and the exchange-correlation is approximated by:

$$E_{\mathrm{xc}} = \int n(\mathbf{r}) \epsilon_{\mathrm{xc}}(n) d\mathbf{r},$$

where $\epsilon_{\mathrm{xc}}(n)$ is the exchange-correlation density for the homogeneous electron gas. For a spin polarised system, one simply applies the same assumptions using the exchange-correlation energy density of the spin-polarised electron-gas, $\epsilon_{\mathrm{xc}}(n_\uparrow, n_\downarrow)$.

[3]Note, since these 'Kohn-Sham' (KS) orbitals are merely an expansion of the charge density, strictly they cannot be interpreted as one-electron states.

This is termed the local spin density approximation (LSDA) and implementing this within DFT is often termed local spin density functional theory (LSDFT).

It is possible to go beyond the *local* approximation, and include further derivative terms in the density, termed the gradient correction [29]. However, the merits of such an approach are not accepted universally: with the improvement in ground state energy the gradient correction generally leads to a deterioration in the structure.

2.10 Determination of the Kohn-Sham orbitals

The KS orbitals are determined by minimising the total energy, E, with respect to n_s, subject to the constraint that both the total spin and the number of electrons are conserved. Then applying the variational principle, one arrives at the KS equations:

$$\begin{aligned} \left\{ -\frac{1}{2}\nabla^2 - \sum_a \frac{Z_a}{|\mathbf{r}-\mathbf{R}_a|} + V^{\mathrm{H}}(\mathbf{r}) + V_{s_\lambda}^{\mathrm{xc}}(n_\uparrow, n_\downarrow) - E_\lambda \right\} \psi_\lambda(r) &= 0 \\ \sum_s \int |\psi_\lambda(r)|^2 d\mathbf{r} &= 1, \end{aligned}$$

where

$$V_s^{\mathrm{xc}} = \frac{d(n\epsilon_{\mathrm{xc}})}{dn_s}.$$

These sets of equations (one set for each spin state) can be solved to generate the KS levels, E_λ, and KS wave-functions. In contrast to HF, the wavefunctions derived are not strictly those belonging to one-electron states, and the eigenvalues under LSDFT are not the ionisation energies as is the case in HF theory (Koopman's theorem), but instead are related to the quasi-particle energies. It is possible to augment the density functional theory via, for example, GW theory[4] which predicts quasi-particle energies with reasonable accuracy [31].

2.11 Pseudopotentials

In practice, the all-electron potential representing the interaction between the nuclei and electrons is replaced by a pseudopotential, in which only the valence electrons are considered explicitly. This approximation can be crucial since a treatment including core states has a number of associated difficulties.

[4] A full discussion of GW theory is beyond the scope of this thesis, but the framework within which the GW approximation is formulated is that of a perturbation expansion of one particle greens function $G(p, w)$. See for example Ref. [30]

- First, the total energy generated by using an all-electron potential is very large. Then when comparing total energies of similar systems large errors can be generated by subtracting similar values.

- Secondly, as one adds more and more core electrons, wavefunction orthonormality means that the wavefunctions will become very oscillatory. This makes the fitting to a Gaussian or plane-wave basis very difficult. Furthermore, a small error in the fit to the wavefunction for one of the core states can have a dramatic effect on the energy of the core eigenvalue.

- Thirdly, as the atomic number increases, the core states become relativistic in nature. The use of pseudopotentials immediately removes this difficulty.

Since the core electrons do not take a significant role in bonding, one can justify the use of pseudopotentials in solid state problems. However, the core electrons undergo exchange interactions with the valence electrons, the constructions of pseudopotentials is a non-trivial exercise.

The way one goes about constructing a pseudopotential is dependent on the application for which the potential is to be used. For example, for a plane-wave approach, one would desire a functional form that decays rapidly with wave-vector, such as the soft-pseudopotentials of Vanderbilt [32], but this is not important in the real-space methodology adopted in AIMPRO.

We have adopted the approach of Bachelet *et al.* [11] who developed a set of norm-conserving pseudopotentials for atomic species with atomic number ranging from 1 (hydrogen) to 94 (plutonium). The term 'norm-conserving' simply implies that the pseudopotential possesses exactly the same atomic charge density beyond the core radius as that of the the all-electron potential.

The sequence of processes required to produce a potential is as follows:

1. The KS equations are solved for the atom. To do this, the spherically symmetric atomic configuration is chosen so that the KS levels are labelled by angular momentum, l, in the case of the lighter atoms, and $j = l \pm 1/2$ for the heavy atoms where the Dirac equation is required. It is important to include in the construction all the orbitals that will take part in bonding the solid state. For example, in the case of carbon, the atomic configuration is normally taken as $1s^2 2s^2 2p^2$, which does not contain any d-orbital dependence. To rectify this, the $l = 2$ potential is constructed using the *ionised* configuration $1s^2 2s^{0.75} 2p^1 3d^{0.25}$. This procedure is tailored to each atomic species.

2. Then, the solutions to the all-electron KS equations for the atom produce a set of all-electron wavefunctions and energy levels, which in turn can construct the

all electron potential, denoted $V^\nu(r)$. This potential contains the exchange-correlation, Hartree and nuclear potentials, and is singular at $r = 0$.

3. From these all-electron quantities, one constructs a first approximation to the pseudopotential for each value of the angular momentum, l, or in the case of relativistic treatment, $j = 1 \pm 1/2$. This first guess removes the singularity:

$$V_l(r) = V^\nu(r)(1 - f(r/r_{c,l})) + c_l^\nu f(r/r_{c,l}).$$

The function $f(x)$ tends to unity as $x \to 0$, and rapidly decreases to zero as x increases. Such a function might be $e^{-x^{3.5}}$. Then, $V_l(r) \to c_l^\nu$ as $r \to 0$, where c_l^ν is a constant chosen so that the lowest energy level generated by V^ν is the same as that generated by $V_l(r)$. Then the normalised pseudo-wavefunction of V_l, denoted by ω_{1l}^ν, is, to within a normalisation constant, the same as the true, all-electron wavefunction at large r, since $V_l(r)$ is the same as $V^\nu(r)$ there.

4. $r_{c,l}$ is the radius at which the pseudo-wavefunction and true wavefunction approach each other, and is termed the core radius. Care must be taken in the choice of value for $r_{c,l}$ since taking too large a value will remove critical bonding information from the potential. Generally, $r_{c,l}$ is chosen to be midway between the last node and last extremum.

5. The next stage is to modify the pseudo-wavefunctions so that they agree with the true wavefunctions exactly, and not just to a normalisation constant. This is done using the expression:

$$\omega_{2l}^\nu = \gamma_l^\nu \{\omega_{1l}^\nu(r) + \delta_l^\nu r^{l+1} f(r/r_{c,l})\}.$$

Here the quantities γ_l^ν and δ_l^ν are simply the normalisation constants.

6. The potential that gives rise to the pseudo-wavefunction ω_{2l}^ν is obtained by inverting the Schrödinger equation using the energy levels of the all-electron system. Such a potential would then give rise to a wavefunction that agrees with the all electron wavefunction outside the core radius, and also generates the all-electron energy levels. However, this potential still includes the Hartree and exchange-correlation potentials.

7. The Hartree potential arising from the pseudo-wavefunction can be removed exactly, but a removal of the exchange-correlation potential can only be performed approximately. This approximation can be improved upon by instead subtracting the exchange-correlation potential due to the all-electron charge

density and spin-polarisation [33]. Once this is done, one is left with the bare electron-ion pseudopotential, $V_l(r)$.

8. For relativistic atoms, an average pseudopotential is defined as being:

$$V_l(r) = \frac{1}{2l+1}\left\{lV_{l-\frac{1}{2}}(r) + (l+1)V_{l+\frac{1}{2}}(r)\right\},$$

which is termed the scalar relativistic potential. The spin-orbit potential is given by:

$$V_l^{so}(r) = \frac{2}{2l+1}\left\{V_{l+1/2}(r) - V_{l-1/2}(r)\right\},$$

which leads to the full pseudopotential:

$$V^{ps}(\mathbf{r}) = \sum_l |l\rangle \left\{V_l(r) + V_l^{so}(r)\mathbf{L}.\mathbf{S}\right\} \langle l|.$$

9. Finally, the potentials have been parameterised by fitting to simple functions, such that:

$$\begin{aligned} V_l(r) &= -\frac{Z_\nu}{r}\left\{\sum_{i=1}^{2} c_i^c erf(\sqrt{\alpha_i^c}r)\right\} + \sum_{i=1}^{3}\left\{A_{i,l} + r^2 A_{i+3,l}\right\} e^{-\alpha_{i,l}r^2} \\ V_l^{so}(r) &= \sum_{i=1}^{3}\{B_{i,l} + r^2 B_{i+3,l}\}e^{-\alpha_{i,l}r^2}. \end{aligned}$$

Here, the values Z_ν and α_i^c are the valence electron charge and the inverse of the extent of the core charge density.

10. Note, the coefficients, c_i^c, in the first term in the potential are *independent* of the angular momentum, l, and hence this part of the potential is termed *local*. Since $\sum_{i=1}^{2} c_i^c = 1$, at distances where $\alpha_i^c r \gg 1$, the first term is simply the Coulomb potential due to the valence electrons, $-Z_\nu/r$. The second term has coefficients that *do* depend on l, and this part of the potential is thus termed non-local.

11. The constants, Z_ν, c_i^c, α_i^c, $A_{i,l}$, $B_{i,l}$ and $\alpha_{i,l}$ are tabulated in Ref. [11].

Note, although these pseudopotentials are generated to include spin-orbit interaction, this term is currently neglected by AIMPRO.

2.12 AIMPRO methodology

In this section the details of the approach adopted in AIMPRO are discussed. This will include an explanation of the mathematical constructions used in generating

the Hartree and exchange-correlation energies, and end in the expression of the Kohn-Sham equations in the form of a matrix-eigenvalue problem (Sec. 2.12.3).

The wavefunctions are expanded in a basis of localised orbitals such that:

$$\psi_\lambda(\mathbf{r}, s) = \chi_\alpha(s) \sum_i c_i^\lambda \phi_i(\mathbf{r} - \mathbf{R_i}), \quad c_i^\lambda \in \Re, \tag{2.22}$$

where the basis functions are Gaussian orbitals:

$$(x - R_{ix})^{n_1}(y - R_{iy})^{n_2}(z - R_{iz})^{n_3} e^{-a_i(\mathbf{r}-\mathbf{R}_i)^2}, \quad n_i \in \mathcal{N}.$$

From suitable combinations of n_i, one can construct the s, p, d, ... orbitals. For example $n_i = 0$, $i = 1, 2, 3$ generates an s-Gaussian orbital.

The charge density, $n(\mathbf{r})$, for each spin is constructed in terms of a *density matrix*, $b_{ij,s}$, such that :

$$\begin{aligned} n_s(\mathbf{r}) &= \sum_{ij} b_{ij,s} \phi_i(\mathbf{r} - \mathbf{R}_i)\phi_j(\mathbf{r} - \mathbf{R}_j), \\ b_{ij,s} &= \sum_{\lambda_{occ}} \delta(s, s_\lambda) c_i^\lambda c_j^\lambda \end{aligned} \tag{2.23}$$

Then it is necessary to calculate each term in Eq. 2.21 in terms of this basis. Since the basis is made up of Gaussian functions, the kinetic and pseudopotential terms are readily (analytically) found:

$$\begin{aligned} T_{ij} &= -\frac{1}{2} \int \phi_i(\mathbf{r} - \mathbf{R}_i) \nabla^2 \phi_j(\mathbf{r} - \mathbf{R}_j) d\mathbf{r}, \quad \text{and} \\ V_{ij}^{ps} &= \int \phi_i(\mathbf{r} - \mathbf{R}_i) \sum_a V_a^{ps}(\mathbf{r} - \mathbf{R}_a) \phi_j(\mathbf{r} - \mathbf{R}_j) d\mathbf{r}. \end{aligned}$$

2.12.1 Evaluation of the Hartree energy

Writing down the expression for the Hartree energy, one finds that the term requires $O(N^4)$ integrals, where N is the number of basis functions. To calculate all of these integrals would make the calculation prohibitively time consuming, and therefore a number of approximations are made. One option is to integrate these terms over a mesh [34], but the approach adopted for AIMPRO is to reduce the integral *analytically* to a simpler, approximate form. This is achieved by using an approximate charge density, $\tilde{n}_s(\mathbf{r})$. This is in turn an expansion of a set of basis functions [35, 36]:

$$\tilde{n}_s(\mathbf{r}) = \sum_k c_{k,s} g_k(\mathbf{r}), \quad \tilde{n}(\mathbf{r}) = \sum_s \tilde{n}_s(\mathbf{r}).$$

The exact Hartree energy is replaced by $\tilde{E}_{\mathrm{H}}$, such that:

$$\tilde{E}_{\mathrm{H}} = \int \frac{n_s(\mathbf{r})\tilde{n}_s(\mathbf{r}_2)}{|\mathbf{r}_1 - \mathbf{r}_2|} d\mathbf{r}_1 d\mathbf{r}_2 - \frac{1}{2} \int \frac{\tilde{n}_s(\mathbf{r})\tilde{n}_s(\mathbf{r}_2)}{|\mathbf{r}_1 - \mathbf{r}_2|} d\mathbf{r}_1 d\mathbf{r}_2,$$

which is clearly exact if $\tilde{n} = n$. The fitting function coefficients are chosen so that the error in the Hartree energy is minimised:

$$E_{\rm H} - \tilde{E}_{\rm H} = \frac{1}{2}\int \frac{\{n(\mathbf{r}_1) - \tilde{n}(\mathbf{r}_1)\}\{n(\mathbf{r}_2) - \tilde{n}(\mathbf{r}_2)\}}{|\mathbf{r}_1 - \mathbf{r}_2|} d\mathbf{r}_1 d\mathbf{r}_2,$$

which in turn is done by differentiating with respect to the c_k to give:

$$\sum_l G_{kl} c_l \;=\; \sum_{ij} t_{ijk} b_{ij}, \tag{2.24}$$

where

$$\begin{aligned} t_{ijk} &= \int \phi_i(\mathbf{r}_1 - \mathbf{R}_i)\phi_j(\mathbf{r}_1 - \mathbf{R}_j) g_k(\mathbf{r}_2) \frac{1}{|\mathbf{r}_1 - \mathbf{r}_2|} d\mathbf{r}_1 d\mathbf{r}_2, \quad \text{and} \\ G_{kl} &= \int g_k(\mathbf{r}_1) g_l(\mathbf{r}_2) \frac{1}{|\mathbf{r}_1 - \mathbf{r}_2|} d\mathbf{r}_1 d\mathbf{r}_2. \end{aligned}$$

The basis functions, g_k, are a set of atom centred Gaussian functions[5]:

$$\left\{1 - \frac{2b_k}{3}(\mathbf{r} - \mathbf{R}_k)^2\right\} e^{-b_k(\mathbf{r}-\mathbf{R}_k)^2}, \tag{2.25}$$

which give rise to a Gaussian potential:

$$\int \frac{g_k(\mathbf{r}_1)}{|\mathbf{r} - \mathbf{r}_1|} d\mathbf{r}_1 = \frac{3b_k}{2\pi} e^{-b_k(\mathbf{r}-\mathbf{R}_k)^2}.$$

Since the integrals of the g_k vanish, we need to add a further simple Gaussian, which will then contribute to the total number of electrons. Since all terms in the integral t_{ijk} are Gaussian, they can be evaluated analytically, and very rapidly. Nevertheless, evaluating this matrix scales like $O(N^3)$, where N is the number of basis functions and will be the most time consuming part of the calculation when the clusters are small. For larger clusters ($\gtrsim 100$ atoms), a number of integrals can be ignored, since the overlap of orbitals distant from each other in the cluster is essentially zero. Then, it is the solution of the eigenvalue problem (Sec. 2.12.3) that is the time limiting step.

2.12.2 Exchange-correlation energy

In a similar approach to that adopted for calculating the Hartree energy, the exchange-correlation energy is replaced by using the approximate charge density $\tilde{n}$:

$$\tilde{E}_{\rm xc} = \int \epsilon_{\rm xc}(\tilde{n}_\uparrow, \tilde{n}_\downarrow)\tilde{n} d\mathbf{r}.$$

[5]This is actually only one of the basis set options within AIMPRO, and one might also use a simple Gaussian basis set which does not include the term in braces.

Again, $\tilde{n}$ is an expansion of basis functions,

$$\tilde{n}_s(\mathbf{r}) = \sum_k d_{k,s} h_k(\mathbf{r}),$$

where $h_k(\mathbf{r})$ are simple Gaussians, and the $d_{k,s}$ are found by minimising

$$\int \{n_s(\mathbf{r}) - \tilde{n}_s(\mathbf{r})\}^2 d\mathbf{r}.$$

Differentiating with respect to $d_{k,s}$ leads to the equations:

$$\begin{aligned} \sum_l H_{kl} d_{l,s} &= \sum_{ij} u_{ijk} b_{ij,s}, \qquad (2.26) \\ H_{kl} &= \int h_k(\mathbf{r}) h_l(\mathbf{r}) d\mathbf{r}, \\ u_{ijk} &= \int \phi_i(\mathbf{r} - \mathbf{R}_i) \phi_j(\mathbf{r} - \mathbf{R}_j) h_k(\mathbf{r}) d\mathbf{r}. \end{aligned}$$

Once the coefficients are found, one can simply substitute the basis expansion into the expression for E_{xc} to get (in the non-spin-polarised case)

$$\tilde{E}_{\mathrm{xc}} = \sum_k d_k \int h_k(\mathbf{r}) \epsilon_{\mathrm{xc}}(\tilde{n}) d\mathbf{r}.$$

Since the h_k have been chosen to be Gaussian functions, this value is simply proportional to the average value of the exchange-correlation density under these functions, $\langle \epsilon_{\mathrm{xc}}(\tilde{n}) \rangle_k$. Now, ϵ_{xc} varies slowly with density, and thus we can approximate $\langle \epsilon_{\mathrm{xc}}(\tilde{n}) \rangle_k$ by $\epsilon_{\mathrm{xc}}(\langle \tilde{n} \rangle_k)$, which is equivalent to replacing the exact exchange-correlation density at a point by the value for the homogeneous electron gas with the average density, $\langle \tilde{n} \rangle_k$. This approximation can be improved upon by using the more accurate expression for the exchange-correlation density:

$$\epsilon_{\mathrm{xc}}(n) \approx A n^s,$$

($s = 0.30917$) leading to an expression for $\tilde{E}_{\mathrm{xc}}$:

$$\tilde{E}_{\mathrm{xc}} = \sum_k d_k \epsilon_k, \qquad (2.27)$$

where

$$\begin{aligned} \epsilon_k &= I_k \epsilon_{\mathrm{xc}}(\langle \tilde{n} \rangle_k) e^{f_k}, \\ f_k &= \frac{1}{2} s(s-1) \ln \left(\frac{\langle \tilde{n}^2 \rangle_k}{\langle \tilde{n} \rangle_k^{\,2}} \right), \\ I_k &= \int h_k(\mathbf{r}) d\mathbf{r}. \end{aligned}$$

All of the integrals in this expression can be solved analytically. This theory has been extended to the spin-polarised system [37]. The true exchange-correlation is written (referring to Sec. 2.7 and Table 2.2):

$$E^{\mathrm{xc}}(n_\uparrow, n_\downarrow) = \sum_{i,s} A_i \int n_s^{p_i+1} n_{1-s}^{q_i} d\mathbf{r},$$

and again we substitute $\tilde{n}$ for n, although in this case, the density is spin polarised:

$$\tilde{E}_{\mathrm{xc}} = \sum_{ks} d_{k,s}\epsilon_{k,s}, \quad \epsilon_{k,s} = \sum_i A_i I_k \langle \tilde{n}_s^{p_i} \tilde{n}_{1-s}^{q_i} \rangle_k. \tag{2.28}$$

The spin-polarised exchange-correlation energy is then evaluated by interpolating between the integer values of:

$$f(p,q) = \frac{1}{2}p(p-1)f(2,0) + \frac{1}{2}q(q-1)f(0,2) + pqf(1,1),$$

which are known. Here, f is defined by the expression:

$$f(p,q) = \ln\left(\frac{\langle \tilde{n}_s^p \tilde{n}_{1-s}^q \rangle_k}{\langle \tilde{n}_s \rangle_k^p \langle \tilde{n}_{1-s} \rangle_k^q}\right).$$

2.12.3 Arrival at the eigenvalue equation

Ultimately, combining all the expressions for the components of the total energy results in the a *matrix* formulation of the KS equations. The total energy can be written

$$E = \sum_{ij} \{T_{ij} + V_{ij}^{ps}\} b_{ij} + \tilde{E}_H + \tilde{E}_{\mathrm{xc}} + E_{\mathrm{i-i}},$$

where i and j label the coefficients of the basis orbitals. Then E is minimised with respect to the orthonormal set of wavefunctions, $\psi_\lambda(r)$, by introducing Lagrange multipliers, E_λ, to get the expression:

$$\sum_{ij\lambda} c_i^\lambda \{T_{ij} + V_{ij}^{ps} - E_\lambda S_{ij}\} c_j^\lambda + \tilde{E}_{\mathrm{H}} + \tilde{E}_{\mathrm{xc}} + E_{\mathrm{i-i}}, \tag{2.29}$$

$$S_{ij} = \int \phi_i(\mathbf{r} - \mathbf{R}_i)\phi_j(\mathbf{r} - \mathbf{R}_j) d\mathbf{r}.$$

Differentiating Eq. 2.29 with respect to c_i^λ, we arrive at the KS equations:

$$\sum_j \left\{T_{ij} + V_{ij}^{ps} + V_{ij}^{\mathrm{H}} + V_{ij,s_\lambda}^{\mathrm{xc}} - E_\lambda S_{ij}\right\} c_j^\lambda = 0, \tag{2.30}$$

where the Hartree and exchange-correlation potentials are introduced by:

$$\frac{\partial \tilde{E}_{\mathrm{H}}}{\partial c_i^\lambda} = \sum_j V_{ij}^H c_j^\lambda, \qquad V_{ij}^{\mathrm{H}} = \sum_{kl} G_{kl} c_l \frac{\partial c_k}{\partial b_{ij}}$$

$$\frac{\partial \tilde{E}_{\mathrm{xc}}}{\partial c_i^\lambda} = \sum_j V_{ij,s_\lambda}^{\mathrm{xc}} c_j^\lambda, \qquad V_{ij,s}^{\mathrm{xc}} = \sum_k \left\{\epsilon_{k,s} + \sum_l d_{l,s} \frac{\partial \epsilon_{l,s}}{\partial d_{k,s}}\right\} \frac{\partial d_{k,s}}{\partial b_{ij,s}},$$

and Eqs. 2.24 and 2.26 provide the expressions:

$$\sum_l G_{kl}\frac{\partial c_l}{\partial b_{ij}} = t_{ijk} \quad \sum_l H_{kl}\frac{\partial d_{l,s}}{\partial b_{ij,s}} = u_{ijk}.$$

The KS equations in Eq. 2.30 can be written in matrix form

$$(H - ES)c = 0,$$

which is just the generalised eigenvalue problem. The overlap matrix, S, is then Choleski decomposed, i.e. $S = U^tU$, where U is upper triangular, which takes $O(N^3)$ operations. Then, by writing $Uc = d$, we arrive at the standard eigenvalue problem:

$$\left[(U^{-1})^t H U^{-1} - E\right] d = 0.$$

The eigenvalues are then found using the standard Householder method, and since there are many more unoccupied states than occupied, a subset of the eigenvectors are found using an inverse iteration method. For large clusters, it is the solution of the generalised eigenvalue problem that in practice is the most time consuming step in the computation, and scales as $O(N^3)$.

2.13 The self-consistent cycle

In order that a method may correctly model the redistribution of charge from one atom to another, it is essential to perform electronic structure calculations *self consistently*. Self-consistency simply means that the charge density generated by an external potential is the same as the charge density that generated that potential, to within some tolerance.

The initial guess at the charge density coefficients is taken either to be those of the neutral atom or those output from a previous calculation. First, these initial charge density coefficients, labelled c^i_k and $d^i_{k,s}$, are fed into the KS equations and the density matrix, $b_{ij,s}$, is generated. Then Eqs. 2.24 and 2.26 are used to determine the *output* charge density coefficients, say c^o_k and $d^o_{k,s}$. Then one takes a weighted average of the input and output charge densities:

$$c'_k = c_k + w(c^o_k - c_k), \quad d'_{k,s} = d_{k,s} + w(d^o_{k,s} - d_{k,s}).$$

The procedure is identical for the c_k's and $d_{k,s}$'s.

The generation of an output charge density can be viewed as a non-linear operator acting on the input charge density, $c^o_k = \hat{L}_k(c)$. Then the output charge density generated from an input charge density made up from the weighted average would be written as:

$$c^{o\prime}_k = \hat{L}_k(c') = \hat{L}_k(c + w(c^o - c)).$$

If the weighting factor, w, is sufficiently small, then this non-linear operation can be approximated by a Taylor expansion linear in w:

$$\begin{aligned} c_k^{o\prime} &= \hat{L}_k(c) + w\sum_l D_{kl}(c_l^o - c_l) \\ &= c_k^o + w\sum_l D_{kl}(c_l^o - c_l), \end{aligned}$$

where

$$D_{kl} = \frac{\partial \hat{L}_k}{\partial c_l}.$$

For self-consistency, the input and output charge densities must be the same to within some tolerance, i.e. $c_k^{o\prime} = c_k'$. Thus, one can write down an expression for generating w:

$$c_k^o + w\sum_l D_{kl}(c_l^o - c_l) = c_k + w(c_k^o - c_k),$$

which leads to

$$\frac{(1-w)(c_k - c_k^o)}{w} = \sum_l D_{kl}(c_l^o - c_l). \tag{2.31}$$

In practice one needs to choose a trial value of the weighting factor, $w = w_1$, where w_1 is small. Then, the output charge density, termed $c_{1k}^{o\prime}$, can be expressed as:

$$c_{1k}^{o\prime} = c_k^o + w_1\sum_l D_{kl}(c_l^o - c_l),$$

and hence

$$\sum_l D_{kl}(c_l^o - c_l) = \frac{(c_{1k}^{o\prime} - c_k^o)}{w_1}. \tag{2.32}$$

Then, comparing Eqs. 2.31 and 2.32, w can be chosen such that it minimises

$$\sum_k e_k g_k(\mathbf{r}), \tag{2.33}$$

where e_k is the difference between Eqs. 2.31 and 2.32,

$$\frac{(1-w)(c_k - c_k^o)}{w} - \frac{(c_{1k}^{o\prime} - c_k^o)}{w_1}.$$

Generally, the charge density converges very rapidly, and self-consistency is considered to have been reached when the difference in the input and output Hartree energies is less than 10^{-5} a.u.

2.13.1 The 'Fermi temperature'

Although in general, the above self-consistency cycle converges rapidly, when two levels are close together or degenerate, this algorithm can lead to discontinuities in the charge density as levels cross. This problem, known as 'charge sloshing' can in most cases be corrected by the introductions of Fermi statistical filling of the states, i.e. where the electron density is *smeared out* over those levels near the Fermi-level. Then the energy to be minimised is a free energy and includes the entropy:

$$F = E + k_B T \sum_{\lambda} \{ f_\lambda \ln f_\lambda + (1 - f_\lambda) \ln(1 - f_\lambda) \} - \mu \left\{ \sum_{\lambda} f_\lambda - M \right\}, \qquad (2.34)$$

where the energy level E_λ is occupied by f_λ electrons, μ is the chemical potential, k_B is Boltzman's constant, and M is the total number of electrons. Minimising Eq. 2.34 with respect to the chemical potential and the occupancies gives the familiar Fermi distribution:

$$f_\lambda = \frac{1}{e^{(E_\lambda - \mu)/k_B T} + 1}.$$

The expression for the density matrix must also be changed, and becomes

$$b_{ij,s} = \sum_{\lambda} \delta_{s,s_\lambda} f_\lambda c_i^\lambda c_j^\lambda.$$

Typically, a value of $k_B T = 0.04$ eV is used.

A couple of points should be made with regards to this procedure. First, the Fermi occupancies are not being used to simulate a system for $T > 0$, merely to aid the self-consistency procedure. Secondly, this procedure may actually obscure the *physics* of the system one is studying such as in the case of a Jahn-Teller distortion. In such cases, the method used to achieve a self-consistent solution is to dictate the *symmetry* of the states that are to filled, such as in the case of the substitutional Ni^- impurity in Si.

2.14 Structural optimisation

Following the evaluation of a self-consistent charge density, one is able to calculate the atomic forces, *analytically*. The forces can then be used to generate a search direction for minimising the energy of the cluster with respect to the location of the ion cores, $\mathbf{R}_a$. This is done via a conjugate gradients algorithm. Both expressions for the forces and minimisation routine follow.

2.14.1 Atomic forces

The force on any given atom a in a direction l is given by the expression:

$$f_{la} = -\frac{\partial E}{\partial R_{la}}, \quad l = x, y, z.$$

This can be evaluated by calculating the change in energy, ΔE when atom a is displaced by ΔR_{la}. From each term in Eq. 2.29, this can be written as:

$$\begin{aligned} \Delta E &= \sum_{ij} b_{ij}\Delta\{T_{ij} + V_{ij}^{ps}\} + \sum_{ij}\{T_{ij} + V_{ij}^{ps}\}\Delta b_{ij} \\ &\quad +\Delta\tilde{E}_{\mathrm{H}} + \Delta\tilde{E}_{\mathrm{xc}} + \Delta E_{\mathrm{i-i}} \\ \Delta\tilde{E}_{\mathrm{H}} &= \sum_{kl} c_k G_{kl}\Delta c_l + \frac{1}{2}\sum_{kl} c_k c_l \Delta G_{kl} \\ \Delta\tilde{E}_{\mathrm{xc}} &= \sum_{k,s} \epsilon_{k,s}\Delta d_{k,s} + \sum_{k,s} d_{k,s}\Delta\epsilon_{k,s}. \end{aligned} \tag{2.35}$$

From Eqs. 2.24 and 2.26, the Δc_k and $\Delta d_{k,s}$ can be evaluated, and gathering like terms, Eq. 2.35 can be rewritten as:

$$\Delta E = \sum_{ij}\{T_{ij} + V_{ij}^{ps} + V_{ij}^{\mathrm{H}}\}\Delta b_{ij} + \sum_{ij,s} V_{ij,s}^{\mathrm{xc}}\Delta b_{ij,s}.$$

From the KS equations (2.30) this can expressed as:

$$\Delta E = \sum_{\lambda} E_\lambda \Delta\{\sum_{ij} c_i^\lambda c_j^\lambda S_{ij}\} - \sum_{ij\lambda} E_\lambda c_i^\lambda c_j^\lambda \Delta S_{ij}.$$

Since $\sum_{ij} c_i^\lambda c_j^\lambda S_{ij}$ is simply the number of electrons, M, which is a constant, the first term vanishes. Hence, just as with the Hellmann-Feynman forces [38], the AIMPRO atomic forces do *not* contain derivatives of the wavefunction coefficients. Despite the expressions for the forces being rather complex, the fact that they are all obtainable analytically means that the time required to evaluate them is small in comparison with the overall time taken to calculate the self-consistent total energy.

2.14.2 Conjugate gradients optimisation

Once the atomic forces have been found, one can relax the atoms so that the total energy is reduced. One scheme might be to use the forces as a search direction along which one can calculate a number of total energies and find the minimum by interpolation. This method is termed 'steepest descents', but this is not the most efficient method. Algorithms that retain knowledge from previous search directions are in general much faster. It is therefore common practice to employ a conjugate gradients formalism.

Here, the initial search direction is in fact the steepest descents, but subsequent searches are performed in a direction which is conjugated to the previous ones. Thus, if the forces are labelled as above, f_{la}, then the search direction is defined to be:

$$d_{la} = f_{la} - \frac{\sum_{la} f_{la}(f_{la} - f^o_{la})}{\sum_{la}(f^o_{la})^2} d^o_{la},$$

where the superscript 'o' refers to the forces and search direction for the previous iteration. In general, this method results in a rapid convergence to an energy minimum.

One can superimpose restrictions on the atoms that are allowed to move, and more importantly, the point group symmetry to which the cluster must transform. Thus, when relaxing, say, a C_{3v} defect such as the neutral nitrogen impurity in diamond, the symmetry of the defect can be precisely controlled to be at least C_{3v} *throughout relaxation*, which leads to a considerable speed up in the running of the program, as well as a precise description of the degeneracies of the KS levels and vibrational modes.

If such constraints are not employed, noise in the forces, can lead to a loss of symmetry, and, typically, a larger number of iterations are required before the equilibrium structure is located.

2.15 Vibrational modes

One of the most important requirements of theoretical simulations of this type is to be able to reproduce quantities that are *experimentally* observable. One such observable is the infra-red absorption due to atomic vibrations, described in Sec. 3.2.

To simulate atomic vibrations theoretically, one calculates the energy double derivatives. In Eq. 2.4, the term $E(R)$ is essentially the potential energy seen by the ions due to the electrons, and is a minimum at the equilibrium structure. Thus, one can expand this function in terms of the ion displacements:

$$E(R) = E(R_o) + \frac{1}{2} \sum_{la,mb} \left(\frac{\partial^2 E}{\partial R_{la} \partial R_{mb}} \right) \Delta R_{la} \Delta R_{mb} + ..., \tag{2.36}$$

where the terms R_{la} refer to the displacement of the ion a in the l-direction, and the equilibrium nuclear coordinates are $\mathbf{R}_o$. Then the *harmonic* normal modes of the system are described by the solutions of the dynamical matrix [39]:

$$\begin{aligned} \sum_{mb} E_{la,mb} u^i_{mb} &= \omega_i^2 u^i_{la}, \\ E_{la,mb} &= \frac{1}{\sqrt{M_a M_b}} \left(\frac{\partial^2 E}{\partial R_{la} \partial R_{mb}} \right), \end{aligned}$$

where ω_i^2 and u_{la}^i are the normal mode frequencies and co-ordinates respectively.

In practice the energy double derivatives, $E_{la,mb}$, are approximated by the difference formula:

$$D_{la,mb} = \frac{(f_{mb}^{+}(l,a) - f_{mb}^{-}(l,a))}{2\varepsilon}.$$

Here, $f_{mb}^{+}(l,a)$ is the self-consistent force on atom b in the m direction when atom a is displaced by a small amount, ε in a direction l. The term $f_{mb}^{-}(l,a)$ is the corresponding force when atom a is moved in the opposite direction by ε. Then $D_{la,mb}$ is the energy second derivative up to second order in ε, but since this method is a difference and not a derivative, it includes all even powers of ε. Therefore, the modes thus generated are termed *quasi-harmonic* [40].

At each stage of the calculation of the energy double derivatives, the self-consistent energy and forces must be found, which means that only a limited number of atoms in the cluster can be practically included in the dynamical matrix in this fashion. In practice the energy double derivatives are only calculated for the defect atoms and those directly bonded to them. The remaining atoms are included in the dynamical matrix via some form of valence force potential. The one used here is due to Musgrave and Pople [41].

2.15.1 Musgrave-Pople valence force potentials

The Musgrave-Pople (MP) valence force potential is made up from all the combinations of stretch and bend up to second order:

$$\begin{aligned} V_a \;=\; & \frac{1}{4}\sum_b k_r^{(a)}(\Delta r_{ab})^2 + \frac{r_0^2}{2}\sum_{b>c} k_\theta^{(a)}(\Delta\theta_{bac})^2 \\ & + r_0 \sum_{c>b} k_{r\theta}^{(a)}(\Delta r_{ab} + \Delta r_{ac})\Delta\theta_{bac} + \sum_{c>b} k_{rr}^{(a)}\Delta r_{ab}\Delta r_{ac} \\ & + r_0^2 \sum_{d>c>b} k_{\theta\theta}^{(a)}\Delta\theta_{bac}\Delta\theta_{cad}. \end{aligned}$$

where Δr_{ab} is the change in the distance between atoms a and b, and $\Delta\theta_{bac}$ is the change in the angle subtended by atoms b and c at atom a. Note, this potential is only applied to *nearest neighbours*.

Using this potential, one can derive a phonon dispersion spectrum, which has been done for a number of materials using AIMPRO: diamond [42], silicon [43], germanium [44], GaAs [45], AlAs [46], InP [47], and quartz [48]. The high frequency modes are reproduced fairly accurately, but due to the lack of the long range Coulomb potential, the splitting of the longitudinal and transverse optic modes is not reproduced. Furthermore, the low lying modes which involve the motion of more than nearest neighbours are not well reproduced.

Despite its shortcomings, the potential is sufficient to model the interaction of more distant 'bulk' atoms with the core defect atoms. This is the approach adopted in the calculation of local modes, provided the defect modes are not resonant with bulk modes. Where the mode is resonant, an alternative approach is used utilising the Green function for the bulk material. This method is not discussed here, but a full explanation can be found in Refs. [14, 49]. One should note, the most significant factor in the precision of the calculated frequency is the bond-length. For hydrogen modes, approximately a 1% change in bond-length gives a 3% change in frequency, so for a high frequency mode like the 2635 cm^{-1} stretch mode of C_{As}-H in GaAs, a 0.01 Å change in bond-length might raise or lower the calculated frequency by as much as 70 cm^{-1}. Despite the error in the absolute frequencies, isotopes shifts are usually much more accurately described.

One often finds that the number of modes observed experimentally for a certain defect is less than the number one would theoretically expect. This can arise for a number of reasons. First, the modes in question may lie in a frequency range where there the absorption is dominated by another band. Secondly, symmetry selection rules may dictate that a mode is IR- or Raman-inactive (see Sec. 3.2). More subtly the mode may be invisible due to anharmonic effects, which has been suggested for the case of the overtone of the stretch mode of the C_{As}-H centre in GaAs [40]. Alternatively, if the induced dipole is small, i.e. the effective charge of the vibration is small, the mode may not be observed. The methods for quantifying anharmonicity and effective charges are outlined in the following sections.

2.15.2 Anharmonicity

In many cases, the quasi-harmonic approximation for the vibrational modes is very good, but where the amplitude of the vibration is large, such as in H-stretch modes, a larger range of the vibronic potential is sampled. This means that terms of r^3 and higher become increasingly important, where r is the atomic displacement from the equilibrium position. The consequent asymmetry in the vibronic potential breaks the symmetry selection rules, allowing transitions between states that possess the same parity in the harmonic approximation. Thus, the overtone can be observed.

2.15.2.1 Quantifying anharmonicity

If one labels the energies of the vibronic states of a given potential E_i, $i = 0, 1, 2, ...$, then the frequency of the fundamental vibration ω_{01} is given by $\hbar\omega_{01} = E_1 - E_0$, and the overtone by $\hbar\omega_{02} = E_2 - E_0$. The anharmonicity of a vibration may be quantified by the parameter A given by the difference in frequency between twice

the fundamental and the overtone, i.e.

$$A = 2\omega_{01} - \omega_{02}. \tag{2.37}$$

In the case of heavily hydrogenated amorphous silicon, the anharmonicity of the 2005 cm^{-1} Si-H band thus defined is 60 cm^{-1} [50].

Generally, the harmonic vibrational frequency of an oscillator moving in one-dimension with spring constant k and effective mass m^* is

$$\nu = \sqrt{\frac{k}{m^*}} \tag{2.38}$$

where the effective mass is written

$$\frac{1}{m^*_{\rm imp}} = \frac{1}{m_1} + \frac{1}{\chi m_2}. \tag{2.39}$$

Here m_1 is the mass of the light atom (such as H) labelled atom 1 and m_2 is the mass of the atom 2 to which atom 1 is bound. χ is a measure of how the atom 2 interacts with the atoms to which it is bound, and will thus be unity for a diatomic molecule. Generally, one would expect $\chi \geq 1$ because and back-bonds would tend to make atom 2 appear to be heavier than it is really. However, this is not necessarily the case. If the C atom were to be very tightly bound to another atom, the slight movement of the C atom during the vibration might cost energy which would actually push the mode up. Hence a value of $\chi < 1$ would be appropriate. This is found in the case of the prussic acid molecule, H-C-N, and this is described in detail in Sec. 6.2. However, this is not the case for the 2635 cm^{-1} stretch mode of C_{As}-H in GaAs [51]. The value of χ as calculated from simply substituting the isotopic data into Eq. 2.38 is less than one. Now, χ is a measure of how, in this case, the carbon atom is bound to the rest of the lattice, and the strong binding argument for the H-C-N molecule does *not* apply in this case.

The overtone of C_{As}-H is not observed, so one needs an alternative way of quantifying the anharmonicity to A. An approach [51] which can be adopted provided there is sufficient isotopic data for a vibration is described as follows. The *anharmonic* frequency is written as:

$$\omega = \nu - \frac{B}{m}, \tag{2.40}$$

where ν is simply the harmonic frequency (Eq. 2.38), and B is the measure of anharmonicity.

There is accurate data for both isotopes of C and H. The ratios

$$R_\omega(H) = \left(\frac{\omega(H - {}^{12}C)}{\omega(H - {}^{13}C)}\right)^2$$

and

$$R_\nu(H) = \left(\frac{\nu(H - {}^{12}C)}{\nu(H - {}^{13}C)}\right)^2$$

are equal to first order, and can thus be used to estimate χ. Another value for χ can be obtained from $R_\omega(D)$. These are both greater then unity. B can also be obtained [52] from the expression

$$B \approx 2\omega_D \frac{r' - r}{2 - r'}$$

where $r = \omega_H/\omega_D$ and $r' = \nu_H/\nu_D$. The value of m in Eq. 2.40 might be the mass of a hydrogen atom, as used in Ref. [51], or the effective mass, as defined in Eq. 2.39.

$A \times m^*$ is equal to B in low order perturbation theory, i.e. when the quartic terms are treated in first order and the cubic terms in second order, and are equal to:

$$\frac{(15a_3^2 - 12a_2a_4)}{8a_2^2},$$

where the parameters a_i are the coefficients of the x^i in the quartic vibronic potential. The parameter $A \times m^*$ is termed B_o.

2.15.2.2 Theoretical approach

The vibronic potential is generated by stepping the appropriate atoms in the direction of the normal coordinate generated by the quasi-harmonic methodology. At each point, the self-consistent total energy is calculated. It is crucial to sample a broad range of displacements so that the outermost points are well outside the tails of the vibronic wavefunction. In principle, one should also consider the coupling of stretch and bend characters, but for high frequency modes, such as that of the C-H stretch mode of the $C_{As} - H$ complex in GaAs, this coupling is expected to be rather small, and is therefore be neglected.

Previous *ab initio* theoretical studies have often used a one-dimensional quartic polynomial potential to model the vibronic potential, for example of H on the (111) surface of diamond [53]. In this case they found the calculated 2727 cm^{-1} stretch mode to exhibit anharmonicity (A=113 cm^{-1}). Unlike Ref. [53], we find that a polynomial expansion of terms up to and including x^8 is required to model the potential accurately. However, although polynomials are commonly used [53, 54], a Morse potential [55]:

$$V(r) = D(1 - e^{-ar})^2,$$

possesses phenomenologically the correct shape. Morse potentials have also been used for anharmonic calculations [56], and, perhaps surprisingly, we find that these two-parameter potentials fit the *ab initio* data as accurately as the x^8 polynomial.

Whatever form of potential is taken, the vibrational modes are calculated by solving the one-dimensional Schrödinger equation. If a polynomial fit to the potential is chosen, this can be readily written in terms of a secular matrix equation. The Hamiltonian is a combination of the harmonic and anharmonic terms $\hat{H}_o + \hat{V}$, and the Schrödinger equation can be written as

$$(\hat{H}_o + \hat{V})\Psi_i(x) = E_i\Psi_i(x).$$

$\Psi_i(x)$ is then expanded in terms of a set of (orthonormal) harmonic wavefunctions,

$$\begin{aligned}
\Psi_i(x) &= \sum_{j=0}^{\infty} c_{ij}\phi_j(x), \\
\phi_j(x) &= H_j(\sqrt{\beta}x)\left(\frac{\sqrt{\beta\pi}}{2^j j!}\right)^{\frac{1}{2}} e^{-\beta x^2/2}, \quad \beta = \frac{\sqrt{mk}}{\hbar}.
\end{aligned}$$

Here m is the mass of the oscillator, k is the spring constant, and $H_j(\eta)$ is the j^{th} Hermite polynomial defined iteratively by the expression:

$$H_{j+1}(\eta) = 2\eta H_j(\eta) - jH_{j-1}(\eta), \quad H_0 = 1, \quad H_1 = 2\eta.$$

In practice, of course, the expansion of the anharmonic wavefunction is a *truncated* series of harmonic functions. Typically the number of terms, N_o is around fifty. Substituting the expansion into the Schrödinger equation, multiplying on the left by ϕ_k and integrating over x gives the secular equations

$$\begin{aligned}
\langle k|\hat{H}\sum_j c_{ij}|j\rangle &= \langle k|E_i\sum_j c_{ij}|j\rangle \\
\sum_j c_{ij}\langle k|\hat{H}|j\rangle &= E_i\langle k|\sum_j c_{ij}|j\rangle \\
&= E_i\sum_j c_{ij}\langle k|j\rangle \\
&= E_i\sum_j c_{ij}\delta_{kj} \\
\sum_j c_{ij}\langle k|\hat{H}|j\rangle &= E_i c_{ik} \qquad (2.41)
\end{aligned}$$

The matrix elements are of the form

$$\left\langle k \left| \hat{H}_o + \sum_{\lambda=3}^{N_x} a_\lambda x^\lambda \right| j \right\rangle = \langle k|\hat{H}_o|j\rangle + \sum_{\lambda=3}^{N_x} a_\lambda\langle k|x^\lambda|j\rangle.$$

The first term on the right is simply the harmonic energy levels given by $E_i^o = (i + \frac{1}{2})h\nu$, where ν is the harmonic fundamental frequency. The anharmonic terms

can be found by analytically constructing each term in x using creation and annihilation operations. Alternatively, since the matrices X^n_{kj} with elements $\langle k|x^n|j\rangle$ are symmetric, one can generate any value of n from X^1_{kj} by matrix multiplication:

$$X^n_{kj} = (X^1_{kj})^n.$$

Using this, the matrix elements of the full anharmonic Hamiltonian for *any* choice of N_x and N_o can be readily evaluated.

Once the Hamiltonian is set up, one solves the secular equation in the usual way to generate a set of eigenvalues and eigenvectors which correspond to the vibronic energy levels and wavefunctions respectively.

The accuracy of the calculation is mainly dependent on two factors: the number of terms in x in the polynomial fit, and the number of harmonic functions used in the expansion of the anharmonic wavefunction. If too few terms in x are used, then the fit to the potential is poor, but as one adds terms, one also adds further minima, albeit outside the *ab initio* data range. One or more of these (unphysical) minima might be lower in energy than that at $x = 0$. Then, as the number of terms in the wavefunction expansion is increased, the range of x sampled by the sum increases, and hence the ground state anharmonic wavefunction may become centred on one of these false minima. This situation is illustrated in Fig. 2.1, which shows the first three energy levels and wavefunctions for $N_o = 30$ and $N_o = 90$.

Both of these problems can be avoided with a judicious choice of N_o and N_x, but it is perhaps better to choose an alternative type of fit that does not possess false minima. If one retains the polynomial fit, one can set the potential to be a simple function of x outside a critical region.

The Morse potential which does not posses any minima other than at $x = 0$. A direct comparison is made in Fig. 2.2. Despite having only two fitting parameters, the Morse potential is very nearly as good a fit as an eighth order polynomial.

If one adopts a polynomial expansion to fit the vibronic potential, then one can immediately identify the coefficient of x^2 with $k/2$. Then the harmonic frequency is given by $\nu^2 = 2a_2/m^*$, which in general will be higher than the quasi-harmonic frequencies since this does not include higher order even powers of x. If the Morse potential is used, then $k = 4Da^2$.

In general, the matrix elements, $\langle i|\hat{H}|j\rangle$ are not analytically available, and it is desirable to adopt an approach that can be generalised to any form of fit that one might choose. Therefore, instead of solving the secular equation, one might choose to integrate the Schrödinger equation directly, for instance using the shooting method. Comparing the solutions of the secular equation and shooting method for the polynomial, one finds that they agree to within a small error.

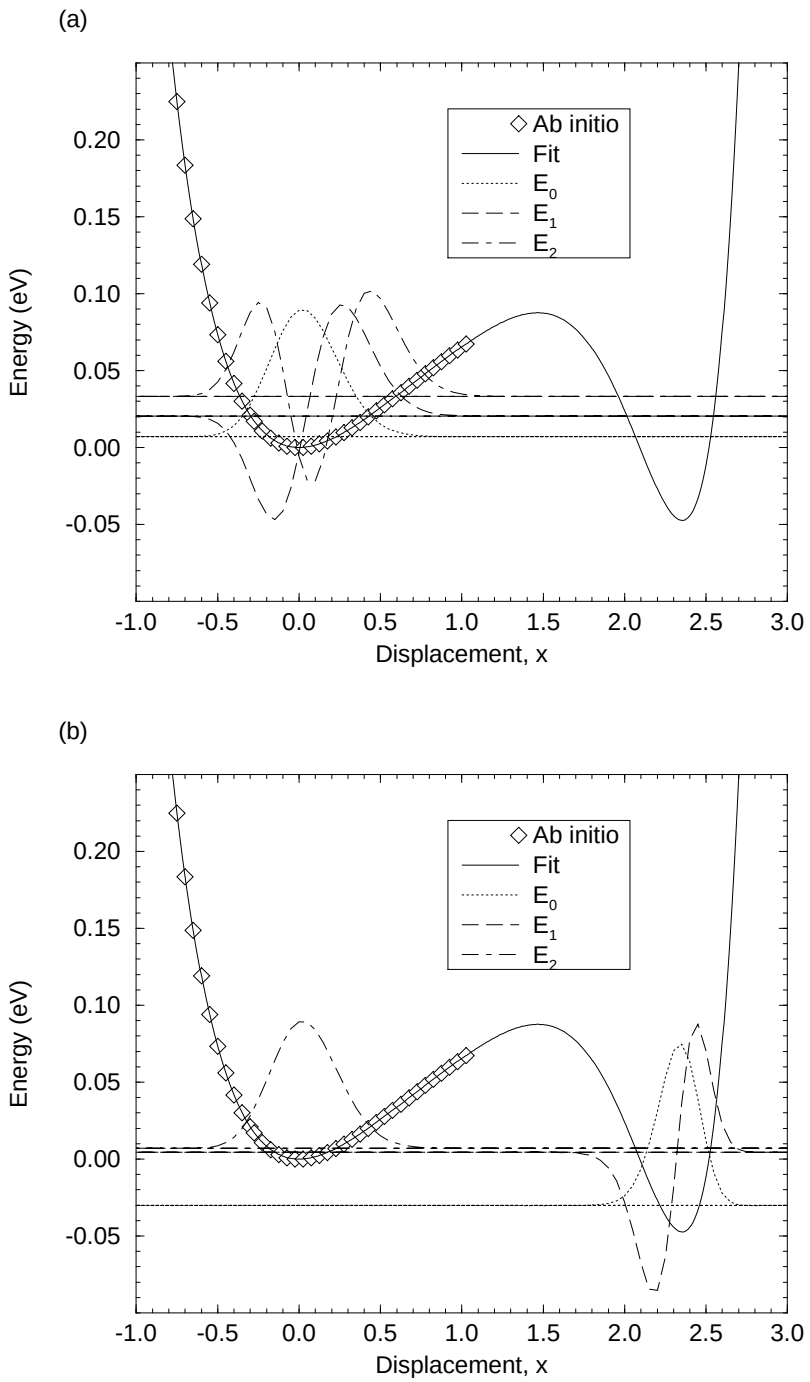

Figure 2.1: Plots showing the solutions to the secular equations 2.41 where (a) $N_o = 30$, and (b) $N_o = 90$. The displacement, x, is in a.u., and the wavefunctions have been shifted vertically so that each is zeroed about its energy level.

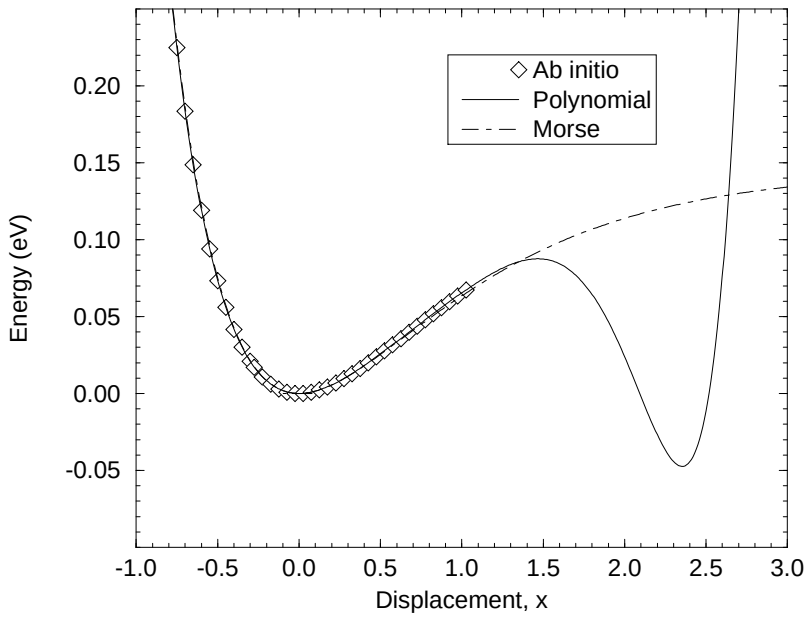

Figure 2.2: A plot of the polynomial potential as plotted in Fig. 2.1 also showing the Morse potential fit.

Using the above method for calculating the anharmonic vibrations, one can examine how the calculated frequencies vary with changing values of χ or bond-length. The effect of χ is very small: neglecting χ in the case of the C_{As}-H complex in GaAs leads to a 30 cm^{-1} ($\sim$1%) shift in frequency. The equilibrium bond length cannot be altered in the calculations directly. This is simulated by the application of a linear shift to the potential that changes the location of the minimum. Changing the effective bond-length in this way reveals a marked sensitivity.

In fact, as highlighted in Sec. 2.15.1, bond-length is the critical quantity for the absolute magnitude of local vibrational modes (LVMs), but differences are somewhat less sensitive. This appears to remain true for anharmonicity, as described in detail for the C_{As}-H case (Sec. 6.2).

2.15.2.3 Electrical anharmonicity

The above analysis treats the *mechanical* anharmonicity, but there is also an anharmonicity in the *electrical* characteristics of the vibration, that is to say that the dipole moment is not linear in x. In general, under the dipole approximation, the integrated intensity of a local vibrational mode is proportional to

$$\left|\langle \Psi_i \left| p(x) \right| Psi_j \rangle\right|^2 ,$$

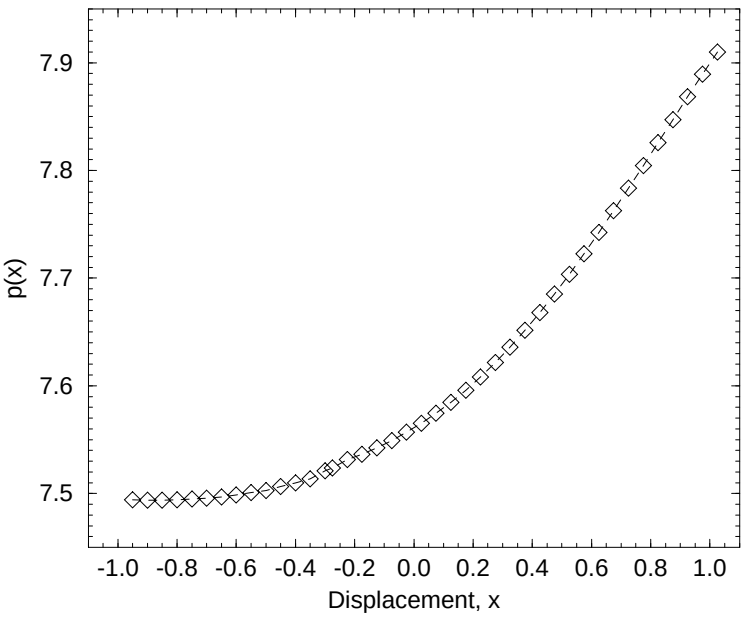

Figure 2.3: A plot of the *non-linear* dipole moment of the $C_{As} - H$ complex in GaAs, $p(x)$, x in a.u.

where $p(x)$ is the dipole operator. Thus, for the ratio of overtone and fundamental intensities, one is required to calculate the expression

$$\left| \frac{\langle \Psi_2 | p(x) | \Psi_0 \rangle}{\langle \Psi_1 | p(x) | \Psi_0 \rangle} \right|^2 \tag{2.42}$$

The function $p(x)$ for the $C_{As} - H$ complex in GaAs is plotted in Fig. 2.3. It can clearly be seen that this function is non-linear. This is discussed in more detail in Sec 6.2.

2.15.2.4 Theoretical evaluation of χ.

To calculate χ from quantities evaluated in AIMPRO, one can take the following approach. Again, the method is illustrated using the example of the C_{As}-H complex in GaAs. One may write the double derivatives of energy with respect to the H and C atoms as $E_{X,Y}$ where X and Y may be H or C. Then, assuming that the H-stretch mode is decoupled from all other vibrational modes, the only derivatives of interest are along the stretch direction. The quasi-harmonic frequencies then take the value:

$$\nu^2 = \frac{E_{H,H}}{M_H} - \frac{E_{C,H}^2}{M_H(E_{C,C} - M_C\nu^2)}. \tag{2.43}$$

Substituting Eq. 2.38 with $k = E_{\mathrm{H,H}}$, one can express χ as follows:

$$\chi = \left(\frac{E_{\mathrm{H,H}}}{E_{\mathrm{C,H}}}\right)^2 \left\{1 - \frac{E_{\mathrm{C,C}}}{E_{\mathrm{H,H}}}\frac{M_{\mathrm{H}}}{M_{\mathrm{C}}} + \frac{M_{\mathrm{H}}}{\chi M_{\mathrm{C}}}\right\}. \tag{2.44}$$

Note, χ is only weakly dependent the hydrogen mass if the 2$^{\mathrm{nd}}$ and 3$^{\mathrm{rd}}$ terms in braces in Eq. 2.44 are small. This is true when

$$\frac{E_{\mathrm{C,C}}}{E_{\mathrm{H,H}}} \ll \frac{M_{\mathrm{C}}}{M_{\mathrm{H}}}.$$

If this were not the case, and if $E_{\mathrm{C,C}}$ is large (such as if the C-back bonding is strong) then χ can reasonably be less than unity. If the C atom was decoupled from the rest of the lattice, then translational symmetry would require:

$$E_{\mathrm{H,H}} = E_{\mathrm{C,C}} = -E_{\mathrm{C,H}}.$$

Then Eq. 2.44 gives χ=1 and

$$\nu^2 = E_{\mathrm{H,H}}\left(\frac{1}{M_{\mathrm{H}}} + \frac{1}{M_{\mathrm{C}}}\right),$$

as expected.

2.15.3 Effective charges

The integrated intensity, I of a vibrational mode is related to the induced dipole moment through the expression [57]:

$$\begin{aligned} I &= \frac{2\pi^2\rho}{ncm}\eta^2, \\ \eta^2 &= \sum_k m\left(\frac{\partial M_x}{\partial Q_i^k}\right)^2, \end{aligned} \tag{2.45}$$

where ρ is the concentration of the impurity, n is the refractive index, c is the speed of light, m is the impurity mass, η is the effective charge of the LVM, M_x is the induced dipole in the direction of the applied electric field (x), Q_i is the normal coordinate of the i^{th} normal mode, and the sum is over any degeneracy in the normal modes.

The induced dipole $\mathbf{M}$ can be evaluated in the cluster formalism using the expression

$$\mathbf{M} = \sum_a Z_a \mathbf{R}_a - \int \mathbf{r} n(\mathbf{r}) d\mathbf{r},$$

where the atoms are displaced according to the normal co-ordinate, that is to say by

$$\frac{Q_i u_{la}^i}{\sqrt{m}}.$$

If the defects are randomly oriented, then it is necessary to average over the different orientations, so that, for example, the effective charge on a non-degenerate mode at a C_{3v} centre is given by [58]:

$$\eta^2 = \frac{m}{3} \sum_l \left(\frac{\partial M_l}{\partial Q} \right)^2 .$$

Note however, defects are not always randomly oriented. For example the $(C_{As})_2-H$ centre in GaAs is preferentially aligned along one $\langle 110 \rangle$ direction (see Chapter 6).

Using this method, the effective charge for all the modes of a given centre can be calculated. Suppose that only one mode is observed experimentally. Then, if one of the modes possesses a value of η greater than the others, this is a strong indication that this is the one that is experimentally observed.

2.16 Multiplets

The derivation of DFT is strictly applicable only to ground state systems, for which the theory predicts properties with quantitative accuracy. However, problems arise when several degenerate orbitals are only partially filled, such as in the case of high symmetry defects. An example in diamond of such as a (C_{3v}) defect is the vacancy bordered by a single nitrogen atom (see Chapter 4). This type of problem involves *multiplet structures* and therefore should strictly be beyond the theory. However, von Barth [59] developed a method for obtaining approximate multiplet energies using DFT.

Under this approach the density functional energy is related to a specific determinental wavefunction, the contents of which are in turn dictated by the choice of occupancy of the KS levels. The energies of different multiplets can therefore be generated by a judicious choice of these occupancies. Each determinant can be written as a linear combination of multiplets, $|D\rangle = \sum_a c_a |M_a\rangle$. Operating on each determinant with the Hamiltonian and finding the expectation gives:

$$\langle D|\hat{H}|D\rangle = E = \sum_a |c_a|^2 \langle M_a|\hat{H}|M_a\rangle.$$

Given sufficient independent determinants, one can then deduce values for the multiplet energies, such as in the neutral vacancy-nitrogen complex in diamond. However, this is not always possible, as in the case of the neutral vacancy in diamond.

2.17 Electronic transitions

Experimentally, for a particular electronic transition the symmetry of the ground and excited states, the zero-phonon energy, and the radiative lifetime may be known.

Of all of these terms, all but the first is related to an excited state of the system. Fortunately, as described above, we can get around this problem in a number of favourable cases where multiplet structures can be found. Thus, but occupying the orbitals appropriately, we can estimate the energy of the excited state, and hence the energy of the optical transition between this state and the ground state. Alternatively, theory due to Slater [16] allows one to estimate the transition energy with a single calculation.

2.17.1 Transition states

The problem is to calculate the energy of a transition between electronic states with energy E_λ and E_μ. According to the Slater transition state method, the transition energy is given by the difference between the KS levels, $E_\mu - E_\lambda$ when *half* an electron is promoted from the lower to the higher orbital, i.e. both E_λ and E_μ are half filled. Note that this transition energy is not the same as the zero-phonon energy, and differs from it by the relaxation energy. This method has been used successfully in a number of cases in diamond [60], and gives energies very similar to the energy difference between the ground and excited multiplets.

2.17.2 Radiative lifetimes

The rate at which electrical dipole transitions occur between states λ and μ can be estimated using the following relationship [61]:

$$\frac{1}{\tau_{\lambda\mu}} = \frac{4n\omega^3}{3c^3\hbar}\frac{e^2}{4\pi\varepsilon_o}|\mathbf{r}_{\lambda\mu}|^2 \tag{2.46}$$

$$\mathbf{r}_{\lambda\mu} = \sum_s \langle\psi_\lambda(\mathbf{r},s)|\mathbf{r}|\psi_\mu(\mathbf{r},s)\rangle,. \tag{2.47}$$

where n the refractive index, e the electron charge, c the speed of light and ω the transition frequency.

Within AIMPRO this integral is calculated for the pseudo-wavefunctions of the KS-levels, which is not strictly correct since the wavefunctions are zero near the atomic nuclei. Also, due to the cubic dependence of the transition rate on the frequency, the calculations are very sensitive to errors in ω. Despite these short comings, these calculations have given correct order of magnitude estimates in the case of vacancy-impurity defects in diamond [60].

2.18 Clusters

It is important to select an appropriate basis set and cluster to treat a particular defect.

In general, the wavefunction basis for each atom is made up of a number of atom centred s- and p-Gaussian orbitals. For transition elements there are further d-Gaussian orbitals, and for the lanthanides f-Gaussian orbitals. GaAs, Si and Ge also require d-orbital character in the basis set, and this can be achieved either by explicitly having atom centred d-Gaussian orbitals or, more simply, by adding *bond centred* Gaussians.

The wavefunction basis functions are as introduced in Sec. 2.12,

$$(x - R_{ix})^{n_1}(y - R_{iy})^{n_2}(z - R_{iz})^{n_3} e^{-a_i(\mathbf{r}-\mathbf{R}_i)^2}, n_i \in \mathcal{N}.$$

$n_i = 0, i = 1, 2, 3$ gives one the s-Gaussians, $n_1 = 1, n_i = 0, i = 2, 3$ generates the p-Gaussian functions, and the d- and f-Gaussians can be generated if $\sum_i n_i = 2$ and $\sum_i n_i = 3$ respectively. The complete wavefunction basis is then made up of a linear superposition of the atom- and bond-centred orbitals.

The exponents, a_i, for a particular atom are found by minimising the total energy of the pseudo-atom. This procedure also generates a set of coefficients, c_i^λ from Eq. 2.22. Then these coefficients can be used in the fixed linear combination with different exponents to form a 'minimal basis'. If the coefficients multiplying the orbitals are treated as variational parameters, the basis is termed 'big'. In a large cluster one usually has the central atoms of the defect and the nearest neighbours in big basis and the remaining, more remote atoms in minimal basis.

As described above, the charge density is also expanded in terms of basis functions (Eq. 2.25 and pure Gaussians), both at atom- and bond-centres. In this case the optimal basis is established by maximising the estimated Hartree energy $\tilde{E}_{\mathrm{H}}$, as described above in Sec. 2.12.1.

Typically, for a *sp* bonding material such as C or Si, the basis is made up of 3-4 sets of Gaussians in the wavefunction expansion and 4-5 charge density fitting functions, although for some problems a bigger basis is required, with, for instance, eight sets of wavefunction Gaussians, and eight charge density fitting functions. For transition metal elements, the number of charge density fitting functions increases dramatically since the atomic charge density increases near the origin as r^4, and is poorly represented by the functions in Eq. 2.25. In applying the basis selection to a cluster, it is important that the arrangement of big/minimal basis atoms and bond-centres reflects the symmetry of the defect.

One consequence of using a Gaussian basis set is that increasing the number of functions can lead to an 'over-complete' basis, which results in an instability in the Choleski decomposition of the overlap matrix. Therefore, in contrast to the calculations using a plane-wave basis, one cannot strictly converge the total energy. However, in practice it is usual to be examining *energy differences*, such as

in the relative stabilities of defect structures or the excitation energy of an electron from one multiplet to another, and these energies are usually well described using AIMPRO.

The clusters are terminated with hydrogen, with the X-H bonds oriented along the bulk bond direction. The cluster itself takes two main forms. The first is atom-centred surrounded by concentric shells of bulk atoms. This cluster therefore possesses a tetrahedral symmetry. For the III-V's, this means that there is an excess of either the group-III or group-V atom type, and consequentially the neutral cluster would have the incorrect number of bonding electrons. For all of the bonding orbitals to be filled, the neutral charge state is modelled by charging the cluster by the difference in the number of, group-III and group-V atoms. For example, a Ga centred cluster $Ga_{19}As_{16}H_{36}$ would be charged by $3e$.

The second type of cluster is bond centred, which avoids the charging problem encountered in the atom centred III-V cluster as these clusters contain the same number of group-III and group-V atoms (by symmetry). This type of cluster is referred to as stoichiometric, and possesses trigonal symmetry. One disadvantage of using stoichiometric clusters for III-V compound semiconductors is that they possess an inherent dipole. Consequentially the central bond is longer than the six equivalent back bonds. However, for most III-V materials all bonds are reproduced to within 3% of the experimental value.

It is well known that DFT *underestimates* the band gaps of semiconductors, and band gaps in clusters are *overestimated* due to the confining nature of the H-termination. In the case of diamond, these effects conspire to give approximately the correct values. Fig. 2.4 shows how the band gap, as estimated by the difference in the energies of the highest occupied and lowest unoccupied KS-eigenvalues. For Si, Ge, and GaAs, there is a clear decrease in the band-gap with increasing cluster size, as expected. All but diamond compare rather badly with the experimental values: 5.5, 1.17, 0.75, and 1.42 eV for diamond, Si, Ge, and GaAs respectively.

The overestimation of band gaps can be corrected by applying the so-called *scissors operator*:

$$\Delta(r, r') = V \sum_{\lambda'} \psi_{\lambda'}(r)\psi_{\lambda'}(r') \quad \text{for } \lambda' \text{ unoccupied.}$$

Δ can also be defined in terms of the occupied levels,

$$\Delta(\mathbf{r}, \mathbf{r}') = V \sum_{ij} (\delta_{i,j} - b_{ij})\phi_i(\mathbf{r} - \mathbf{R}_i)\phi_j(\mathbf{r}' - \mathbf{R}_j),$$

and it is this form of the scissors operator that is used in AIMPRO. This is simply added to the Hamiltonian and shifts the unoccupied states of the cluster containing

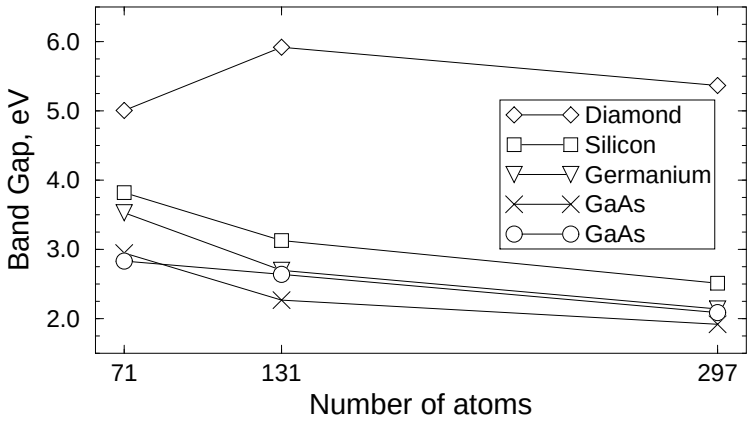

Figure 2.4: A graph showing the dependence on cluster size of the band-gap for diamond, Si, Ge, and GaAs. The group-IV materials clusters are made up as follows: $X_{35}H_{36}$, $X_{71}H_{60}$, and $X_{181}H_{116}$. There are two possible arrangements of each GaAs cluster - Ga centred and As centred. The three clusters are $X_{19}Y_{16}H_{36}$, $X_{31}Y_{40}H_{60}$, and $X_{89}Y_{92}H_{116}$. In the graph, $\times$'s indicate Ga centred clusters and $\bigcirc$'s As centred clusters. (*cf.* experimental values of the band-gap: 5.5, 1.17, 0.75, and 1.42 eV for diamond, Si, Ge, and GaAs respectively.)

no defect upwards by a quantity V. V is chosen such that the 'pure' cluster possesses the experimental band-gap. The scissors operator is not often employed but has been used in the case of gold and gold-hydrogen centres in Si.

2.19 Summary

In this chapter, I have tried to give a relatively detailed description of the road to the methods used in AIMPRO. I have also included a description of a couple of rival methods, namely Hartree-Fock and the parameterised methods of CNDO.

A number of sections are referred to regularly in the applications chapters, and are of a technical nature. These include the methods used for calculations of transition energies and rates, vibrational modes and other observables, as well the basis functions used to model each atom.

Chapter 3

Experimental techniques

> 'An expert is someone who knows some of the worst mistakes that can be made in his subject and how to avoid them.'
>
> - Werner Heisenberg

3.1 Introduction

A range of experimental methods have been successfully employed in the study of defects in semiconductors and a number of these techniques (such as the frequencies of localised vibrational mode spectroscopy and approximately the transition energy in photoluminescence) measure quantities that are directly calculable using AIMPRO. Some other aspects of experimental procedure, such as uniaxial stress, are less readily simulated directly, but still provide essential information such as defect symmetry to the theorist.

Data on a specific defect derived from a single experiment or even single type of experiment often proves insufficient for an unequivocal assignment to a particular atomic and electronic structure. It is necessary to combine and correlate data from different types of experiments, such as the optical and magnetic measurements, which has proved effective in the case of the vacancy-nitrogen complex in diamond.

In this chapter the main experimental techniques referenced in later chapters are outlined. Although it is not possible to examine the technicalities of each method, the scope and accuracy is discussed in general terms. The methods covered are: localised vibrational mode spectroscopy (especially in reference to hydrogen-related centres); electron paramagnetic resonance; photoluminescence and related techniques; and finally deep level transient spectroscopy.

3.2 Localised vibrational mode spectroscopy

Localised vibrational mode spectroscopy (LVMS) encompasses a range of techniques that measure the frequency of atomic vibrations, both bulk and those originating from defects. The two main methods are infra-red (IR) absorption and Raman scattering and since the selection rules for the two processes are different they can provide complementary information. As an introduction, I shall begin with a description of the vibrational properties of a crystal.

Diamond and zinc blende structures are comprised of two interlocking face-centred cubic lattices. These crystal structures possess three optical and three acoustic phonon bands, however, the physics can be understood by simplifying this problem to one-dimension. In 1-D the phonon-dispersion possesses only one acoustic and one optical branch [62]:

$$\omega^2(q) = \frac{k}{m^*} \pm k\sqrt{\frac{1}{(m^*)^2} - \frac{4\sin^2(qa)}{m_1 m_2}}. \tag{3.1}$$

Here k is the force constant, a is the inter atomic separation, m_1 & m_2 ($m_1 \geq m_2$) are the atomic masses and $1/m^* = 1/m_1 + 1/m_2$. The $\pm$ distinguishes between the acoustic (-) and optic (+) branches. Fig. 3.1 shows Eq. 3.1 in graphical form for a compound structure with the maximum frequency, $\omega_{\max} = \omega(q = 0) = \sqrt{(2k/m^*)}$. Also shown is the gap between the optical and acoustic branches at the zone boundary ($q = \pm\pi/2a$) which arises from the difference in basis atom mass and therefore is not present in the elemental semiconductors. The frequencies at the zone boundary are $\omega_{\mathrm{a}} = \sqrt{(2k/m_1)}$ and $\omega_{\mathrm{o}} = \sqrt{(2k/m_2)}$ for the acoustic and optic branches respectively.

3.2.1 Infra-red absorption

IR-absorption is particularly important for the characterisation of light impurities, especially hydrogen. Only the basic principles and points relevant to the present work are covered in this section. For a more complete description see Ref. [63].

For absorption in a pure crystal the crystal momentum and the energy must be conserved. Since the momentum associated with a photon is rather small in the case of atomic vibrations, this means that in one-phonon processes, absorption can only occur close to $q = 0$. Multi-phonon processes can occur provided that the sum of the momenta is close to zero. The absorption coefficient (i.e. the strength of absorption) is proportional to the dipole matrix element (Sec. 2.15.3), and since there is no induced dipole moment under the bulk normal modes of elemental semiconductors, there is no first order absorption. However, in compound semiconductors there is

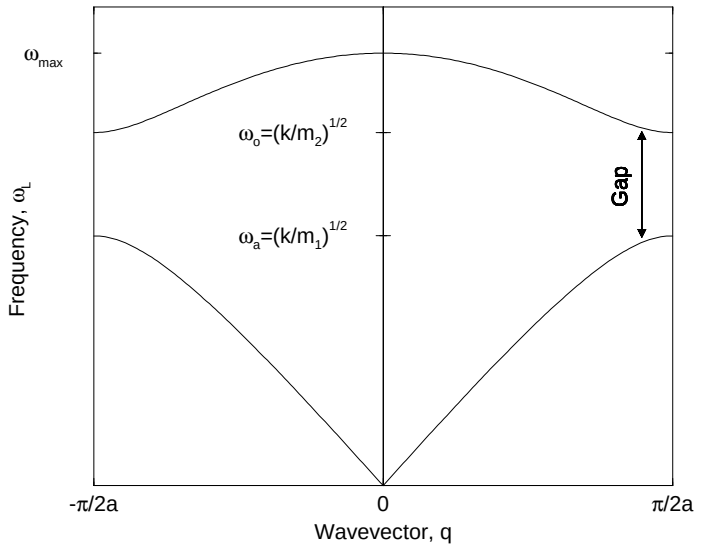

Figure 3.1: The one-dimension phonon-dispersion for a material with zinc blende like structure.

a large induced dipole, and thus strong absorption around $\omega_{\max}$. This absorption band is known as the 'Reststrahl band'.

In principle, absorption can occur in processes involving any number of phonons. However, as the number increases, the probability of such a process occurring decreases rapidly, and in practice only one- and two-phonon processes are important. The frequency range $\omega_{\max} \rightarrow 2\omega_{\max}$ is where many defect related features of interest lie[1], and therefore it is essential that the bulk absorption in this range is minimised. Fortunately, this can be achieved by cooling samples to T < 77 K.

Impurities introduce local changes in symmetry and therefore break the absorption selection rules. In general, a prerequisite for IR-absorption is the presence of an induced dipole moment. When the frequency of an impurity vibration is far from lattice mode frequencies, the vibration cannot propagate through the sample, and such a mode is termed a localised vibrational mode (LVM). If the impurity mass is large, i.e. $m_{\text{imp}} > m_1$, the impurity will possess normal modes that lie in the bulk absorption bands, which may be observed as resonances, such as those of nitrogen in diamond. Resonant mode absorption peaks tend to be broad, making them difficult to observe unless the concentration of the impurity is very high[2]. However, the presence of heavy impurities can sometimes be inferred from modes

[1]For example, GaAs possess $\omega_{\max} \approx 285$ cm^{-1} [64], and Si_{Ga}:GaAs has a local mode at 384 cm^{-1}.

[2]In the case of diamond, it is known that nitrogen may be present in concentrations as high as parts per thousand.

of light impurities (such as hydrogen) when they are attached to them.

As noted above, there is a gap in the density of phonon modes between the acoustic branch maximum and optical branch minimum. Impurity modes at between these frequencies may be detected. For example, As at an P site in GaP exhibits such a local mode [65], where the increase in mass (from 31 to 75 amu) lowers a mode into the gap. Other examples of gap-modes in GaP are B_{Ga} and Si_{Ga}. Note, both B and Si also possess higher frequency modes. The phonon density of states may possess other local minima that allow observation of local modes, such as the 156 cm^{-1} mode of B_{Ga} in GaP.

Despite the fortuitous location of some LVMs for frequencies $< \omega_{max}$, infrared-absorption spectroscopy is usually employed in the detection of higher frequency modes which invariably arise from impurities with a low mass[3]. These modes can be represented by Eqs. 2.38 and 2.39 (see Sec. 2.15.2). All terms in Eq. 2.45 are known except for the defect concentration (ρ) and the 'effective charge' of the vibration (η). To determine these, experimental calibrations must be made by estimating the concentration using an alternative method, such as secondary ion mass spectroscopy (SIMS)[4], but this procedure is complicated and destructive. Note, this calibration must be performed for each defect.

The symmetry of a centre can be established by applying uniaxial stress in (say) the [100], [011], and [111] directions and observing the absorption peaks. The way in which the peaks split with stress indicates the symmetry. This is called stress dichroism, and can be applied to most spectroscopic techniques. As an example, one can consider the case of the fully hydrogenated vacancy in silicon [13]. Uniaxial stress shows here that the (threefold degenerate) 2222 cm^{-1} band splits into two components under a $\langle 111 \rangle$ applied stress. In the $\langle 100 \rangle$, $\langle 110 \rangle$ and non-symmetric directions, the band is split into three. This is indicative of a cubic symmetry, e.g. T_d. In fact just knowing that the mode is threefold degenerate is sufficient to identify this symmetry.

The application of uniaxial stress can also be used to gain information about the energy required to reorient a defect between equivalent configurations. This process is known as stress induced alignment and is carried out as follows. As an illustration the case of the C_{As}-H centre in GaAs is used [67]. First, uniaxial stress is applied in one of the $\langle 111 \rangle$ (say [111]) directions at a (relatively[5]) high temperature. The stress makes the four alignments of the C_{As}-H centre *inequivalent*, and since the

[3]relative to m_2.

[4]SIMS involves the bombardment of the sample with primary ions and the detection of secondary ions sputtered from the sample surface. This procedure can be used to detect the presence of dopants, and their distribution with depth. For a full explanation see Ref. [66].

[5]This temperature must be greater than the temperature at which the defect can reorient.

centre can reorient, the lowest energy directions will be preferentially occupied. In the C_{As}-H case the $[\bar{1}\bar{1}1]$, $[1\bar{1}\bar{1}]$ and $[\bar{1}1\bar{1}]$ directions are equivalent. The sample is then rapidly cooled while the stress is maintained, and the alignment is frozen in. If an absorption experiment is then performed, in the different $\langle 111 \rangle$ directions the C_{As}-H absorption will be different. One can then anneal the sample at increasing temperatures. The absorption will follow the relation [68]

$$n(t) - n_o = [n(0) - n_o]e^{-t/\tau},$$

where n_o is the equilibrium value of the concentration of the defect oriented along one $\langle 111 \rangle$ direction, which at a time t is $n(t)$. The reorientation time constant, τ is given by the expression

$$\frac{1}{\tau} = \nu_o e^{-U/k_B T},$$

with ν_o being an attempt frequency and U the barrier to reorientation. For C_{As}-H in GaAs, $U = 0.63$ eV.

To establish the chemical constituents of a defect one can examine the fine structure in the absorption bands due to different isotopes. For example, Si_{Ga} : GaAs gives rise to bands at 384, 379, and 373 cm^{-1} with intensities that correlate to the abundances of ^{28}Si, ^{29}Si, and ^{30}Si. For the complex of H with C_{As} in GaAs, there are modes at 2635 and 2628 cm^{-1} for ^{12}C and ^{13}C respectively. Thus, hydrogen is can be used as a probe to identify impurities to which it binds. This is especially useful for the heavy impurities that cannot be directly observed by IR-absorption, such as the H-passivation of Zn acceptors in GaAs [69].

Isotopic data can also provide information about symmetry. For an impurity at an As site, isotopic shifts will be seen due to ^{69}Ga and ^{71}Ga. The number of equivalent Ga atoms can be deduced from the relative intensities of the mixed isotope lines, and hence some information regarding the local symmetry. For a sufficiently small change in mass, the isotopic shift is given approximately (by assuming Eq. 2.38) as

$$2\frac{\delta\nu}{\nu} = \frac{\delta m^*}{m^*}.$$

Whether or not the charge state induces a change in the LVM is dependent on the position of the defect state in the gap. If the level is shallow, then the associated wavefunction is dispersed over a large region of space. Then, occupying or not occupying this state will have little effect on the local geometry of the defect, and hence the LVMs. However, if the gap-level is deep, this correspond to the wavefunction being more localised, and the occupancy is more likely to affect the structure.

The breadth of an absorption peak is dependent on a number of factors: the lifetime of the excited vibronic state, the strains inherent in the sample, and the

isotopic shifts. The lifetime can be increased by lowering the temperature, and the strains can be reduced by improving the sample quality. Typically, the full width at half peak is 1 cm^{-1} or less at 77K, and Fourier transform IR-spectroscopic techniques lead to a precision in the frequency of as good as 0.01 cm^{-1}.

The concentration required for detectability is dependent on the quality of the sample, the sample dimensions and the induced dipole of the LVM. However, typically a concentration of at least $\rho \sim 10^{15}$ cm^{-3} is required for a 1 mm thick sample. In favourable conditions this minimum may be reduced: for sharp peaks, concentrations as low as 10^{13} cm^{-3} can be detected.

Due to the IR-absorption selection rules, some LVMs are not IR-active (i.e. the induced dipole is zero by symmetry). However, the scattering selection rules are different from those for absorption, and one can combine IR-absorption and Raman spectra to provide a more complete picture of a defect centre. For example the 739 cm^{-1} mode of the C_{As}-H complex in GaAs is not seen in IR-absorption (despite being IR-active by symmetry) but *is* seen in Raman [70] (see Chapter 6).

3.2.2 Raman scattering

If one illuminates a crystal with monochromatic light (frequency ω_o), the resulting scattered radiation spectrum includes a strong line at ω_o, and weaker lines at $\omega_o \pm \omega_j(q)$, where $\omega_j(q)$ are the optical phonon frequencies. The central peak is due to *elastically* or Rayleigh scattered photons, whereas those at $\omega_o - \omega_j(q)$ and $\omega_o + \omega_j(q)$ are *inelastic* or Raman scattered and termed Stokes and anti-Stokes lines. This can be viewed more quantatively as follows.

One can write down the (time dependent) induced dipole as

$$M(t) = \sum e_i r_i(t) \tag{3.2}$$

If the incident radiation possess an oscillatory electric field given by $E = E_o \cos \omega_o t$, then the induced dipole M can be expressed as a series in E:

$$M = \alpha E + \frac{1}{2}\beta E^2 + \text{ higher terms} \tag{3.3}$$

α is the electronic polarisability of the system, and β is a third rank tensor termed the *hyper-polarisability.* β is responsible for the so-called hyper-Raman effect which is beyond the scope of this chapter.

α is dependent on the charge distribution in the system and thus, in general, will vary with atomic vibrations. One can expand α as a Taylor series:

$$\alpha = \alpha_o + \left(\frac{\partial \alpha}{\partial Q}\right) Q + \frac{1}{2}\left(\frac{\partial^2 \alpha}{\partial Q^2}\right) Q^2 + ... \tag{3.4}$$

where Q is the normal co-ordinate of the vibration. If one writes $Q = Q_o \cos\omega_s t$, where ω_s is the characteristic frequency of the mode, one can re-write the induced dipole to first order in polarisability as:

$$\begin{aligned} M(t) &= a\cos\omega_o t + b\left[\cos(\omega_o - \omega_s)t + \cos(\omega_o + \omega_s)t\right] \\ a &= \alpha_o E_o, \quad b = \frac{1}{2}\left(\frac{\partial\alpha}{\partial Q}\right) Q_o E_o. \end{aligned} \tag{3.5}$$

Here, the first term is Rayleigh peak with frequency ω_o, and the remaining terms are the Stokes and anti-Stokes shifted peaks.

This classically based theory then can be used to predict the relative intensities of the Stokes and anti-Stokes peaks, but does so incorrectly. The intensity is proportional to

$$\left|\frac{d^2M}{dt^2}\right|^2,$$

which results in a ratio intensities of

$$\frac{I_{\text{Stokes}}}{I_{\text{Anti-Stokes}}} = \frac{(\omega_o - \omega_s)^4}{(\omega_o + \omega_s)^4}.$$

Clearly, this quotient is less than unity indicating that the anti-Stokes peak is more intense, whereas experimentally the Stokes peak is the most intense.

In order to correct this error, one needs to perform a quantum mechanical derivation of the Raman effect. This results in an intensity ratio of

$$\frac{I_{\text{Stokes}}}{I_{\text{Anti-Stokes}}} = \frac{(\omega_o - \omega_s)^4}{(\omega_o + \omega_s)^4} e^{\hbar\omega_s/k_B T},$$

which correctly gives a ratio > 1.

Whether or not a vibrational mode is Raman active is dependent on the polarisability tensor, $\alpha_{\rho\sigma}$. The induced dipole to first order in E is written:

$$\begin{pmatrix} M_x \\ M_y \\ M_z \end{pmatrix} = \begin{pmatrix} \alpha_{xx} & \alpha_{xy} & \alpha_{xz} \\ \alpha_{yx} & \alpha_{yy} & \alpha_{yz} \\ \alpha_{zx} & \alpha_{zy} & \alpha_{zz} \end{pmatrix} \begin{pmatrix} E_x \\ E_y \\ E_z \end{pmatrix} \tag{3.6}$$

Since $\alpha_{\rho\sigma}$ is symmetric, one can perform a transformation $(x, y, z) \rightarrow (x', y', z')$, that will diagonalise this set of equations:

$$\begin{pmatrix} M'_{x'} \\ M'_{y'} \\ M'_{z'} \end{pmatrix} = \begin{pmatrix} \alpha'_{x'x'} & 0 & 0 \\ 0 & \alpha'_{y'y'} & 0 \\ 0 & 0 & \alpha'_{z'z'} \end{pmatrix} \begin{pmatrix} E'_{x'} \\ E'_{y'} \\ E'_{z'} \end{pmatrix}. \tag{3.7}$$

(x', y', z') are termed the principle axes of the equilibrium structure, and in general, one can always choose a set of co-ordinates that give a diagonal polarisability tensor.

For convenience the primes are dropped, and equilibrium values denoted by the superscript ^{o}:

$$\begin{pmatrix} \alpha^o_{xx} & 0 & 0 \\ 0 & \alpha^o_{yy} & 0 \\ 0 & 0 & \alpha^o_{zz} \end{pmatrix}$$

When the system is perturbed under the motion of a normal mode, there is a change in the polarisability. One can write down the polarisability for the perturbed system in terms of a Taylor expansion:

$$\alpha_{\rho\sigma} = \alpha^o_{\rho\sigma} + \sum_s \alpha_{\rho\sigma,s} Q_s + \frac{1}{2} \sum_{s1,s2} \alpha_{\rho\sigma,s1,s2} Q_{s1} Q_{s2} + ... \tag{3.8}$$

where the notation

$$\alpha_{\rho\sigma,s} = \frac{\partial \alpha_{\rho\sigma}}{\partial s}.$$

To first order, the change in polarisability is $\alpha_{\rho\sigma,s} Q_s$, which is itself a tensor quantity. This leads to a generalised expression of the form of Eq. 3.5

$$\begin{aligned} M(t) &= a_\rho \cos\omega_o t + \sum_s b_{s,\rho} \left[\cos(\omega_o - \omega_s)t + \cos(\omega_o + \omega_s)t\right] \\ a_\rho &= \sum_\sigma \alpha^o_{\rho\sigma} E_{o\sigma}, \\ b_{s\rho} &= \frac{1}{2} Q_o \sum_\sigma \left(\frac{\partial \alpha_{\rho\sigma}}{\partial Q_s}\right) E_{o\sigma} \end{aligned} \tag{3.9}$$

As before, the first term is Rayleigh scattering, and the remaining two terms Stokes and anti-Stokes. The latter are dependent on the terms $\alpha_{\rho\sigma,s}$. Therefore, in order for Raman scattering to occur it is necessary that $b_{s\rho} \neq 0$. In other words, the change in polarisability with the normal mode must, in some direction, be non-zero.

Despite the difficulty in performing Raman scattering experiments to characterise defects in solids, the fact that the selection rules mean that modes that are IR-inactive may be seen in Raman makes the technique very useful. Note, it is not true that all IR-active modes are Raman-inactive or visa versa.

3.2.3 Summary

In summary, LVMS can be used to identify the vibrational frequencies of bulk modes and a range of defects, with particular emphasis on the lighter elements such as hydrogen. Uniaxial stress and isotopic data can be used to determine a detailed picture of the defect responsible for a particular LVM. Typically, however, a large concentration of the defect is required. Modes that do not possess an induced dipole moment are not visible under IR, but may be Raman active and visa versa.

3.3 Electron paramagnetic resonance

Where there is an excess of one electronic spin at a defect site (i.e. the effective spin S is non-zero) the centre possesses a net magnetic dipole moment and, provided that they do not interact, such centres are termed *paramagnetic*. An applied magnetic field, B_o, will align these unpaired spins which will possess discrete energies E_i. If a sample is subsequently exposed to electromagnetic radiation with frequency ν, such that $h\nu$ is equal to the separation between E_0 and E_1, absorption will occur. This phenomenon is termed electron paramagnetic resonance (EPR), also known as electron spin resonance (ESR). The discussion presented in this section is not intended to be exhaustive, and further details may be found in Refs. [71] and [72].

EPR can be used to find a range of qualitative and quantitative properties of defects. These include symmetry, nuclear spin of the defect atom, nuclear spin of neighbouring atoms and the localisation of the wavefunction associated with the unpaired electron.

3.3.1 Dipolar magnetic moment

One needs to begin by considering an electron in a magnetic field: an electron in a magnetic field will move in a circular path. This is termed the cyclotron orbit. An electron with an orbital angular frequency ω gives rise to a current

$$I = \frac{-e\omega}{2\pi} = -e\nu,$$

which in turn gives rise to a magnetic dipole moment, μ_o. The electron angular momentum, $\mathbf{l}$, in units of $\hbar$, is given by $m_e\omega r^2$, where r is the radius of the orbit and m_e is the electron rest mass, and hence the dipole magnetic moment is given by

$$\mu_o = -g_o\mu_B\mathbf{l},$$

where the constant $g_o = 1$ and

$$\mu_B = \frac{e\hbar}{2m_e}$$

is the Bohr magneton.

The dipole magnetic moment is aligned in the direction normal to the plane of the orbit. Next, one must include the contribution due to the intrinsic electron spin angular momentum, $\mathbf{s}$. This is given by

$$\mu_s = -g_s\mu_B\mathbf{s},$$

where g_s is the electron spin g-factor[6] Finally, one can write down a total magnetic moment, $\mu = \mu_o + \mu_s$.

[6] g_s is 2.0023 for the free electron.

Let us first consider the simplest case: the unpaired electron is in an orbitally non-degenerate state. The electron spin is limited to $\pm 1/2$ and the interaction energy of the external field with the unpaired electron is given by $-\mu_s.\mathbf{B} = g_s\mu_B\mathbf{s}.\mathbf{B}$ which is the electronic Zeeman energy. If we choose the magnetic field to be aligned along z, this simplifies to

$$E_{\mathrm{el-Zeeman}} = g_s\mu_B B_o m_s, \quad m_s = \pm\frac{1}{2}, \tag{3.10}$$

since the eigenvalues of s_z are $\pm\frac{1}{2}$. Then, the condition for resonance is that the incident radiation has the same energy as the difference in the Zeeman energies, i.e. $h\nu = \Delta E_{\mathrm{el-Zeeman}} = g_s\mu_B B_o$. For an applied magnetic field of around a third of one Tesla, this gives frequencies in the microwave band.

3.3.2 Absorption and derivative outputs

In practice the incident frequency is constant and the magnetic field is varied, giving a graph of absorption against field. However, the absorption is often extremely weak and superimposed on a large, slowly changing background. A modulated technique is needed to enhance the signal [7].

This uses a second, alternating magnetic field applied in the direction of the static B_o at 100 kHz with an amplitude somewhat less than the absorption line-width. The (weak) output signal is usually further enhanced as follows: the detector output is put into a lock-in amplifier which multiplies the signal by a weighting with the same frequency as the oscillating field. The amplifier also integrates the signal over many periods. When B_o is in resonance this produces a signal (provided that the modulated field is sufficiently small) with an amplitude proportional to the gradient of the absorption peak. This is illustrated in Fig. 3.2. The figure shows the derivative plot with an amplitude W, and a line-width defined as the separation between the two peaks ΔB_o. The integrated intensity is then given by $W \times \Delta B_o$ which is proportional to the concentration of spins. To convert this into an actual concentration, as with IR-absorption the signal must be calibrated using a sample where the spin concentration is known.

3.3.3 Nuclear Zeeman effect

Just as an electronic spin gives rise to a dipolar magnetic moment, so does a nuclear spin. The nuclear Zeeman energy can be written down in exactly the same way as

[7] There is an alternative method where the signals are measured in 'dispersion mode' and the output is like an absorption. This allows the use of higher microwave powers for the detection of weak signals, but lacks the resolution of the modulated scheme.

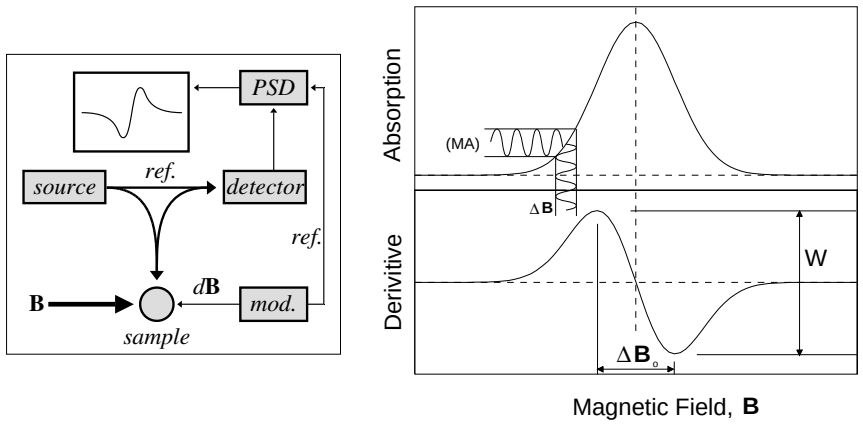

Figure 3.2: On the left is shown how the experiment is set up such that the modulation is used as a reference to enhance the modulated output using a phase sensitive detector (PSD). On the right is shown a schematic of the absorption and absorption derivative EPR spectra. The 'wave' indicated by '(MA)' shows the modulated absorption produced by the modulated magnetic field, $\Delta\mathbf{B}$.

the electronic Zeeman energy:

$$E_{\text{nuc}-\text{Zeeman}} = g_N \mu_N B_o m_I, \quad m_N = \pm\frac{1}{2}$$

where $\mu_N = e\hbar/2m_p$ is the nuclear magneton, and the (proton) nuclear g-factor is $g_N = 5.5854$. m_p is the rest mass of a proton. Note, g_N is dependent on the actual nucleus under study. The nuclear magneton is some three orders of magnitude smaller than the Bohr magneton, and hence the nuclear Zeeman splittings correspond to much higher frequency resonances (O(10 MHz)). The nuclear Zeeman effect gives rise to an extra set of peaks split off from the main peaks.

In the same way as a resonance in the microwave frequency range is sought in EPR, a radio frequency resonance can be sought for the nuclear Zeeman splittings. The simultaneous resonance in terms of both the electronic and nuclear spins is termed electron nuclear double resonance (ENDOR). The interpretation of ENDOR data is even more complicated than that of EPR.

3.3.4 The hyperfine interaction

The hyperfine interaction is due to the magnetic coupling between the nuclear and electronic spins:

$$H_{\text{hyp}} = g_s g_N \mu_B \mu_N \left[\frac{\mathbf{s}.\mathbf{I}}{r^3} - \frac{3(\mathbf{s}.\mathbf{r})(\mathbf{I}.\mathbf{r})}{r^5}\right] \tag{3.11}$$

Once again, aligning the applied field along z only the z-components are retained, and the hyperfine interaction can be written:

$$H_{\text{hyp}} = \frac{1}{r^3} g_s g_N \mu_B \mu_N s_z I_z (1 - 3\cos^2\theta), \tag{3.12}$$

where θ is the angle between $\mathbf{r}$ and z.

Typically, the hyperfine energy is of the order of 100 times smaller than the electronic Zeeman energy, and thus can be considered as a perturbation. H_{hyp} in the above form is singular at $r = 0$, which must be corrected for the finite probability of finding the electron in the nuclear core. This correction is called the *Fermi contact term* and is incorporated in the central hyperfine term:

$$H_{\text{central-hyp}} = g_s g_N \mu_B \mu_N \frac{8\pi}{3} |\psi(0)|^2 \mathbf{s}.\mathbf{I}, \tag{3.13}$$

Here, $\psi(r)$ is the wavefunction associated with the unpaired electron. Reducing everything to the z-direction, one can write Eq. 3.13 as

$$H_{\text{central-hyp}} = A m_s m_I,$$

where A is the central hyperfine parameter. This term is typically comparable to the hyperfine energy. In general, the nuclear spin I may take any half-integer value, and hence give rise to $(2I + 1)$ values of resonant field.

3.3.5 Spin orbit coupling

The spin-orbit interaction leads to an anisotropy in the electronic g-factor, and this can be used to examine the symmetry of the defect. The spin-orbit interaction is characterised by the Hamiltonian term $H_{\text{S-O}} = \eta \mathbf{l}.\mathbf{s}$, where deviations from isotropy are determined by the sign and magnitude of $\eta/(E_1 - E_0)$. Here, the energy subscripts 0 and 1 refer to the ground and excited electronic Zeeman split levels respectively. The direction of the applied field is varied, and the measured g-factor obeys the relation

$$g^2 = g_{\parallel}^2 \cos^2\theta + g_{\perp}^2 \sin^2\theta,$$

where θ here refers to the angle between the direction or the spin and the applied field.

3.3.6 High spin centres

In some cases the electronic spin of the centre is $S > \frac{1}{2}$, in which case there will be $(2S + 1)$ electronic Zeeman levels, $E_0, E_1, ..., E_{(2S)}$. For example, the $S = 1$, negatively charged vacancy-nitrogen complex in diamond would possess three Zeeman split energy levels.

3.3.7 Low symmetry defects

The expressions thus far have been applicable specifically to a system with T_d symmetry. In general one should include terms in the total energy for lower symmetries.

For systems with lower than axial symmetry system there are the extra terms:

$$D\left[S_x^2 - \frac{S(S+1)}{3}\right] + E\left(S_x^2 - S_y^2\right).$$

Then for axial symmetry $E = 0$, and for tetrahedral systems, $D = 0$, to return to the original expression. These additional energy terms give rise to an additional $2S$ lines in the absorption, which is referred to as *fine structure*.

To disentangle the peaks due to the fine and hyperfine terms, one can use the fact that the hyperfine interaction is independent of the incident radiation frequency whereas the fine structure is not. Then, by comparison of spectra of different microwave cavity dimensions, one can identify the hyperfine and fine structure.

There are a number of other effects that are not mentioned here in detail. These include the so called super-hyperfine interaction, which relates to nuclear spins in atoms adjacent to the defect and high order interactions such as the magnetic quadrupole effect.

EPR can detect, in general, lower concentrations of defect centres than infrared absorption, but the actual resolution is dependent on the line width of the absorption. Typically, concentrations from greater than 10^{12} cm^{-3} can be detected.

3.3.8 Optical detection of magnetic resonance

An allied method to EPR is optical detection of magnetic resonance (ODMR). Here the microwave transitions are induced in an optically excited state of the centre and detected through a change in the luminescence intensity or luminescence polarisability. An ODMR spectrum consists of variation in luminescence with magnetic field, and thus the detection is much more sensitive than EPR since a photon detector is much more sensitive than a microwave detector.

3.3.9 Summary

In summary, EPR and related techniques can provide a great deal of information about defects with unpaired electrons, such as the localisation of the wavefunction associated with the unpaired spin, and the symmetry of the defect. However, the deconvolution of the various terms in the spin Hamiltonian is not simple and a number of approximations are made, such as treating the unpaired electronic and nuclear spins as points when estimating their separations. This has been done in some cases by splitting the hyperfine interaction into isotropic (a) and anisotropic (b) terms. Then assuming a the hyperfine interaction is essentially a dipole-dipole interaction the separation is estimated from the expression: $b = g\mu_B g_N \mu_N / r^3$. For more details, see, for example, Ref. [73].

3.4 Photoluminescence

Photoluminescence (PL) is one of many optical techniques that have been widely employed in the characterisation of semiconductors. Other techniques closely related to PL are cathodoluminescence (CL) where the incident radiation takes the form of electrons rather than photons, photoluminescence excitation (PLE) and absorption, all of which shall be touched upon in this section.

During PL, samples are exposed to illumination with light of a frequency such that $h\nu > E_g$,[8] which creates electron-hole pairs. The electrons rapidly relax into lower energy states, particularly at defect sites. This may be via radiative or more likely non-radiative mechanisms. They ultimately recombine with a hole in the valence band or at another defect related state, emitting a photon with an energy equal to difference in energy between the ground and excited states. This kind of system is illustrated in Fig. 3.3(a).

Where the transition between the lowest excited state and the ground state has a long radiative lifetime or forbidden by symmetry, the transition may be from a higher excited state. This is the model proposed for the (trigonal) N3 optical feature in diamond [74], where the presence of an A state (Ref. [74] suggests an A_2-state) is inferred from the presence of a vibronic system labelled N2. N2 is correlated with N3 but possesses no zero-phonon transition.[9] This leads to a picture of the radiative decay from the second excited ^2E-state as illustrated in Fig. 3.3(b).

PL and absorption differ in that absorption will (in principle) reveal all excited states, provided that the optical transition is allowed by symmetry. Under absorption a continuum of optical frequencies is incident on the sample, and the *transmitted* spectrum is recorded. Then, the difference between the incident and transmitted spectra is the absorption. This is illustrated in Fig. 3.4(a). This technique has the advantage that it can be used directly to establish the concentrations of centres [75] (as in IR absorption and EPR). However, absorption experiments are difficult where samples are thin or where defect concentrations are small.

PLE avoids both of these problems. This experiment is essentially a PL measurement where the incident radiation is from a tunable laser, and the energy of the incident photons is (at least to begin with) below band-gap energy. The detector is tuned to a specific frequency (say the lowest energy optical transition) and the incident frequency increased incrementally. When the incident radiation is in resonance with the next excited state, the population of the state will increase. The second excited state will non-radiatively decay very rapidly into the excited state

[8] E_g = the band-gap energy.

[9] For a system that transforms under the C_{3v} symmetry point group, dipole selection rules prevent any transition between A_1 and A_2 states, and some transitions between A_1 and A_1 states.

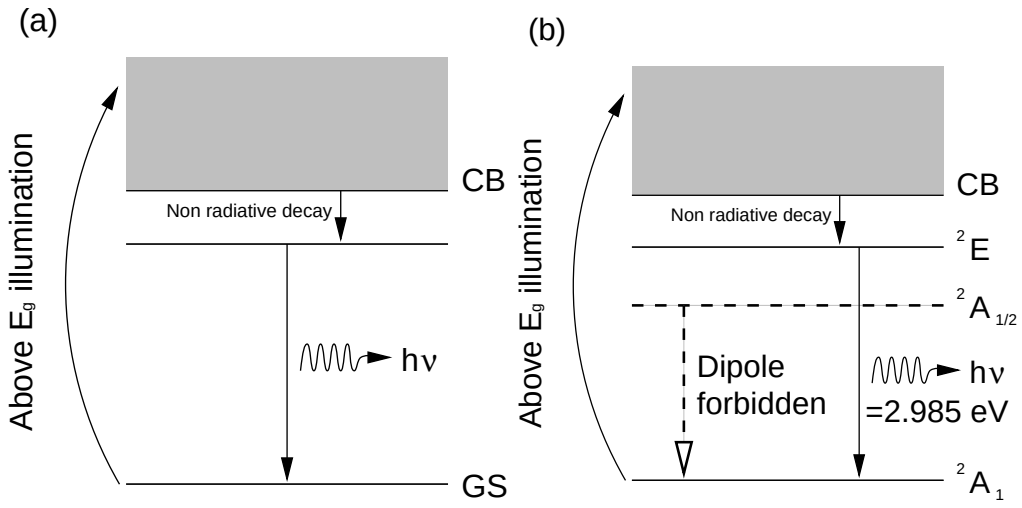

Figure 3.3: Schematic representations of PL in the cases where (a) the transition observed is from the first excited state to the ground state, and (b) where, since such a transition is forbidden, a transition from the second excited state to the ground state, as suggested for the N2/N3 optical systems in diamond [74].

of the transition being monitored. Since the population of the first excited state is now being increased, the luminescence intensity will also increase. A plot of incident frequency vs. luminescence intensity will therefore produce a number of peaks coincident with excited state energies. A schematic diagram of the PLE method is shown in Fig. 3.4(b).

CL involves the exposure of the sample to an electron beam. Luminescence then occurs via relaxation in the same way as for PL. However, this technique can lead to defect ionisation, and one finds that PL and CL exhibit differences based on defect charge states. For example, the vacancy-nitrogen complex in type Ib diamond[10] exists in neutral and negative charge states. The 2.156 eV zero-phonon line due to the neutral charge state is seen both in PL and CL, whereas the 1.945 eV line is seen in PL but not in CL [76, 77].

As stated above, PL cannot in general be used to directly estimate the concentration of the luminescent centre. This is due to the large number of factors that feature in the processes, such as temperature and capture cross-sections as well as non-radiative transitions. However, one should note that under certain, favourable circumstances, the concentration of donors and acceptors can be found directly from PL. When the defect concentrations are low, the luminescence is dominated by free-exciton and donor and acceptor luminescence [78]. Then, the acceptor and donor concentrations are proportional to the ratio of the area of the zero-phonon-line (ZPL) and the peak-height of the free-exciton recombination luminescence.

[10]Type Ib diamond contains nitrogen predominantly in the isolated substitutional form. The classification of diamonds is summarised in Chapter 4

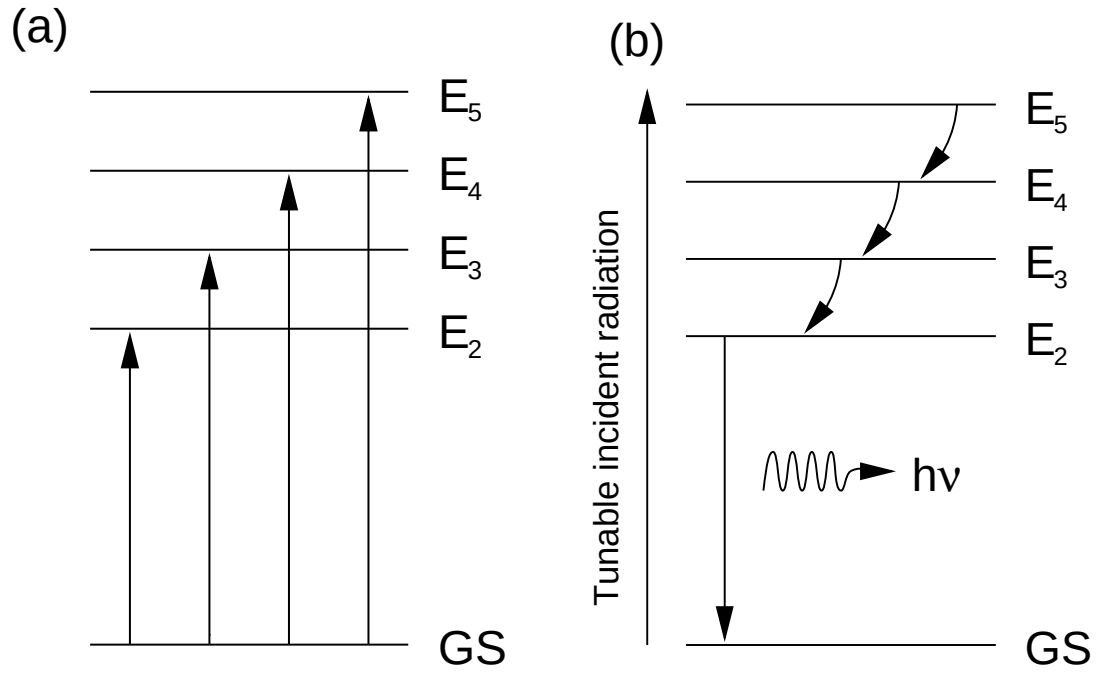

Figure 3.4: Schematic representations of (a) absorption and (b) PLE where transitions involving all excited states are seen.

The calibration constant has been determined in a number of cases, and, in the absence of any other major contaminants, this technique can be used to detect concentrations of as low as 10^{10} cm^{-3} [79, 80].

Along with the ZPL, these optical techniques reveal transitions that are mediated by one or more phonons, termed phonon side bands. The difference in energy between the ZPL and a one-phonon side-band in equivalent to the phonon energy, $\hbar\omega$. Hence, these methods can be employed to determine the local vibrational modes of the defect responsible for the ZPL.

Now, as with the interpretation of IR-absorption, a key to assigning PL features to atomic species are isotopic effects. The zero-point energy of an atom differs for different isotopes and the optical transition energy therefore is also different. However, care must be taken in interpreting results. The ZPL is related to difference in the ground-state and excited-state total energies: $\langle\Psi_{\rm GS}|H|\Psi_{\rm GS}\rangle - \langle\Psi_{\rm Ex}|H|\Psi_{\rm Ex}\rangle$. If these wavefunctions have no amplitude at one of the impurity atoms, then there will be no isotopic shift due to that atom. This behaviour is exhibited in the T-line in Si. Recent collaborative work between experiment and theory [12] has led to an assignment of this optical centre to a complex containing two C atoms in a split interstitial arrangement, with a H atom bound to one C. The ground and excited wavefunctions of the electron states involved in the optical transition have a very small amplitude on one of the C atoms. Consequentially the ZPL exhibits isotopic

fine structure consistent with the defect containing a single C atom. However, since the C atoms are bonded to each other, phonon-assisted transitions exhibit isotopic shifts consistent with a defect containing two C atoms.

As with other tools, uniaxial stress measurements can determine the symmetry of the centre, as well as the symmetries of the electronic states involved in the optical transition. This information is crucial to the establishment of a microscopic structure, and can immediately eliminate possible charge states of a centre. For example, as stated above, the trigonal vacancy-nitrogen centre in diamond occurs in two charge states. The 2.156 eV ZPL system is known to possess a ^2E ground state. In the one-electron picture of the complex, the band-gap contains an a_1- and an e-level derived from the vacancy like t_2-level. Thus, the e-level must contain either one or three electrons to give the correct ground state symmetry, i.e. the 2.156 eV ZPL must arise from the neutral or the double negative charge state of the N-V complex. This system is discussed in detail in Chapter 4. The manner in which the peak positions change with stress can also give information about the presence of other states in the gap, such as split off vibronic states due to Jahn-Teller coupling [81].

Observing how ZPLs change with temperature can determine the energy splittings of nearby gap-states, such as in the 1.682 eV 12-line system in diamond. The 12 lines are believed to arise from three sets of four lines, one set for each isotope of Si. Now, the four lines might arise from a transition from two types of systems.

1. A non-degenerate ground state to four nearby excited states.

2. Transitions between a double degenerate ground state to a doubly degenerate excited state which have both been slightly split.

However, the change in relative intensities with temperature of the four lines would be dramatically different for these two cases. Experiment shows that the ground state is made up of two, slightly split levels, the separation being only 0.02 meV. In Sec. 4.4 this centre is discussed in more detail. Time resolved optical measurements give a measure of radiative lifetimes for individual ZPLs which can be modelled theoretically (Sec. 2.17.2).

In summary, PL and related techniques can provide a wealth of information about a defect, including symmetry, vibrational modes, and, in some cases, defect concentrations. It can provide quantitative information on Jahn-Teller systems, and a full picture of the electronic structure favourable situations. However, as with all experimental techniques, the interpretation of the data requires care, and must always be viewed in the context of other experimental and theoretical information.

3.5 Deep level transient spectroscopy

Deep level transient spectroscopy (DLTS) is a powerful method developed in the 1970s [82] to probe deep (>0.1 eV) electron and hole traps in the band gap. For a review of the method, see Ref. [83].

In order to characterise a sample using DLTS, the sample must either be in the form of a p-n junction or Schottky barrier. The characteristics of deep electron and hole traps can then be determined by measuring changes in capacitance with time and temperature. The method is powerful, and can determine values for the trap energy[11], the capture cross section, and the defect concentration. For the purposes of this section I shall only examine the case of deep electron traps, but the principles can easily be applied to hole traps.

Consider the system which is shown schematically in Fig. 3.5(a). The region to the right of the junction is depleted of majority carriers due to the band bending, with the depletion depth given as x_1 in the reverse bias V_1. This configuration thus acts as a parallel plate capacitor with contact area A and has a capacitance

$$C_1 = \frac{\varepsilon_r \varepsilon_o A}{x_1}. \tag{3.14}$$

When the bias is increased to V_2, the capacitance decreases to a value C_2, which corresponds to the larger depletion region x_2 (Fig. 3.5(b)).

To perform the DLTS measurement, the reverse bias V_2 is applied, with a short pulse of the reduced bias V_1. When the bias returns to V_2, the decrease in capacitance is almost immediate, with the depletion region now being $x_3 > x_2$. However, the filled traps in the region $x_2 < x < x_3$ are not in thermal equilibrium, and over time lose their electrons to bring the depletion region, and hence the junction capacitance back to C_2. This decay process has an exponential form as shown in Fig. 3.6.

The decay can be measured either as a transient current or a transient change in capacitance. The latter is invariably adopted. The capacitance transient is written as:

$$\Delta C(t) = C_2 - C(t) \tag{3.15}$$

$$= \Delta C(0) e^{t/\tau} \tag{3.16}$$

where $\Delta C(0)$ is $|C_2 - C_3|$ and τ is the lifetime of the electron in the trap, which can be written as:

$$\frac{1}{\tau} = \sigma v N_C e^{-\frac{E_C - E_T}{k_B T}} = e_n. \tag{3.17}$$

[11] The trap energy is usually quoted with respect to a band edge: $E_C - E_T$ for electron traps, and $E_V + E_T$ for hole traps.

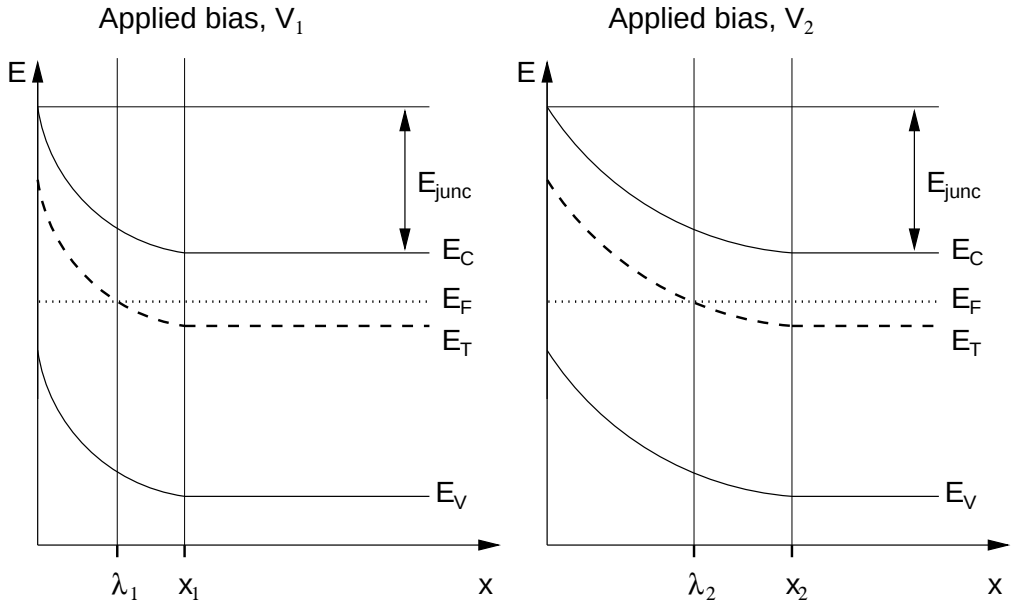

Figure 3.5: Schematics of the conduction (E_C) and valence (E_V) bands bending at the p-n or Schottky junction. Plots are shown for two reverse biases, V_1 and V_2. The junction is located at x=0, and the distances x_i and λ_i are described in the text.

σ is the capture cross-section of the electron trap, v is the average velocity of electrons in the conduction band, and N_C is the density of states in the conduction band. e_n is simply the decay rate of electrons from the trap.

One possible measurable quantity using DLTS is an estimate of the trap concentration. If the trap concentration, N_T is much smaller than the donor concentration, N_d, and if one assumes that N_T is only weakly dependent on x, an approximate value may be determined as follows. The capacitance of the junction for an applied bias V_1 is given as:

$$C_1 = A\left[\frac{\varepsilon_r \varepsilon_o e}{2(V_1 + V_{\text{junc}})}\right]^{\frac{1}{2}} \sqrt{N_d},$$

where V_{junc} is simply the potential difference across the junction for no applied potential, and is indicated in Fig. 3.5. Hence,

$$\frac{dC_1}{C_1} = \frac{1}{2}\frac{dN_d}{N_d}.$$

One can then associate dC_1 with $\Delta C(0)$ and dN_d with N_T to arrive at the expression for the trap concentration:

$$N_T = \frac{2\Delta C(0) N_d}{C_1}. \tag{3.18}$$

Eq. 3.17 shows that the decay rate is critically dependent on temperature, as one might expect. This means that as the temperature is increased, the capacitance

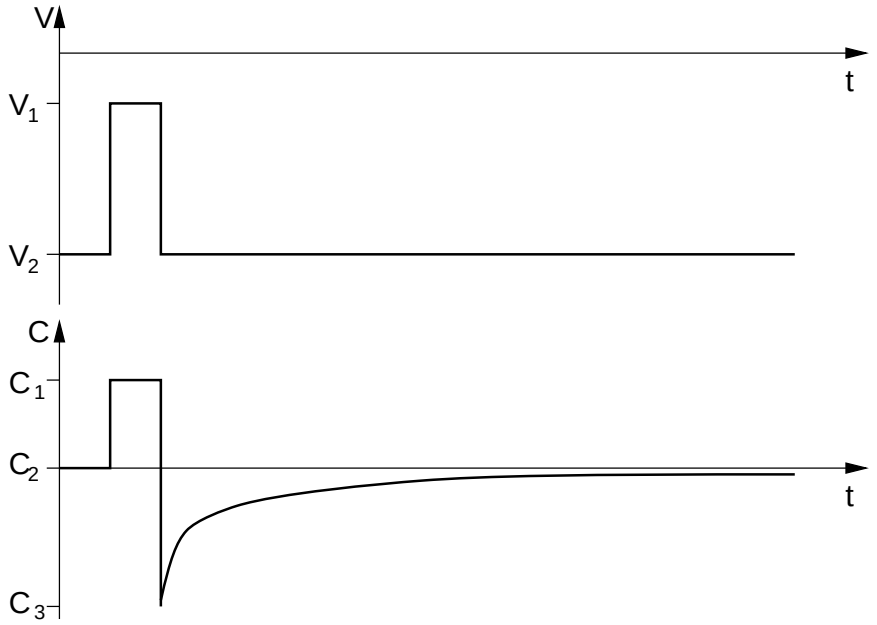

Figure 3.6: A plot of the reverse bias pulse and capacitance response.

returns to the equilibrium value more rapidly, as shown schematically in Fig. 3.7. Also marked on this Figure is the 'time window', defined by the times t_1 and t_2.

An individual DLTS spectrum is obtained for a given time window by varying temperature and plotting the change in capacitance (ΔC) over the time window. Such a plot shows the DLTS peaks characteristic of deep traps. A schematic DLTS spectrum is shown in Fig. 3.8. Also indicated on Fig. 3.8 are the energies of the traps, but in fact this picture is not strictly correct, since all terms in Eq. 3.17 are dependent on temperature.

To determine an *accurate* value of E_T, a series of measurements are performed with different time windows. v and N_C in Eq. 3.17 are proportional to $T^{1/2}$ and $T^{3/2}$ respectively which means that Eq. 3.17 can be written

$$\ln\left(\frac{e_n}{T^2}\right) = \chi - \left(\frac{E_C - E_T}{k_B}\right)\frac{1}{T},$$

where χ is a constant related to the natural logarithm of σ. Then, plotting $\ln(e_n/T^2)$ against T^{-1} gives a straight line with slope $-(E_C - E_T)/k_B$. Trap energies can be evaluated in this way to within a few %.

This plot can also be used to evaluate σ since the y-intercept is related to the capture cross section. In practice, this method is not used since the resulting value is not very accurate. An alternative method for estimating σ uses the fact that for a sufficiently short applied bias pulse only a proportion of the traps will be filled. As the pulse length is increased, the DLTS peak height increases due to more traps being filled. Ultimately, the peak height will saturate as all the traps in the

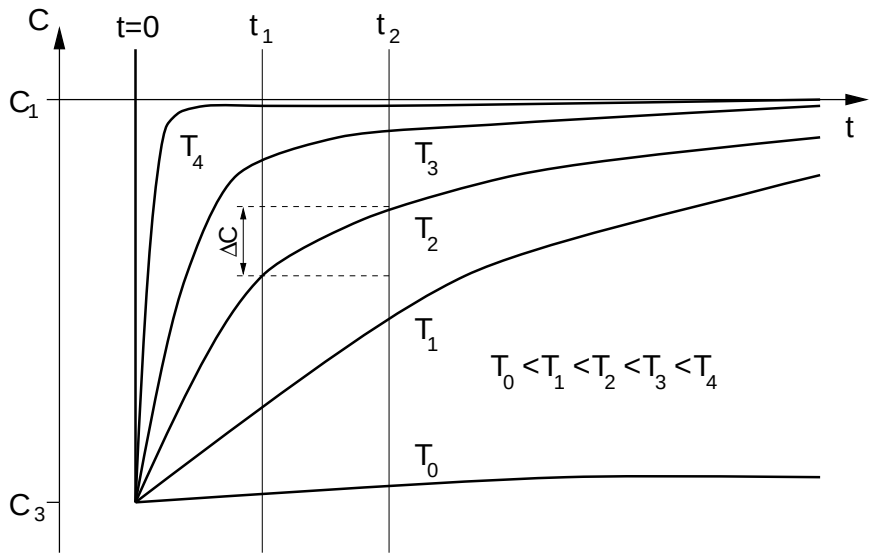

Figure 3.7: A graph showing how the capacitance transient changes with increasing temperature, T. $T_0 < T_1 < T_2 < T_3 < T_4$. Also marked is the *time-window* for which the DLTS spectrum is taken. Note, for temperatures T_0 and T_4 there is no change in capacitance over the range of the time-window.

depletion region are filled. The characteristic time for filling the traps, τ' is related to the capture cross-section by the relation:

$$\sigma = \frac{1}{\tau' v n},$$

where $n = N_d - N_T \approx N_d$ is the effective doping concentration. Thus, an Arrhenius plot of peak height against pulse length can be used to evaluate σ.

Finally, it should be noted that Eq. 3.18 is only an approximate expression for the trap concentration. The derivation of this expression uses the depletion length x_1 as determined from Eq. 3.14. However, the correct distance is that from the interface to where the trap energy crosses the Fermi-level. This is denoted by λ in Fig. 3.5. This error can be accounted for by including a correction factor to the right hand side of Eq. 3.18,

$$\frac{x_2^2}{\lambda_1^2 - \lambda_2^2}.$$

λ can be determined from:

$$\lambda = x - \left(\frac{2\varepsilon_r \varepsilon_o (E_F - E_T)}{e^2 (N_d - N_T)} \right)^{\frac{1}{2}},$$

which is itself dependent on the trap concentration, N_T. Thus, N_T must be evaluated from the corrected version of Eq. 3.18 *iteratively*.

In summary, the use of DLTS to characterise deep traps can provide the theorist with valuable information. The position of the trap level in the gap can be calculated

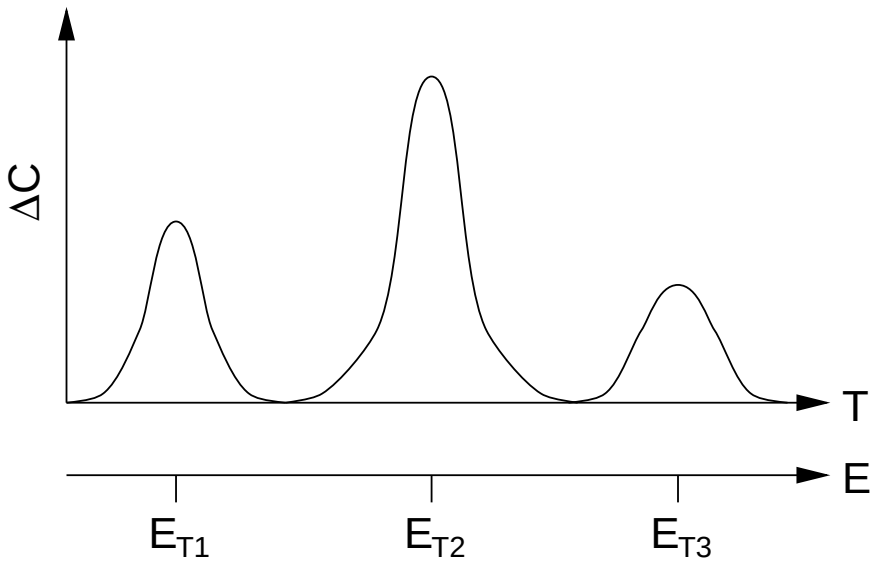

Figure 3.8: A plot showing a typical DLTS spectrum. There are three peaks which correspond approximately to the energies of three deep traps.

approximately using AIMPRO. DLTS has been used to investigate a large number of centres, specifically the deep traps in GaAs produced by radiation damage, and transition metals in Si.

Chapter 4

Vacancy-X complexes in diamond

'... His party, cried "Advance and take thy prize
The diamond;"' but he answer'd, "Diamond me
No diamonds! for God's love, a little air!
Prize me no prizes, for my prize is death!
Hence will I, and I charge you, follow me not."'

Alfred Tennyson from '*Idylls of the King. Lancelot and Elaine.*'

4.1 Introduction

Diamond has, for many centuries, fascinated mankind. The hardness, thermal conductivity as well as the rarity and aesthetic appeal of diamond gem-stones has led to scientific as well as commercial interest. Moreover, the availability of synthetic diamond has led to the a desire to develop techniques for discriminating between the more valuable gem stones and the man-made samples.

Diamonds can be grown using a number of techniques, the most important of which are the high temperature, high pressure (HTHP), and chemical vapour deposition (CVD) methods. During the development of diamond growth techniques a number of materials with properties similar to diamond have been produced. These include what is termed 'diamond-like carbon' and 'tetrahedral amorphous carbon'. Diamond-like carbon can be produced in large area films at relatively modest expense, and diamond coating has made it into the realm of high-street fashion: Rayban has recently put diamond coated sunglasses onto the market [84] costing about £30 more than the untreated variety. They are reputed to have a ten-fold increase in lifetime!

Viewed from an electronics point of view, these materials contain both sp^2 and sp^3 bonded carbon. This leads to an effective lowering of the conduction band bottom, and n-type semiconducting samples can be produced.

Ia	Nitrogen is present in the form of aggregates of several types.
IaA	The N-aggregates are predominantly in the form of A-centres – substitutional N pairs.
IaB	The N-aggregates are predominantly in the form of B-centres – a vacancy surrounded by four N atoms.
Ib	Nitrogen is present in the form of isolated substitutional (deep) donors, N_s.
IIa	Contains undetectable concentrations of N and B impurities – these diamonds are rather rare.
IIb	Contains no detectable nitrogen but has substitutional boron giving a variety of shades of characteristic blue colour depending on the concentration. Such diamonds are (p-type) semiconductors.

Table 4.1: A summary of the classification of diamonds.

Diamonds can be classified according to the content and form of nitrogen and/or boron in the sample, and a summary is presented in Table 4.1. This system was developed for *natural* diamond samples. Each form of nitrogen complex is characterised by an absorption band from which the concentration of each defect type can be estimated. Naturally, this categorisation is rather broad, and in practice there are different forms of N-related defects in each sample – diamonds with A- and B-centres are termed type IaA/B.

Besides the mechanical properties of diamond, technologically the most important characteristic of diamond is its transparency to visible and infrared light. This has led to the use of diamond for lenses in IR-detectors and in optical windows for scientific equipment.

Optical properties are most often related to defects within diamond. The small carbon mass generates substantial electron-phonon coupling, which together with the high degeneracy associated with symmetric defects, often leads to important and subtle Jahn-Teller (J-T) effects. A brief description of the J-T effect is given in Appendix B. The high purity and large band gap of diamond facilitate experimental studies of isolated centres in great detail. Positron annihilation studies [85] show that vacancies are common defects in chemical vapour deposited (CVD) diamond. They can occur in aggregates with concentrations up to 50 ppm which persist up to 1100°C. At a temperature around 600°C neutral vacancies begin to migrate [86], and readily complex with impurities creating further optically active defects.

In Sec. 4.2 a brief review of the single vacancy is presented, followed by vacancy-nitrogen (Sec. 4.3) -silicon (Sec. 4.4) -phosphorus (Sec. 4.5) and -hydrogen complexes (Sec. 4.6). The conclusions from all the V-X centres are summarised in the

final section.

4.2 The vacancy

As indicated in the introduction, the presence of vacancies and related centres leads to absorption and emission in the diamond samples, and hence colour. Vast amounts of experimental and theoretical work has been published on the matter, and it is not practical to present a detailed review of the literature here. Instead, I present a summary of the the current understanding of the optical and electronic structure of the neutral and negatively charged vacancy.

The early theoretical work of Coulson and Kearsley [87] using a 'modified linear combination of atomic orbitals' approach suggested that the unrelaxed vacancy possesses a filled (orbitally non-degenerate) a_1- and a partially filled (orbitally triply-degenerate) t_2-level in the band-gap made up from combinations of the four 'dangling-bond' orbitals.

In the negative charge state the vacancy has the electronic configuration $a_1^2 t_2^3$. It is believed that this gives rise to the ND1 optical-band (3.149 eV), which has been shown to be a transition between A and T electronic states [88]. EPR and ENDOR studies [89] have determined that V^- possesses a $^4A_2$ ground state, consistent with the optical data, and shows that Hund's rule is obeyed (S=3/2). This result has been reproduced theoretically many times [15, 90, 91, 92, 93].

The neutral charge state of the vacancy is somewhat more complicated due to the t_2 level containing only two electrons and hence giving rise to $T_2 \otimes T_2$ multiplets: Coulson and Kearsley lists the possible symmetries of the $a_1^2 t_2^2$ electronic configuration as (adopting their notation):

$$^1A_1 + {}^1E + {}^3T_1 + {}^1T_2.$$

Thus the one-electron configuration with two electrons in the t_2 level gives rise to these four many-body configurations. Similarly, the one-electron excited state ($a_1^1 t_2^3$) gives rise to the eight many-body states

$$^5A_2 + {}^3A_2 + {}^3E + {}^1E + {}^3T_1 + {}^1T_1 + {}^3T_2 + {}^1T_2.$$

Transitions can occur between multiplets with the same spin[1], provided that the transition is symmetry allowed. For example, only transitions from T_1 and T_2 states are allowed to an E state. The neutral vacancy, V^0, is believed to be responsible for a number of optical features of which GR1 (1.673 eV) is most prominent. This

[1]Transitions involving a change in effective spin do exist, but are generally much weaker than spin conserving transitions.

band arises from an electronic transition between a ^1E ground state and a $^1T_2$ excited state. Now, both the $a_1^2t_2^2$ and $a_1^1t_2^3$ one-electron configurations possess states with $^1T_2$ symmetry. However, it is believed [87, 94] that the GR1 band does not involve the transition of an electron between one electron states, but instead from a transition between multiplets arising from the $a_1^2t_2^2$ electron configuration.

This 'internal transition' is possible due to the high symmetry of the centre. Provided Hund's rule is obeyed, trigonal (e.g. vacancy-impurity) centre related optical features necessarily involve the transition of an electron between one-electron states. This follows since the only electron configuration that gives rise to multiplets is e^2: $E \otimes E$ gives rise to $^3A_2 + {}^1E + {}^1A_1$. Hund's rule requires the ground state to possess $^3A_2$ symmetry (as in the case of the negatively charged vacancy-nitrogen complex below), and transitions between this and the other two states does not conserve spin.

Returning to V^0, it is worth noting that the von Barth method (Sec. 2.16) for estimating multiplet energies is not available due to an inadequate number of independent Slater determinants. However, the calculated multiplet structure due to Coulson and Kearsley is in agreement with the experimental observations of the GR1 band, and has formed the basis of the interpretation of other vacancy related centres.

4.3 Vacancy-nitrogen complexes

One of the most thoroughly studied vacancy-impurity complexes is the vacancy-nitrogen, $[V\text{-}N]^-$, complex (see for example Refs. [95, 96, 97, 98]) . This trigonal centre gives an emission peak at 1.945 eV which has been correlated with an S=1 EPR centre [95]. In samples exposed to relatively high levels of neutron irradiation, and hence where the Fermi-level is relatively low [99], the 1.945 eV line has a decreased intensity whilst a new line at 2.156 eV grows. It is suggested that the neutral [V-N] defect is responsible for the 2.156 eV optical transition. Recently [100], an $S = \frac{1}{2}$ EPR centre attributed to this centre was observed. Other $[V\text{-}N_n]$ defects also exist: the H3 centre for n=2; the N3 centre for n=3 and the B centre for n=4. All but the B-centre[2] are known to be optically active [101, 102].

The energy levels of the C_{3v} [V-N] defect can be understood from those of a perturbed vacancy [93, 104]. As discussed above, the vacancy introduces a filled a_1 and partially filled t_2-level into the band gap. For neutral [V-N], where a N atom replaces one of the neighbours of the vacancy, the t_2-level is now occupied by three electrons and lies above the occupied a_1-level. In fact the results of these

[2]Absorption has been tentatively associated with the B-centre – see Ref. [102].

calculations show that the a_1-level was pushed downwards towards the valence band leaving a t_2-level deep within the band gap. The trigonal symmetry of [V-N] splits t_2 into a filled a_1 state lying below an e-level containing one electron. Thus it is expected that [V-N] possesses an S=1/2 ground state.

In the negative charge state, the e-level contains two electrons and thus the system can possess an effective spin of either S=1 or S=0 resulting in $^3A_2$, $^1A_1$ and ^1E states. If the orthonormal e-orbitals are denoted by x and y, then the many-body states constructed from the pair of electrons occupying these orbitals are:

$$\begin{aligned}
\Psi(^3A_2) &= \frac{1}{\sqrt{2}}(x_1y_2 - x_2y_1)\left\{\begin{array}{c}\alpha_1\alpha_2\\ (\alpha_1\beta_2+\alpha_2\beta_1)/\sqrt{2}\\ \beta_1\beta_2\end{array}\right.\\
\Psi(^1A_1) &= (x_1x_2 + y_2y_1)(\alpha_1\beta_2 - \alpha_2\beta_1)/2\\
\Psi(^1E) &= \left.\begin{array}{c}(x_1y_2 + x_2y_1)\\ (x_1x_2 - y_1y_2)\end{array}\right\}(\alpha_1\beta_2 - \alpha_2\beta_1)/2
\end{aligned}$$

The energies of these states can be evaluated using the method outlined in Sec. 2.16 where the determinental configuration wave-functions $|x_1 \uparrow y_2 \uparrow\rangle$, $|x_1 \uparrow x_2 \downarrow\rangle$, and $|x_1 \uparrow y_2 \downarrow\rangle$ give the energies of $^3A_2$, $\frac{1}{2}(^1E + {}^1A_1)$ and $\frac{1}{2}(^1E + {}^3A_2)$, and hence each multiplet.

4.3.1 Cluster and basis.

The structure of the nitrogen-vacancy and tri-nitrogen-vacancy complexes are modelled using 70 atom clusters centred on the vacant site: $NC_{34}H_{35}$ and $N_3C_{32}H_{35}$. The basis adopted for each of the atomic species are listed in Table 4.2. In each case, the 16 atoms (two shells) in the centre of the cluster were in big basis, as defined in Sec. 2.18.

Atom	Wavefunction	Charge density
N	$4 \times sp$	5
C	$4 \times sp$	4
H	$2 \times sp$	3

Table 4.2: The atomic basis used for the calculations in Sec. 4.3.

In diamond, structures and energies are insensitive to the presence of bond-centred Gaussians, and consequentially, the relaxation was performed without including these. For calculations of transition energies, rates and the multiplet energies, the basis was increased so that all but the surface H atoms were in 'big-basis'.

4.3.2 The vacancy bordered by a N atom

The relaxed [V-N]$^-$ (S=1) defect has trigonal symmetry with three N-C bond lengths at 1.44 Å. The bond lengths of the three C radicals are 1.45 Å. The Kohn-Sham energy levels revealed the t_2-derived $a_1^{\uparrow}$- and $a_1^{\downarrow}$- levels (occupied) to lie 1.08 and 1.32 eV below the $e^{\uparrow}$- and $e^{\downarrow}$-levels. The Kohn-Sham levels in the region of the band-gap are plotted in Fig. 4.1. The wavefunctions of the e-levels have little amplitude on N in agreement with EPR studies [95] and are derived from the three radicals of the vacancy, as indicated in Fig. 4.2. The total energies of the electronic configurations gave the $^3A_2$, ^1E, $^1A_1$ ordering of the multiplets, with energies of 0.00, 0.44 and 1.67 eV respectively. Thus, in agreement with experiment, Hund's rule is satisfied.

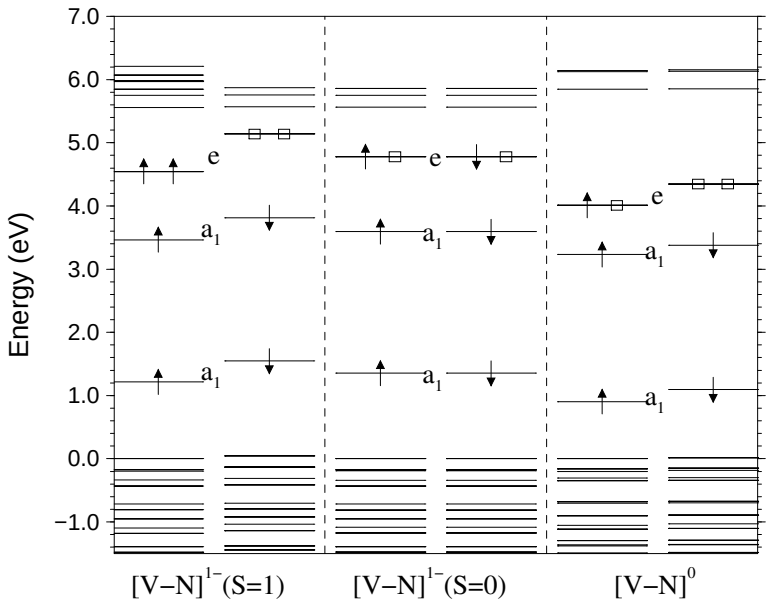

Figure 4.1: The spin-polarised Kohn-Sham eigenvalues for the V-N complex in diamond. Only the states in the region of the gap are plotted. Arrows indicate occupation and spin, and the empty boxes show empty states. The 'valence band tops' have been aligned to facilitate comparison.

Now consider the optically excited state found by promoting an electron from $a_1^{\downarrow}$- to the $e^{\downarrow}$-level. This leaves a single hole in the e-level and corresponds to a ^3E term. The vertical excitation energy is the energy difference of these configurations and differs from the ZPL by the relaxation energy of the excited state. A transition state calculation gave an optical energy of 1.77 eV in fair agreement with the 1.945 eV experimentally observed for $^3A_2 \rightarrow {}^3E$. The radiative lifetime of ∼20 ns, compared to the experimental value of 13 ± 0.5 ns [76] is found using the expression

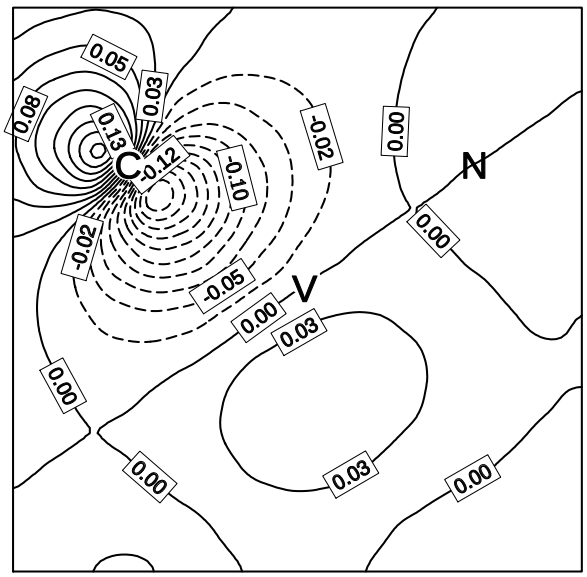

Figure 4.2: A contour plot for one of the e-level wavefunctions (au) of $[\text{V-N}]^-$. The plane passes through the vacancy site which is at the centre of the plot, and also through the N and one C atom. Note that the level is nodal at the N atom. The second e-level is qualitatively similar.

in Sec. 2.17.2. It is worth re-emphasising that estimates of the radiative lifetime are sensitive to the transition energy and spatial extent of the wavefunction. If the experimental transition energy is used in this expression, the estimated lifetime is reduced to 15 ns.

For neutral [V-N], the e-level contains one electron and hence the ground state has ${}^2E$ symmetry. A transition from the a_1-level to the e-level (Fig. 4.1) is allowed. A transition state calculation estimates the energy to be 1.57 eV, and radiative lifetime is estimated to be 20 ns, which is broadly in agreement with the 2.156 eV observed ${}^2E \rightarrow {}^2A_1$ transition [81] which has a $\sim$ 29 ns lifetime [106]. This estimate is reduced to $\sim$10 ns if the experimental transition energy is used. The ground state permits a dynamic J-T effect and an A_2-level is then expected to lie close to the ${}^2E$ ground-state [103]. The additional ${}^2A_2 \rightarrow {}^2A_1$ optical transition[3] has been detected about 100 cm^{-1} below the 2.156 eV line.

In both charge states of [V-N], there is a filled a_1-level just above the valence band top, and a transition from this level to the e-level has an energy of 3-3.5 eV, and a radiative lifetime of the order of 1 ns. This (extremely fast) transition has an energy in the nitrogen absorption band, and as a consequence may not be observed. In any case it is not likely to be responsible for either the 1.945 or 2.156 eV spectra.

It is worth noting that if the N atom is moved from a site neighbouring the vacancy to one lattice site separation, the total energy of the cluster increases by

[3]This transition is forbidden in the C_{3v} point group, but can be induced under stress.

$\sim$3.3 eV in the neutral charge state. However, the dissociated system would act more like isolated V^- and N_s^+. This would give rise to an associated Coulomb energy

$$-\frac{e^2}{\varepsilon r},$$

which amounts to around 1 eV.

The large value of the stabilisation energy has important implications. One would expect these centres to be stable to high temperatures. However, before they dissociate, one might expect them to migrate. In fact, the idea of '*vacancy-enhanced aggregation of nitrogen*' [76] has long been mooted.

4.3.3 The vacancy bordered by three N atoms

For the [V-N_3] defect, the ordering of levels in the band-gap is the reverse of the [V-N] centre, with the a_1-level derived from the vacancy t_2-level now lying above the e (Fig. 4.3). This a_1-level contains just one electron in the neutral charge state, and

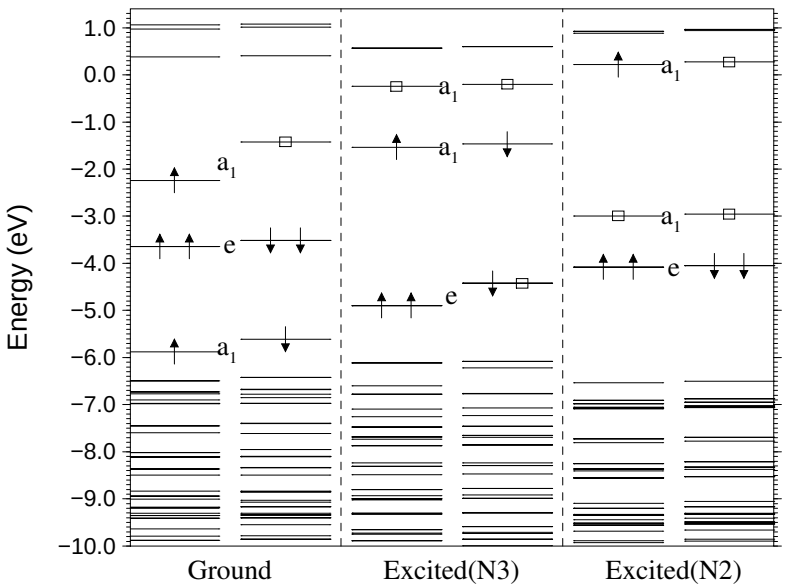

Figure 4.3: The spin-polarised Kohn-Sham eigenvalues for the [V-N_3]^0 complex in diamond. Shown are the $^2A_1$ ground state, and the ^2E excited state associated with the N3 optical transition. Also shown is an $^2A_1$ excited state which is found to be the lowest in energy. This is associated with the N2 vibronic centre. Only the states in the region of the gap are plotted. Arrows indicate occupation and spin, and the empty boxes show empty states.

is largely localised on the C dangling bond. No J-T effects are then expected for the ground state of this defect. The excited state generated by promoting an electron

from the e-level to fill the a_1-level possesses ^2E-symmetry, and might undergo a J-T distortion, but this is not experimentally observed [105]. The $S = \frac{1}{2}$ EPR centre labelled P2 has been correlated with the N3 optical centre [107, 108].

The calculated N-C bond lengths are 1.43-1.44 Å and the C-C bond lengths of the unique C atom are 1.46 Å. The $e \rightarrow a_1$ transition state energy at 2.8 eV is in good agreement with the observed value of 2.985 eV for the $^2A_1 \rightarrow {}^2E$ transition, and the calculated radiative life-times are 10 and 8 ns using the calculated and experimental transition energies respectively.

Now, the interpretation of the experimental data for the decay times of the N3 centre is rather complex [74]: the lifetime not only varies with temperature, but there is a strong sample dependence, which appears to be correlated with the concentration of A-centres. At low temperature, the seven samples reported in Ref. [74] have decay times ranging with increasing A-centre concentration from 18 to 41 ns. The temperature dependence for any particular sample assumes that there is some thermal activation from the excited state of the N3 transition to a lower excited state. The lower excited state is associated with the N2 vibronic system. Then the experimentally observed decay time, τ, is given by the expression:

$$\frac{1}{\tau} \approx \frac{1}{\tau_{\rm rad}} + \nu e^{-E_A/k_B T}, \tag{4.1}$$

where $\tau_{\rm rad}$ is the true radiative lifetime of the N3 transition, ν is an attempt frequency and E_A is the activation energy. The temperature dependent term is a phonon-assisted decay into the excited state of the N2 system which is directly correlated with the N3 centre [74, 108]. The temperature effect is significant above temperatures around 500 K. Using a least squares fit, the parameters in Eq. 4.1 are found to be found to be $\tau_{\rm rad} = 41$ ns, $\nu = 590 \pm 200$ ns^{-1}, and $E_A = 530 \pm 20$ meV for the sample with lowest A-centre concentration. If a theory including tunnelling effects is used, the fit to experiment is poor, and gives a value of $\tau_{\rm rad} = 150$ ns.

The fact that there is no ZPL associated with N2 suggests that this lower excited state may have A_2 symmetry, since transitions between A_2 and A_1 states are not allowed in C_{3v}. If this is the case, this presents a serious problem to the interpretation of these *ab initio* results: the only way to construct a multiplet which transforms as A_2 is from an e^2 electronic configuration. This can be done by exciting the two electrons from the $e^{\downarrow}$-level in Fig. 4.3 to give a $e^2 a_1^2 a_1^1$. This would be higher in energy than the ^2E state.

In principle, the undetected state may be A_1 symmetry, provided that the dipole moment of the centre is aligned in such a way that $\langle \Psi_{A_1} | \mathbf{r}.\mathbf{E} | \Psi_{A_1} \rangle = 0$. Thus, the hidden state may arise from an $a_1^1 e^4 a_1^2$ electron configuration, i.e. the a_1-level above the valence band is depopulated. However, one would expect this to be a high energy

system (a transition state calculation would place such a transition at 4.7 eV), and in these calculations the dipole matrix element shows that a transition would be allowed, so a ZPL would be expected.

An alternative excited state is found by exciting the electron from the partially filled a_1-level to the a_1-level above it. The resulting KS-levels are also plotted in Fig. 4.3, and this is in fact a lower excited state (by around 0.5 eV) than that with ^2E symmetry. More significantly, the dipole matrix element $\langle A_1|\mathbf{r}|A_1\rangle$ is orders of magnitude smaller than $\langle A_1|\mathbf{r}|E\rangle$, consistent with the N2 centre. The much longer lifetime of this transition is due mainly to the highly dispersed nature of this second a_1 KS-level.

Naturally, there are many further excited states that can be generated from arrangements of occupancies of the e, and two a_1-levels. The most likely of these is the $e^3a_1^1a_1^1$ configuration which possesses an energy around 0.7 eV higher in energy than the ^2E excited state.

4.3.4 Conclusions

To conclude, in the case of the [V-N] complex, the theory is able to account for the ground state electronic structure, the symmetries of the principal optical transitions with semi-quantitative estimates of their energies and rates.

Furthermore, the multiplet structure assigned to [V-N_3] has been reproduced although the first excited state is found to be of A_1 rather than A_2 symmetry. However, the calculated radiative lifetime of the $^2A_1 \rightarrow {}^2E$ transition is too short by at least a factor of four.

4.4 The vacancy-silicon complex

A number of experiments over the past ten years have added evidence to the idea that Si can be present in the form of isolated impurities in diamond. Initial studies where natural diamonds were implanted with Si ions [109] revealed an optical feature near 1.68 eV, which at the time was attributed to lattice damage due to the proximity in energy to the GR1 band. However, the same signals were seen in CVD diamond where the substrate was made of Si [110] or where the growth chamber was made of fused silica [111], and the common Si-factor led to suggestions that Si may be present in the form of an interstitial or Si-X complex. Combining the requirement for Si with the fact that the 1.68 eV line is enhanced when the vacancy becomes mobile [112], naturally leads to the assignment to some form of vacancy-silicon complex.

In contrast to the single or double luminescence lines that arise from the [V-N] centres, the 1.682 eV ZPL was resolved into complex set of *twelve* photo-luminescent and absorption peaks [113]. Each of the three naturally occurring Si isotopes account for a set of four lines, representing a transition from an orbitally twofold degenerate ground state, split by 0.20 meV, to a doublet excited state split by 1.07 meV. The results presented here show that the origin of these doublets lies in the extraordinary structure of the [V-Si] defect.

4.4.1 Cluster and basis.

The silicon-vacancy complex is modelled using a 85 atom cluster centred on a bond: $SiC_{42}H_{42}$. The basis adopted for each of the atomic species are listed in Table 4.3. The central six C atoms and the Si atom were treated in 'big basis' as described in Sec. 2.18. For the calculation of transition energies and rates, the bases was augmented by including a single bond-centre in all but C-H bonds.

Atom	Wavefunction	Charge density
Si	$4 \times sp$	5
C	$4 \times sp$	4
H	$2 \times sp$	3
Bond-centres	$1 \times sp$	1

Table 4.3: The atomic basis used for the calculations in Sec. 4.4.

4.4.2 Results

In contrast to the [V-N] defects, the Si atom is unstable at the lattice site and spontaneously moves to the split-vacancy site yielding a defect of D_{3d} symmetry as illustrated in Fig. 4.4. The separation between the Si atom and its six nearest neighbours for the neutral cluster is 2.01 Å, and is relatively insensitive to the charge state, being 2.00 Å in the negative charge state. The six dangling bonds form two gap e-levels (Fig. 4.5) whose states are made up of bonding and anti-bonding combinations. The lower level is filled and possesses odd parity (e''), whilst the upper is half-filled and has even parity (e'). These calculations show that the S=1 spin configuration is around 0.25 eV more stable than S=0 thus agreeing with Hund's rule. The orbitally non-degenerate $^3A_2'$ ground state rules out this charge state as a candidate for the 1.682 eV band.

However, the position of the deep e-levels shown in Fig. 4.5, suggests that the defect can readily act as an acceptor in synthetic or type Ib diamonds and in the negative ionised case, the upper e'-level has a single hole leading to a $^2E'$ ground

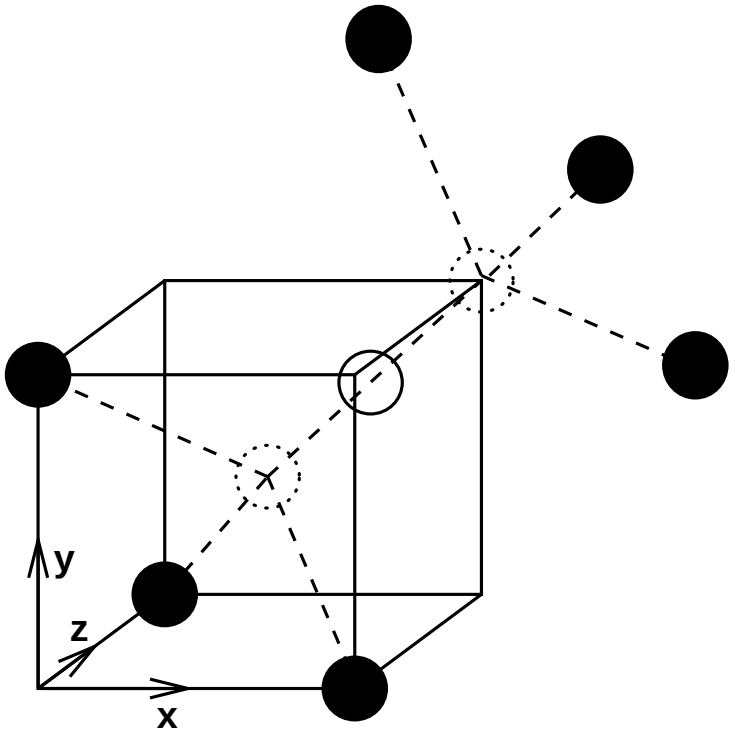

Figure 4.4: A schematic representation of the relaxed split-vacancy geometry of the V-Si complex. The solid circles represent C atoms, the empty circle the relaxed Si site, and the dashed circles the diamond lattice sites.

state. An internal optical transition can then occur between the e-levels leading to a ${}^2E' \rightarrow {}^2E''$ optical line at 1.86 eV in good agreement with the observed line at 1.682 eV. The doublets are likely to be split by spin-orbit or more likely a J-T effect. The radiative lifetimes of the transition are estimated to be 3 ns using the calculated transition energy, and 2 ns using the experimental value, which is in excellent agreement with experimental value of 1-4 ns [114].

In a similar calculation to that performed for $[\text{V-N}]^0$, the energy increase in separating the vacancy and Si by a lattice site is found to be 0.32 eV. This is a much smaller stabilisation energy due to (at least in part) the large strain around a substitutional Si atom.

Preliminary calculations show that in [V-Ge], the impurity does not prefer this site but remains at a C site pushing away its three C neighbours, although a metastable configuration exists in the split-vacancy structure.

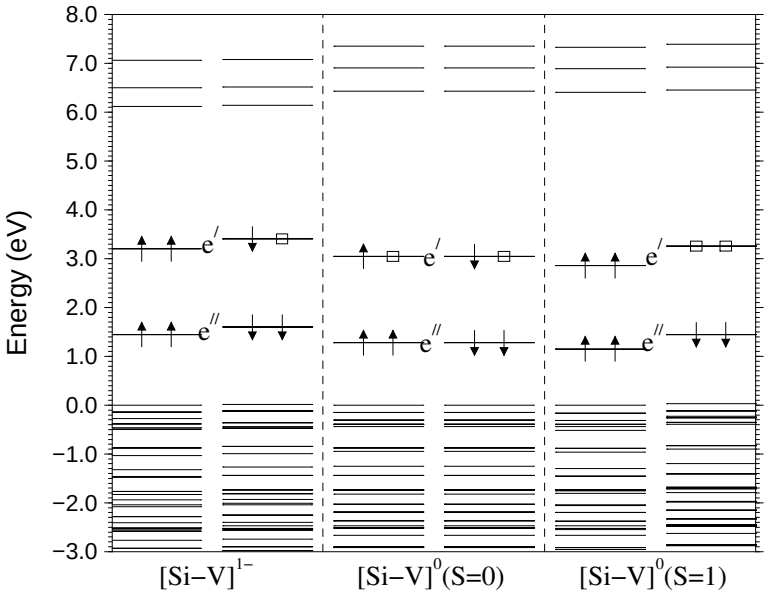

Figure 4.5: The spin-polarised Kohn-Sham eigenvalues for the V-Si complex in diamond in the region of the band gap. The notation is as in Fig. 4.1, and the 'valence band tops' aligned.

4.5 The vacancy-phosphorus complex.

4.5.1 Introduction

There has been a considerable amount of work carried out on incorporating phosphorus in diamond with the aim of making a shallow donor defect. However, almost all studies have succeeded in making highly resistive material despite substitutional P (P_s) being expected to behave as a donor [115, 116, 117]. Electron paramagnetic resonance (EPR) provides some evidence for P_s [118], and a second P defect is found in P doped diamond grown by the high pressure method [119]. The latter defect is trigonal with very little spin density at the P nucleus.

P has also been incorporated into chemical vapour deposition grown (CVD) diamond by adding PH_3 to the gas phase [120, 121]. Nitrogen apparently increases the incorporation of P within the films yielding concentrations as high as 3×10^{19} cm^{-3} (as measured via SIMS). In spite of these large concentrations, the films were highly resistive. PL experiments revealed broad intense bands around 1.7 eV which increased with [P]. These were assigned to donor-acceptor pair recombination although the identities of the defects are not known. Significantly, no sharp optical lines due to P or the vacancy were detected.

Success at making conducting, n-type diamond has been achieved through a

cold implantation of P ions followed by rapid thermal annealing [122]. It may be that this process rapidly removed vacancies resulting from the implantation.

CVD diamond usually contains a high concentration, up to $\approx 5 \times 10^{18}$ cm^{-3} of vacancies [85]. The lack of an optical signal due to vacancies in the P rich material suggests that they are bound up with P in some form. As with the N-V and Si-V centres, a P-V complex may be understood in terms of the vacancy.

It might be thought that the P-V defect would be similar to N-V. In that case we would expect it to act as an acceptor, with spin 1 in the ionised state, and to possess a sharp luminescence line arising from the $a_1 \rightarrow e$ internal transition. However, it shall be shown below that this is not the case and [P-V]$^-$ has spin S=0 and no internal optical transitions are possible.

P-V acts as a deep acceptor and would compensate substitutional P and N. This would explain the insulating properties of P-rich diamond, the lack of P-related sharp luminescent bands, as well as the presence of broad donor-acceptor optical bands.

4.5.2 Cluster and basis.

The calculations for the P-V complex have been performed on a 85 atom cluster in the same way as the Si-V complex. The basis used is given in Table 4.4. The initial runs had the central (P+6C) atoms in 'big basis' (Sec. 2.18).

Atom	Wavefunction	Charge density
P	$4 \times sp$	5
C	$4 \times sp$	4
H	$2 \times sp$	3

Table 4.4: The atomic basis used for the calculations in Sec. 4.5.

4.5.3 Results

Previously [117], substitutional phosphorus has been examined using AIMPRO: it is found to be an on-site defect with a (resonant) LVM around 380 cm^{-1}.

In the first case the P atom was placed as far away from the vacancy and the surface as possible. The structure was relaxed in the neutral charge state. Then the P atom was moved to border the vacancy and the cluster re-relaxed. The energy in this case was lower by 1.5 eV than the case where P was separated from the vacancy. This shows that substitutional P is unstable in the presence of vacancies and readily forms the P-V complex.

In the P-V complex, the P atom did not remain at its lattice site but drifted away until it lay mid-way between two lattice sites as with the split-vacancy Si-V complex. Fig. 4.4 can also be used to understand the inner core of the relaxed 86 atom (D_{3d}) cluster. The six P-C separations are 2.00 Å, the same as the Si-C distances in the negative Si-V complex. In fact the only difference in the two systems is the species of the impurity at the centre. The reason for the stability of the split-vacancy is partially connected with the large atomic size of P although Ge-V does not appear to assume the same structure. Fig. 4.6 shows the spin-polarised Kohn-Sham energy levels of the P-V defect in the vicinity of the band gap, together with those of a similar sized cluster without any defects. These reveal a mid-gap e'-level (even) containing three electrons and an e''-level just above the valence band top, resulting in an effective spin of S=1/2. The position of this mid-gap level is qualitatively similar to that found in the Si-V defect and thus the defect would be expected to trap electrons arising from say substitutional N or indeed P. Thus the P-V defect acts as a deep *acceptor*. However, the e' levels are then filled and the defect must be diamagnetic and no internal optical transitions are possible.

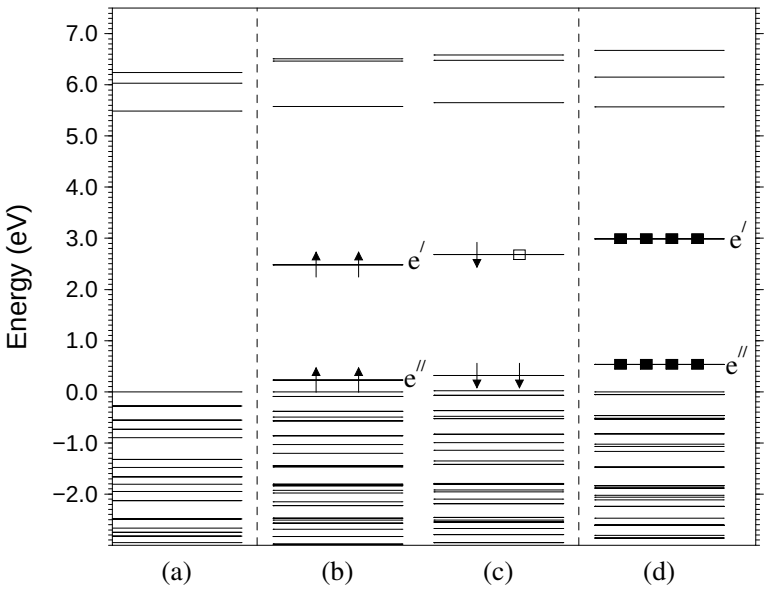

Figure 4.6: Kohn-Sham eigenvalues of the [P-V] complex in diamond in vicinity of the band gap. The arrows and filled boxes denote spin polarised and non-polarised occupied levels respectively and the empty boxes empty levels. (a) An 86 atom cluster representing pure diamond. (b,c) Spin-polarised levels for the neutral P-V defect. Note the $e''^{\uparrow}$-level is full and the $e'^{\downarrow}$ level is half-filled giving a $^2E'$ ground state. (d) shows the levels of $[\text{P-V}]^-$ where all gap levels are filled.

When the Fermi-level is low, such as for example when the material is irradiated

or the absence of substitutional N, then a neutral P-V defect would be formed having S=1/2. The wave-functions of the e' gap levels are combinations of sp^3 orbitals on the six C atoms surrounding P and possess very little amplitude on P itself as shown in Fig. 4.7. The trigonal symmetry of the defect and the fact that the spin density

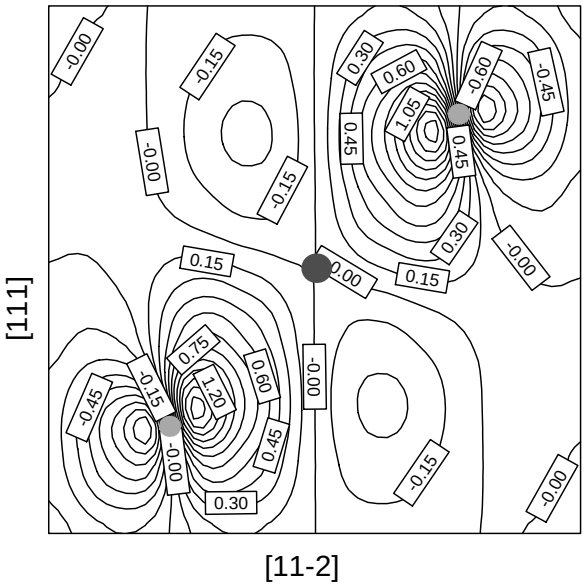

Figure 4.7: The pseudo-wavefunction for an $e''^{\uparrow}$ state (au×10). Note that the amplitude near P is negligible.

is very low on P suggests that this defect might be the EPR centre investigated in Ref. [119].

Although no internal optical transitions are possible for the ionised defect, neutral pairs of N^+ and $(P\text{-}V)^-$ defects could luminesce and be the source of the broad band donor-acceptor recombination band observed in Ref. [121]. The luminescence energy would then be given by the difference in energies of the (excited) system containing the neutral N and P-V centres:

$$\{E(N^0) + E([P-V])\},$$

and the (ground state) system containing the ionised centres:

$$\left\{(E(N^+) + E([P-V]^-)) - \frac{e^2}{\varepsilon r}\right\}.$$

Note, the energy of the ionised system includes the Coulomb interaction energy[4]. With the N donor level and the P-V acceptor level (Fig. 4.6) at $E_c - 1.7$ eV and approximately $E_c - 2.7$ eV respectively (where E_c is the conduction band edge), then for r about 5 Å, this transition would be around 1.5 eV, close to the observed value.

[4]The Coulomb energy, $e^2/\varepsilon r = 13.606 \times 2/5.5r$ which = 0.26 eV for r=10Å.

4.5.4 Summary

In conclusion, the calculations suggest a strong binding energy of P with vacancies. In the P-V centre, the P atom lies mid-way between two vacancies. The centre has D_{3d} symmetry with spin S=1/2 in the neutral charge state, and there is little spin-density on the P atom consistent with EPR experiments. The defect acts as a deep acceptor and together with N would explain the pronounced broad PL bands seen around 1.7 eV in P-doped diamond. The defect could also compensate remaining substitutional P atoms, provided that there are vacancies present in the sample[5]. This would explain the difficulties in making phosphorus electrically active in diamond.

4.6 Vacancy-hydrogen complexes

4.6.1 Introduction

It is well known that hydrogen readily complexes with vacancies in silicon; infrared-absorption experiments [13] have shown that VH_n, $n = 1, 2, 3, 4$, defects are present in ion-implanted samples. Furthermore, it is well established that impurities trap hydrogen, such as Si_{Ga} in GaAs [123], P in Si [124], B in Si [125], and it has been suggested that similar effects may be seen in diamond [126].

However, the location of H in diamond is not universally agreed upon, despite numerous studies. It is well known that CVD grown samples can contain as much as 1 at.% of H [127], but it is believed that most of this lies at grain boundaries and surfaces.

Calculations have provided evidence that if H exists in an isolated form in bulk diamond, it would preferably occupy a bond centre [128, 129, 130], with the tetrahedral interstitial site being variously reported to be between 1.7 and 2.7 eV higher in energy.

It has been suggest [131, 132, 133] that hydrogen may also be being trapped at A-centres (neighbouring substitutional N atoms). Recent calculations [134] suggested that the saving in energy by moving a single H atom from the bond-centred site to that in between the two N atoms is around 4 eV. The intermediate stage where the H atom is adjacent to only one of the N atoms is 3 eV higher in energy than the N-H-N system. So it seems clear that if isolated H atoms exist in bulk diamond, they would prefer to occupy sites in the lattice close to other defect sites.

H_2 might be present in molecular form, and calculations predicted that a centre with a H_2 molecule in an interstitial space would be stable [135]. However, later it

[5]This is highly likely in the P-implanted samples.

was shown that a system made up of one bond-centred H and one anti-bonded was much lower in energy (by 3.3 eV). This structure has since been termed H_2^*, and is seen in Si [136] and Ge [137]. A similar centre is believed to exist in GaAs [138].

Experiment has provided a number of clues as to the presence of H in diamond. IR-absorption studies [139] have reported C-H related stretch and wag LVMs at 3107 and 1405 cm^{-1} respectively. H on the $\langle 111 \rangle$ surface of diamond has a fundamental stretch mode somewhat lower [140] at 2829 cm^{-1}. This suggests that the C-H bond giving rise to the 3107 cm^{-1} band is somewhat shorter, perhaps reflecting a more confined local environment.

Cathodoluminescence (CL) has revealed the presence of optically active H-related centres [141], with a ZPL at 540 nm (2.30 eV), close to the feature seen in H-implanted natural diamond [142] which persists up to 1000°C and exhibits isotopic shifts with deuterium. The 540 nm line appears to arise from centres located at grain boundaries.

A number of EPR studies have reported signals that might be related to H-dangling-bond centres [73, 143, 144, 145]. In Refs. [73, 145] two signals are reported labelled H1 and H2, with estimated separations between the unpaired electron spin and nuclear spin of 1.9 and 2.3 Å respectively. It has been suggested that these centres are highly distorted hydrogenated vacancies, where two of the dangling bonds reconstruct to leave a unique radical. Ref. [143] suggests that the defects are dispersed throughout the sample, and thus the centre is simply V-H, whereas the later studies suggest that the experimental evidence is more consistent with centres close to grain boundaries where local distortions are rather strong. In Ref. [73], a number of cluster-calculations where reported, which supported the assignment of the H1 signal to a single H at a perturbed V site.

4.6.2 Cluster and basis

Reported here are the atomic and electronic structure of VH_n, $n = 1 - 4$, with their LVMs. The calculations were performed on (70+n)-atom clusters ($H_nC_{35}H_{35}$) centred at the vacant lattice site. The basis used is summarised in Table 4.5, with the central 4C+nH defect atoms in 'big-basis' as described in Sec. 2.18. Further relaxation calculations were performed on the larger 130+n-atom cluster $H_nC_{70}H_{60}$. For electronic structure calculations, the relaxed structures were embedded in a 186+n-atom cluster $H_nC_{104}H_{82}$. In the case of the divacancy, a bond-centred, 85-atom cluster was used($HC_{42}H_{42}$).

Atom	Wavefunction	Charge density
C	$4 \times sp$	4
H	$2 \times sp$	3
Bond-centres	$1 \times sp$	1

Table 4.5: The atomic basis used for the calculations in Sec. 4.3.

4.6.3 VH

VH was relaxed with a single hydrogen placed ~ 1.1 Å along the $\langle 111 \rangle$ direction from one of the C atoms neighbouring the vacancy. All but the surface H atoms were allowed to relax. The final H-C bond was 1.053 Å, and the distance between the H and the three unsaturated C atoms at 2.028 Å, where these atoms have relaxed away from the vacancy site by around 12%. The C bonded to the hydrogen relaxed by around 10%.

Now, Zhou *et al.* suggest that the $S = \frac{1}{2}$ EPR centre arises from unpaired spin centred at one of the unsaturated C atoms, and analysis of the hyperfine anisotropy provides an estimate of a ~ 1.9 Å separation between the electronic and nuclear (hydrogen) spin. This is in good agreement with the VH geometry as calculated here. Note, the experimental estimate of the separation is not the H-C separation, but the H-C-dangling-bond distance. This is less than the inter-atomic distance.

In order to model the electronic structure of the VH complex, the relaxed geometry taken from the 70-atom cluster was embedded in a larger (187-atom) cluster, and the self-consistent KS-levels calculated. The KS-eigenvalues for the neutral VH complex are plotted in Fig. 4.8. The defect gives rise to filled singlet below a doublet containing only a single electron, where both levels are deep in the gap, and could give rise to ${}^2E \rightarrow {}^2E \otimes {}^2E$ internal optical transitions. If it is assumed that the system is analogous to the $[\text{V-N}]^0$ centre, the lowest excited state is ${}^2A_1$, although the calculations have not been performed to confirm this. A transition state calculation predicts the transition energy to be about 1.1 eV (1127 nm). The ${}^2E$ ground state is a candidate for a Jahn-Teller distortion. The electronic structure indicates that the defect could act both as a donor, or more likely, as an acceptor.

In the positive charge state, the re-relaxed geometry puts the H 1.046 Å from the C to which it is bonded, and 2.072 Å from the remaining unsaturated atoms. The KS-levels are also plotted in Fig. 4.8. The doublet is now completely empty, and the singlet level lies around 2 eV below. This defect would be EPR inactive, but could give luminescence: a transition state calculation predicts a transition at around 1.2 eV.

In the negative charge state, the defect can adopt either a $S = 1$ or an $S = 0$

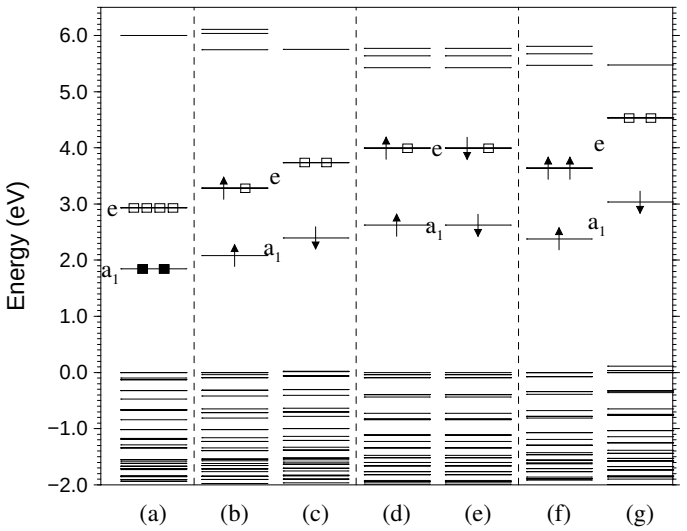

Figure 4.8: The Kohn-Sham eigenvalues for the VH^n (n=+1,0,-1) complex in diamond as follows: (a) 1+, (b)&(c) neutral, (d)&(e) 1- (S=0), and (f)&(g) 1- (S=1). The eigenvalues of different charge states have been shifted to bring the valence band tops into agreement to facilitate comparison, and only the levels in the region of the gap are plotted. Arrows indicate occupation and spin-direction, the filled boxes indicate filled *spin-averaged* levels and the empty boxes show unoccupied levels.

electronic configuration. To examine the stabilities of the two spin configurations of VH^-, the relaxed VH^0 geometry was re-relaxed in each case, and the final total energies compared. The calculations indicate Hund's rule is obeyed, with the high-spin, $S = 1$ state being around 0.25 eV more stable than that with $S = 0$.

The relaxed geometries for the 1- charge state are very similar for both spin configurations, with the C-H separations being 1.064 and 2.058 Å in each case. If this defect exists, it is likely to be EPR active, and may give rise to optical transitions. A transition state calculation predicts that the $^3A_2 \rightarrow {}^3E$ transition would be around 1.5 eV, and the lifetime is estimated at around 5 ns. The KS-levels are plotted in Fig. 4.8 for both spin states. Now, this optical transition is rather lower than the optical transition seen experimentally around 2.3 eV, but an assignment cannot be ruled out on this evidence.

Finally, for each of the charge states, the dynamical matrix has been constructed, and the normal modes calculated as described previously (Sec. 3.2). The local vibrational modes are listed in Table 4.6. Note, in principle all of these modes are IR-active, although it is possible that they would not be observed due to insufficient concentration or a small induced dipole, which has not been calculated. It is possible that this is the system responsible for the 3107 cm^{-1} band, but the calculated stretch

mode is (for the neutral charge state) some 10% higher. Now, as is discussed in more detail in Chapter 6, a 10% change in LVM can be obtained from around a 3% change in bond length, which is around the tolerance of AIMPRO. In the VH complex in Si which has been identified experimentally [13], the stretch mode was overestimated by 9%[6]. In fact, increasing the C-H bond length in the VH complex by around 3% increases the total energy by only around 30 meV but decreases the stretch mode to 3114 cm^{-1}, which is in much better agreement with the experimental mode. However, due to a lack of experimental data, no firm assignment can be made.

1+		Neutral		1-(S=1)		1-(S=0)	
H	D	H	D	H	D	H	D
3563	2607	3411	2501	3214	2350	3240	2372

Table 4.6: The H/D stretch modes (cm^{-1}) associated with four charge/spin states of VH.

4.6.4 VH_2

If the assignment of the H1 centre to VH is incorrect, and in fact H2 arises from this centre, it is possible that H1 arises from a vacancy where more than one dangling-bond is saturated by H. This suggestion was originally made in Ref. [145].

The calculations performed in a similar way to those for VH but where either two or three of the vacancy's dangling-bonds are decorated with H indicate that the more H present, the *shorter* the unsaturated C to H distance, in broad agreement with this alternative model.

VH_2 is C_{2v} with the two equivalent H atoms lying 1.049 Å from their C neighbours. The unsaturated C atoms lie 2.008 Å from the closest hydrogens. The relaxation of the C atoms away from the vacancy site is slightly less pronounced in this case with the two unsaturated C atoms moving around 12% further from the vacancy centre and those bonded to H relax by around 11%. The electronic structure, as plotted in Fig. 4.9, indicate that there is a filled a_1-level around 1 eV below an empty b_2-level, both of which lie mid-gap. A transition state calculation on $a_1 \rightarrow b_2$ predicts an energy of around 0.9 eV. Around 0.5 eV above the valence band maximum is a filled b_1-level, and there could possibly be a transition from this level at around 3 eV. A transition between levels with b_1 and b_2 symmetry is not allowed.

For VH_2 to be responsible for the reported $S = 1/2$ $g = 2.0028$ EPR-signal, it would have to adopt either a positive or negative charge state. In the positive

[6]The observed mode assigned to VH is at 2068 cm^{-1} whereas the calculations find the VH stretch mode to be 2248 cm^{-1}.

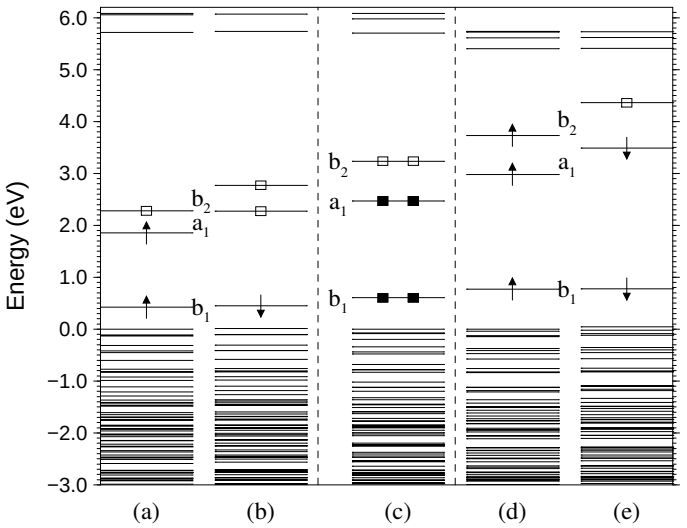

Figure 4.9: The Kohn-Sham eigenvalues for the VH_2^n (n=1+,0,1-) complex in diamond as follows: (a)&(b) 1+, (c) neutral, and (d)&(e) 1-. The notation is as in Fig. 4.8, and the charge states have been shifted to bring the valence band edges into alignment.

1+			Neutral			1-		
2H	HD	2D	2H	HD	2D	2H	HD	2D
3392	3272	2464	3540	3504	2578	3347	3290	2435
3150	2382	2311	3470	2562	2544	3229	2401	2371

Table 4.7: The H/D stretch modes (cm^{-1}) associated with three charge states of VH_2.

charge state, the C-H bonds lengthen slightly to 1.064 Å with the unsaturated C to H separation being slightly shorter at 2.060 Å. The a_1-level is now only half filled, as indicated in Fig. 4.9. There are several possible optical transitions. However, again those between the b_1 and b_2 levels are not allowed. Table 4.10, lists the remaining two transitions, of which the time dominant transition (at 30 ns) is $b_1^{\uparrow} \rightarrow a_1^{\uparrow}$ which is estimated to lie around 1.8 eV. In the negative charge state, the C-H and $C_{\text{unsaturated}}$-H distances are 1.064 and 2.060 Å respectively. The electronic structure plotted in Fig. 4.9 shows that there is only one low energy transition mechanism between the gap states. This is $a_1^{\downarrow} \rightarrow b_2^{\downarrow}$ and estimated to be around 1 eV.

The highest local vibrational modes for all three charge states are listed in Table 4.7

4.6.5 VH_3 and VH_4

VH_3 is trigonal and has an effective spin $S = 1/2$ in the neutral charge state. The electronic structure of the triply hydrogenated vacancy is the reverse of that calculated for VH, i.e. the doublet lies below the singlet, and the singlet is partially filled, as can be seen in Fig. 4.10. The singlet lies mid-gap, with the doublet around 0.6 eV above the valence band top. In analogy to [V-N_3], this defect may give rise to an ${}^2A_1 \rightarrow {}^2E$ internal optical transition. Again, a transition state calculation was performed, and the estimated energy is some 3.2 eV, and is likely to be obscured by nitrogen related optical activity.

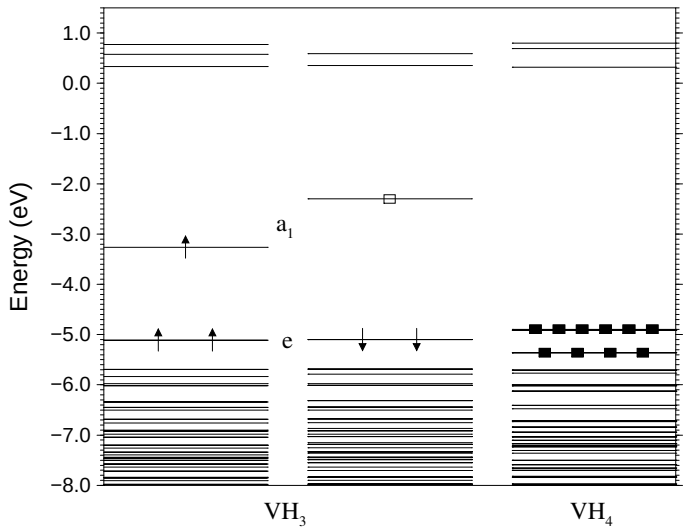

Figure 4.10: The Kohn-Sham eigenvalues for the neutral VH_3 and VH_4 complexes in diamond. The notation is as in Fig. 4.8.

Although the fully hydrogenated vacancy is patently diamagnetic, and thus cannot possibly be responsible for optical or EPR activity, for the sake of completeness, the structure of VH_4 has also been calculated. The C-H bond-length is only 1.023 Å. The KS-levels indicate that there are two levels that may be in the gap. However, since they are shallow and filled, the vacancy has been effectively passivated (Fig. 4.10), and would not give rise to any optical activity.

The LVMs of the VH_n (n=3,4) defects have also been calculated, and are listed in Table 4.8. It is interesting to note that as the number of H atoms in the vacancy increases, so does the frequency of the highest stretch mode. This follows from the fact that as H is added to the vacancy, the Coulombic repulsion from the neighbouring H atoms increases and the attraction from the remaining dangling

VH_3				VH_4					V_2H	
3H	2HD	H2D	3D	4H	3HD	2H2D	H3D	4D	H	D
3571	3531	3489	2584	4039	3994	3946	3895	2907	3123	2293
3442	3441	2559	2522	3842	3842	3842	2877	2805		
3440	2539	2522	2521	3842	3842	2851	2805	2805		
				3842	2827	2805	2805	2805		

Table 4.8: The H/D stretch modes (cm^{-1}) associated with the neutral VH_3, VH_4, and V_2H complexes.

bonds decreases. This leads to shortened C-H bond lengths and the LVMS are pushed up in frequency. This is seen in the observations of analogous defects in Si [13]. Note, in the case of VH_4, the highest mode is rather high, but if a 10% overestimation is present, this might be reduced to around 3600 cm^{-1}. Furthermore, this breathing mode would be infra-red inactive, and the second, degenerate mode is the one that would be experimentally observed (including a 10% error gives around 3460 cm^{-1}).

4.6.6 Stabilities of VH_n

n	E(VH_n) (au)	E(VH_{n-1}-H_{b-c}) (au)	Stabilisation energy (eV) [27.212 eV=1 au]
1	-432.873	-432.757	3.16
2	-435.998	-435.883	3.14
3	-434.014	-433.919	2.60
4	-437.124	-437.045	2.15

Table 4.9: The total energies of the clusters containing VH_n and VH_{n-1}-H_{b-c} systems for n=1,2,3,4. Note that in all cases, H prefers to be located within the vacancy.

In order to estimate the stability of each of the VH_n, n=1,2,3,4 centres, the following calculations were performed. VH_n and VH_{n-1}+$H_{bond-centred}$ were relaxed in the larger (130+n-atom) cluster. Then, the difference in energy is an upper bound on the stabilisation energy of each centre. The results are summarised in Table 4.9.

These results show that vacancies, as one might expect, are deep hydrogen-traps, but it should be noted that these energies are with reference to *bond-centred* H. As discussed above, previous calculations have suggested that there are even deeper traps in competition with these.

4.6.7 V_2H

H1 possesses a H–dangling-bond distance of ~ 1.9 Å, but when the H concentrations are much lower, this signal disappears to be replaced by the weaker H2 signal with a separation around 2.3 Å. The H–dangling-bond distance of 2.3 Å is somewhat more than one would expect in a single vacancy, as confirmed by these and other [73] calculations. Therefore, we suggest that this weaker defect may be a divacancy containing hydrogen. We have relaxed an 85-atom cluster centred on a bond between the two atoms that are removed to produce the divacancy, where a single H is placed close to one of the C atoms neighbouring a vacancy. The C-H bond length is found to be 1.078 Å. Then the distances between the H and the 5 remaining dangling-bonds are 2.004, 2.005, 2.595, 2.596, and 3.060 Å. The H/D LVMs are listed in Table 4.8. The H and the unpaired electron spins are in different halves of the divacancy, and therefore the measured interaction would be related to the 2.6 Å separation. This is in reasonable agreement with the experimental value 2.3 Å.

4.6.8 Conclusion

In conclusion, we find that all four VH_n, $n = 1, 2, 3, 4$ defects are stable and that VH, $VH_2^{\pm}$ and VH_3 are all consistent with the H1-EPR spectrum in terms of the separation of the electronic and nuclear spins. However, the fact that experimental evidence [73] points toward a single radical and a single H in the centre means that the true origin of the EPR signal cannot be any of these. The modelling outlined in Ref. [73] finds that the relaxed structure exhibits a weakly reconstructed bond between two of the unsaturated C atoms neighbouring the vacancy. No such reconstruction is seen in the calculations performed for this study.

All VH_n complexes are optically active, and the various transitions are listed in Table 4.10. It is possible that any one of these centres may give rise to the 540 nm hydrogen-related CL peak reported in Ref. [141]. However, there is insufficient experimental data to make any firm assignment. Furthermore, one would expect these centres to possess characteristic LVMs, and an experiment correlating LVM-absorption to the H1- and H2-EPR centres could provide valuable insight into their atomic structure. However, EPR can detect much lower concentrations of defects, and it is possible that IR-absorption experiments would not be able to resolve VH-related modes.

Now, H in a vacancy is strongly bonded to C, but the remaining dangling-bonds exert a Coulomb attraction on the proton. This tends to lengthen the C-H bond. Thus, one might expect that as more H is added, the C-H bonds would shorten,

Defect	Transition	Energy (eV)
VH^+	$a_1^\uparrow \rightarrow e^\uparrow$	1.2
VH^0	$a_1^\uparrow \rightarrow e^\uparrow$	1.1
	$a_1^\downarrow \rightarrow e^\downarrow$	1.4
$VH^-(S=1)$	$a_1^\downarrow \rightarrow e^\downarrow$	1.5
VH_2^+	$a_1^\uparrow \rightarrow b_2^\uparrow$	0.8
	$b_1^\downarrow \rightarrow a_1^\downarrow$	2.1
VH_2^0	$a_1 \rightarrow b_2$	0.9
VH_2^-	$a_1^\downarrow \rightarrow b_2^\downarrow$	0.9
VH_3^0	$e^\downarrow \rightarrow a_1^\downarrow$	3.2

Table 4.10: A table of the main optical transitions expected for VH_n, $n = 1, 2, 3$ in diamond.

and consequently, the H-dangling-bond separation increases. Then if H1 is VH, H2 might be VH_n, $n > 1$. However, this is inconsistent with the fact that H2 is only seen in samples with a low [H].

More likely, as suggested in Ref. [73] H1 is the VH centre (either in the bulk or close a grain boundary), and H2 is a related centre, also with a single H atom. This is consistent with the model of the divacancy-hydrogen complex which possesses a structure that is consistent with the 2.3 Å separation. Furthermore, one might expect that when there is more H around, the divacancy would trap one H atom in each of the vacancies, and become diamagnetic. If the divacancy was a deeper trap to the H than the single vacancy, then this would also lend weight to this assignment.

Note, the calculations can not predict where in the sample VH centres would lie, and it is quite possible that they would all be present in a region close to the surface and grain boundaries.

4.7 Summary

In conclusion,

- The calculations give a good account of the optical properties of the [V-N] and $[V\text{-}N]^-$ defects; the transition state calculations are in reasonable agreement, as are the radiative lifetimes.

- Using the von Barth approach for calculating multiplet structure has proved successful for $[V\text{-}N]^-$.

- Although the calculated transition energy of the neutral $[V\text{-}N_3]$ centre is in

good agreement with experiment, the radiative lifetime is up to an order of magnitude too short.

- Including the shallow KS-level in the electronic structure of this defect provides an explanation of the N2 vibronic centre which has been correlated with N3. Further excited states are available, one of which is likely to give rise to the N4 signal.

- The calculations show that the $[\text{V-Si}]^-$ defect possesses an unusual, D_{3d} structure where Si occupies a split-vacancy site.

- These results point to $[\text{V-Si}]^-$ being responsible for the twelve optical lines seen around 1.682 eV. This spectrum results from an internal transition between two doubly-degenerate e-levels.

- The centre is paramagnetic but there is little wave-function amplitude at the Si nucleus.

- A phosphorus-vacancy complex also adopts the D_{3d} split-vacancy structure, and would act as an acceptor. It is likely that P forming this centre is a reason for the difficulty in producing n-type semiconducting samples.

- $[\text{P-V}]^-$ would not give rise to any sharp, internal optical transitions.

- An optical transition between [P-V] and the nitrogen donor may be responsible for the broad 1.7 eV band seen in P-doped diamond samples.

- A complex of hydrogen with a vacancy produces an EPR (S=1/2) centre. The deep vacancy t_2-state is split into an e-level lying above an a_1 and is expected to give rise to an optical transition around 1.1 eV. It is possible that a complex similar to this is responsible for the H1-EPR system.

- VH_n, n=2,3,4 are also stable, and for n=2,3 the centre is expected to possess deep gap states which would give rise to optical transitions. VH_4 is completely passivated.

- In all cases, there are large binding energies between impurities and vacancies.

Chapter 5

Nickel and Ni-X centres in diamond and Si

'The best preparation for good work tomorrow is to do good work today.'

Elbert Hubbard.

5.1 Nickel in diamond

5.1.1 Introduction

Synthetic diamonds grown using high-pressures and high-temperatures (HPHT) are produced by heating together a carbon source[1] typically with a diamond seed crystal[2]. The presence of a transition metal (TM) catalyst is not strictly necessary, but the 'direct conversion' methods yield only small crystals (typically < 100 nm grains [146]). The catalyst can take several forms [146], including water, phosphorus, and transition metals (e.g. Cr, Mn, Fe, Co, Ni). With a transition metal catalyst typical temperatures[3] and pressures for synthesis are 1400°C and 5 GPa respectively [146]. Growth rates vary between companies, but Ref. [146] lists typical values of 2-15 mg/h. The largest example is that grown by De Beers at 2840 mg (6 mg/h) which implies a growth time of nearly twenty days!

Despite the wide variety of transition metals used, until recently, the only one found to contaminate the diamonds in the form of dispersed impurities was Ni, the reason for which is not clear. Recently, however, photoluminescence and absorption experiments have identified cobalt-nitrogen complexes [147].

[1]The C source is usually graphite, although other sources including SiC are used.

[2]If a seed crystal is not used, spontaneous nucleation takes place at higher temperatures and pressures.

[3]For other catalysts, higher temperatures are required - for oxyacid salts the synthesis temperature is above 1600°C, and for H_2O T$\sim$2000°C.

As the synthesis of diamonds using the HPHT has become more technologically and commercially important, the need for characterisation of the diamonds produced using this method has prompted a great deal of experimental and theoretical work.

In this Chapter, a number of Ni-related centres are examined, and comparisons made to experiment and previous theory. The layout of the Section is as follows: first the experimental results are described, then the theory of transition metal impurities in diamond is outlined (Sec. 5.1.3). In Sec. 5.1.4 previous theoretical studies of Ni_i^+ and Ni_s^- are discussed, in Sec. 5.1.5.1 the approach used for this study is described and the results are given in Sec. 5.1.5. Conclusions are in Sec. 5.1.6.

5.1.2 Experimental background

Ni impurities are known to occur in synthetic diamonds grown using the HPHT method with solvent catalysts containing Ni. Since prominent optical features are associated with these impurities, there have been great interest in these centres and a wide range of experimental techniques have been used to characterise the defects.

5.1.2.1 Magnetic centres

EPR studies have unambiguously shown that substitutional nickel (hereafter referred to as Ni_s) exists in isolated form: the signal is isotropic even at 4 K, consistent with an on-site defect and the 'super-hyperfine' interactions (from ^{13}C) indicates twelve next-nearest neighbours. A tetrahedral interstitial Ni impurity (hereafter referred to as Ni_i) would possess only six such neighbours. This defect has been associated with an optical transition at 2.51 eV [148, 149]. Various theoretical studies [150, 151, 152] have shown that TMs to the right of the periodic table possess a partially filled t_2-level in the band-gap, and in the case of Ni, the effective spin of $S = \frac{3}{2}$ suggests the negative charge state [25]. This is consistent with the relatively high concentration of N-donors in samples exhibiting this EPR signal.

Two other EPR centres labelled NIRIM-1 and NIRIM-2 are associated with nickel [153], tentatively in the interstitial site. They are observed in Ni-containing synthetic diamond when the concentration of N is lowered by the addition of titanium and/or zirconium getters to the melt. The NIRIM-1 signal ($g = 2.0112,\ S = \frac{1}{2}$) is isotropic at 25 K (implying T_d symmetry) but anisotropic at 4 K where it exhibits C_{3v} symmetry. The signal is not observed in samples where Ni is not present in the melt and is enhanced by the addition of boron dopants, suggesting a positively charged defect, although the effect apparently disappears for high concentrations of B. This has led to speculation that Ni forms complexes with B [153], but might just as well arise due to a change in charge state.

It has been suggested that this signal originates from isolated Ni_i^+ slightly distorted away from an interstitial T_d site [153]. However, there are no super-hyperfine measurements which would exclude an assignment to Ni_s^+. The latter model was rejected due to the observation of the NIRIM-1 and Ni_s^- EPR signals in measurements on the same sample. This argument is not conclusive: since if the material is *inhomogeneous*, Ni_s could certainly exist in more than one charge state. Such inhomogeneity is illustrated by the fact that both the neutral (2.156 eV) and negative (1.945 eV) charge states of the [V-N] complex coexist (Chapter 4).

NIRIM-2 ($g = 2.3285,\ S = \frac{1}{2}$) exhibits trigonal symmetry at all temperatures. It seems likely that NIRIM-1 is either Ni_i^+ or Ni_s^+ and NIRIM-2 is then a complex of NIRIM-1 with an unknown acceptor X^-. It was suggested that X is a vacancy [153], but this seems unlikely if interstitial Ni is involved, as then Ni_i^+ should easily migrate to the vacancy forming Ni_s^+. On the other hand, if the Ni atom is in the substitutional site, then one can imagine a vacancy at a neighbouring site being energetically favourable, such as in the case of [P-V], [N-V] and [Si-V] complexes. Other possibilities for an acceptor are boron or aluminium. The NIRIM-2 signal is also enhanced by the addition of B although no hyperfine interactions with 'X' are observed requiring the spin-density at 'X' to be small.

Finally, a class of EPR-defects labelled NE1-7 have been reported by Nadolinny and Yelisseyev [154, 155]. They all involve Ni, and possibly a number of combinations of vacancies and nitrogen, although the actual structures are speculative. One interesting hypothesis in Refs. [154] and [155] is the formation of a split-vacancy structure as seen in Si-V and P-V when Ni and a vacancy are combined. This then forms the basis of aggregation of N atoms to form the more elaborate structures.

5.1.2.2 Optical centres

In samples where the concentration of N-donors is low (typically $[N_s]<10$ ppm), the dominant optical feature is a pronounced optical band with a zero-phonon transition at 1.40 eV superimposed on a broad band centre around 1.4 eV. The ZPL is made up from two peaks separated by 2.7 meV [156], upon which is resolved fine structure correlating with the natural abundances of the five Ni isotopes [157]. Uniaxial stress [149] reveals that the 1.40 eV ZPL arises from a C_{3v} centre. Nazaré *et al.* [149] then suggest that the NIRIM-2 EPR defect is responsible for this ZPL, although this seems to be based largely on the fact that the centres are both trigonal and exist in samples with low donor concentrations. The transition occurs between a ^2E ground state and an ^2A excited state.

Other optical features seen in samples where $[N_s]$ is low are peaks at 1.22 [158], 2.56 and 3.1 eV [159]. The lowest energy peak is believed to arise from a more

positive[4] charge state of the 1.40 eV doublet. The 2.56 eV band is only seen in luminescence and exhibits a complicated structure which has proved difficult to interpret [160]: it is thought that Ni_s acts as an acceptor to another impurity centre which is responsible for the ZPL. The peak at 3.1 eV also appears to exhibit structure [159]. Both the 1.22 and 3.1 eV lines are only detected in absorption.

In samples containing concentrations of N exceeding ∼50 ppm, bands at 1.883 and 2.51 eV become dominant. Using uniaxial stress, Nazaré *et al.* [161] found that the 1.883 eV structure arises from a system with C_{2v} symmetry. The 2.51 eV band has only been reported in absorption.

An emission peak at 2.968 eV correlated with Ni has been observed in optical detection of magnetic resonance experiments (ODMR) [162]. The ZPL associated with the centre is very weak. The radiative lifetime of the transition is very long (40 μs at low temperature).

Recently [163], samples containing Ni_s^- defects and high concentrations of N_s impurities were annealed at 1900°C. A complex set of ZPLs around 1.693 eV appear at the temperature when N_s becomes mobile. These lines were not seen in samples where Ni is absent and it is suggested that they are due to a complex containing a single N close to a Ni impurity. The possibility that this complex is of the form Ni_s^--N_s^+ is examined in this Chapter.

5.1.3 Electronic structure of Ni in group IV semiconductors

The electronic structure of TM impurities in group-IV semiconductors is often discussed in terms of the Ludwig-Woodbury model (LW) [150] and the vacancy model [151]. The $3d^n4s^2$ atomic configuration of a first row transition metal atom[5] is expected to be changed by the environment of the lattice: first, the crystal field causes the $3d$-levels to drop below the $4s$-level, and secondly, the crystal field splits the d-levels into e- and t_2-levels.

First, according to the LW-model *neutral* interstitial impurities possess a t_2-level lying below the e and the $3d^{n+2}$ configuration becomes $t_2^6e^{n-4}$. For Ni_i^+, the highest state is then e^3 which gives an $S = \frac{1}{2}$ defect. This would thus be a candidate for a Jahn-Teller distortion, but a distortion along $\langle 111 \rangle$ would not split the e-level. Such a distortion might then cost energy. However, the spin-orbit coupling *would* split the degenerate e-state when Ni_i^+ is displaced along $\langle 111 \rangle$, and the consequent lowering of energy might exceed the energy required to move Ni off-site. Since these energy changes oppose each other, one would expect that the net lowering of energy,

[4]It is only observed in samples where $[N_s]$ is very low (<5 ppm), resulting in a lower Fermi energy.

[5]For Ni, $n = 8$.

as well as the splitting of the e-level, to be very small and the effect would disappear at temperatures when the upper level becomes occupied, or when k_BT exceeds the reorientation energy barrier.

This would explain why the anisotropic signal of NIRIM-1 at 4 K, attributed to Ni_i^+, becomes isotropic at 25 K [153]. Indeed, the spin-orbit interaction splits the e-level in the trigonal 1.4 eV optical defect by 2.7 meV [164] which corresponds to 34 K. Thus spin-orbit interactions have the correct order of magnitude.

However, an alternative viewpoint is prevalent [165, 166]: a chemical re-bonding force drives Ni_i^+ off-site. According to this model, Ni_i^+ spontaneously distorts along $\langle 111 \rangle$. Now, chemical re-bonding forces are usually rather strong and this makes the disappearance of the trigonal symmetry at temperatures as low as 25 K unlikely. Substitutional N in diamond moves off-site by this mechanism and the reorientation barrier between the equivalent minima is observed [167], and calculated [168], to be 0.7 eV. In the chemical re-bonding model, Ni_i^+ should be identified with NIRIM-2 which is known to be a trigonal defect rather than NIRIM-1 and this leaves unresolved the assignment of NIRIM-1. The almost T_d symmetry of NIRIM-1 suggests a simple defect, such as Ni_i^+ or Ni_s^+ whereas there there many possibilities for the trigonal NIRIM-2 centre involving pairs.

The LW-model for substitutional TM impurities places the e-level below the t_2-level. Now, the four sp^3 bonds of the C atoms surrounding Ni form a_1 and t_2 states. The Ludwig-Woodbury model asserts that these t_2-levels lie below those of the TM and consequently are filled leaving $n-6$ electrons in the t_2-levels of the TM impurity. For Ni_s^-, the t_2-level has three electrons which, if Hund's rule operates, yields an $S = \frac{3}{2}$ state. This model implies that the highest occupied gap-levels are localised on Ni.

On the other hand, the 'vacancy' model of substitutional TM impurities on the far-right of the periodic table considers that the associated $d-$levels lie deep in the valence band and couple weakly with the t_2-levels arising from the T_d symmetry of the ideal vacancy, V [151, 152, 169, 170, 171]. Now V^- has an electronic configuration $a_1^2t_2^3$ and if Hund's rule is *not* obeyed, a Jahn-Teller distortion occurs leading to a structure with C_{2v} symmetry. This distortion splits the t_2 level into an a_1 lying below b_1 and b_2 [172]. In Si, Ni_s^-, Pd_s^- and Pt_s^- possess this C_{2v} symmetry although the level ordering is inverted from V^-, i.e. b_1, b_2 and a_1 [173, 174]. However, in diamond Hund's rule *is* obeyed for V^- and calculations similar to those described here [93] show that the $a_1^2t_2^3$, $S = \frac{3}{2}$ configuration has a lower energy than a Jahn-Teller distorted $S = \frac{1}{2}$ state.

Thus applying the LW-model or the vacancy model leads to the prediction that Ni_s^- should exist in an $S = \frac{3}{2}$ state. Notably they differ on the question of whether

the gap wavefunctions are mainly localised on Ni or on the C atoms surrounding it. This is discussed below.

It is expected then that Ni_i can act as a donor whereas Ni_s acts as an acceptor. The types of diamond in which these centres are founds suggests that these acceptor and donor levels lie above the acceptor level due to B_s^- level at E_v+0.37 eV [175] and below the donor level of N_s^+ level at E_c-1.7 eV [176]. In fact, photo-EPR experiments [177] show that Ni_s^- possesses an acceptor level at E_v+3.03 eV. These experiments also support the correlation of the 1.883 and 2.51 eV ZPLs to Ni_s^-.

There is a possibility that Ni_s can act as a donor. This would require the t_2 level to lie in the upper part of the gap with an extended wavefunction so that correlation effects are small. The levels of Ni_s^+ would then be close to those of Ni_s^-. In Ni_s^+, the t_2 level contains one electron and this would provoke a Jahn-Teller distortion. If the distortion led to a trigonal defect, the t_2 level splits into e and a_1. It is not yet clear whether the e-level would lie above or below the a_1-state, but the splitting is likely to be very small, and if the e-level is lower, a further spin-orbit splitting is expected – just as in the Ni_i^+ case. For such a distortion to disappear at 25 K, as with NIRIM-1, either the interval between the split levels, or alternatively the barrier to reorientation, must be less than around 2 meV.

5.1.4 Previous calculations

CNDO calculations (see Sec. 2.5.1) have been carried out [24, 165] on Ni_i and Ni_s. Ni_s^- possesses T_d symmetry in agreement with experiment. However, the ordering of electronic gap levels appears to be at variance with experiment. Ni_s^0 was found to possess a filled mid-gap a_1-level lying *below* the empty t_2-level [165]. Tetrahedral Ni_s^- must then have a t_2-level containing one electron, which is plainly inconsistent with the assignment of an effective spin $S = \frac{3}{2}$.

This result may be affected by the positions of the nearest neighbours. If the surrounding shell of C neighbours is allowed to relax outwards, the splitting between the a_1^2 and t_2^1 states was reported to decrease, and it was suggested that *eventually* they would cross giving a configuration $t_2^3 a_1^0$ which is consistent with experiment.

Similar CNDO calculations were then carried out on Ni_i^0. In agreement with the discussion above, a filled e-level was found to lie just above the valence-band top. On removal of one electron this level moves to mid-gap. The tetrahedral site was found, however, to be unstable and a structure with 1.5 eV lower energy arises when Ni_i^+ is moved 0.1 Å along the $[\bar{1}\bar{1}\bar{1}]$ direction[6], with the four nearest neighbours allowed to relax. However, if the neighbours were held fixed, the nickel

[6]Here the convention that one neighbour is along [111] is adopted, and the distortion in the $[\bar{1}\bar{1}\bar{1}]$ direction is therefore towards three nearest C-neighbours.

atom moved 0.042 Å along [111] *towards* a C neighbour. This C_{3v} distortion does not alter the degeneracy of the level, and cannot be attributed to a Jahn-Teller effect since it does not raise the degeneracy of the e-level. It must therefore be a chemical re-bonding effect. Subsequent to the observation of the 1.22 eV band, the structure and transition energy of a Ni_i^{++} system was reported [178]. Here the 1.22 eV ZPL was assigned to a $^3E \rightarrow^3 T_1$ transition at this centre. This would suggest that a further EPR-active centre should be observed in low N samples.

Recently, Ni_i^+ has been investigated using a discrete variational local density functional method [166]. The calculations were based on clusters of 30 carbon atoms around the central tetrahedral interstitial Ni atom with two types of boundary conditions were applied: the first is a free boundary condition, in which the surface dangling bonds are left unsaturated for calculation of the geometry of the defect, and the second is a Watson sphere approach which enabled the electronic structure to be found. Only the central five atoms were allowed to relax and the symmetry constrained to be trigonal.

Again the on-site defect was found to be unstable. The Ni atom moved 0.2 Å from the T_d site along $[\bar{1}\bar{1}\bar{1}]$, away from one C neighbour. When relaxed, this C neighbour also moved along [111]. The total nearest neighbour relaxation lowers the binding energy by around 8 eV. Such a distortion energy is far too big to explain the properties of the NIRIM-1 signal. The ordering of gap levels leads to the electronic configuration $e^4a_1^2e^3$. The shortest resulting Ni-C bond-length (which lies along [111]) is just 1.52 Å, with the other three Ni-C bonds being 1.58 Å. These are surprising short bond lengths. The Ni-C bond-length observed in the $Ni(CO)_4$ molecule is 1.84 Å [179], and one would have expected the large Ni atom to have repelled the surrounding carbon atoms. These calculations also led to assignments to this defect for the experimentally observed optical transitions at 1.40 and 3.1 eV.

It appears then that previous calculations identify Ni_i^+ with the NIRIM-2 defect.

5.1.5 AIMPRO calculations

5.1.5.1 Cluster and basis

The atomic basis used in the calculations for this chapter are listed in Table 5.1. In each case, the central defect atoms and their neighbours were treated using a 'big-basis' as defined in Sec. 2.18, with the remaining atoms in 'minimal-basis'. In the case of $Ni_i^+B_s^-$, additional orbitals were placed on bond-centred sites around the central 6 atoms. The clusters used consisted of 71 atoms centred on the Ni impurity atom with the surface dangling bonds saturated with hydrogen atoms. Substitutional defects are modelled using the tetrahedral cluster $NiC_{34}H_{36}$, whereas

Atom	Wavefunction	Charge density
Ni	$7 \times spd$	14
B	$4 \times sp$	5
N	$4 \times sp$	5
C	$4 \times sp$	4
H	$2 \times sp$	3
Bond-centres	$1 \times sp$	1

Table 5.1: The atomic basis used for the calculations in Sec. 5.1.

interstitial Ni was modelled using the cluster, $NiC_{30}H_{40}$, centred on a T_d interstitial site. In the case of the Ni-vacancy complex, a bond-centred cluster was adopted: $NiC_{42}H_{42}$.

It should be noted that since the charge density is fitted using s-Gaussians, a large number of functions are required to adequately fit the highly peaked charge density of d-orbital elements. This can lead to near singularities in the inversion of the density matrix. Consequently the results presented here should be regarded as near to or at the limit of stability of the current incarnation of AIMRPO.

5.1.5.2 Nickel carbonyl

The Ni-basis[7] has been tested on the relatively simple $Ni(CO)_4$ molecule, which is ideally suited due to the tetrahedral structure and Ni-C bonds. The Ni-C and C-O bond lengths have been determined experimentally to be 1.837 and 1.141 Å respectively [179]. AIMPRO produced optimised bond lengths of 1.819 and 1.150 Å, errors of just 1.0 and 0.8%. These results provide confidence that the basis used well describes the structural behaviour of Ni-C bonds.

5.1.5.3 Interstitial Ni^+

This defect was found to remain on-site retaining T_d symmetry in contrast to the previous calculations described above. In order to confirm the stability of the defect, the nickel atom was displaced along [111], towards one of the C neighbours, by 0.4 Å. Then it, and its four nearest C neighbours were allowed to relax. The Ni atom returned to the tetrahedral site with the four nearest carbon neighbours at a distance of 1.72 Å. The six next-nearest neighbours were at 1.78 Å. This cluster was then relaxed further with all the atoms allowed to move. This resulted in an expansion and the final structure has Ni-C nearest neighbour lengths of 1.84 Å and next nearest neighbour lengths of 2.00 Å. This shows that there is extensive

[7]For this calculation all atoms were in 'big-basis', and additional bond-centred functions were placed between C and O atoms.

movement of the first two shells and limiting the movement to nearest neighbours is insufficient. The Ni-C lengths are very close to those found in $Ni(CO)_4$ (1.837 Å).

The energy necessary to distort Ni_i^+ from its T_d site was evaluated as follows. The total energy of cluster was calculated for various Ni displacements along $\langle 111 \rangle$ for two cases: in case (i) only the Ni atom is moved, and in case (ii) the surrounding neighbours are allowed to relax at each step. The resulting potential profiles are plotted in Fig. 5.1. This graph shows that the *global* energy minimum is to be

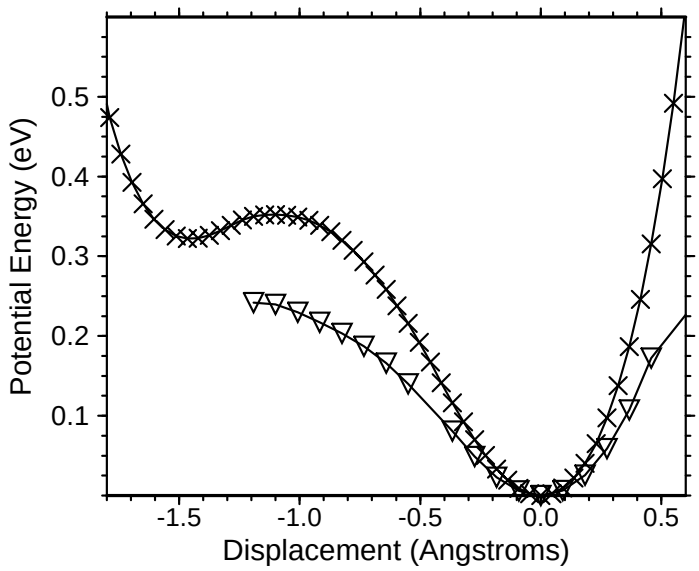

Figure 5.1: The variation of potential energy with $\langle 111 \rangle$ displacement of the interstitial nickel atom from the relaxed structure. The curve shown with X's denotes case (i) when the four surrounding carbon atoms are not relaxed at each Ni position, and the curve shown with triangles denotes case (ii) when the four nearest neighbours are free to relax.

found at the tetrahedral site, in both cases, and the amount of energy required to move the Ni off-site by 0.1 Å towards a C is around 0.01 eV. Thus our calculations give no support to the idea of a chemical rebonding force responsible for Ni moving spontaneously away from the T_d site.

The electronic levels of the positive charged relaxed cluster are shown in Fig. 5.2 (a,b). The only low energy dipole allowed optical transition for Ni_i^+ arises from a $^2E \rightarrow {}^2T_2$ estimated to be 1.38 eV using the Slater transition state method (Sec. 2.17.1).

We consider the defect could be a candidate for the NIRIM-1 centre. As already explained, spin-orbit interaction might stabilise a $\langle 111 \rangle$ distortion, below 20 K, with a splitting of the e-level by perhaps 2 meV. No optical lines have so far been associated with the NIRIM-1 defect.

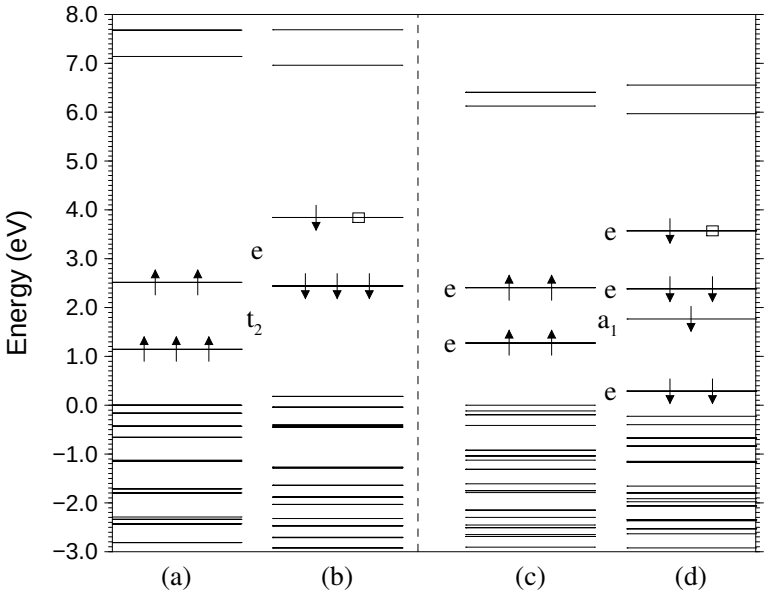

Figure 5.2: A schematic representation of the electronic structure (Kohn-Sham eigenvalues) of the two interstitial Ni defects examined in this work. (a) and (b) correspond to the Ni_i^+ spin up and spin down electronic levels respectively, with the arrows signifying filled states and the boxes empty states. Similarly, (c) and (d) corresponds to the up and down KS-levels of the Ni_i^+-B_s^- complex. The levels have been shifted linearly to facilitate comparison.

5.1.5.4 The Ni_i^+-B_s^- complex

Ni_i^+ might be expected to complex with negatively charged acceptors and hence the Ni_i^+-B_s^- defect has been investigated. Here B is substituted for one of the four nearest C neighbours and the cluster then allowed to relax. Ni moves slightly away from the T_d site along $\langle\bar{1}\bar{1}\bar{1}\rangle$, by 0.16 Å. The boron atom relaxes radially outwards (along [111]), with a relaxed Ni-B bond-length of 1.98 Å. The three C neighbours also relaxed outwards with final Ni-C bond-lengths of 1.87 Å.

The electronic structure (Fig. 5.2(c,d)) can be understood as arising from that of Ni_i^+ where the t_2-levels are split into an e- and a_1-level by the trigonal symmetry. It is assumed that the $a_1^\uparrow$-level drops into the valence band. The highest occupied $e^\downarrow$-level contains a single hole 2.4 eV below the lowest empty, (anti-bonding) $a_1^\downarrow$ state, giving the system a ^2E ground state. The corresponding $e^\uparrow$-level is filled, and lies 3.7 eV below the unoccupied a_1-level which is believed to represent the conduction band edge. The least energetic optical transition would be between the $e^\downarrow$- and an $e^\downarrow$-level 1.2 eV below. Such a transition is not consistent with the experimentally observed symmetries of Ni-related optical reanstitions. A second low-energy transition between the $e^\downarrow$- and $a_1^\downarrow$-levels ($\sim$1.8 eV). As discussed in Sec. 5.1.5.9, the

estimated transition rate via these route are rather low compared to the 2.4 eV $e^{\downarrow} \rightarrow a_1^{\downarrow}$ transition corresponding to ${}^2E \rightarrow {}^2A_1$.

The C_{3v} symmetry of the final structure, the ${}^2E$ and ${}^2A_1$ ground and excited states and the effective spin of $S = \frac{1}{2}$ are all consistent with an assignment to the 1.4 eV and NIRIM-2 centres. No strong hyperfine interaction with B would be expected, or is observed, because the hole occupies an e state which has a node at the B site. Hence Ni_i-B or possibly Ni_i-Al complex are candidates for these defects.

Transition state calculations have been performed on the two optical transitions highlighted above. $a_1^{\downarrow} \rightarrow e^{\downarrow}$ gives 1.61 eV, and the $e^{\downarrow} \rightarrow a_1^{\downarrow}$ is 2.78 eV. Although the higher energy transition is calculated to be the more rapid, there may be several reasons for discounting it. First, and most important, identifying a_1-level with the bottom of the conduction band would suggest a broad optical feature, contrary to experiment. Secondly, a conduction state is rather diffuse, and the artificial confinement of the cluster would therefore exaggerate the dipole matrix element for this transition.

If B rather than Al is involved, and since B possesses two naturally occurring isotopes, one might expect that the optical line would be split by zero-point motion effects of the two isotopes. This follows as the frequencies of the defective lattice are different in the ground and excited states. However, the effect would not occur if the ground and excited state wavefunctions had nodes at the B site. This splitting would be in addition to the 2.7 meV splitting due to spin-orbit coupling. No additional splitting is observed in the 1.4 eV centre. Now, although the e wavefunction is nodal at the B site, the a_1 wavefunction is not. Hence, the model implies a splitting for B although it might not be resolvable as for example the absence of isotopic fine structure in the 856 meV ZPL in Si [12].

The conclusions are that this defect remains a possible candidate for the 1.4 eV ZPL and the NIRIM-2 EPR centres.

5.1.5.5 Substitutional Ni^-

The cluster containing the substitutional defect, Ni_s^-, was relaxed with an effective spin of $S = \frac{3}{2}$. The inner 17 atoms (three shells of C atoms) were allowed to move. Ni remained on the T_d site with four nearest-neighbours at 1.89 Å and the twelve next-nearest neighbours at 2.58 Å. The pseudo-wavefunction associated with one of the filled $t_2^{\uparrow}$ states possesses a nodal surface between the Ni and neighbouring C atoms (Fig. 5.3) but it is difficult to draw definite conclusions as to the localisation of the pseudo-wavefunctions: there is always a near nodal surface through C as a consequence of using pseudo-potentials.

The spin-polarised energy levels are shown in Fig. 5.4(a,b). The highest occupied

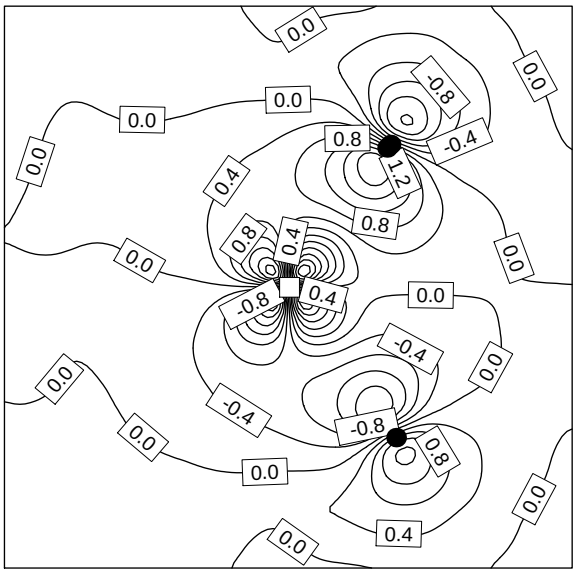

Figure 5.3: A contour plot of the pseudo-wavefunction associated with one of the three Ni_s^- $t_2^\uparrow$ states taken through the $\{1\bar{1}0\}$ plane; the x-axis is along $\langle 001 \rangle$, and the y-axis along $\langle 110 \rangle$. The wavefunction amplitude is in au$\times$10. The Ni atom is at the centre of the plot and marked with the white square. The two C atoms are marked with black circles. The plot shows the *anti-bonding* character of the wavefunction, i.e. there is a node in the wavefunction between the Ni atom and its four C neighbours.

spin-up energy level has t_2 symmetry and lies 3.0 eV above another occupied t_2 spin-up level and 3.1 eV below an unoccupied spin-up singlet which is believed to be the bottom of the conduction band. The corresponding empty spin-down t_2-levels are 1.7 eV above an occupied doublet. These results suggest dipole allowed optical transitions around 1.7 and 3.1 eV whereas an observed transition occurs around 2.51 eV [148].

If a transition state calculation is performed, then the average energy of the transition between the e- and t_2-levels is 2.33 eV.

Note, a transition to the conduction band is likely to be rather broad, and it is therefore not likely that this transition is responsible for any of the sharp ZPLs correlated with Ni. The experimentally observed transition at 1.883 eV found in N-rich material [159] is also thought to be related to the substitutional defect.

The same cluster was then relaxed with effective spin of $S = \frac{1}{2}$ which corresponds to an average of the ^2E, $^2T_1$ and $^2T_2$ states which arise from the $e^2t_2^3$ electronic configuration. The total energy for this structure was some 1.03 eV higher in energy than that with $S = \frac{3}{2}$. Thus the $^4A_2$ configuration is found to be the most stable, in agreement with experiment.

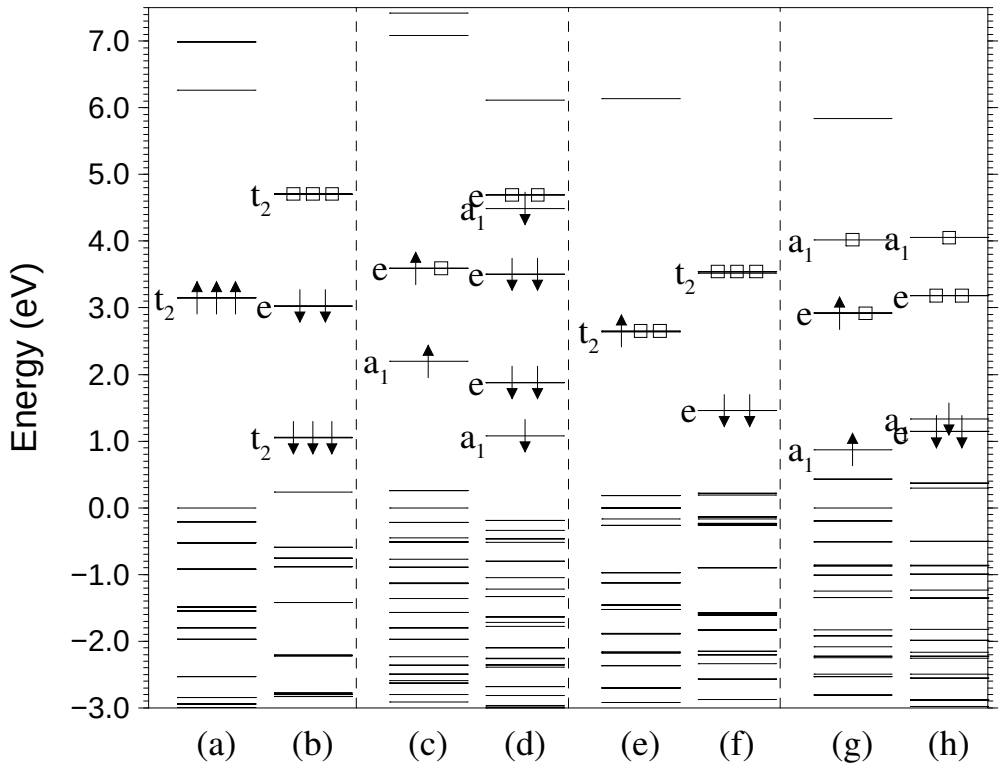

Figure 5.4: A schematic representation of the electronic structure (Kohn-Sham eigenvalues) of the four substitutional Ni defects examined in this work. (a) and (b) correspond to the Ni_s^- spin up and spin down electronic levels respectively, with the arrows signifying filled states and the boxes empty states. Similarly, (c) and (d) correspond to $Ni_s^-N_s^+$, (e) and (f) to Ni_s^+, and (g) and (h) to $Ni_s^+B_s^-$. Once more, all the levels have been linearly shifted to facilitate comparison.

5.1.5.6 The Ni_s^--N_s^+ complex

One might expect Ni_s^- to attract an ionised N donor and form a close by donor-acceptor pair Ni_s^--N_s^+, as suggested in Ref. [147]. A cluster centred on Ni_s, with with one of the nearest carbon neighbours replaced by N, was relaxed with effective spin $S = \frac{1}{2}$. The final structure retained C_{3v} symmetry: the Ni-N bond length was 1.92 Å and the three Ni-C bond lengths were 2.07 Å. The N atom has moved slightly (~ 0.15 Å) away from Ni.

The presence of the N atom split the triply degenerate $t_2^{\uparrow}$-level of Ni_s^- into an occupied $a_1^{\uparrow}$-level lying 1.4 eV below an $e^{\uparrow}$-level occupied by one hole as shown schematically in Fig. 5.4(c). This could account for the 1.693 eV transition found by Lawson *et al.* [163]. Similarly, the $t_2^{\downarrow}$-level is split into an occupied $a_1^{\downarrow}$-level 0.2 eV below an empty $e^{\downarrow}$-level (Fig. 5.4(d)). This electronic configuration has ^2E

symmetry.

We have assumed here that the splitting of the t_2 level of Ni_s^- into a_1 lying below an e level would cause the $a_1^{\downarrow}$ level to be occupied leading to a $S = \frac{1}{2}$ state. However, there is a possibility that the $a_1^{\downarrow}$ remains empty and $S = \frac{3}{2}$: the same as for Ni_s^-. The cluster was relaxed in this $^4A_1$ configuration and found to be ~ 0.8 eV higher in energy than ^2E - the ground state.

The excited state structure is rather complicated. An optical transition from the ground state must conserve spin. The excitation of an electron from the a_1-level would produce $^2A_1 + {}^2A_2 + {}^2E$ states, but there are further multiplets arising from the promotion of an electron from a lower e-level. Such a calculation is beyond the scope of the methods used here. However, Ni_s^--N_s^+ possesses optical transitions that may account for the band around 1.693 eV seen in type Ib diamonds annealed to 1900°C [163].

During the formation of the 1.693 eV centre, the strength of the 1330 cm^{-1} LVM absorption attributed to N_s remains constant. This has caused some uncertainty in the interpretation of the 1.693 eV centre as a Ni_s^--N_s^+. Now, the lattice absorption at 1330 cm^{-1} arises as free "neutral" N_s where both N and one C neighbour move away from each other. The decreased C-C back bonds give a local mode at 1330 cm^{-1} [180]. However, N_s^+ would remain on-site and no local mode would be expected from this charge state. If the annealing process caused Ni_s^- to complex with N_s^+, there would then be no loss of IR absorption at 1330 cm^{-1}. We conclude that the optical line at 1.693 eV is probably due to Ni_s^--N_s^+ defect.

5.1.5.7 Substitutional Ni^+

When the N donor concentration is lowered and the Fermi level drops, one might expect the Ni_s^- t_2^3-level to be depopulated and form an EPR active Ni_s^+ centre with an effective spin of $S = \frac{1}{2}$. The gap $t_2^{\uparrow}$ level is occupied with one electron and a Jahn-Teller distortion would be expected.

In this simulation, the Ni atom was displaced from the T_d site along [111] by ~ 0.4 Å and it and all the C atoms were allowed to relax. The Ni atom moved back to the T_d site, with the first two shells of C atoms at 1.94 and 2.58 Å. The shortest Ni-C bonds are now 0.12 Å longer than those in Ni_s^-.

In order to obtain self-consistency for the positive charge state, it was necessary to impose a finite temperature upon the calculation, i.e. the $t_2^{\uparrow}$ level had a single electron 'smeared' over the three degenerate levels using the method outlined in Sec. 2.13.1. This, as mentioned there, reduces the driving force for a Jahn-Teller distortion. We can say that the distortion must be very small and consequently the levels are close to being degenerate. It appears that a trigonal distortion is a

possibility – although it is not possible to rule out a displacement of Ni along [100] say giving C_{2v} symmetry. Moving one of the C nearest neighbours away from Ni along [111] causes the t_2 level to split into an e-level lying *below* a_1. The defect then possesses a ^2E ground state. Spin-orbit coupling (or another Jahn-Teller distortion) would then split of the e level in an identical way with the Ni_i^+ centre.

Since the $t_2^\uparrow$ level is now occupied by only one electron, it possesses $^2T_2$ symmetry. An optical transition from the e-level below this state is allowed, which results in $T_2 \otimes T_2 \otimes E$ multiplets. The spin $S = \frac{1}{2}$, and the near T_d symmetry are both consistent with an assignment to the NIRIM-1 EPR centre.

5.1.5.8 The Ni_s^+-B_s^- complex

A complex of Ni_s^+ with B_s^- might anticipated in low [N] or boron doped material. This would lead to a stable trigonal defect somewhat analogous with Ni_i^+-B_s^-. In the calculation, both the Ni and B atoms moved along [111], and the defect is stable with a long B-Ni length of 2.32 Å. The three Ni-C bonds were 2.11 Å, and the Ni next-nearest neighbour-shell occurred at 2.51-2.56 Å.

The energy levels are shown in Fig. 5.4(g,h) where it can be seen that the Ni_s-t_2 levels have split into an e state lying below a_1. A single electron occupies the $e^\uparrow$ state, which lies above an a_1-level, leading to a ^2E ground state. Of the possible optical transitions, $e^\uparrow \rightarrow a_1^\uparrow$ (1.1 eV) $a_1^\uparrow \rightarrow e^\uparrow$ (2.1 eV) and $a_1^\downarrow \rightarrow e^\downarrow$ (1.8 eV) are the lowest in energy considering only the difference in Kohn-Sham levels.

However, when the multiplets are considered, one finds that there are expected to be a large number of $S = \frac{1}{2}$ systems due to the number of unoccupied levels in the gap. However, the transition from the $a_1^\downarrow$- to the (empty) e-level above it is the most rapid as estimated using the method outlined in Sec. 2.17.2, and a transition state calculation provides an estimated energy of 2 eV. This would lead to a $^2A_1$ excited state, which is consistent with the 1.40 eV ZPL. The complex is also a candidate for the NIRIM-2 defect.

5.1.5.9 Radiative lifetimes

For each dipole allowed transition mechanism for each centre, an estimate for the radiative transition rate can be calculated using Eq. 2.47. We suppose here that the transition energy is given by the difference in the Kohn-Sham eigenvalues. The calculated rates are listed in Table 5.2. To my knowledge, the only radiative lifetimes obtained experimentally for a Ni-related centres are 140 μs the 2.56 eV luminescence peak at 2.3 K and 40 μs for the 2.968 eV emission band at temperatures <15 K.

Broadly, these estimates indicate that although there a numerous potential radiative transition mechanisms, it would appear that in each case there is a single

Ni_i^+				Ni_i^+-B_s^-			
Trans.	P_{ij}^2	ΔE	τ	Trans.	P_{ij}^2	ΔE	τ
$t_2^\downarrow \rightarrow e^\downarrow$	0.62	1.4	227	$e^\uparrow \rightarrow a_1^\uparrow$	0.38	3.7	21.0
				$e^\downarrow \rightarrow e^\downarrow$	1.08	1.2	207
				$a_1^\downarrow \rightarrow e^\downarrow$	0.05	1.8	1.3μs
				$e^\downarrow \rightarrow a_1^\downarrow$	0.40	2.4	68.2
Ni_s^-				Ni_s^--N_s^+			
Trans.	P_{ij}^2	ΔE	τ	Trans.	P_{ij}^2	ΔE	τ
$t_2^\uparrow \rightarrow a_1^\uparrow$	6.50	3.1	2.1	$a_1^\uparrow \rightarrow e^\uparrow$	2.63	1.4	53.3
$t_2^\uparrow \rightarrow e^\uparrow$	1.22	3.8	7.3	$e^\uparrow \rightarrow e^\uparrow$	0.57	3.3	18.8
$e^\downarrow \rightarrow t_2^\downarrow$	1.77	1.7	44.2	$e^\uparrow \rightarrow a_1^\uparrow$	1.31	3.5	6.8
				$a_1^\downarrow \rightarrow e^\downarrow$	2.35	0.2	20.5μs
				$e^\downarrow \rightarrow e^\downarrow$	0.96	1.2	231
				$a_1^\downarrow \rightarrow a_1^\downarrow$	0.76	1.6	1.1
				$e^\downarrow \rightarrow a_1^\downarrow$	0.01	2.6	1.5μs
Ni_s^+				Ni_s^+-B_s^-			
Trans.	P_{ij}^2	ΔE	τ	Trans.	P_{ij}^2	ΔE	τ
$e^\uparrow \rightarrow t_2^\uparrow$	1.30	2.5	20.1	$e^\uparrow \rightarrow a_1^\uparrow$	0.52	1.1	550
$t_2^\uparrow \rightarrow a_1^\uparrow$	10.99	3.5	0.8	$a_1^\uparrow \rightarrow e^\uparrow$	1.58	2.0	30.5
$e^\downarrow \rightarrow t_2^\downarrow$	1.38	2.1	30.1	$e^\uparrow \rightarrow e^\uparrow$	0.35	2.5	69.7
				$e^\uparrow \rightarrow a_1^\uparrow$	0.45	2.9	34.7
				$a_1^\uparrow \rightarrow a_1^\uparrow$	0.13	3.1	100
				$a_1^\downarrow \rightarrow e^\downarrow$	5.17	1.8	12.7
				$e^\downarrow \rightarrow e^\downarrow$	0.79	2.0	60.6
				$a_1^\downarrow \rightarrow a_1^\downarrow$	0.20	2.7	96.7
				$e^\downarrow \rightarrow a_1^\downarrow$	0.51	2.9	31.0

Table 5.2: The dipole-allowed transitions for Ni and Ni-X centres. The transitions are written in terms of the absorption. All transition energies [eV], ΔE, are found from the difference between the calculated Kohn-Sham eigenvalues, and the dipole matrix elements squared are also listed (P_{ij}^2). The radiative lifetimes, τ are listed in ns unless stated otherwise.

dominant transition so that the others would then not be observed experimentally. For each defect, the dominant transitions appear to be as follows:

- $\mathbf{Ni}_i^+$ The only dipole allowed transition is at 1.4 eV ($t_2^\downarrow \rightarrow e^\downarrow$), and has an estimated lifetime of 0.2 μs.

- $\mathbf{Ni}_i^+\mathbf{B}_s^-$ The time dominant transition listed in Table 5.2 is at 3.7 eV. The 1.8 eV optical transition $e \rightarrow a_1$ may account for the 1.40 eV centre, however, the estimated transition time is 1.3 μs, and thus is unlikely to be seen since there appear to be more rapid decay routes.

- $\mathbf{Ni}_s^-$ The dominant transitions appear to be from the $t_2^\updownarrow$ state to the conduction band estimated at 2 ns. Now, the theory used does not describe the conduction band well, so the interpretation of the rates has to be very careful. Thus it is suggested that the dominant transition is $t_2^\uparrow \rightarrow$ conduction band, but the $e^\downarrow \rightarrow t_2^\downarrow$ transition is not ruled out.

- $\mathbf{Ni}_s^-\mathbf{N}_s^+$ Again, the dominant transition is rather high in energy, so it is suggested that the dominant observable transition would be the $a_1^\uparrow \rightarrow e^\uparrow$ 1.4 eV (53 ns) transition.

- $\mathbf{Ni}_s^+$ As before, the high energy ($t_2^\uparrow \rightarrow a_1^\uparrow$, 3.5 eV) transition is dominant, but the $e \rightarrow t_2$ transitions are in the 2-3 eV range and possess transition times of around 20-30 ns.

- $\mathbf{Ni}_s^+\mathbf{B}_s^-$ This defect possesses more dipole allowed transitions than any of the others, but it is clear from the rates that the 1.8 eV, $a_1^\downarrow \rightarrow e^\downarrow$ transition is dominant with an estimated radiative lifetime of 13 ns.

5.1.6 Conclusions

To summarise, the conclusions are as follows:

1. It is clear from this work that Ni defects cause substantial movements to C atoms lying beyond the Ni nearest neighbours. Erroneous results may occur if these atoms are prevented from moving.

2. Ni_i^+ is stable at the tetrahedral interstitial site with an effective spin of $S = \frac{1}{2}$ and, in the absence of spin-orbit coupling, has no tendency to distort along $\langle 111 \rangle$, in contrast with previous calculations. Spin-orbit coupling promotes a [111] distortion leading to a slight splitting of the e-level. The splitting would be of the order of the splitting observed in the 1.40 eV optical defect, i.e.

around 2.7 meV. This would imply that the distortion would vanish above 30 K. The defect is a candidate for the NIRIM-1 defect observed in low N diamonds, especially when B is present. NIRIM-1 is known the have T_d symmetry above 25 K [148]. However, it is not the only candidate. The defect results in an expansion of the cage of nearest neighbours by almost 10% which might be observable by X-ray experiments. There is a mid-gap doublet e-level with single hole lying $\sim$1.4 eV above a filled triplet t_2 level. The transition time between these levels is estimated to be 227 ns. Surprisingly, no optical bands are correlated with the NIRIM-1 defect.

3. The Ni_i^+-B_s^- donor-acceptor complex has effective spin $S = \frac{1}{2}$ with trigonal symmetry. The presence of B splits the fully occupied t_2 level of Ni_i^+ but not the highest occupied e-level. The optical transition energies are then similar to Ni_i^+ (see Fig. 5.2). The $a_1 \rightarrow e$ ($^2E \rightarrow {}^2A_1$) 2.4 eV transition which has a transition time estimated to be 68 ns could be responsible for the 1.40 eV optical centre. The transition should be split by the zero-point energy of the two B isotopes present, assuming this to be resolvable. The ground state would also be split by the spin-orbit interaction. The complex is a also candidate for NIRIM-2; we note that the NIRIM-2 signal initially increases with B, but apparently disappears for larger concentrations of B. This may be because as the Fermi-level drops, Ni_i^{2+} defects may be created, but this would then be seen as an $S = 1$ centre (which is estimated to be around 0.9 eV more stable than $S = 0$). Alternatively, a number of complexes could form which lead to broad EPR signals. The absence of a hyperfine interaction with ^{11}B [153] may be due to the e-wavefunctions containing the hole having a nodal surface that passes through the B site.

4. Ni_s^- is stable at a lattice site and the $S = \frac{3}{2}$ configuration has an energy more than 1 eV lower than that with $S = \frac{1}{2}$. The C-Ni bond lengths are 1.86 Å and the t_2 pseudo-wavefunctions overlap both Ni and its C neighbours. It possesses a filled triplet $t_2^{\uparrow}$ level around mid-gap, and a corresponding empty $t_2^{\downarrow}$ level lies about 1.4 eV above a filled $e^{\downarrow}$ level. The defect has been identified by EPR experiments and associated with the 2.51 eV optical absorption band seen in N rich diamonds defect [148]. Another transition at 1.883 eV is always found along with the 2.51 eV line but the two have not been formally correlated. The transition state calculation estimates 2.3 eV for the $^4A_2 \rightarrow {}^4T_2$ optical transition, which is fair agreement with experiment . We suspect that the CNDO result which predicts a spin $S = \frac{1}{2}$ configuration, $a_1^2 t_2^1$, is due to an incorrect parameterisation used to describe the interaction of the Ni atom

with the surrounding diamond lattice. This in turn leads to the *rogue* a_1-level lying below the t_2-level.

5. The donor-acceptor complex, Ni_s^--N_s^+ ($S = \frac{1}{2}$), is found to be stable with C_{3v} symmetry. It possesses a hole in a mid-gap $e^\uparrow$ level about 1.4 eV above a filled $a_1^\uparrow$ level. This would explain the 1.693 eV transition observed in Ref. [163] and attributed to Ni-N defects. We note there would be a correlation between the loss of Ni_s^+ centres and the growth of the 1.693 eV system, assuming that the only sinks for N_s^+ are the Ni_s^- defects. There would be no correlation expected, and none found, with the density of neutral N_s defects. The latter are related to the strength of the lattice absorption at 1330 cm^{-1}.

6. Ni_s^+ ($S = \frac{1}{2}$) lies close to the T_d lattice site and possesses two optical transitions around 2 eV, and one around 3.5 eV. The symmetry and spin state are also consistent with the NIRIM-1 centre. Ni_s^{2+} would empty the t_2 level altogether, and thus be EPR-inactive (S=0).

7. The Ni_s^+-B_s^- ($S = \frac{1}{2}$) defect has trigonal symmetry and a ^2E ground state. The complex gives rise to a large number of optical transitions and is a candidate for NIRIM-2 and the 1.40 eV zero phonon doublet defect.

8. The high symmetry of isolated interstitial and substitutional impurities leads to a number of degenerate gap levels, and in practice (depending on the charge state), these will be split into multiplets. If the multiplet splittings are of order 0.5 eV [93] then each defect will give a small number of optical transitions broadened by this amount. However, if the negative and positive charge states are adopted for the substitutional and interstitial impurities respectively, then the ground states are well defined ($^4A_2$ and ^2E). Conserving spin gives well defined excited states ($^4T_2$ and $^2T_2$). It is interesting to note that these results suggest that Ni_i^0 would be electrically and optically inactive. Other charge states are generally more complex. For example, Ni_s^0 would have a ground state arising from the $e^4t_2^2$ electronic configuration which leads to $T_2 \otimes T_2$ multiplets (the same a the neutral vacancy - Sec. 4.2) which could conceivably have an internal transition.

9. In general, when Ni_i and Ni_s are complexed with other impurities, the gap states split to produce a larger number of possible transitions at smaller energies. Table 5.2 shows that one would expect at least 20 absorption lines from the 6 defects studied. However, experiment has only identified a small number, about 6[8], of optical lines associated with Ni, which suggests that either

[8] 1.22, 1.40, 1.883, 2.51, 2.56, and 3.1 eV

only a small number of complexes exist, the optical transitions possess small oscillator strengths, there is a dominant transition mechanism for each defect type, or the transitions are hidden by other absorption. This is especially true at higher energies, say $\sim$ 3.5 eV, where Ni related peaks are buried in the nitrogen absorption band. Using the crude estimate for transition times indicated in the text, it would appear that a dominant transition mechanism occurs for each defect, and this could account for the small number of observed Ni-related optical centres.

10. As the only defect for which there is convincing evidence is Ni_s^-, one wonders whether all the Ni related optical and EPR defects are simply different charge states of substitutional Ni possibly complexed with other impurities. Furthermore, if Ni was found at interstitial site, one would expect Ni_i^{2+} ($S = 1$) to be seen under EPR, and to date this is not the case. However, Ni_s^{2+} would have zero effective spin, and would therefore not generate an EPR signal. Hence, we suggest that NIRIM-1 and NIRIM-2 may be Ni_s^+ and Ni_s^+-B_s^- complexes respectively. It is noteworthy that all the optical features due to Ni are confined to octahedral growth sectors of diamond [159] and this also suggests that the centres are incorporated as substitutional defects at the growing (111) surfaces.

11. An alternative acceptor to those reported here is the vacancy in analogy to the complexes with P, N and Si substitutional impurities. Preliminary studies into this system strongly suggest that the structure would possess the D_{3d} structure preferred by the Si and P impurities, but due to problems in obtaining a self-consistent charge density for Ni-V, no detailed results will be presented here. This is an on-going area of study.

5.2 Nickel and nickel-hydrogen complexes in Si

5.2.1 Introduction

As stated above in Sec. 5.1.3, the vacancy model of substitutional TM-impurities on the far-right of the periodic table [151, 181], considers that the d levels of the TM impurity lie deep in the valence band of Si and couple weakly with the t_2 levels arising from the T_d symmetry of the ideal vacancy. The important implication is then that the gap-levels and structure of the defect are largely determined by those of a perturbed vacancy [152, 169, 170, 171]. For Pt^-, Pd^- and Ni^-, the gap t_2 levels contain three electrons and according to the Jahn-Teller theorem, a distortion will occur for an S=1/2 state, leading to a splitting of these levels and a lowering of

energy. DLTS shows that Ni_s possesses acceptor and donor activation energies at $E_c - 0.45$ and $E_v + 0.16$ eV respectively [182]. EPR measurements on Ni^- [183] and Pt^- [181, 184] reveal that the defect has C_{2v} symmetry and furthermore, uniaxial stress measurements on the EPR lines have shown [173, 184] that the gap t_2 levels split into a configuration $b_1^{\uparrow\downarrow}\ b_2^{\uparrow}\ a_1^0$. This ordering of levels is the reverse to that found for the negatively charged vacancy. Further evidence for the vacancy model has been suggested recently when it was found that Pt-H complexes can be created by high temperature in-diffusion of the impurities [185, 186, 187, 188]. Two LVMs attributed to Si-H have been observed which undergo small shifts in mixed H-D implantation or when the charge state of the defect is changed. These results establish the presence of more than one H in the defect. The first suggestion was that the H atoms bond to two of the four Si atoms surrounding the vacancy. It is the purpose of this work to investigate this model.

As far as I am aware, there have been no *ab initio* calculations of the Jahn-Teller distortion or the splitting of the t_2 levels, nor of the complexes with H.

Reported in this Section are spin-polarised calculations on substitutional nickel, Ni_s, and Ni-H_2 complexes using large (up to 133 atoms) clusters. A key ingredient is that we allow the atoms surrounding the defect to move and this enables us to investigate in detail the Jahn-Teller distortion due to Ni_s^- and to obtain the structure and the LVMs of the Ni-H_2 defect. The LVMs are found by two methods: the first is finding the solutions to the dynamical matrix as outlined in Sec. 2.15. In the second method (Sec. 2.15.2, Ref. [40]) the energies corresponding to displacing the H atoms from their equilibrium sites were found and the Schrödinger equation for the oscillator solved numerically using these energies as a potential in accordance with the Born-Oppenheimer approximation. The two methods give rather similar results.

5.2.2 Cluster and basis

Ni is investigated since spin-orbit coupling is less important in this case than for Pd and Pt. The basis used is listed in Table 5.3. In each case the central defect atoms (Ni and H) and the four Si-neighbours where treated in 'big basis' as described in Sec. 2.18. Ni_s^- is modelled using a 71 atom cluster, $NiSi_{34}H_{36}$, whereas the effect

Atom	Wavefunction	Charge density
Ni	$7 \times spd$	14
Si	$4 \times sp$	5
H	$2 \times sp$	3

Table 5.3: The atomic basis used for the calculations in Sec. 5.2.

of H was investigated in a 133 atom, negatively charged cluster $NiSi_{70}H_{62}$ where 19 central atoms were relaxed.

5.2.3 Results

The Ni atom was placed along [100] so that the symmetry of the cluster is C_{2v}. Three close-by levels for each spin lay in the gap region and these are occupied with three electrons according to Fermi-statistics corresponding to 0 K, i.e. the lowest was filled, the next filled in the up-spin case only and the others were empty. The self-consistent energy and forces acting on the central 17 atoms were then found for this $S = 1/2$ configuration, and these atoms were allowed to move to minimise the energy of the cluster. The Ni atom moved closer to the substitutional site while the surrounding Si atoms moved outwards from their lattice positions. The splitting between the t_2-derived levels gradually decreased and eventually we were unable to obtain a self-consistent solution. This arises because during the course to self-consistency, the three close-by gap levels, the uppermost of which is empty, cross over and if, for example, the a_1 state falls below the b_1 state, the charge density and hence potential changes discontinuously. On the next iteration, the level ordering often reverses and the process never converges. This problem of 'charge sloshing' is well-known and often occurs for close-by levels. It can be overcome by occupying the gap-levels with Fermi-statistics corresponding to a finite temperature (as described in Sec. 2.13.1) larger than the splitting of the t_2 levels. This spreads out the electrons among the three gap levels and the discontinuity in the charge density arising from cross-over is reduced. However, this almost eliminates the Jahn-Teller driving force for the Ni atom to lie off-site. For the finite-temperature calculation the lowest energy configuration corresponded to a structure where the Ni atom is essentially on site but the four surrounding Si atoms were displaced outwards from their lattice sites by 0.270 Å and two of them were further displaced along [100] by 0.006 Å. Second shell Si atoms were displaced by ~ 0.07 Å. The three gap levels were split by only 5 meV and the highest occupied spin-up level was 0.6 eV below the corresponding (but empty) spin-down level. Thus the departure from T_d symmetry is extremely small. The ordering of the t_2-derived gap levels is $b_1^{\uparrow\downarrow}\ b_2^{\uparrow}\ a_1^0$ is the same as that found experimentally.

The problem of obtaining self-consistent solutions can now be overcome by restricting the electronic configuration to be $b_1^{\uparrow\downarrow}\ b_2^{\uparrow}\ a_1^0$. Then during the passage to self-consistency, there is no discontinuity in the charge density but the energy levels that are occupied at each stage are not necessarily in ascending order. However, towards the end of the self-consistency cycle the energy levels ordered correctly and the final energy obtained was lower than that obtained by the imposition of a tem-

perature. The Ni atom was then moved along [100] and the equilibrium structure was found to correspond to a displacement of 0.13 Å from the lattice site. The two Si atoms with Cartesian components along [100] were displaced almost radially by (0.15, ± 0.25, ± 0.22) Å and moved away from each other, whereas the other two Si atoms with components along [$\bar{1}$00] were displaced (-0.07,± 0.16, ∓ 0.13) Å so that they approached each other. Curiously, the four Ni-Si bonds are almost identical in length at 2.645 Å. This distortion is similar to that found experimentally for the negatively charged vacancy [172].

Suppose now, we occupy the t_2 derived states according to $a_1^{\uparrow\downarrow}\ b_1^{\uparrow}\ b_2^0$. This is the configuration found experimentally for the negatively charged vacancy [172] but not for Ni_s^-. Then the self-consistent cluster energy is higher than the previous configuration by 17 meV. We note that although we have shown that the C_{2v} distortion has a lower energy than T_d it leaves open the possibility that other symmetries, e.g. D_2, have even lower energies as suggested in Ref. [189]. The slight distortion from T_d to C_{2v} symmetry is consistent with the ease of reorientation of Pt around the central lattice site. This motion occurs for temperatures above 12 K or even when the slightest stress is imposed on the crystal at 2 K [184].

The pseudo-wave function of the t_2-derived levels all possess a nodal surface lying between the TM impurity and the surrounding Si atoms and peaks on either side of the Si atoms along ⟨111⟩. This suggests that H atoms will lie either between Si and Ni in the configuration suggested previously [173, 185, 187, 188], or outside at anti-bonding (AB) sites as shown in Fig. 5.5. There were no problems with self-consistency in the present case. For the first defect where the H atoms are within the 'vacancy' occupied by the Ni atom, the H atoms repelled Ni along [100] from its lattice site by 0.20 Å and formed Si-H bonds of length 1.508 Å with a H-H separation of 1.517 Å. The LVMs due to H were calculated to lie at 2477 and 2511 cm^{-1}. These values are far from the experimental ones for PtH_2 [173, 185, 186] and strongly suggest that this model is incorrect. The strong coupling between the H atoms occurs because there is so little room for both Ni and H within the vacancy. The second defect (Fig. 5.5) when relaxed yielded an energy 0.08 eV below the first structure and the Ni atom moved 0.3 Å along [100] towards the H atoms and the Si-H lengths became 1.557 Å. The separation between the H atoms was 7.3 Å. The vibrational modes are given in Table 5.4. The two H related modes are slightly split, by 7 cm^{-1}, with the higher mode being A_1. Now, uniaxial stress splitting experiments on PtH_2 [186] show that the upper and lower modes also have A_1 and B_1 symmetries respectively. The stretch modes are close to those reported for PtH_2 but the bend modes have not yet been detected.

Anharmonic effects are known to be important for H modes (Sec. 6.2, Refs. [40,

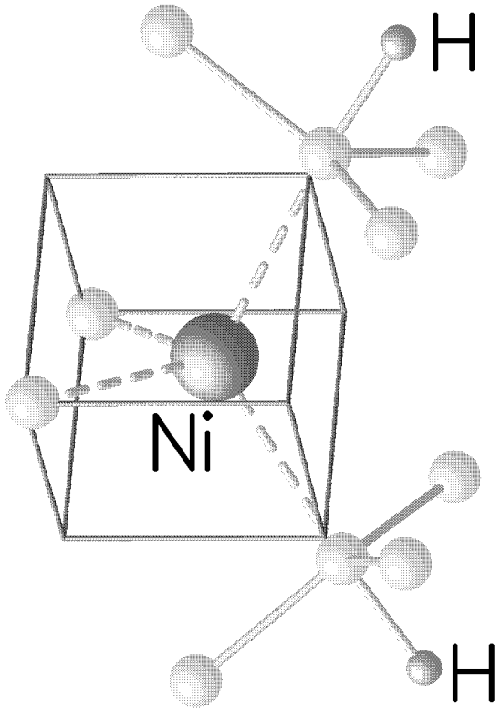

Figure 5.5: Ni-H_2 Complex with H at anti-bonding (AB) sites.

54, 56]) and we investigated their influence in the following way: the two modes at 2009.9 and 2003.2 cm^{-1} represent A_1 and B_1 vibrational modes in which the H atoms move either in phase or out of phase with each other. The energies necessary to displace the H atoms by an amount r, parallel to the Si-H bonds, were evaluated for each of these modes. This energy contains only even powers of r in the B_1 mode whereas it contains both even and odd powers in the A_1 mode. The Schrödinger equation for the oscillator was solved numerically [40] and the A_1 and B_1 frequencies were then found to be 2037 and 2060 cm^{-1} and are separated by 23 cm^{-1}. However, now the B_1 mode lies *above* the A_1 mode contrary to experiment. Thus even though the separation of the H atoms is very large, 7.3 Å, the two modes are split and their ordering reversed by these anharmonic effects by an amount twice as large as that observed for Pt-H_2. However, there are other anharmonic terms which should be considered. For example, $r_1\theta_1^2 + r_2\theta_2^2$ terms where r_k and θ_k are the changes in the equilibrium Si_k-H_k lengths and angles respectively. These mix the stretch and bend modes and are only present in the A_1 mode where $r_1 = r_2$. These have the effect of decreasing the mean Si-H length hence pushing up the A_1 frequency. Such a term then might well displace the A_1 mode above that of B_1.

Several other models of the defect were investigated, but all gave energies above that of the AB structure. In addition, their vibrational modes were far from the

Calc.	A_1	B_1	A_2	B_2	A_1	B_1
Ni-H_2	2009.9	2003.2	903.0	897.2	890.4	889.4
Ni-HD	2006.6	1442.5	900.1	889.8	636.6	630.6
Ni-D_2	1445.1	1439.9	638.7	634.6	631.6	629.5
Expt[a,b]						
Pt-H_2	1901.6	1888.2				
Pt-HD	1894.6	1366.9				
Pt-D_2	1370.7	1362.5				

[a]Ref. [185, 186] [b]Ref. [190]

Table 5.4: Vibrational Modes (cm^{-1}) for the TM-H_2^- AB defect

observed values and often, the B_1 mode lay higher than that of the A_1. We suggest then that the H atoms lie at AB sites in the Pt case especially as its larger size makes it even less likely that H would lie inside.

Further arguments against the configuration in which H atoms are inside the vacancy come from the comparison with LVMs assigned to the vacancy-hydrogen, VH_2, and H_2^* complexes. The former are observed at 2122 and 2144 cm^{-1} [13]. The separation between the H modes here, $\sim$23 cm^{-1}, is larger than that observed in PtH_2 where it might be expected that the TM squeezes the H atoms together, increasing their interaction and the mode splitting. In the case of H_2^*, the AB sited H atom gave an LVM at 1838 cm^{-1} [136] rather close to the stretch mode of the PtH_2 complex, whereas the other H-LVM, attributed to H-Si stretch where Si has a tetrahedral environment, has a frequency at 2061.5 cm^{-1} – somewhat higher than that found for Pt-H_2. Recently, Uftring *et al.* [190] analysed the anisotropic hyperfine parameter in PtH_2 and concluded that the Pt-H distance is about 4.5 Å which is close to the calculated Ni-H length of 4.28 Å in the AB sited model.

The wave-function for the highest occupied level in NiH_2^- (AB) has b_2 symmetry and *vanishes* in the (011) plane containing the two H atoms. This level occurs around mid-gap in our calculations and the next lower level is very close to the valence band. The positions of these levels is only approximate but they suggest that the observed EPR signals are due to PtH_2^- complexes, for it is known that when E_f lies above $E_c - 0.1$ eV, then the defect is not paramagnetic. There must be a second acceptor level corresponding to the filling of $b_2^{\downarrow}$ around $E_c - 0.1$ eV and leading to diamagnetic NiH_2^{--}. Uftring *et al.* [190] also concluded that the defect has two acceptor levels as the effect of illumination on the paramagnetic complex is easily understood to arise from the capture of photo-generated holes by PtH_2^-. In addition, they suggested that the Pt hyperfine data is consistent with the H atoms lying in the nodal plane of the highest occupied level. For NiH_2^-, the contour plots of the pseudo-wavefunctions suggest that the isotropic hyperfine interaction with H

would vanish leaving only an anisotropic one. However, spin-polarisation causes a difference in all the spin-up and spin-down valence wave-functions and results in a small polarised charge density of -0.007 a.u. at each proton. This is only -2% of the charge density of a H atom in vacuo. Its magnitude is within a factor of three found experimentally for PtH_2 [173, 185, 186, 188]. It is unclear whether this discrepancy is due to calculational errors or differences between Ni and Pt.

5.2.4 Conclusions

In conclusion, the calculations show that the substitutional Ni^- defect with T_d symmetry is unstable against a displacement along the $\langle 100 \rangle$ axis. The t_2 gap level is split into b_1, b_2 and a_1 levels in ascending energy. Ni_s can complex with two H atoms at AB sites and act as a double acceptor. It gives two H-LVMs around 2000 cm^{-1}. The polarisation charge density is very small and negative at the H nuclei and we suggest that PtH_2 complexes assume the same structure.

Chapter 6

Carbon-Hydrogen complexes in GaAs.

> 'The great tragedy of Science: the slaying of a beautiful hypothesis by an ugly fact.'
>
> Thomas Huxley

6.1 Introduction

Carbon is a very important dopant in GaAs due to its low diffusivity and high solubility. In this Chapter, the details of the interaction of substitutional C_{As} with hydrogen is explored in the cases of the isolated C_{As}-H complex and a class of complexes due to C_{As}-dimers. The former case has been the subject of much experimental and theoretical work, but the emphasis in Sec. 6.2 is the anharmonic nature of the LVM observed experimentally at 2635 cm^{-1}.

A number of C-H stretch modes have been observed at frequencies higher than that due to C_{As}-H, a number of which exhibit a strong polarisation in one of the $\langle 110 \rangle$ directions. This is believed to be a consequence of the manner C is incorporated during growth, and the available experimental data points toward C_{As} dimer complexing with H. The structures and modes of a range of possible configurations are presented in Sec. 6.3.

6.2 Anharmonic theory of the C_{As}-H complex.

6.2.1 Introduction.

As discussed in Sec. 2.15.2, anharmonicity is especially important for vibrations where the amplitude is large (typically > 0.1 Å). Thus, anharmonic effects have

become evident experimentally where hydrogen is involved [54, 56], and in particular the high frequency stretch mode of the C_{As}-H complex in GaAs [51]. As discussed in Sec. 2.15.2, C_{As}-H in GaAs exhibits an anomalous isotope shift, and Davidson *et al.* found that the anharmonic vibration is characterised by the parameters $\chi = 1.1$ and $B = 176$ amu cm^{-1}. Now, absorption due to the overtone of a mode is made possible by anharmonicity, but despite the large anharmonicity of the 2635 cm^{-1} mode, no overtone has been reported. An overtone *has* been observed for the C-H vibration of the HCN molecule which has an anharmonicity parameter of B_o=102 amu cm^{-1} [191]. This is only 58% of the value of B for the stretch mode in GaAs. These experimental results raise the question as to why the anharmonicity is so large for C_{As}-H in GaAs and yet the intensity of the overtone seems to be so low. The aim of this section is to provide a possible answer.

The theory is applied to HCN in Sec. 6.2.4 and to C_{As}-H in GaAs in Sec. 6.2.5. In Sec. 6.2.6 the effects of electrical anharmonicity are considered. First, a brief review of carbon and carbon-hydrogen complexes in GaAs is presented.

6.2.2 Experimental background & previous theoretical studies.

Carbon is known to preferentially substitute for As in GaAs [192]. Its low diffusivity [193, 194, 195] and high solubility make it an ideal dopant. Acceptor concentrations of the order of 10^{20} cm^{-3} and higher have been achieved in molecular beam epitaxy (MBE) [196], metalorganic MBE (MOMBE) [193, 194, 197, 198, 199], and metalorganic vapour phase epitaxy (MOVPE) [200, 201, 202]. However hydrogen introduced during growth leads to a degradation in electrically activity: it can lead to premature device failure [203, 204], and passivate up to 60% of C_{As} [205].

The hydrogen passivation of single carbon acceptors to form $C_{As}H$ pairs was first reported by Pan *et al.* [206], and the 2635 cm^{-1} infrared absorption band has been assigned to the H-stretch mode of this centre [207]. The isotopic shifts arising from ^{13}C (Ref. [207]) and D (Ref. [208]) unambiguously identify the constituent chemical species, and uniaxial stress studies indicate that H lies along a trigonal axis [207]. Previous theoretical studies have shown that the lowest energy atomic configuration in the neutral charge state is the hydrogen atom sited near a C-Ga bond-centre, as shown in Fig. 6.1 [45, 209].

As well as the intense infra-red absorption due to the C-H stretch mode, a complete set of lower lying vibrational modes have been observed experimentally for C_{As}-H. Infra-red spectroscopy on GaAs containing high concentrations of C and H grown by MBE and CVD revealed modes at 453 (labelled X) and 563 cm^{-1} (labelled Y) [199]. Both were subsequently shown to be due to C_{As}-H as they exhibited shifts

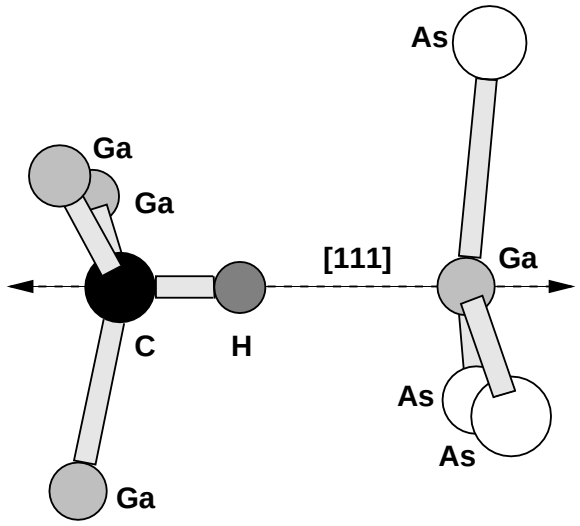

Figure 6.1: The C_{As}-H defect in GaAs.

with ^{13}C and D. A Raman scattering experiment [210, 211] assigned the 453 cm^{-1} band to the C-related A_1-band. Y is now believed to be the E^+ band [51]. The E^- band was not observed in the early experiments. However, in deuterated samples, the E^- band was detected at 637 cm^{-1}. This must imply that the unobserved H-related E^--band lies above 637 cm^{-1} and a simple force constant model [51] predicted the band to lie at 745.2 cm^{-1}. The failure of the infra-red experiments to locate this band was explained by the *ab initio* theory as the consequence of a small transition dipole moment [212]. This band has since been detected at 739 cm^{-1} by Raman scattering experiments [70].

The early calculations [45, 213] performed using AIMPRO predicted the high frequency, stretch modes of C_{As}-H in good agreement with experiment, but represented the low frequency, bend-modes rather poorly. The basis used in these calculations was rather modest, and when the basis was increased (Ref. [214]), the modes at low frequency were much better reproduced. However, the stretch modes became much higher in frequency, overestimating by more than 300 cm^{-1}. I shall show in Sec. 6.2 that this discrepancy can, at least in part, be mitigated by the inclusion of anharmonic terms in the calculation of the vibrational mode.

The C_{As}-H complex has also been treated in a plane wave basis, super-cell approach [209]. The calculation produced C-H and C-Ga lengths of 1.2 Å and 2.0 Å respectively, and vibrational modes of 2781 and 724 cm^{-1} for the C-H stretch and E^- modes respectively, although the lower modes were not reported.

C_{As}-H			HCN		
Atom	Wavefunction	Charge density	Atom	Wavefunction	Charge density
Ga	$8 \times sp$	8	H	$2 \times sp$	3
As	$8 \times sp$	8	C	$6 \times sp$	6
C	$8 \times sp$	8	N	$8 \times sp$	8
H	$2 \times sp$	3	Bond-centres	$1 \times sp$	1
Bond-centres	$1 \times sp$	1			

Table 6.1: The atomic basis used for the calculations in Sec. 6.2.

Bond-lengths		
Bond	Calc	Expt
H-C	1.07	1.06
C-N	1.15	1.15

Vibrational modes			
^{12}C-H		^{12}C-D	
Calc	Expt	Calc	Expt
3318.9	3312	2611.5	2629
2125.0	2089	1944.5	1906
764.3	712	609.1	569

Table 6.2: The calculated and experimental [191] structure (Å) and vibrational modes (cm^{-1}) of the HCN molecule.

6.2.3 Clusters and basis.

The basic theory and approach used to estimate the effects of anharmonicity are detailed in Sec. 2.15.2. The cluster used in all the following calculations on the anharmonicity of the C-H stretch mode is bond-centred, and has 87-atoms: (CH)-$Ga_{22}As_{21}H_{42}$. The basis adopted for each of the atomic species are listed in Table 6.1.

For C_{As}-H, the central C and H atom, as well as the four surrounding Ga atoms were treated in big basis, as defined in Sec. 2.18. The remaining atoms were treated using a minimal basis. A single bond-centre was placed between all neighbouring atoms, except where one of these atoms was H. For HCN, all atoms were in big basis, and a bond centre was placed in each bond.

The quasi-harmonic vibrational modes were calculated as described in Sec. 2.15, where for C_{As}-H, energy double derivatives were found between each of the big-basis atoms, and the remaining atoms treated using the Musgrave-Pople valence force potential. Naturally, for HCN, all the double derivatives were computed.

6.2.4 Prussic acid molecule: HCN

The calculated structure and quasi harmonic LVMs are listed in Table 6.2. The agreement with the experimental values [191] is excellent.

The values of the double derivatives calculated for HCN are listed in Table 6.3,

$E_{C,C}$	$E_{C,H}$	$E_{H,H}$
1.565	-0.374	0.376

Table 6.3: Calculated energy double derivatives for HCN (a.u.).

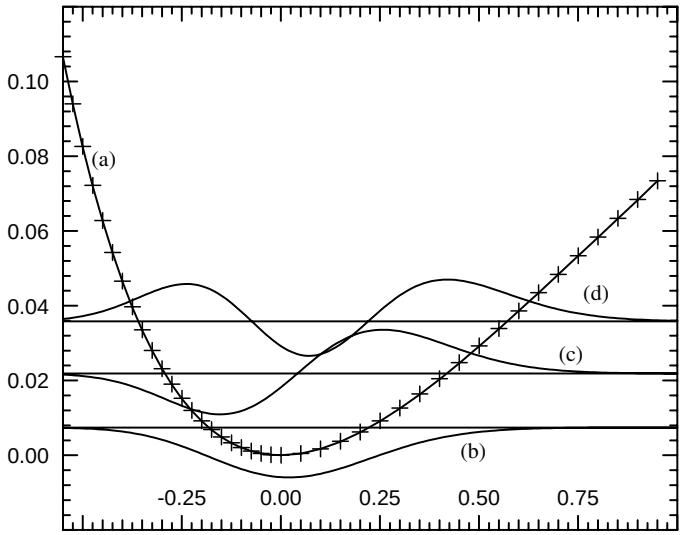

Figure 6.2: (a) Potential energy (au) versus displacement from equilibrium, x, (au) for C-H stretch in HCN. The oscillator wavefunctions for the ground (b), first (c) and second (d) excited states are also shown. The horizontal lines show the energies of these states.

which show that $E_{C,C}$ is rather large. In particular, $E_{C,C}/E_{H,H}$=4.2, which is the same order of magnitude as M_C/M_H. This satisfies the conditions for a physical value of $\chi < 1$ (Sec. 2.15.2.4). Inserting the double derivatives from Table 6.3 into Eq. 2.44 and iterating provides a value of $\chi = 0.77$ for H and $\chi = 0.59$ for D. Evaluating the quasi-harmonic frequencies instead from the expression $\nu^2 = E_{H,H}(1/m_H + 1/\chi m_C)$ gives values of 3305 and 2512 cm^{-1} for H and D respectively. Hence, the neglect of motion of the N atom is valid in the case of H since this frequency is very close to that derived from diagonalising the dynamical matrix. This is not the case for D, due to the coupling between the C-D and N-C modes.

The anharmonic potential is calculated as prescribed in Sec. 2.15.2, where the motion of the N atom is neglected. Note, if the N atom is allowed to relax at each point in the vibronic potential, little change is observed. The potential is shown in Fig. 6.2, along with the polynomial fit $f(x) = \sum_{n=2}^{8} a_n x^n$. The maximum error in the fit, $|f(x) - E_{ai}(x)|$ where $E_{ai}(x)$ is the *ab initio* energy at a displacement x, is 7×10^{-5} a.u. (=16 cm^{-1}). The coefficients of the fit are given in Table 6.4.

Equating a_2 with $k/2$ and setting $\chi = 0.77$ gives a harmonic frequency of 3552.5 cm^{-1}. This is much higher than the quasi-harmonic and experimental values because higher order even terms in displacement are present in quasi-harmonic

a_2	a_3	a_4	a_5	a_6	a_7	a_8
0.1846	-0.1932	0.1473	-0.0780	0.0234	-0.0265	0.0210

Table 6.4: Calculated polynomial coefficients (a.u.) for the fit to the vibronic potential of HCN.

modes, which tend to reduce them. Also plotted in Fig. 6.2 are the lowest three energy levels and their wavefunctions as calculated using the secular equation described in Sec. 2.15.2. Two features are worthy of note. First, the wavefunction amplitudes are essentially zero outside of the range of energies calculated for the vibration. If this were not the case, then the fit to the potential might be unreliable in a region important to the vibration, and hence the wrong frequencies would be found. Secondly, the amplitude of the peaks are larger for positive x than negative x, due to the repulsive nature of the C-N bond. This asymmetry is important when considering the electrical anharmonicity.

The calculated *anharmonic* modes are listed in Table 6.5. They are some 4% lower than experiment, but the anharmonicity parameter, A is in good agreement. Note, A is little changed by neglecting χ, despite the absolute value of the frequency changing by 34 cm^{-1}.

Mode	$\chi = 0.77$	$\chi = 1.0$	Observed	a_{5-8}=0	x^4 fit
Fundamental	3189	3155	3312	3229.7	1947.2
Overtone	6273	6206	6521.7	6448.2	4006.6
Anharmonicity, A	105	104	102.3	11.2	-112.2

Table 6.5: Calculated and observed anharmonic C-H frequencies (cm^{-1}) of the HCN molecule.

The primary source of error in the vibrational frequencies comes from the precision with which theory can predict bond-lengths. The bond-length can effectively be changed by adding a linear term to the potential energy (Sec. 2.15.2). If, using this method, the C-H bond is decreased from the calculated 1.07 Å to 1.06 Å the vibrational modes are almost coincident with experiment. A plot showing how the vibrational modes vary with effective bond-length is shown in Fig. 6.3. Note, the anharmonicity does not significantly change, showing that this parameter is only weakly dependent on bond-length. A similar treatment for the DCN system is hampered by the coupling between D-C and C-N modes.

It is instructive to compare these results with those of lowest order perturbation theory. In order to do this, we must have a potential with only up to cubic and quartic terms in x. This can be achieved in one of two ways. First, one might set the coefficients a_i, i=5,6,7,8 all equal to zero. This resultant frequencies are shown alongside the experimental values in Table 6.5, and are in very poor agreement.

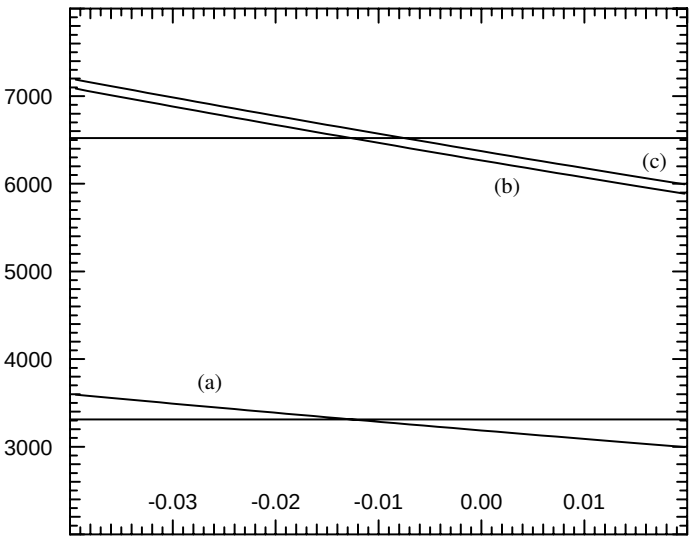

Figure 6.3: The variation of the fundamental (a) and overtone (b) frequencies in cm^{-1} with the change in the equilibrium C-H length (Å) in HCN. Curve (c) shows the the fundamental frequency $\times 2$ and its difference from (b) demonstrates that the anharmonicity varies slowly with the C-H length. The horizontal lines show the experimental frequencies (3312 and 6521.7 cm^{-1}) [191]).

The alternative is to fit a quartic potential. The maximum error in the fit is much greater than before (7.8×10^{-3} a.u. (1711cm^{-1}), and consequentially the vibrational modes are very poor. These are also shown in Table 6.5, where it can be seen that the anharmonicity parameter is even the wrong sign. This is clear evidence that such a procedure is insufficient to describe these vibrations.

In summary, using the relatively simple example of the tri-atomic molecule, it has been shown that the anharmonic treatment described in Sec. 2.15.2 can describe both the absolute frequencies and the anharmonicities of di-atomic vibrations. The anharmonicity parameter, A, is relatively insensitive to bond-length and mass. Significantly, low order perturbation theory is insufficient to model these systems.

6.2.5 The C_{As}-H stretch mode

The 87 atom bond-centred GaAs cluster with C at the central As site, and H placed close to the centre of the C-Ga bond, was fully relaxed. The equilibrium C-H and H-Ga lengths were 1.126 and 2.253 Å respectively. The calculated energy double derivatives are listed in Table 6.6, and the quasi-harmonic modes calculated by diagonalising the dynamical matrix made up from these and valence force potential terms are listed in Table 6.7.

Notice that the stretch mode is in poor agreement with experiment (11% error), but that the lower lying, C-related modes are much more accurate.

If one uses Eq. 2.38 to derive a value for χ using the experimental values of

$E_{C,C}$	$E_{C,H}$	$E_{H,H}$
0.342	-0.277	0.311

Table 6.6: Calculated double derivatives for C_{As}-H (a.u.).

	Expt	Theory		Expt	Theory
C-H Stretch			A_1 modes		
^{12}C-H	2635	2950	^{12}C-H	453	456
^{13}C-H	2628	2942	^{13}C-H	438	440
^{12}C-D	1969	2154	^{12}C-D	440	442
^{13}C-D	1958	2144	^{13}C-D	427	428
E^- H-like modes			E^+ C-like modes		
^{12}C-H	739	888	^{12}C-H	563	553
^{13}C-H	730	883	^{13}C-H	548	536
^{12}C-D	637	707	^{12}C-D	466	495
^{13}C-D	617	693	^{13}C-D	464	487

Table 6.7: Calculated and observed [70, 215] LVMs (cm^{-1}) due to C_{As}-H in GaAs.

the stretch mode, one gets a value around 0.6. However, if instead one uses the theoretical values shown in Table 6.7, then one gets $\chi = 1.17$ and if one uses Eq. 2.44, then one gets $\chi = 1.23$. Thus, it is clear that, unlike the case of HCN, the anomalous isotope shifts are due to anharmonicity (as suggested by Davidson *et al.* [51]) instead of a tightly bound C atom.

The vibronic potential for the C-H stretch mode was derived in the same was as for HCN, and is plotted in Fig. 6.4, along with the polynomial fit. The fit coefficients are listed in Table 6.8, and the maximum error in the fit was 3×10^{-5} a.u. (6 cm^{-1}). Again, also plotted are the first three energy levels and their wavefunctions.

a_2	a_3	a_4	a_5	a_6	a_7	a_8
0.1703	-0.1771	0.1025	-0.0503	0.0378	-0.0225	0.0047

Table 6.8: Calculated polynomial coefficients (a.u.) for the fit to the vibronic potential of C_{As}-H in GaAs.

Table 6.9 lists the harmonic, fundamental, and overtone frequencies for C_{As}-H as calculated using a value of $\chi = 1.23$. Notice, that in contrast to the case of HCN, the fundamental frequency is in reasonable agreement with the quasi-harmonic frequency, and overestimates the experimental value by some way. The parameter A is 144cm^{-1}, some 37% greater than that for HCN. As with HCN, altering χ has a small effect on the vibrational frequencies, but virtually none on A.

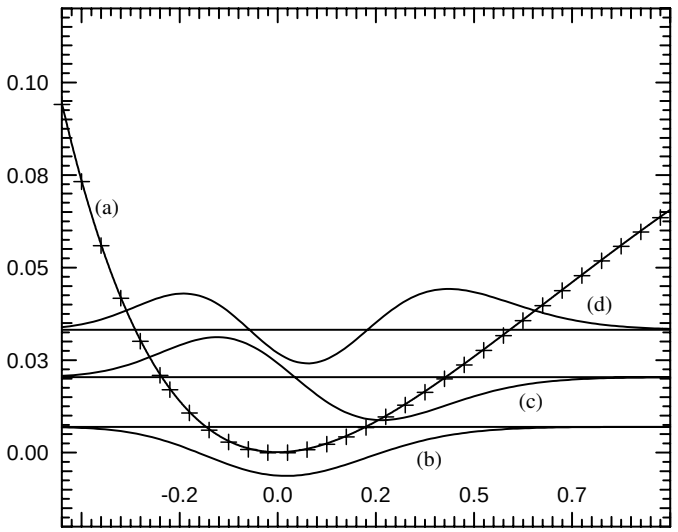

Figure 6.4: (a) Potential energy (au) versus displacement from equilibrium, x, (au) for C-H stretch in GaAs. The oscillator wavefunctions for the ground (b), first (c) and second (d) excited states are also shown. The horizontal lines show the energies of these states.

Mode	Expt	Harmonic	Fundamental	Overtone	Mass (a.m.u.)	B	B_o
^{12}C-H	2635	3108.1	2963.2	5782.3	0.937	135.7	134.9
^{13}C-H	2628	3100.5	2956.3	5769.2	0.941	135.7	134.9
^{12}C-D	1969	2266.4	2189.3	4301.2	1.761	135.8	136.3
^{13}C-D	1958	2256.0	2179.6	4282.5	1.778	135.8	136.3

Table 6.9: Calculated and experimental [51, 207, 208] anharmonic C_{As}-H frequencies (cm^{-1}) for the *ab initio* bond length, 1.126 Å.

Again, the error in absolute frequency is mainly due to the sensitivity to bond-length. To examine this dependence, an additional linear term in the potential was employed in the case of C_{As}-H in the same was as for HCN. The results are shown in Fig. 6.5. The experimental frequency is reproduced when the bond-length is increased by 0.035 Å from the *ab initio* length. The anharmonicity at the new bond-length is A=156 cm^{-1}. The calculated modes for the longer bond-length are summarised in Table 6.10.

If, as with HCN, the coefficients a_i of the polynomial fit are set to zero for

Mode	Expt	Harmonic	Fundamental	Overtone	Mass (amu)	B	B_o
^{12}C-H	2635	3012.8	2635.2	5114.3	0.937	159.1	146.2
^{13}C-H	2628	3005.5	2629.1	5102.7	0.941	159.1	146.5
^{12}C-D	1969	2196.9	1954.5	3819.0	1.761	160.3	158.4
^{13}C-D	1958	2186.8	1945.9	3802.7	1.778	160.3	158.4

Table 6.10: Calculated and experimental [51, 207, 208] anharmonic C_{As}-H frequencies (cm^{-1}) for the lengthened C-H bond (1.161 Å).

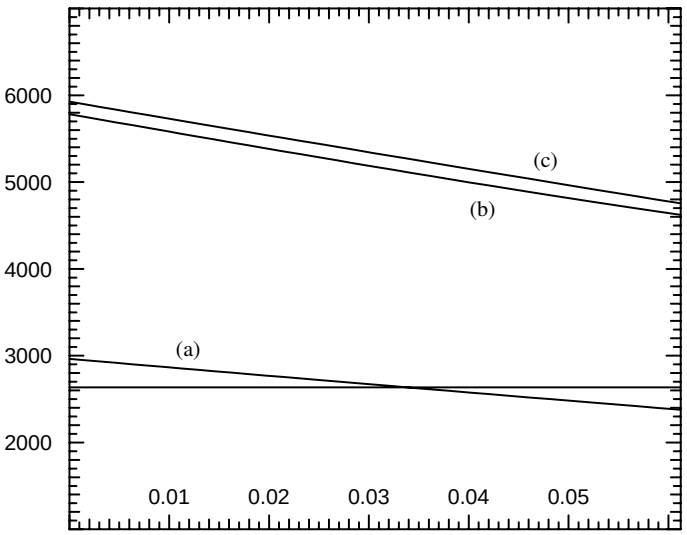

Figure 6.5: The variation of the fundamental (a) and overtone (b) frequencies in cm^{-1} with the change in the equilibrium C-H length (Å) for C-H in GaAs. Curve (c) shows the the fundamental frequency $\times 2$ and its difference from (b) demonstrates that the anharmonicity varies slowly with the C-H length. The horizontal line shows the experimental frequency (2635.2 cm^{-1} [51])

$i > 4$, then the fundamental and overtone H frequencies are 2988 and 5897 cm^{-1} (χ=1.23 and C-H=1.126 Å). The anharmonicity parameter A is then much lower at 79 cm^{-1}. B still approaches the asymptotic value given by low order perturbation theory for large m^*, but the rapid approach to the asymptotic value is only valid for certain ranges of the coefficients a_i, $i > 4$ and outside these ranges, masses very much bigger than unity are needed for B to be given by its asymptotic value. This means that low order perturbation theory is inapplicable. If the potential was fitted with a quartic polynomial, then, as with the case of HCN, the error in the fit is much larger and the frequencies of the fundamental and overtone are 2897 and 4269 cm^{-1}. We therefore conclude that perturbation theory cannot be used to describe the parameters B and B_o.

In summary, the calculated effective mass parameter χ is greater than unity for the case of C_{As}-H in GaAs, but anharmonic effects are important. Thus, the calculated transition frequencies depend critically on the C_{As}-H length. An increase in length of the C-H bond by as little as 0.035 Å brings the calculated fundamental frequency into agreement with the observed frequency. The anharmonicity parameter B is about 160 amu cm^{-1} and close to the estimate of 176 amu cm^{-1} given in Ref. [51]. The anharmonicity is sensitive to high order derivatives in the potential energy and it effects cannot be described by low order perturbation theory.

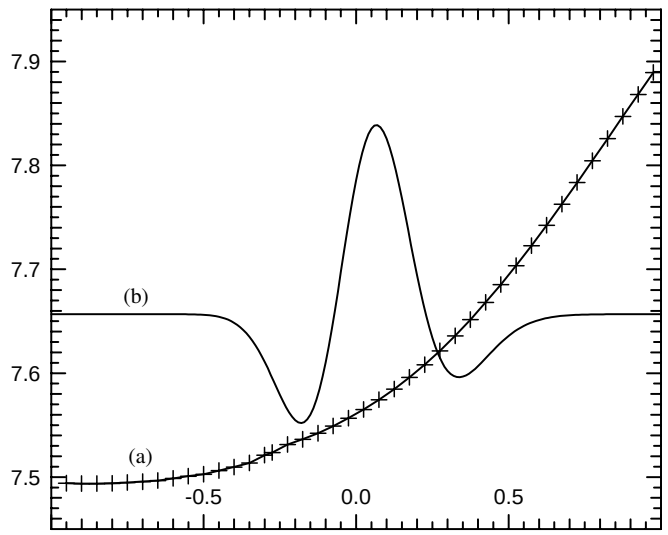

Figure 6.6: Curve (a) shows the dipole moment of the cluster (au) versus the change in the equilibrium C-H length (Å) for GaAs. Curve (b) shows the product of oscillator wavefunctions $\Psi_0(x)\Psi_2(x)$ shifted vertically upwards.

6.2.6 The intensity of the overtone

Ignoring electrical anharmonicity, the intensity of the overtone is simply proportional to

$$\int \Psi_2 x \Psi_0 dx,$$

where Ψ_i is the i^{th} vibronic state. However, as discussed in Sec. 2.15.2, the approximation that the dipole operator is simply x is incorrect, and the true form of $\hat{p}$ is shown in Fig. 6.6.

The ratio of the overtone to fundamental intensities is given in Eq. 2.42 The product $\Psi_2\Psi_0$ is also shown in Fig. 6.6, the asymmetry in which is a consequence of the mechanical anharmonicity. Carrying out the integral with a linear dipole operator gives an intensity ratio of 1.6%. Then, using the non-linear dipole, the integral gives a ratio of 0.33%, a decrease of nearly 80%! Using the wavefunctions generated for the elongated C-H bond, the ratios are 1.0 and 0.28% respectively, which is a decrease of around 70%. Taking either of these results, a highly significant reduction in the intensity of the overtone is due solely to electrical anharmonicity.

It is of interest to determine how the ratio varies as the electrical anharmonicity is 'turned on' by instead of writing the ratio as in Eq. 2.42, writing

$$I(\lambda) = \left(\frac{\int \Psi_2(x)(x + \lambda p'(x))\Psi_0(x)dx}{\int \Psi_1(x)(x + \lambda p'(x))\Psi_0(x)dx} \right)^2. \tag{6.1}$$

Here, $p'(x)$ is the purely anharmonic part of the dipole operator, which can be included incrementally by varying λ from zero to one. The results of performing

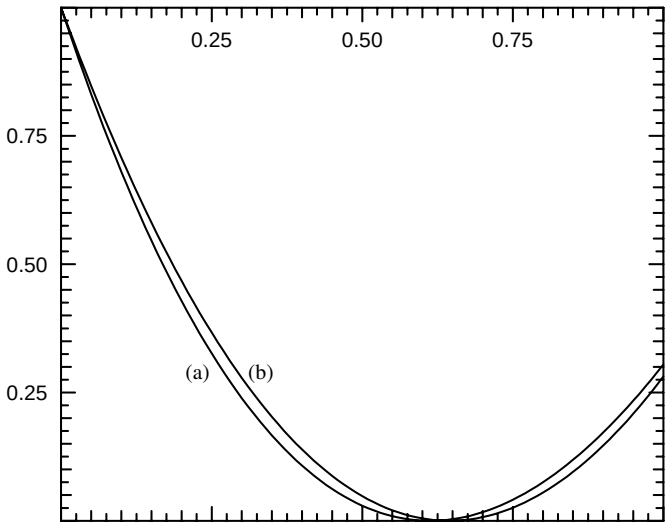

Figure 6.7: The intensity of the overtone versus the degree of electrical anharmonicity λ. The C-H length is 1.126 Å in curve (a) and 1.161 Å in curve (b).

this calculation are summarised in Fig. 6.7, which plots the intensity ratio as a proportion of the value where electrical anharmonicity is absent. It is interesting to note that for a certain value of λ the intensity ratio is predicted to be zero.

6.2.7 Conclusions

A number of general conclusions can be drawn from this work. They are:

- The bonding parameter, χ, in the effective oscillator mass (Eq. 2.39) need not be greater than unity to be physical.
- The local density functional approach adopted here can give quantitative information on the anharmonicity of vibrations.
- Low order perturbation theory cannot be used to describe anharmonic vibrations.
- The intensity of the overtone can be significantly reduced by electrical anharmonic effects. In the case of C_{As}-H in GaAs this may be more than a 70% reduction.

Specifically concerning the C_{As}-H in GaAs, it is concluded that the high frequency stretch mode (observed experimentally at 2635 cm^{-1}) is very anharmonic, some 50% more so than the similar mode in the HCN molecule, and much greater than the vibration of H on the $\langle 111 \rangle$ surface of diamond where A=113 cm^{-1} [53].

The reduction in the intensity ratio due to the electrical anharmonicity makes it tempting to assign the lack of observation of the overtone to a combination

of mechanical and electrically anharmonic effects. However, one should bear in mind that the reorientation barrier for the H to an adjacent bond-centre is only 0.5 eV (Ref. [67]), and the frequency of the overtone is calculated to lie at around 5114 cm^{-1}, which corresponds to an energy of more than 0.6 eV. Thus the lifetime of the overtone may be too short to allow it to be observed.

6.3 Theory of hydrogenated C_{As}-dimers.

Recent papers [205, 208] have reported bands of localised vibrational modes (LVMs) at 2643, 2651, and 2688 cm^{-1}, all of which have been assigned to C-H stretch modes. It is speculated that the lower two bands are due to $C_{As}H$ pairs perturbed by the proximity of another defect, such as a vacancy, an anti-site, or a nearby C-centre. Interestingly, the 2651 and 2688 cm^{-1} bands are strongly polarised along one of the $\langle 110 \rangle$ directions perpendicular to the [001] growth direction [216, 217, 218]. This means that the $C_{As}-H$ unit is preferentially oriented along a *specific* $\langle 110 \rangle$ direction. The [110] and $[\bar{1}10]$ directions are crystallographically equivalent in the zinc-blende structure, but this is not true at the surface [219]. Using a simple model, Cheng *et al.* [216] were able to account the intensities of the 2688 cm^{-1} band in terms of the expected concentration of a $(C_{As}\text{-}H)\text{-}C_{As}^{-}$ complex. Hence, the model for the 2688 cm^{-1} band is a pair of substitutional C atoms at neighbouring As sites, with a single H passivating one of the C acceptors, as indicated schematically in Fig. 6.8. A series of experiments by Cheng *et al.* [216] suggest that $(C_{As})_2H$ dissociates at around 600°C, releasing first a H atom, followed by the dissociation of the C-pairs. The complex starts to reform by annealing in a H_2 ambient at 500°C, but would not be oriented along any particular (110) axis. This suggests that C_{As}-H defects are sufficiently mobile at 500°C to bond with C-acceptors.

When samples containing the 2688 cm^{-1} band are exposed to a hydrogen plasma at 320°C, the intensity of the band decreases essentially to zero, and two new bands at 2725 and 2775 cm^{-1} bands appear [217]. A subsequent anneal at 450°C removes the 2725 and 2775 cm^{-1} bands and the polarised 2688 cm^{-1} band reappears. Hence, it was thought that these new bands may be due to a $(C_{As})_2H_2$ complex which partially dissociates by releasing a single H at 450°C whilst the C atoms are undisturbed. The 2725 and 2775 cm^{-1} bands do not exhibit the strong polarisation seen in the 2688 cm^{-1} band. Further work, however, has suggested that the 2725 and 2775 cm^{-1} bands do not arise from the same centre [220].

A recent study [221] reported another band at 2729 cm^{-1} that *is* polarised. This band is observed in samples where the 2688 cm^{-1} band is present, but is polarised in the orthogonal $\langle 110 \rangle$ direction. It may be that this 2729 cm^{-1} band comes

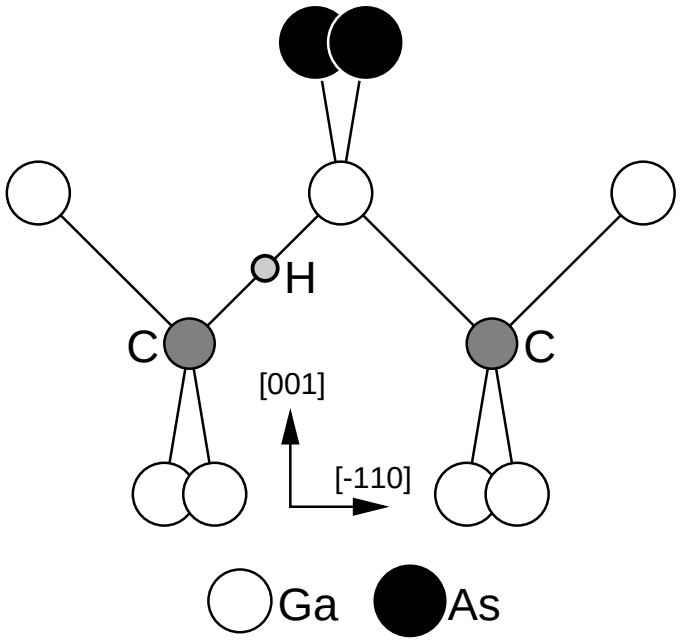

Figure 6.8: Schematic diagram of the C_2H defect thought to be responsible for the 2688 cm^{-1} band as suggested in Ref.[216].

from a different, metastable $(C_{As})_2H$ defect in which the C_{As}-H bond direction is orthogonal to that in the 2688 cm^{-1} centre. If this were the case, one would expect the 2729 cm^{-1} band to decay under annealing together with a corresponding growth in the 2688 cm^{-1} band.

Previous studies [45, 209] have modelled the C_{Ga} and the C_{As}-C_{Ga} dimer. Recently, first principles calculations [222] have shown that the model proposed in Ref. [216] is the lowest energy configuration of the $(C_{As})_2$-H complex, and reported the structures of $(C_{As})_2$-H_2 complexes, but did not report the local vibrational modes of these systems. Other models for C-dimers in GaAs have been examined in literature [223, 224], but these complexes offer no obvious way to explain the polarisation.

There are three possible configurations for $(C_{As})_2H$ in which H occupies a bond-centre located next to C, as indicated in Fig. 6.9. Similarly there are seven possible configurations of $(C_{As})_2H_2$, assuming that one H bonds to each C, as indicated in Fig. 6.10. It is the aim of this paper to establish which sites are most stable, and to investigate theoretically the assignment made for the 2688 cm^{-1}, and comment on the 2729, 2725, and 2775 cm^{-1} vibrational systems.

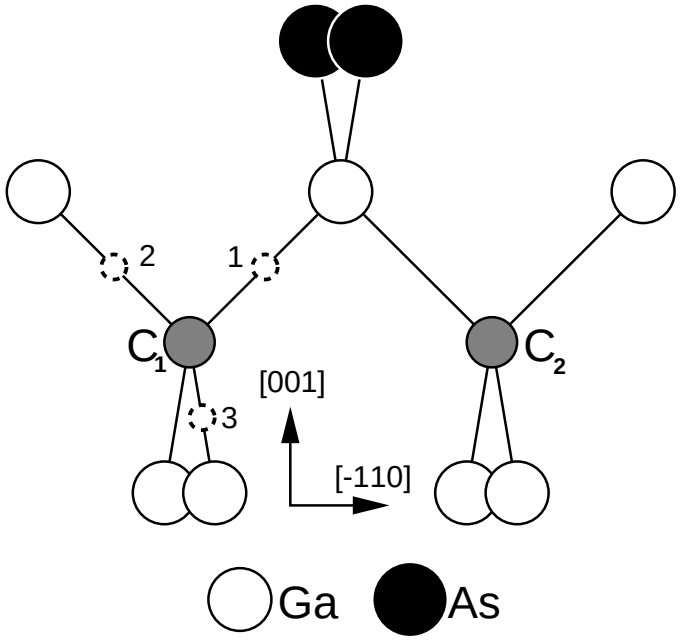

Figure 6.9: Schematic diagram of the three configurations of the C_2H defect. 1, 2, and 3 label bond centred sites in which the H atoms have been sited in this study.

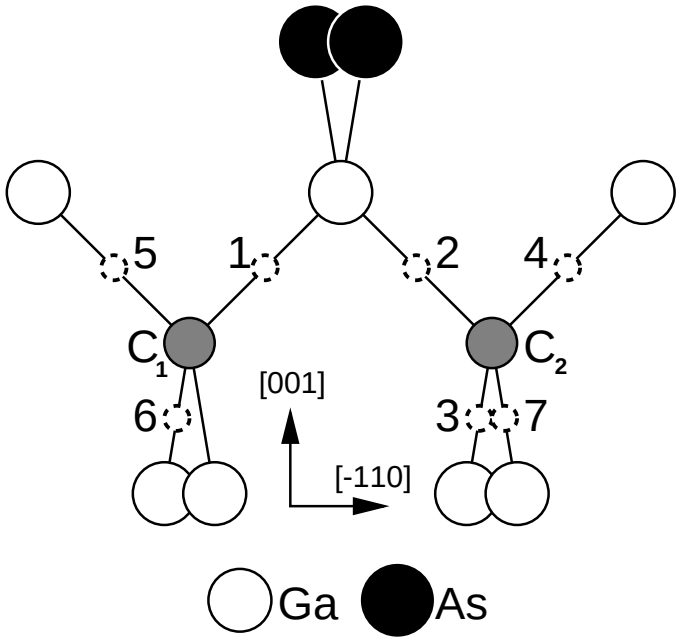

Figure 6.10: Schematic diagram of seven configurations of the C_2H_2 defects examined in this paper. The H sites are labelled using the numbers 1-7, and they can be paired into seven unique defect configurations as follows: (1,2), (1,3), (1,4), (3,5), (3,6), (4,5), and (6,7).

Atom	Wavefunction	Charge density
Ga	$4 \times sp$	5
As	$4 \times sp$	5
C	$4 \times sp$	4
H	$2 \times sp$	3
Bond-centres	$1 \times sp$	1

Table 6.11: The atomic basis used for the calculations in Sec. 6.3.

6.3.1 Clusters and basis.

In this study, the clusters are centred on a central Ga site surrounded by alternate shells of As and Ga atoms. Most calculations are based on the defect free cluster which contains 131 atoms: $Ga_{31}As_{40}H_{60}$. To model the defects, one or two of the nearest neighbours to the central Ga are replaced by C, and zero, one, or two H are placed in the appropriate C-Ga bond centres. The clusters are charged to take account of the difference in the number of Ga and As atoms. In a number of cases, a larger, 163-atom cluster ($Ga_{43}As_{44}H_{76}$) has also been optimised for comparison.

The number of basis functions for Ga, As, C and H are listed in Table 6.11. The central three shells of atoms are treated in big basis (as defined in Sec. 2.18), including the central defect atoms. The remaining atoms are in minimal basis, and a single set of functions was placed between neighbouring atoms. Recalling the differences between the results with the different bases in the early calculations of C_{As}-H, one might consider that this basis is rather small. However, since the clusters themselves are somewhat larger, the overall cluster basis is reasonable.

6.3.2 Results.

The carbon-dimer is made up of two C_{As} centres separated by a single Ga site. Since isolated C_{As} is a single acceptor, the dimer is expected to be a double acceptor and the results presented here are for the double negative charge state. Starting with the two C ionised atoms at neighbouring ideal As lattice sites, all but the surface H atoms in the 131-atom cluster were relaxed subject to a C_{2v} symmetry constraint. In the final structure, the C-atoms have moved apart due to the strong Coulomb repulsion. The final bond-lengths are summarised in Table 6.12. The total energy of the $(C^-_{As})_2$ system as described above, is around 1.2 eV higher in energy than a configuration where the two C atoms are separated by two Ga sites, i.e. the (C-Ga-C)$^{--}$ structure is metastable. This is consistent with the observations (Ref. [216]) that once H is lost from the defect, it rapidly dissociates.

Defect	# atoms	C_1-Ga	C_1-H	C_2-Ga	C_2-H	C_1-Ga_{back}	C_2-Ga_{back}
$(C_{As})_2$	131	2.18	-	2.18	-	2.02, 2.02, 2.07	2.02, 2.02, 2.07
(C_{As})-H	132	3.32	1.124	-	-	2.03, 2.03, 2.03	-
	164	3.27	1.125	-	-	1.96, 1.96, 1.96	-
$(C_{As})_2$-H	132	3.40	1.128	1.94	-	2.01, 2.03, 2.03	2.07, 2.08, 2.08
	164	3.36	1.128	1.88	-	1.95, 1.96, 1.96	1.99, 2.00, 2.03
$(C_{As})_2$-H_2	133	3.44	1.127	1.94	1.120	2.01, 2.02, 2.04	2.02, 2.02, 3.52
	165	3.41	1.129	1.89	1.132	1.94, 1.96, 1.97	1.97, 1.97, 3.35

Table 6.12: The bond lengths of the relaxed $(C_{As})_2$, $(C_{As})-H$, $(C_{As})_2-H$ and $(C_{As})_2-H_2$. The C_1-Ga and C_2-Ga lengths are to the common Ga neighbour. The 'back' bonds refer to the three remaining C-Ga separations shown in Figs. 6.9 and 6.10. All lengths are in Å.

6.3.2.1 The $(C_{As})_2$-H complex.

Fig. 6.9 shows schematically the three sites that the H can adopt if one assumes that the H atom lies at a C-Ga bond-centre. In each case, all but the surface atoms in the 132 atom cluster were relaxed, and we have assumed that the centre would be a single acceptor. From our calculations, the lowest energy configuration is that suggested by Cheng *et al.* with the H in the bond-centre site 1 in Fig. 6.9. The configurations with the H atoms at sites 2 and 3 are 0.5 and 0.9 eV less stable respectively. The bond-lengths and LVMs of the lowest energy structure are listed in Tables 6.12 and 6.13 respectively. The calculated C-H stretch mode is 2826 cm^{-1}, 5% greater than the experimental value of 2688 cm^{-1}, which is within the error bounds of the method. The lower lying modes are characterised by C-H wag and C-related modes.

Defect masses	132 atoms	164 atoms
$^{12}C_1$-H-Ga-$^{12}C_2$	2826	2830
$^{12}C_1$-D-Ga-$^{12}C_2$	2070	2072
$^{13}C_1$-H-Ga-$^{12}C_2$	2818	2822
$^{13}C_1$-D-Ga-$^{12}C_2$	2059	2061

Table 6.13: The C-H stretch modes of the lowest energy C_1-H-Ga-C_2 system (cm^{-1}) for the various combinations of carbon and hydrogen isotopes in the 132 and 164 atom clusters. Note, the C_1-H stretch mode is unaffected by a change in mass of C_2.

It is pertinent to compare these results with the structure and modes of the $C_{As}H$ centre. The final C_{As}-H bond length was 1.12 Å, which is very slightly ($\sim 0.3\%$) shorter than that of C_2H. Generally, the shorter the C-H bond-length, the higher one would expect the LVM to be, however, the calculated C-H stretch mode of the $C_{As}H$ centre was also 2826 cm^{-1}. Thus, the experimentally observed 53 cm^{-1} splitting between the 2635 and 2688 cm^{-1} bands is not reproduced in these calculations. Previous studies have shown that anharmonic terms are important for C-H stretch

modes in GaAs [40]. In general, the anharmonic corrections for the two defects would be different, and this might account for the discrepancy. Perhaps more fundamentally, however, LVMs are extremely sensitive to the C-H length: roughly, a 3% change in bond length gives rise to a 10% change in the LVM. Applying this to the C_2H complex, a decrease in bond length of around 0.01 Å would increase the stretch mode to lie 50 cm^{-1} above that of $C_{As}H$. To test this hypothesis, the C-H bond in the $(C_{As})_2H$ system was shortened to 1.12 au (a decrease of 1%), and the LVMs re-evaluated. The stretch mode increased to 2913 cm^{-1} (an increase of 3%). The total energy of the system increased by around 2 meV. Thus, the calculated frequencies are consistent with experiment to within the limitations of the method.

Now, for the stretch mode to be polarised along [110], it is sufficient to show that the displacement of the H atom is also along [110]. Our calculation shows this to be the case, and we list the projection of the normal co-ordinates onto the [110], $[\bar{1}10]$ and [001] directions in Table 6.14. In fact, this is also the case with the H

	[110]	$[1\bar{1}0]$	[001]
C_1	0.00	0.21	-0.17
C_2	0.00	0.00	0.00
H	0.00	-0.75	0.61

Table 6.14: The projection onto the [110], $[1\bar{1}0]$, and [001] directions of the C-H stretch mode of the C_{1h} symmetry $(C_{As})_2H$ complex, calculated in the 132 atom cluster (cm^{-1}). The C atoms are labelled 1 and 2 according to Fig. 6.9. The mode is symmetric about the C_{1h} mirror plane.

atom in either of the other bond-centred sites. The only requirement for the C-H stretch mode to be polarised is that the C-dimers must be preferentially aligned in one $\langle 110 \rangle$ direction.

The stability of the defect can be seen from the following argument. When H is at site 1 (Fig. 6.9), the Ga neighbour with the broken bond relaxes away from the C-H unit and becomes close to C_2, relieving the local strain. Now, a larger C-(H)-Ga separation tends to lead to a shorter C-H bond due to a reduction in the covalent bonding with the Ga atom. If H is at site 3, the Ga neighbour does not relax to the same extent since there is no local strain there. This leads to a relatively long C-H bond and hence a lower vibrational frequency. The C-H stretch mode for the high energy C_2H configuration with H at site 3 is calculated to lie at 2774 cm^{-1}. Consistent with the above argument, this is somewhat lower than that of the lowest energy structure (site 1). Consequently, this metastable defect *cannot* account for the experimentally observed 2729 cm^{-1} band polarised orthogonally to the 2688 cm^{-1} band.

	Model	(1,2)	(1,3)	(1,4)	(3,5)	(3,6)	(4,5)	(6,7)
	Stretch modes	2640	2895	2819	2791	2749	2806	2783
		2586	2836	2779	2770	2747	2803	2779
E_{tot}	133 atoms	0.95	0.00	0.26	0.22	0.75	0.03	0.64
	165 atoms	-	0.00	-	-	-	0.16	-

Table 6.15: The C-H stretch modes for the 133 atom clusters (cm^{-1}) and total energies for the 133 and 165 atom clusters, E_{tot} (eV), relative to the (1,3) pairing for the seven configurations of the $(C_{As})_2H_2$ complex. The models are labelled according to pairing of hydrogen atoms as described in Fig. 6.10.

Isotopes	133 atoms	165 atoms
$^{12}C_1$-H-Ga-$^{12}C_2$-H	2836, 2895	2827, 2788
$^{13}C_1$-H-Ga-$^{12}C_2$-H	2829, 2895	2819, 2788
$^{12}C_1$-D-Ga-$^{12}C_2$-H	2077, 2895	2069, 2788
$^{13}C_1$-D-Ga-$^{12}C_2$-H	2066, 2895	2058, 2788
$^{12}C_1$-H-Ga-$^{13}C_2$-H	2836, 2887	2826, 2780
$^{12}C_1$-H-Ga-$^{12}C_2$-D	2836, 2121	2826, 2039
$^{12}C_1$-H-Ga-$^{13}C_2$-D	2836, 2109	2826, 2029

Table 6.16: The C-H stretch modes of the lowest energy $(C_{As})_2H_2$ model (1,3) (Fig. 6.10) in the 133 and 165 atom clusters (cm^{-1}). Since the two C-H units are practically decoupled, only a subset of the permutations of isotopes is required. The modes are not shifted significantly by the Ga mass.

6.3.2.2 The $(C_{As})_2$-H_2 complex.

There are a number of possible configurations of the defect. If one assumes that both of the H atoms are approximately C-Ga bond centred, and only one H atom is bonded to each of the C atoms, then there are seven possible combinations of sites. The possible H locations are shown schematically in Fig. 6.10, labelled 1-7, and the seven combinations are denoted by the sites of the pairs of H atoms: (1,2), (1,3), (1,4), (3,5), (3,6), (4,5), and (6,7). All of these defects are fully passivated, and the band-gap is free from defect levels.

The lowest energy system is (1,3), and the total energy of each model quoted in Table 6.15 relative to this. The two C-H and stretch modes are also listed in for each configuration. Note, the (1,3) pairing is only marginally more stable than that of (4,5). This result may be sensitive to cluster size, and we investigate below the results in larger clusters.

The various bond lengths of the (1,3) model are listed in Table 6.12, and the values of the stretch modes for the H and C isotopes are listed in Table 6.16. It can be clearly seen the two H atoms are practically decoupled. As with $(C_{As})_2H$, the normal modes of the $(C_{As})_2H_2$ are polarised in the [110] and [1$\bar{1}$0] directions,

	133 atoms				165 atoms			
	Mode	[110]	[1$\bar{1}$0]	[001]	Mode	[110]	[1$\bar{1}$0]	[001]
C_1	2895	0.00	0.01	-0.01	2827	0.00	-0.21	0.16
H_1		0.00	-0.03	0.02		0.01	0.76	-0.58
C_2		0.23	0.01	0.14		-0.02	0.00	-0.01
H_2		-0.81	-0.04	-0.51		0.08	-0.01	0.04
C_1	2836	-0.01	-0.21	0.16	2788	0.00	-0.02	0.02
H_1		0.02	0.76	-0.59		0.00	0.07	-0.05
C_2		0.01	0.00	0.01		0.23	-0.03	0.12
H_2		-0.03	0.00	-0.02		-0.84	0.12	-0.45

Table 6.17: The projection onto the [110], [1$\bar{1}$0], and [001] directions of the normal stretch modes of the C_1 symmetry $(C_{As})_2H_2$ complex (cm^{-1}). The C atoms are labelled 1 and 2 according to Fig. 6.10.

and consequentially the IR absorption of the system should be strongly polarised. In fact, all of the seven models examined for this centre would also be strongly polarised, and it is unlikely that there is a configuration that would not be polarised since in each case the C-H bond directions are largely in the [110] and [1$\bar{1}$0] directions. The normal coordinates of each of the stretch modes projected onto the [110], [1$\bar{1}$0], and [001] directions are listed in Table 6.17. These show that the deviation from [110] and [1$\bar{1}$0] polarisation of the vibrations due to the relaxation of the atoms is to small to account for the lack of polarisation observed in the 2725 and 2775 cm^{-1} bands. Therefore, since the experimental bands are not polarised, they cannot be attributed to the $(C_{As})_2H_2$ complex.

As stated above, the calculated values of the LVMs are extremely sensitive to bond lengths, which are in turn affected by the proximity of the centre to the cluster surface. To explore the effect of cluster size in the case of the lowest energy configuration we have also calculated the relaxed structure and LVMs for the (1,3) and (4,5) systems for the $(C_{As})_2H_2$ complex in the 165 cluster. Then the (1,3) system is again more stable than the (4,5) pairing by 0.16 eV. The final (1,3) pair structure possessed C-H bond lengths of 1.129 and 1.132 Å, and stretch modes lying at 2827 cm^{-1} and 2787 cm^{-1} for the stretches involving the hydrogen atoms at sites 1 and 3 respectively in Fig. 6.10. However, in contrast with the calculation performed on the smaller cluster, the lower frequency mode now arises from the H atom at site 3. The calculated splitting of the two stretch modes is 40 cm^{-1}. A summary of the bond lengths and local modes are listed in Tables 6.12 and 6.16 respectively.

As with the smaller cluster, the modes are polarised in the [110] and [1$\bar{1}$0] directions (Table 6.17). For comparison, we have also calculated the structures and LVMs of the $C_{As}H$ and $(C_{As})_2H$ systems in 164 atom clusters, and they possess

stretch modes of 2820 and 2830 cm^{-1} respectively. The bond lengths are listed in Table 6.12.

As indicated above, the $(C_{As})_2H_2$ complex has two stretch modes polarised in orthogonal directions. It may be that the 2729 cm^{-1} band, which cannot be assigned to $(C_{As})_2H$, is due to one of these modes. However, this leaves a second band (higher in frequency) undetected, which should be polarised in the same direction as the 2688 cm^{-1} band.

6.3.3 Conclusions.

The lowest energy structure of $(C_{As})_2H$ is planar in agreement with the model put forward by Cheng *et al.* [216] shown in Fig. 6.8 and also with recent calculations. [222] The $(C_{As})_2H_2$ complex is not planar and the H atoms lie in the bond centred sites marked 1 and 3 in Fig. 6.10. This is also in agreement with recent calculations [222]. The LVMs calculated for these systems broadly agree with the assignments of the $(C_{As})_2H$ complex to the 2688 cm^{-1}. It is possible that the 2729 cm^{-1} band observed by Stavola *et al.* arises from the [110] polarised mode of this system, but no second mode was detected. These calculations do not support the hypothesis that a metastable $(C_{As})_2H$ configuration is responsible for the 2729 cm^{-1} band.

Chapter 7

Conclusions

A conclusion is the place where you got tired of thinking.

- Arthur Block

Although detailed conclusions have been presented at the appropriate places in Chapters 4 to 6, it is worth making a few more general conclusions about the way in which AIMPRO has been used to examine the various defects. Suggestions are made for where areas presented here might be extended.

The detailed study of a number of vacancy-impurity complexes in diamond has revealed that the techniques used here are able to describe semi-quantitatively transition energies and radiative lifetimes. More significantly, in all the situations explored, the symmetries of the ground and excited states have been found to agree with experiment. In the case of the complex of Si with a vacancy, the code was able to predict the unusual structure. Without such a structure it is difficult to imagine how such a centre could give rise to the experimental observations.

The attempts thus far in producing n-type diamond by doping with phosphorus have been mainly unsuccessful. The calculations on the phosphorus-vacancy complex may go some way to explaining why this is. There have been suggestions that alternative ways of generating shallow levels might be analogous to the so called 'shallow thermal donors' seen in silicon. These are thought to be formed when deep donor centres are forced up in energy by the proximity of neighbouring oxygen atoms [225]. Calculations are under way to see how similar complexes in diamond behave.

Ni in diamond has been of interest for more than a decade as catalytic synthesis has become more important. The work presented here has two main implications: first, Ni and Ni-X complexes possess a large number of optical transition mechanisms but in each case there is expected to be a single rate dominant transition. Secondly, the previous assignments of interstitial Ni to optically and electrically active centres

is found wanting. We find that there is no requirement for Ni_i and the previous assignments involving this centre may be incorrect.

There are a large number of further Ni and Co related complexes that require study, most importantly the apparent aggregation of N at these impurities under annealing. This work has been started. Another centre that is thought to be crucial to the understanding of at least Ni in diamond is the Ni-vacancy complex, which is thought to be the core at the centre of the class of EPR centres labelled NE1-7. A number of attempts have been made using AIMPRO to establish the ground state structure and electronic properties. However, to date there have been significant difficulties in establishing self-consistency. This is, at least in part due to the rather large number of fitting functions required to model the charge density, which in turn leads, in this case, to instability in the calculation.

There remain a number of other problems of great interest that are difficult to treat using the approach adopted for this thesis. Of these, the most significant might be why Ni related centres are exclusively found in the octahedral growth sectors. In fact, this is true of other centres, including Co. This polarisation is thought to arise during growth, but simulating this has proved difficult, since it requires the calculation of the relative stabilities of impurity atoms on different surfaces. Another question is why only Ni and Co are found as dispersed impurities, despite the fact that the whole range of first row transition metals are used in diamond synthesis.

Finally, it is worth noting that a number of Ni-related centres exhibit structure due to spin-orbit interaction; in principle, this effect can be treated using AIMPRO, since the Bachelet, Hamann, and Schlüter [11] pseudopotential contain spin-orbit parameters. Naturally, including spin-orbit effects would cost significant extra computing time.

Often, subtle effects (such as Jahn-Teller distortions) are seen experimentally, and it is desirable to be able to resolve these computationally. Two examples contained in this thesis are as follows. For Ni_s^- in Si, it has been shown that the ground state ordering of one-electron levels can be established for the Jahn-Teller distorted system. This is achieved by adopting a sophisticated algorithm that dictates which Kohn-Sham eigenvalues are occupied throughout the self-consistent cycle, and thus avoids discontinuous changes in charge density (so called charge sloshing). In fact a similar approach must be adopted to determine the energies of multiplets as in the $[V\text{-}N]^-$ complex in diamond.

In contrast to these successes, the sensitivity of the vibrational modes of C_{As}-H centres in GaAs to the C-H bond-lengths has proved difficult to resolve. This

regrettably leads to a degree of empiricism to justify certain interpretation[1]. However, since this arises from the density functional theory at the very root of the calculations, there is no obvious route to a better method.

However, when combined with total energies, vibrational modes can be a highly discriminative tool. As an illustration, one can turn to Ni-H_2 in Si. Here, the location of H with respect to the Ni atom, that is whether the H is bond-centred or anti-bonded, is hard to discriminate purely on the grounds of total energies. In fact most arrangements are of a similar energy, but the crucial difference is in the vibrational modes. This will most likely prove to be important in the case of gold-hydrogen complexes which are also under investigation.

As highlighted above, a number of difficulties can be traced to either the fact that the calculations are performed in clusters or there is a problem with the intermediate fit to the charge density. To a large extent, these are solved in a new incarnation of AIMPRO, where the calculations are performed using super-cells, and hence the intermediate fit to the charge density is no longer required. This eliminates the near instability in some situations involving atoms whose basis includes *d*-orbitals, such as Ni-V. Furthermore, calculations of more ionic III-V compounds (such as GaN) as well as the interesting II-VI compounds will also become possible, since the super-cell would not suffer from problem of charge building up at surfaces in the case of clusters.

Whether it is the cluster or super-cell approach, the *parallelisation* of AIMPRO has lead to two important improvements. First, a 71-atom cluster made up from atoms with *s*- and *p*-orbitals can be relaxed very quickly, and single energies calculated in minutes rather than hours. Secondly, very large clusters can be used, without which the study of extended defects (such as the $(C_{As})_2$-H_2 centres in GaAs) would be difficult. Furthermore, a new area of interest being developed in the AIMPRO group is that of proteins and related biological molecules. Even the smallest of these systems contain several hundreds of atoms, and without massively parallel computer platforms, relaxation would be prohibitively slow.

However, there is a severe problem in obtaining relaxed structures for such highly complex molecules, and this is the number of local energy minima. In fact, one can break down a molecule such as a peptide into smaller units - in this case amino acids. Each of these groups will have a number of local minima. Therefore, it is likely that a new strategy will be adopted for the minimisation of the energy, perhaps by calculating the forces using some form of parameterisation of the force constants, hydrogen bonding and so on.

[1]This refers to the 10% change in vibrational frequency for a 3% change in bond-length.

In conclusion, theory can be viewed from two points: first, it can be an aid to experiment, where it is used to explain observation. The second is perhaps more significant, in that theory can be used as a predictive tool, guiding further experiments. For example, the predictions that [Si-V] and $[\text{Si-V}]^-$ would be paramagnetic, and current experiments are underway to test this hypothesis.

Appendix A

Character tables

Tabulated here are character tables for the 3 point groups most often discussed in this thesis: in the Schoenflies (international) notation, C_{2v} ($2mm$), C_{3v} ($3m$) and T_d ($\bar{4}3m$). (For a detailed explanation of their derivation and use, see for example Ref. [226], from which these tables are taken.) Each table also shows some combinations of the coordinates (x, y, z) that transform according to each irreducible representation (IR).

Each IR is denoted by A or B if it is one dimensional, and E or T if it is 2- or 3-dimensional, respectively. The dimensionality is linked to the degeneracies of one-electron Kohn-Sham levels (except for the case of accidental degeneracy), which are usually labelled in lower case. Thus, for example, a Kohn-Sham level that transforms as t_2 in the T_d point group is three-fold degenerate (as well as spin degenerate). Such a level can therefore be occupied by up to 6 electrons.

The symmetry operations are as follows: e is the identity operation; C_n is a rotation through $2\pi/n$; σ_v is a reflection in a vertical plane (passing through the symmetry axis); σ_d is a reflection in a diagonal plane; and S_n is an improper rotation of $2\pi/n$. In the case of C_{2v} there are two inequivalent σ_v operations, one of which is identified by a prime.

C_{2v}	e	C_2	σ_v	σ_v'	
A_1	1	1	1	1	$x^2; y^2; z^2; z$
A_2	1	1	-1	-1	xy
B_1	1	-1	1	-1	$xz; x$
B_2	1	-1	-1	1	$yz; y$

C_{3v}	e	$2C_3$	$3\sigma_v$	
A_1	1	1	1	$x^2 + y^2; z^2; z$
A_2	1	1	-1	
E	2	-1	0	$(x^2 - y^2, xy);$ $(x, y); (xz, yz)$

T_d	e	$8C_3$	$2C_2$	$6\sigma_d$	$6S_4$	
A_1	1	1	1	1	1	
A_2	1	1	1	-1	-1	
E	2	-1	2	0	0	
T_1	3	0	-1	-1	1	
T_2	3	0	-1	1	-1	(x, y, z)

Appendix B

Jahn-Teller distortions

The Jahn-Teller theorem applied to the (ground-state) one-electron picture of the Kohn-Sham levels can be understood as follows (in the absence of spin-orbit interaction).[1] If the highest occupied one-electron level is degenerate and partially occupied, then the system may distort to a lower symmetry such that the degeneracy is lifted. This will lower the total energy provided the reduction in the energy of the occupied orbital(s) is greater than any increase in energy due to the distortion. This follows from the fact that the total energy is related to the sum of the one-electron energies.

Take as an example, a t_2 level in tetrahedral symmetry containing two electron. This is the case for the neutral vacancy in silicon. A trigonal distortion will split the t_2 level into an singlet (a_1) and a doublet (e). This is illustrated in Fig. B.1(a)→(b). The addition of a further electron makes the e-level unstable, and a further Jahn-Teller distortion (say C_{2v}) will split this doublet into two singlets – b_1 and b_2 – as shown in Fig. B.1(b)→(c).

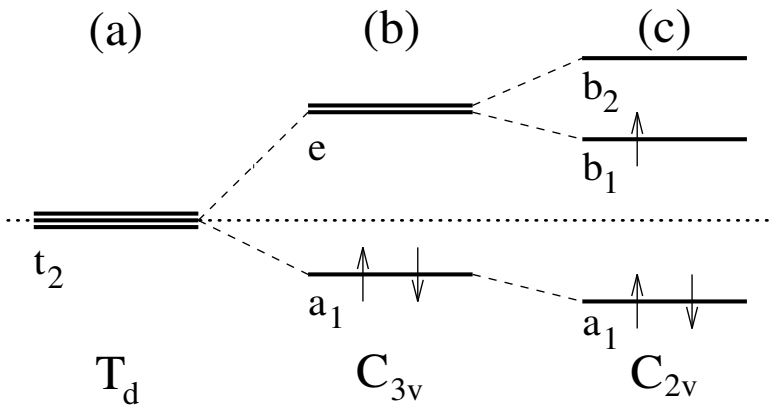

Figure B.1: A diagram showing the splittings of a t_2-level with C_{3v} and C_{2v} distortions to illustrate the Jahn-Teller effect.

[1] Only the *static* Jahn-Teller effect is discussed. For a more detailed explanation of the Jahn-Teller effect, see Ref. [104], and references therein.

If the trigonal distortion had resulted in the e-level *below* the a_1, this would also be unstable against a Jahn-Teller distortion, provided that Hund's rule is *not* obeyed, i.e. the electrons have opposite spins. If instead the electrons are aligned, i.e. a spin S=1 centre, then no Jahn-Teller distortion would be expected.

The above principles can naturally be applied to excited states. Thus, a excited state generated by promoting an electron from the a_1 to e level in Fig. B.1(b) would be a candidate for a further Jahn-Teller distortion.

Bibliography

[1] P. N. Keating, Phys. Rev. **145**, 637 (1966).

[2] J. Tersoff, Phys. Rev. B **56**, 632 (1986).

[3] A review of Hartee-Fock theory and its derivation can be found in 'Many-Body Theory of Solids' by J. C. Inkson, (Plenum Press, New York, 1984).

[4] P. Hohenberg, and W. Kohn, Phys. Rev. B **136** 864 (1964).

[5] W. Kohn, and L. J. Sham, Phys. Rev. A **140**, 1133 (1965).

[6] J. E. Northrup and S. Froyen, Phys. Rev. B **50**, 2015 (1994).

[7] G. P. Srivastava and S. J. Jenkins, Phys. Rev. B **53**, 12589 (1996).

[8] P. K. Sitch, PhD Thesis, 'Ab-initio calculations of dislocation related properties in semiconductors' 1994; P. Sitch, R. Jones, S. Öberg, and M. I. Heggie, Phys. Rev. B **50**, 17717 (1994); S. Öberg, P. K. Sitch, R. Jones, and M. I. Heggie, Phys. Rev. B **51**, 13138 (1995); P. Sitch, R. Jones, S. Öberg, and M. I. Heggie, Phys. Rev. B **52**, 4951 (1995).

[9] See for example: R. Jones. C. D. Latham, M. I. Heggie, V. J. B. Torres, S. Öberg, and S. K. Estreicher, Phil. Mag. Lett. **65**, 291 (1992); S. K. Estreicher, C. D. Latham, M. I. Heggie, R. Jones, and S. Öberg, Chem. Phys. Lett. **196**, 311 (1992).

[10] A. Resende, R. Jones, S. Öberg, P. R. Briddon, and B. R. Eggen, unpublished report (1996).

[11] G. B. Bachelet, D. R. Hamann, and M. Schlüter, Phys. Rev. B **26**, 4199 (1982).

[12] A. N. Safonov, E. C. Lightowlers, G. Davies, P. Leary, R. Jones, and S. Öberg, Phys. Rev. Lett. **77**, 4812 (1996).

[13] B. Bech Neilsen, L. Hoffmann, M. Budde, R. Jones, J. Goss, and S. Öberg, Mat. Sci. Forum **196-201**, Trans Tech Publications, Switzerland, p. 825-829 (1995).

[14] To appear in *Identification of Defects in Semiconductors*, ed. M. Stavola, *Semiconductors and Semimetals*, treatise editors, R. K. Willardson, A. C. Beer, and E. R. Weber, Academic Press.

[15] A. M. Stoneham, *Defects in Solids*, Oxford University Press, London (1975).

[16] J. C. Slater, *Quantum Theory of Atomic Structure*, Vol. 2, McGraw Hill, New York (1960).

[17] See for example J. A. Pople, and D. L. Beverage, '*Approximate Molecular Orbital Theory*' McGraw-Hill, New York (1970).

[18] R. G. Parr, J. Chem. Phys. **20**, 239 (1952).

[19] J. A. Pople, D. P. Santry, and G. A. Segal, J. Chem. Phys. **43**, S129 (1965).

[20] M. Goeppert-Mayer, and A. L. Sklar, J. Chem. Phys. **6**, 645 (1938).

[21] J. A. Pople, D. L. Beverage, and P. A. Dobosh, J. Chem. Phys. **47**, 158 (1967)

[22] R. N. Dixon, Mol. Phys. **12**, 83 (1967).

[23] J. C. Slater, *Quantum Theory of Atomic Structure*, Vol. 1, McGraw Hill, New York (1960).

[24] L. Paslovsky, and J. E. Lowther, J. Phys. Chem. Solids **54**, 243 (1993).

[25] J. Isoya, H. Kanda, J. R. Norris, J. Tang, and M. K. Bowman, Phys. Rev. B **41**, 3905 (1990).

[26] D. M. Ceperley, and B. J. Alder, Phys. Rev. Lett. **45**, 566 (1980).

[27] J. P. Perdew, and A. Zunger, Phys. Rev. B **23**, 5048 (1981).

[28] U. von Barth, and L. Hedin, J. Phys. C **5**, 1629 (1972).

[29] See for example J. P. Perdew, J. A. Chevary, S. H. Vosko, K. A. Jackson, M. R. Pederson, D. J. Singh, and C. Fiolhais, Phys. Rev. B **46**, 6671 (1992).

[30] L. Hedin Phys. Rev. **139**, A796 (1965).

[31] R. Delsole, L. Reining, R. W. Godby, Phys. Rev. B **49**, 8024 (1994).

[32] D. Vanderbilt, Phys. Rev. B **41**, 7892 (1990)

[33] S. G. Louie, S. Froyen, and M. L. Cohen, Phys. Rev. B **26**, 1738 (1982).

[34] X. J. Chen, J. M. Langlois, and W. A. Goddard, Phys. Rev. B **52**, 2348 (1995).

[35] B. I. Dunlap, W. J. Connolly, and J. R. Sabin, J. Chem. Phys. **71**, 4993 (1979).

[36] R. Jones, and A. Sayyash, J. Phys. C: Solid State Phys. **19**, L653 (1986).

[37] G. M. S. Lister, and R. Jones, unpublished (1988).

[38] H. Hellmann, *Einführung in die Quantenchemie* (Deuticke, Leipzig 1937); R. P. Feynman Phys. Rev. **56** 340 (1939).

[39] M. Born, and K. Huang, *Dynamical Theory of Crystal Lattices,* Oxford University Press, London (1954).

[40] R. Jones, J. Goss, C. P. Ewels, S. Öberg, Phys. Rev. B **50**, 8378 (1994).

[41] M. J. P. Musgrave, J. A. Pople, Proc. Roy. Soc. **A268**, 474 (1962).

[42] R. Jones, J. Phys. C: Solid St. Phys. **21**, 5735 (1988).

[43] R. Jones, J. Phys. C: Solid St. Phys. **20**, 271 (1987).

[44] F. Berg Rasmussen, R. Jones, and S. Öberg, Phys. Rev. B **50**, 4378 (1994).

[45] R. Jones, and S. Öberg, Phys. Rev. B **44**, 3673 (1991).

[46] R. Jones, and S. Öberg, Phys. Rev. B **49**, 5306 (1994).

[47] C. P. Ewels, S. Öberg, R. Jones, B. Pajot, and P. R. Briddon, Semicond. Sci. and Technol. **11**, 502 (1996).

[48] J. Purton, R. Jones, M. Heggie, S. Öberg, C. R. A. Catlow, Phys. Chem. Minerals **18**, 389 (1992).

[49] R. Jones, P. R. Briddon, and S. Öberg, Phil. Mag. Lett. **66**, 67 (1992).

[50] Y. J. Chabal, and C. K. N. Patel, Phys. Rev. Lett. **53**, 210 (1984).

[51] B. R. Davidson, R. C. Newman, T. J. Bullough, and T. B. Joyce, Phys. Rev. B **48**, 17106 (1993).

[52] R. C. Newman, Semicond. Sci. and Technol. **5**, 911 (1990).

[53] Xuejun Zhu, and S. G. Louie, Phys. Rev. B **45**, 3940 (1992).

[54] R. C. Newman, Physica B **170**, 409 (1991).

[55] P. M. Morse, Phys. Rev. **34**, 57 (1929).

[56] R. Darwich, B. Pajot, B. Rose, D. Robein, B. Theys, R. Rahbi, C. Porte, and F. Gendron, Phys. Rev. B **48**, 17776 (1993).

[57] R. S. Leigh, and B. Szigeti, Proc. Roy. Soc., A **301**, 211 (1967).

[58] B. Clerjaud, and D. Côte, J. Phys. Condens. Matter **4**, 9919 (1992).

[59] U. von Barth, Phys. Rev. A **20**, 1693 (1979).

[60] J. P. Goss, R. Jones, S. J. Breuer, P. R. Briddon, and S. Öberg, Phys. Rev. Lett. **77**, 3041 (1996).

[61] O. Svelto, *Principles of Lasers*, Plenum Press, New York (1976).

[62] A. J. Dekker, Solid State Physics (MacMillan, London) 1958.

[63] See for example A. S. Barker, A. J. Sievers, Rev. Mod. Phys. **47**, 51 (1975); R. C. Newman, 'Infrared studies of crystal defects' (Taylor and Francis, London) 1973; R. C. Newman, 'Localised vibrational mode spectroscopy' ed. R. A. Stradling, and P. C. Klipstein, Adam Hilger, Bristol and New York, 1990.

[64] Landolt-Börnstein New Series Group III Vol. **17** Semiconductors Sub Vol a: Physics of Group IV Elements and III-V Compounds (Springer-Verlag, Berlin-Heidelberg, 1982) and references therein

[65] G. A. Gledhill, S. S. Kudhail, R. C. Newman, J. Woodhead, G. Z. Zhang, J. de Physique, Colloq. C6, Suppl. No. 12, **42**, 685 (1981).

[66] J. B. Clegg, 'Depth profiling of semiconductor materials by secondary ion mass spectroscopy' in 'Growth and characterisation of semiconductors' ed. R. A. Stradling, and P. C. Klipstein, Adam Hilger, Bristol and New York, 1990.

[67] B. Clerjaud, D. Cote, F. Gendron, W-S. Hahn, M. Krause, and C. Porte, Materials Science Forum **83-7**, 563 (1991).

[68] G. D. Watkins, Proceedings of the NATO Advanced Research Workshop on 'Early Stages of Oxygen Precipitation in Silicon', ed. R. Jones, Kluwer Academic Press, pp. 1-18 (1996).

[69] P. S. Nandhra, R. C. Newman, R. Murray, B. Pajot, J. Chevalliear, R. B. Beall, and J. J. Harris, Semicond. Sci. and Tech. **3**, 356 (1988).

[70] J. Wagner, K. H. Bachem, B. R. Davidson, R. C. Newman, T. J. Bullough, and T. B Joyce, Phys. Rev. B **51**, 4150 (1995).

[71] W. Low, 'Paramagnetic resonance in solid state physics: advances in research and applications', ed. F. Seitz and D. Turnball, Academic Press, New York, 1960.

[72] G. D. Watkins, 'Point defects in solids', ed. J. H. Crawford (Jr.), and L. M. Slifkin, Vol. 2, Semiconductors and molecular crystals, Plenum, New York, 1975.

[73] X. Zhou, G. D. Watkins, K. M. McNamara Rutledge, R. P. Messmer, and Sanjay Chawla, Phys. Rev. B **54**, 7881 (1996).

[74] M. F. Thomaz, and G. Davies, Proc. Roy. Soc. London A **362**, 405 (1978).

[75] D. L. Dexter, 'Solid State Physics', Vol. 6, ed. F. Seitz and D. Turnball, Academic Press, New York, 1958.

[76] A. T. Collins, M. F. Thomaz, and M. I. B. Jorge, J. Phys. C: Solid State Phys. **16**, 2177 (1983).

[77] S. Lawson, private communication.

[78] M. Tajima, Appl. Phys. Lett. **32**, 719 (1978).

[79] P. McL. Colley, and E. C. Lightowlers, Semicond. Sci. and Technol. **2**, 157 (1987).

[80] E. C. Lightowlers, 'Photoluminescence Characterisation' in 'Growth and characterisation of semiconductors' ed. R. A. Stradling, and P. C. Klipstein, Adam Hilger, Bristol and New York, 1990.

[81] G. Davies, J. Phys. C: Solid State Phys. **12**, 2551 (1979).

[82] See for example D. V. Lang, J. Appl. Phys. **45**, 3023 (1974); G. L. Miller, D. V. Lang, and L. C. Kimerling, Ann. Rev. Mater. Sci. pp 377-448, 1977.

[83] See for example D. W. Palmer 'Characterisation by capacitance methods' in 'Growth and characterisation of semiconductors' ed. R. A. Stradling, and P. C. Klipstein, Adam Hilger, Bristol and New York, 1990.

[84] A. Matthews, and S. S. Eskildsen, Diamond and Rel. Mat. **3**, 902 (1994).

[85] S. Dannefaer, W. Zhu, T. Bretagnon, and D. Kerr, Phys. Rev. B **53**, 1979 (1996).

[86] G. Davies, S. C. Lawson, A. T. Collins, A. Mainwood, S. Sharp, Phys. Rev. B, **46**, 13157 (1992).

[87] C. A. Coulson, and M. Kearsley, Proc. Roy. Soc. London Ser. A **241**, 433 (1957).

[88] G. Davies, Nature **269**, 498 (1977).

[89] J. Isoya, H. Kanda, Y. Uchida, S. C. Lawson, S. Yamasaki, H. Itoh, and Y. Morita, Phys. Rev. B **45**, 1436 (1992).

[90] A. Mainwood, J. Phys. C **11**, 2703 (1978).

[91] J. E. Lowther, and J. A. van Wyk, Phys. Rev. B **49**, 11010 (1994).

[92] S. J. Breuer, PhD Thesis, 'A First Principles Study of Defects in Diamond', 1994.

[93] S. J. Breuer and P. R. Briddon, Phys. Rev. B **51** 6984 (1995).

[94] J. E. Lowther, Phys. Rev. B **48**, 11594 (1993).

[95] X.-F. He, N. B. Manson, and P. T. H. Fisk, Phys. Rev. B **47**, 8816 (1993).

[96] A. Mainwood, Phys. Rev. B **49**, 7934 (1994).

[97] G. Davies, and M. F. Hamer, Proc. Roy. Soc. London Ser. A **348**, 285 (1976).

[98] X.-F. He, N. B. Manson, and P. T. H. Fisk, Phys. Rev. B **47**, 8816 (1993).

[99] Y. Mita, Phys. Rev. B **53**, 11360 (1996).

[100] M. E. Newton, private communication (1996).

[101] G. Davies, M. H. Nazaré, and M. F. Hamer, Proc. Roy. Soc. London Ser. A **351**, 245 (1976)

[102] C. D. Clark, R. W. Ditchburn, and H. B. Dyer, Proc. Roy. Soc. London Ser. A **234**, 363 (1956).

[103] F. S. Ham, Phys. Rev. **166**, 307 (1968).

[104] M. Lannoo and J. Bourgoin, *Point defects in semiconductors*, Vols. I and II, Springer series in Solid-State Sciences **22** and **35**, Ed. M. Cardona, Springer-Verlag, New York 1981.

[105] P. A. Crowther and P. J. Dean, J. Phys. Chem. Solids **28**, 1115 (1967).

[106] G. Davies, in *The Properties of Diamond*, edited by J. E. Field (Academic Press, London, 1979), p. 165.

[107] J. van Wyk, J. Phys. C: Solid State Phys. **15**, L981 (1982).

[108] G. Davies, C. M. Welbourn, and J. H. N. Loubser, Diamond Research 1978, published by de Beers Industrial Diamond Division, Ascot, UK, pp. 23-30.

[109] A. M. Zaitsev, V. S. Vavilov, and A. A. Gippius, Sev. Phys. Leb. Inst. Rep. **10**, 15 (1981).

[110] J. Ruan, W. J. Choyka, and W. D. Partlow, Appl. Phys. Lett. **58**, 295 (1991).

[111] L. H. Robins, L. P. Cook, E. N. Frabaugh, and A. Feldman, Phys. Rev. B **39**, 3212 (1989).

[112] A. T. Collins, L. Allers, C. J. H. wort, and G. A. Scarsbrock, Diamond and Rel. Mat. **3** 932 (1994).

[113] C. D. Clark, H. Kanda, I. Kiflawi, and G. Sittas, Phys. Rev. B **51**, 16681 (1995).

[114] H. Sternschulte, K. Thonke, R. Sauer, P. C. Münzinger, and P. Michler, Phys. Rev. B **50**, 14554 (1994).

[115] K. Jackson, M. R. Pederson, and J. G. Harrison, Phys. Rev. B **41** 12641 (1990).

[116] S. A. Kajihara, A. Antonelli, J. Bernholc, and R. Carr, Phys. Rev. Lett. **66**, 2010 (1991).

[117] R. Jones, S. Öberg, Phil. Mag. Letters **64**, 317 (1991).

[118] M. E. Zvanut, W. E. Carlos, J. A. Freitas Jr., K. D. Jamison, and R. P. Hellmer, Appl. Phys. Lett. **65**, 2287 (1994).

[119] N. D. Samsonenko, V. V. Tokil, and S. V. Gorban, Sov. Phys. Sol. State **33**, 1409 (1991).

[120] S. N. Schauer, J. R. Flemish, R. Wittstruck, M. I. Landstrass, and M. A. Plano, Appl. Phys. Lett. **64**, 1094 (1994).

[121] G. Z. Cao, F. A. J. Driessen, G. J. Bauhuis, and L. J. Giling, J. Appl. Phys., **78** 3125 (1995).

[122] J. F. Prins, Diamond and related Materials **4**, 580 (1995).

[123] P. R. Briddon, and R. Jones, Phys. Rev. Lett. **64**, 2535 (1990).

[124] P. J. H. Denteneer, C. G. van der Walle, and S. T. Pantelides, Phys. Rev. B **41**, 3885 (1990).

[125] P. J. H. Denteneer, C. G. van der Walle, and S. T. Pantelides, Phys. Rev. Lett. **62**, 1884 (1989).

[126] S. J. Breuer, and P. R. Briddon, Phys. Rev. B **49**, 10332 (1994).

[127] J. P. F. Sellschop, Abstracts of the De Beers '*Diamond Conference*' pp. 45, 1987.

[128] T. A. Claxton, A. Evans, and M. C. R. Symonds, J. Chem. Soc. Faraday Trans. II **82**, 2031 (1986).

[129] T. L. Estle, S. Estreicher, and D. S. Marynick, Phys. Rev. Lett. **58**, 1547 (1987).

[130] P. Briddon, R. Jones, and G. M. S. Lister, J. Phys. C: Solid State Phys. **21**, L1027 (1988).

[131] S. H. Connell, private communication.

[132] S. H. Connell, E. Sideras-Haddad, C. G. Smallman, J. P. F. Sellschop, I. Z. Machi, and K. Bharuthram, Nuclear Instruments and Methods in Physics Research Section B – Beam Interactions with Materials and Atoms **118**, 332 (1996).

[133] S. H. Connell, J. P. F. Sellschop, I. Z. Machi, P. Schaff, R. D. Maclear, B. P. Doyle, and P. Formenti, proceedings of the De Beers Diamond Conference, pp. 42, 1996.

[134] J. P. Goss, R. Jones, and S. Öberg, unpublished report (1996).

[135] A. Mainwood, and A. M. Stoneham, J. Phys. C: Solid State Phys. **17**, 2513 (1984).

[136] J. D. Holbech, B. Bech Nielsen, R. Jones, P. Sitch, and S. Öberg, Phys. Rev. Lett. **71**, 875 (1993).

[137] M. Budde, B. Bech Neilsen, R. Jones, J. Goss, and S. Öberg, Phys. Rev. B **54**, 5485 (1996).

[138] A. Amore Bonapasta, Phys. Rev. B **51**, 4172 (1995).

[139] See for example G. Davies, A. T. Collins, and P. Spear, Solid State Comm. **49**, 433 (1984).

[140] R. P. Chin. J. Y. Huang, R. Y. Shen, T. J. Chuang, H. Seki, and M. Buck, Phys. Rev. B **45** 1522 (1992).

[141] K. Hayashi, H. Watanabe, S. Yamanaka, H. Okushi, and T. Sekiguchi, Appl. Phys. Lett. **69**, 1122 (1996).

[142] A. A. Gippius, V. S. Vavilov, A. M. Zaitsev, and B. S. Zhakupbekov, Physica **112B**, 187 (1983).

[143] H. Jai, J. Shinar, D. P. Lang, and M. Pruski, Phys. Rev. B **48**, 17595 (1993).

[144] S. L. Holder, L. G. Rowan, and J. J. Krebs, Appl. Phys. Lett. **64**, 1091 (1994).

[145] X. Zhou, G. D. Watkins, and K. M. McNamara Rutledge, Mat. Sci. Forum **196-201**, Trans Tech Publications, Switzerland, p. 825-829 (1995).

[146] H. Kanda, and T. Sekine, in *Properties and Growth of Diamond*, Data Rev. Ser. **9**, (INSPEC, London, 1994), p. 403.

[147] S. C. Lawson, H. Kanda, K. Watanabe, I. Kiflawi, T. Sato, and A. T. Collins, J. Appl. Phys. **79** 4348 (1996).

[148] H. Kanda, T. Ohsawa, and S. Yamaoka, '*Proceedings of the First International Conference on New Diamond Science and Technology*', pp. 339-344, edited by S. Saito, O. Fukunaga, and M. Yoshikawa, Terra Scientific Publishing, Tokyo, Japan, 1990.

[149] M. H. Nazaré, A. J. Neves, and G. Davies, Phys. Rev. B **43**, 14196 (1991).

[150] G. M. Ludwig, and H. H. Woodbury, in *Solid State Physics*, edited by F. Seitz and D. Trunbull, (Academic, New York, 1962), Vol. 13, p. 223.

[151] G. D. Watkins, Physica **117B & 118B**, 9 (1983).

[152] A. Zunger, and V. Lindefelt, Phys. Rev. B **27**, 1191 (1983).

[153] J. Isoya, H. Kanda, and Y. Uchida, Phys. Rev. B **42**, 9843 (1990).

[154] V. Nadolinny, and A. Yelisseyev, Diamond and Rel. Mat. **3**, 1196 (1994).

[155] A. Yelisseyev, and V. Nadolinny, Diamond and Rel. Mat. **4**, 177 (1995).

[156] A. T. Collins, and P. M. Spear, J. Phys. C: Solid State Phys. **16**, 963 (1983).

[157] G. Davies, A. J. Neves, and M. H. Nazaré, Europhys. Lett. **9**, 47 (1989).

[158] S. C. Lawson, H. Kanda, and M. Sekita, Phil. Mag. B **68**, 39 (1993).

[159] A. T. Collins, H. Kanda, and R. C. Burns, Phil. Mag. B **61**, 797 (1990).

[160] E. Pereira, L. Pereira, D. M. Hofmann, W. Stadler, and B. K. Meyer, Rad. Effects and Defects in Solids **133**, 641 (1995).

[161] M. H. Nazaré, L. M. Rino, and H. Kanda, Mat. Sci. Forum Vol. **196-201**, pp 73-78 (1995), Trans Tech Publications, Switzerland

[162] E. Pereira, L. Santos, L. Pereira, D. M. Hofmann, W. Stadler, and B. K. Meyer, Mat. Sci. Forum **143-147**, Trans Tech Publications, Switzerland, p. 57-62 (1994).

[163] S. C. Lawson, and H. Kanda, J. App. Phys. **73**, 3967 (1993).

[164] A. T. Collins, and P. M. Spear, J. Phy. D **15**, L183 (1982).

[165] L. Paslovsky, and J. E. Lowther, J. Phys.: Cond. Matter **4**, 775 (1992).

[166] Yang Jinlong, Zhang Manhong, and Wang Kelin, Phys. Rev. B **49**, 15525 (1994).

[167] C. A. J. Ammerlaan, Inst. Phys. Conf. Ser. No˙**59**, 81 (1981); C. A. J. Ammerlaan, and E. A. Burgemeister, Phys. Rev. Lett. **47**, 954 (1981).

[168] S. Breuer, and P. R. Briddon, Phys. Rev. B **53**, 7819 (1996).

[169] L. A. Hemstreet, Phys. Rev. B **15**, 834 (1977).

[170] J. L. A. Alves, and J. R. Leite, Phys. Rev. B **30**, 7284 (1984).

[171] M. Lannoo, Phys. Rev. B **36**, 9355 (1987).

[172] G. D. Watkins, in *Deep Centers in Semiconductors*, edited by S. T. Pantelides, (Gordon and Breach, New York, 1986), p 147.

[173] P. M. Williams, F. S. Ham, F. G. Anderson, and G. D. Watkins, Mater. Sci. Forum, **83-7**, 233 (1992).

[174] R. Jones, J. Goss, S. Öberg, P. R. Briddon, and A. Resende, Mat. Sci. Forum Vol. **196-201**, pp 921-926 (1995), Trans Tech Publications, Switzerland; R. Jones, S. Öberg, J. Goss, P. R. Briddon, and A. Resende, Phys. Rev. Lett **75**, 2734 (1995).

[175] R. M. Chrenko, Phys. Rev. B **7**, 4560 (1973).

[176] R. G. farrer, Solid State Comm. **7** 685 (1969).

[177] D. M. Hofmann, M. Ludwig, P. Christmann, D. Volm, B. K. Meyer, L. Pereira, L. Santos, and E. Pereira, Phys. Rev. B **50**, 17618 (1994).

[178] J. E. Lowther, Phys. Rev. B **51**, 91 (1995).

[179] L. Hedberg, T. Ijiama, and K. Hedberg, J. Chem. Phys. **70**, 3224 (1979).

[180] P. R. Briddon and R. Jones, Physica B **185**, 179 (1993).

[181] F. G. Anderson, R. F. Milligan, and G. D. Watkins, Phys. Rev. B **45**, 3279 (1992).

[182] H. Nakashima, T. Sadoh, H. Kitagwa, and K. Hashimoto, Mater. Sci. Forum, **143-7**, 761 (1994).

[183] L. S. Vlasenko, N. T. Son, A. B. van Oosten, C. A. J. Ammerlaan, A. A. Lebedev, E. S. Taptygov, and V. A. Khramtov, Solid State Comm. **73**, 393 (1990).

[184] F. G. Anderson, F. S. Ham, and G. D. Watkins, Phys. Rev. B **45**, 3287 (1992).

[185] P. M. Williams, G. D. Watkins, S. Uftring, and M. Stavola, Phys. Rev. Lett. **70**, 3816 (1993).

[186] P. M. Williams, G. D. Watkins, S. Uftring, and M. Stavola, Mater. Sci. Forum, **143-7**, 891 (1994).

[187] M. Höhne, U. Juda, Yu. V. Martynov, T. Gregorkiewicz, C. A. J. Ammerlaan, and L. S. Vlasenko, Mater. Sci. Forum, **143-7**, 1659 (1994).

[188] M. Höhne, U. Juda, Yu. V. Martynov, T. Gregorkiewicz, C. A. J. Ammerlaan, and L. S. Vlasenko, Phys. Rev. B **49**, 13423 (1994).

[189] F. G. Anderson, F. S. Ham, and G. Grossman, Mater. Sci. Forum **83-7**, 475 (1992).

[190] S. J. Uftring, M. Stavola, P. M. Williams, and G. D. Watkins, Phys. Rev. B **51**, 9612 (1995).

[191] G. Herzberg, *Molecular Structure and Molecular Structure, II: Infrared and Raman Spectra of Polyatomic Molecules,* Van Nostrand Rheinhold, New York, 1945.

[192] C. R. Abernathy, Carbon Doping in III-V Materials in State-of-the-Art Program on Compound Semiconductors XX1V, edited by F. Ren, S. J. Pearton, S. N. G. hu, R. J. Shul, W. Pletschen and T. Kamijo, (The Electrochem. Soc.: Pennington NJ ; (1996) 962, p1).

[193] K. Saito, E. Tokumitsu, T. Akatsuka, M. Miyauchi, T. Yamada, M. Konagai, and K. Takahashi, J. Appl. Phys. **64**, 3975 (1988).

[194] C. R. Abernathy, S. J. Pearton, R. Caruso, F. Ren, and J. Kovalchik, Appl. Phys. Lett. **55**, 1750 (1989).

[195] N. Kobayashi, T. Makimoto, and Y. Horikoshi, Appl. Phys. Lett. **50**, 1435 (1990).

[196] W. E. Hoke, D. G. Weir, P. J. Lemonais, and H. T. Hendriks, Appl. Phys. Lett. **64**, 202 (1994).

[197] E. Tokumitsu, Y. Kudou, M. Konagai, and K. Takahashi, Jap. J. Appl. Phys. **24**, 1189 (1985).

[198] See for example T. J. de Lyon, J. M. Woodall, M. S. Goorsky, and P. D. Kirchner, Appl. Phys. Lett. **56**, 1040 (1990).

[199] K. Woodhouse, R. C. Newman, T. J. de Lyon, J. M. Woodall, G. J. Scilla, and F. Cardone, Semicond. Sci. Technol. **6**, 330 (1991).

[200] P. M. Enquist, Appl. Phys. Lett. **57**, 2348 (1990).

[201] See for example M. C. Hanna, Z. H. Lu, and A. Majerfeld, Appl. Phys. Lett. **58**, 164 (1991).

[202] S. A. Stockman, G. E. Höfler, J. N. Baillargeon, K. C. Hsieh, K. Y. Cheng, and G. E. Stillman, J. Appl. Phys. **72**, 981 (1992)

[203] H. Fushimi, and K. Wada, Mat. Sci. Forum **196-201**, Trans Tech Publications, Switzerland, p. 957-962 (1995).

[204] S. J. Breuer, R. Jones, R. R. Briddon, and S. Öberg, Phys. Rev. B **53**, 16289 (1996).

[205] D. M. Kozuch,M. Stavola, S. J. Pearton, C. R. Abernathy, and W. S. Hobson, J. Appl. Phys. **73**, 3716 (1993).

[206] M. Pan, S. S. Bose, M. H. Kim, G. E. Stillman, F. Chambers, G. Devane, C. R. Ito, and M. Feng, Appl. Phys. Lett. **51**, 596 (1987).

[207] B. Clerjaud, F. Gendron, M. Krause, and W. Ulrici, Phys. Rev. Lett. **65**, 1800 (1990).

[208] D. M. Kozuch,M. Stavola, S. J. Pearton, C. R. Abernathy, and J. Lopata, Appl. Phys. Lett. **57**, 2561 (1990).

[209] A. Amore Bonapasta, Phys. Rev. B **48**, 8771 (1993).

[210] J. Wagner, M. Maier, Th. Lauterback, K. H. Bachem, A. Fischer, K. Ploog, G. Mörsch, and M. Kamp, Phys. Rev. B **45**, 9120 (1992).

[211] J. Wagner, M. Maier, Th. Lauterback, K. H. Bachem, M. J. Ashwin, R. C. Newman, K. Woodhouse, R. Nicklin, and R. R. Bradley, Appl. Phys. Lett. **60**, 2546 (1992).

[212] R. Jones, S. Öberg, and A. Umerski, Materials Science Forum **83-7**, 551 (1992).

[213] R. Jones, Phil. Trans. Roy. Soc. London Ser. A **341**, 351 (1992).

[214] J. Wagner, K. H. Bachem, R. Jones, S. Öberg, B. R. Davidson, R. C. Newman, T. J. Bullough, and T. B Joyce, unpublished report.

[215] E. Pritchard, B. R. Davidson, R. C. Newman, T. J. Bullough, T. B. Joyce, R. Jones and S. Öberg, Semicond. Sci. Technol. **9**, 140 (1994).

[216] Y. Cheng, M. Stavola, C. R. Abernathy, S. J. Pearton, and W. S. Hobson, Phys. Rev. B **49**, 2469 (1994).

[217] B. R. Davidson, R. C. Newman, T. Kaneto, and O. Naji, Phys. Rev. B **50**, 12250 (1994).

[218] B. R. Davidson, R. C. Newman and K. H. Bachem, Phys. Rev. B **52** 5179 (1995).

[219] M. S. Skolnick, T. D. Harris, C. W. Tu, T. M. Brennan, and M. D. Struge, Appl. Phys. Lett. **46**, 427 (1985).

[220] B. Davidson, and R. C. Newman, unpublished results.

[221] M. Stavola, J.-F. Zheng, Y. M. Cheng, C. R. Abernathy, and S. J. Pearton, Mat. Sci. Forum **196-201**, Trans Tech Publications, Switzerland, p. 809-816 (1995).

[222] K. J. Chang, and Sun-Ghil Lee, proceedings of the 23rd International Conference on the Physics of Semiconductors, 1996, pp. 2821-80, (World Scientific, Singapore, New Jersey, London, Hong Kong), ed. M. Scheffler and R. Zimmermann.

[223] B.-H. Cheong, and K. J. Chang, Phys. Rev. B **49**, 17436 (1994).

[224] J. Wagner, R. C. Newman, B. R. Davidson, S. P. Westwater, T. J. Bullough, T. B. Joyce, C. D. Latham, R. Jones, and S. Öberg, Phys. Rev. Lett., submitted, 28 June 1996.

[225] C. P. Ewels, R. Jones, S. Öberg, J. Miro, and P. Deák, Phys. Rev. Lett. **77**, 865 (1996).

[226] M. Tinkham, 'Group theory and quantum mechanics', (McGraw-Hill, New York) 1964.